

https://dspace.org/

Synthesis of carbon dots reduced palladium catalysts: application in the hydrogenation of cinnamaldehyde reaction

Magubane, Alice

2022
https://hdl.handle.net/10539/34591

Downloaded from a DSpace repository. https://dspace.org/

Synthesis of carbon dots reduced palladium catalysts: Application in the hydrogenation of cinnamaldehyde reaction

By:

Alice Magubane

(M.Sc.)

Student number: 543749

A Thesis submitted to the Faculty of Science, University of the Witwatersrand, Johannesburg, in fulfilment for the degree of **Doctor of Philosophy** in Chemistry.

Supervisor: Prof. Neil J. Coville

Co-Supervisor: Dr. Manoko Maubane-Nkadimeng

University of the Witwatersrand, Johannesburg. November 2021

DECLARATION

I declare that this Thesis is my own, unaided work. It is being submitted for the Degree of Doctor of Philosophy at the University of the Witwatersrand, Johannesburg. It has not been submitted before for any degree or examination at any other University.

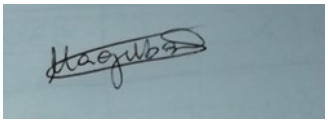

(signed) Alice Magubane

On this 26 day of November 2021

ABSTRACT

The selective hydrogenation of α,β-unsaturated aldehydes, such as cinnamaldehyde (CALD), continues to gain attention in both academic and industrial fields. The selective hydrogenation of CALD is known for the production of the products (hydrocinnamaldehyde (HCALD), cinnamyl alcohol (CA), and 3-phenyl-1-propanol (3P1P)) that are of importance in the production of fine chemicals, spices, and pharmaceutical intermediates. In this study Pd catalysts supported on carbon dots (CDs), solid carbon spheres (SCSs), and hollow carbon spheres (HCSs) were used in the liquid phase hydrogenation of CALD. The influence of varying the CALD hydrogenation reaction conditions (i.e., catalyst mass, temperature, hydrogen flow rate, CALD concentration) on the activity and selectivity of the catalysts were also investigated.

CDs were synthesized via polymerization and carbonization of sucrose and oleic acid, or sucrose and urea under different reaction conditions. CDs with a size range of 0.2 to 16 nm were prepared using a hydrothermal treatment of sucrose and oleic acid. The doping of the CDs using urea resulted in the formation of nitrogen-doped CDs (NCDs) with size < 10 nm, and carbon nanoparticles (size < 100 nm). The as-synthesized CDs (from sucrose and oleic acid) were used to reduce H_2PdCl_4 to metallic Pd nanoparticles (NPs) with $d_{Pd} = 9.1 \pm 1.6$ nm, as confirmed by PXRD and HRTEM studies. Although Pd particles were made to be larger than the CDs, to observe any inverse support effects, the TEM data indicated a formation of carbon layer over the Pd NPs. The synthesized Pd/CDs catalyst (< 1 % loading) and CDs were both tested in the liquid phase hydrogenation of CALD. The CDs gave a CALD conversion (40 %, 4 h) with selectivity towards the reduction of the C=O bond (CA). The Pd/CDs catalyst, by contrast, was only selective in the reduction of the C=C bond (conversion 73 %) indicating the dominance of Pd over the CDs in the reaction.

SCSs were prepared via the polymerization of resorcinol and formaldehyde (RF) resins in the presence of a catalyst (ammonia) followed by carbonization of the RF resins at high temperature (900 °C). From a TEM analysis the SCSs were spherical in morphology and had an average diameter of 535 ± 73 nm. The obtained SCSs were functionalized (fSCSs) using a nitric/sulfuric acid treatment. The Pd NPs nanoparticles were deposited on the surface of the CSs support using a liquid phase reduction method. The Pd particle size varied from 6.0 ± 2.3

and 12.0 ± 3.4 nm for the SCSs and fSCSs respectively. The XPS data confirmed the presence of PdOx in both Pd/SCSs (8.7 %) and Pd/fSCSs (22.6 %). When the Pd/SCSs and Pd/fSCSs were tested in the hydrogenation of CALD, the complete hydrogenation of CALD was obtained. The Pd/SCSs catalyst had a selectivity of 100 % to 3P1P (i.e., complete reduction of the C=C and C=O bond). The Pd/fSCSs catalyst produced CA as a major product followed by 3P1P, by-products, and HCALD.

HCSs (487 ± 28 nm) were prepared using a hard-core templating method, in which polystyrene spheres (PSSs) were used as a hard template followed by coating with an RF polymer followed by the removal of template and annealing of the HCSs using a chemical vapour deposition method under an inert atmosphere. The loading of Pd NPs (6.4 ± 2.9 nm) on the outer surface of the HCSs was shown by TEM and PXRD data. A CALD conversion of 100 % was obtained with the Pd/HCSs catalyst and the catalyst selectivity towards HCALD decreased with an increase in the reaction time. CDs reduced Pd NPs catalyst supported on HCSs (Pd/CDs/HCSs) was also prepared and a Pd particle size of 45.6 ± 26.5 nm was obtained. The catalyst had poor activity in the hydrogenation of CALD, but it was selective to the reduction of the C=C bond, forming HCALD.

DEDICATION

I would like to dedicate this work to the following people:

To my mom Sarah D. Magubane

To the rest of the Magubane family

To my late grandfather and two siblings

ACKNOWLEDGMENTS

- I would like to thank my supervisor Prof. Neil Coville for his guidance, constructive criticism, and support in accomplishing this work.

- To my co-supervisor Dr. Manoko Maubane-Nkadimeng I am grateful for your support and guidance in finishing this work.

- To my mentor Dr. Prakash Gangatharan thank you for your support and assistance with the application set-up and analysis.

- To the CATMAT group I am forever grateful for your kindness and positive criticism, special thanks to Dr. T. Mongwe, Dr. P. Mente, Dr. V. Mashindi, Dr. T. N. Phaahlamohlaka, Miss L. Mokoloko, Miss P. Mphago, Miss T. Buthelezi, Mr T. Ntuli, Mr. O. Mkhari, Mr. T. Molefe, Mr. L. Sikeyi, and Miss B. Thlaole.

- To all the staff at the University of the Witwatersrand Microscopy and Microanalysis unit, thank you all for the training and assistance with the analysis instruments. I would also like to thank Mr Jordaan (NIMSA, CSIR) for XPS analysis, Miss Rhikhotso (DST/CSIR Nanotechnology Innovation Centre) for HRTEM analysis, Mrs Charity Maepa (laboratory for Microscopy and Microanalysis, UP) for HRTEM analysis, Dr. Rudolph Erasmus for PL and Raman analysis (School of Physics), Mrs Petra Dinham (School of Chemical and Metallurgical Engineering, Wits) for SEM analysis, and Prof. M. Lee and Dr. J. O'Connell for HRTEM and HAADF STEM analysis (Centre for High Resolution Electron Microscopy, NMU).

- To all the staff member at the University of the Witwatersrand Physics workshop, I am grateful for their assistance with some of the apparatus used in this work. Special thanks to Mr T. Mashoene and Mr L.A. Mafemba.

- "The support of the DSI-NRF Centre of Excellence in Strong Materials (CoE-SM) towards this research is hereby acknowledged. Opinions expressed and conclusions

arrived at, are those of the aurthor and are not necessarily to be attributed to the CoE-SM.” I acknowledge the University of the Witwatersrand (Postgraduate Merit Award) for funding.

❖ I would like to extend my warmest gratitude to my family, Mr. S. M. Ndala, Miss N. Z. Zondi, and Dr. T. Mongwe for their prayers, support, and love.

LIST OF PUBLICATIONS, PRESENTATIONS, SUMMER SCHOOL, AND AWARD

PUBLICATIONS

- Mente, P.; Mashindi, V.; **Magubane, A**.; Phaahlamohlaka, T.; Gangatharan, P.; Forbes, R.; Coville, N. *Canadian Journal of Chemistry* **2021**. (Role played: Assisted the main author with the catalysis part).
- Sitole, S.; Nyamupangedengu, C.; **Magubane, A**.; Coville, N. Synthesis of Hollow Carbon Spheres for Fabrication of C\Epoxy Nanocomposite Insulation. In *2019 IEEE AFRICON*; IEEE: Accra, Ghana, 2019; pp 1–6. (Role played: Co-supervised the main author (MSc) and assisted with the synthesis of the hollow carbon spheres).
- **Magubane, A**.; Gangatharan, P. M.; Mente, P.; Phaahlamohlaka, T. N.; Maubane-Nkadimeng, M. S.; Lee, M.; O'Connell, J.; Neil, N. J., Hydrogenation of cinnamaldehyde using carbon dots reduced palladium nanoparticles: Catalyst deactivation by carbon growth and sintering of palladium nanoparticles, **(to be submitted to NJC).**
- **Magubane, A**.; Phaahlamohlaka, T. N.; Maubane-Nkadimeng, M. S.; Neil, N. J., Hydrogenation of cinnamaldehyde over palladium nanoparticles supported on a functionalized solid carbon spheres catalyst, **(to be submitted).**
- **Magubane, A**.; Maubane-Nkadimeng, M. S.; Neil, N. J., Hydrogenation of cinnamaldehyde using a palladium catalyst supported on hollow carbon spheres, **(to be submitted).**

PRESENTATIONS

- Alice Magubane, Prakash M. Gangatharan, Manoko Maubane-Nkadimeng, and Neil Coville, Synthesis of Pd/Cdots as potential catalysts in hydrogenation reactions (**Poster presentation**), CoE-SM Annual Student Presentation Workshop, Wits, Johannesburg, April 2018.
- Alice Magubane, Prakash M. Gangatharan, Manoko Maubane-Nkadimeng, and Neil Coville, Carbon dots reduced palladium nanoparticles as potential hydrogenation catalysts (**Poster presentation**), MSSA 2018 workshop, Wits, Johannesburg, 2018.
- Alice Magubane, Prakash M. Gangatharan, Manoko Maubane-Nkadimeng, and Neil Coville, Carbon dots reduced palladium nanoparticles as potential hydrogenation

catalysts (**Poster presentation**), CATSA annual conference, Limpopo, November 2018.

- Alice Magubane, Prakash M. Gangatharan, Manoko Maubane-Nkadimeng, and Neil Coville, Hydrogenation of CALD using carbon dots reduced palladium nanoparticles (**Poster presentation**), CoE-SM Annual Student Presentation Workshop, Wits, Johannesburg, May 2019.
- Alice Magubane, Manoko Maubane-Nkadimeng, and Neil Coville, Carbon dots reduced palladium nanoparticles as potential hydrogenation catalysts (**Poster presentation**), CATSA annual conference, Western Cape, November 2019.

SUMMER SCHOOL WORKSHOP

- Attended summer school and workshop in Calorimetry and Thermal Analysis held in Lyone, France, 17 - 22 June 2018.

AWARD

- Postgraduate Merit Award **(2018 until 2020)** University of the Witwatersrand.

TABLE OF CONTENTS

Synthesis of carbon dots reduced palladium catalysts: Application in the hydrogenation of cinnamaldehyde reaction i

DECLARATION ii

ABSTRACT iii

DEDICATION v

ACKNOWLEDGMENTS vi

LIST OF PUBLICATIONS, PRESENTATIONS, SUMMER SCHOOL, AND AWARD viii

PUBLICATIONS viii

PRESENTATIONS viii

SUMMER SCHOOL WORKSHOP ix

AWARD ix

TABLE OF CONTENTS x

LIST OF FIGURES xviii

LIST OF SCHEMES xxiii

LIST OF TABLES xxiv

ABBREVIATIONS xxvi

Chapter 1: Introduction: Hydrogenation of cinnamaldehyde 1

1.1 Background 1

1.2 Problem statement 3

1.3 The motivation of the study 4

1.4 Aims and objectives of the study 4

1.5 Outline of thesis 5

1.6 References 6

Chapter 2: Literature review 9

2.1 Background on carbon nanomaterials 9

2.2 Carbon dots 9

2.2.1 Introduction to carbon dots 9

2.2.2 Synthesis of carbon dots 11

2.2.2.1 Top-down approaches 12

2.2.2.2 Bottom-up approaches 15

2.2.3 Surface modification of carbon dots 19

2.2.4 Application of carbon dots 20

2.3 Carbon spheres 22

2.3.1 Introduction to carbon spheres 22

2.3.2 Solid carbon spheres 23

2.3.3 Hollow carbon spheres 28

2.4 Catalysts supported on carbon nanomaterials 29

2.4.1 Application of metals supported on carbon nanomaterials in the hydrogenation of cinnamaldehyde 30

2.4.2 Carbon nanomaterials as catalysts (carbocatalysis) 33

2.4.3 Hydrogenation of cinnamaldehyde using carbon nanomaterials supported palladium catalysts 34

2.5 Conclusions 36

2.6 References 36

Chapter 3: Experimental methods and characterization techniques 43

3.1 Introduction 43

3.2 Synthesis of carbon nanomaterials 43
3.2.1 Materials 43
3.2.2 Synthesis of carbon dots 44
3.2.2.1 Reflux method 44
3.2.2.2 Autoclave method 44
3.2.3 Synthesis of functionalized solid carbon spheres 44
3.2.4 Synthesis of hollow carbon spheres 45
3.2.4.1 Synthesis of polystyrene spheres (PSSs) 45
3.2.4.2 Synthesis of HCSs 45
3.3 Synthesis of the catalysts 46
3.3.1 Synthesis of Pd/CDs composite 46
3.3.2 Synthesis of Pd/CSs 46
3.4 Characterization techniques 46
3.4.1 HRTEM, TEM, STEM, and SEM 46
3.4.2 Powder X-ray diffraction (PXRD) 47
3.4.3 Thermogravimetric analysis 47
3.4.4 UV-vis and PL spectroscopy 47
3.4.5 Fourier transform infrared spectrometer 48
3.4.6 X-ray photoelectron spectroscopy 48
3.4.8 Laser Raman spectroscopy 48
3.4.9 Calculation of product yield 48
3.5 Catalyst testing and product analysis 48
3.5.1 Catalytic hydrogenation of CALD 48
3.5.2 Product analysis 49
3.5.3 Calculations of CALD conversion and selectivity (%) 49
3.6 References 49

Chapter 4: Synthesis of carbon dots using hydrothermal treatment of sucrose.....51

4.1 Introduction 51

4.2 Experimental procedure 52

4.2.1 Materials 52

4.2.2 Synthesis of the CDs.....52

4.3 Characterization techniques 52

4.4 Results and discussion.....52

4.4.1 TEM analysis.....52

4.4.2 PXRD analysis.....56

4.4.3 FTIR analysis.....57

4.4.4 Thermal stability analysis.....58

4.4.5 Optical properties 60

4.5 Conclusions 62

4.6 References 62

Chapter 5: Hydrogenation of cinnamaldehyde using carbon dots reduced palladium nanoparticles 64

5.1 Introduction 64

5.2 Experimental procedure 66

5.3 Characterization of materials 66

5.4 Catalytic tests 67

5.5 Results and discussion.....67

5.5.1 Characterization of the CDs 67

5.5.1.1 TEM and PXRD analysis 67

5.5.1.2 Thermal stability (TG analysis).....68

5.5.1.3 FTIR and XPS analysis 69
5.5.1.4 Optical properties 70
5.5.2 Characterization of the Pd/CDs composite 71
5.5.2.1 Morphology analysis 71
5.5.2.2 PXRD and thermal stability analysis 72
5.5.2.3 Optical properties 73
5.5.2.4 FTIR and XPS analysis 74
5.5.2.5 Raman analysis 74
5.5.3 Summary 75
5.5.4 Hydrogenation of CALD using CDs and Pd/CDs composite 76
5.5.4.1 Catalytic reactions of CDs 76
5.5.4.2 Catalytic activity of Pd/CDs 77
5.5.4.3 Comments of the mechanism 80
5.6 Conclusions 81
5.7 References 81

Chapter 6: Hydrogenation of cinnamaldehyde over palladium nanoparticles supported on a functionalized solid carbon spheres catalyst 85
6.1 Introduction 85
6.2 Experimental procedure 88
6.2.1 Materials 88
6.2.2 Synthesis of solid carbon spheres 88
6.2.3 Acid treatment of SCSs 89
6.2.4 Synthesis of 5 wt. % Pd/SCSs or Pd/fSCSs catalysts 89
6.3 Characterization techniques 89
6.4 Catalytic tests 90

6.5 Results and discussion 90
6.5.1 Characterization of the carbon supports 90
6.5.1.1 TEM analysis 90
6.5.1.2 Thermal gravimetric analysis 91
6.5.1.3 PXRD and Raman analysis 92
6.5.1.4 BET surface area analysis 93
6.5.1.5 XPS and FTIR analysis 93
6.5.2 Characterization of Pd/SCSs and Pd/fSCSs 95
6.5.2.1 TEM analysis 95
6.5.2.2 Thermal gravimetric analysis 96
6.5.2.3 PXRD analysis 97
6.5.2.4 BET analysis 97
6.5.2.5 XPS analysis 98
6.5.3 Hydrogenation of CALD 100
6.5.4 Optimization of conditions 100
6.5.4.1 Catalyst selectivity 100
6.5.4.2 Reaction temperature 101
6.5.4.3 Catalyst mass 103
6.5.4.4 H_2 gas flow rate 104
6.5.4.5 CALD concentration 105
6.5.4.6 Stirring rate 106
6.5.4.7 Catalyst stability test 107
6.5.8 Summary on the catalyst activity and selectivity 107
6.6 Conclusions 108
6.7 References 108

Chapter 7: Hydrogenation of cinnamaldehyde using a palladium catalyst supported on hollow carbon spheres 111

7.1 Introduction 111

7.2 Experimental procedures 112

7.2.1 Materials 112

7.2.2 Synthesis of PSSs 112

7.2.3 Synthesis of HCSs 112

7.2.4 Synthesis of 5 wt.% Pd/HCSs composite 113

7.2.5 Synthesis of Pd/CDs/HCSs 113

7.3 Characterization techniques 113

7.4 Catalytic tests 114

7.5 Results and discussion 114

7.5.1 Characterization of materials 114

7.5.1.1 Morphology and thermal stability analysis of the template 114

7.5.1.2 TEM analysis of the support and the catalyst 115

7.5.1.3 PXRD analysis 116

7.5.1.4 Thermal stability analysis 117

7.5.1.5 BET surface area analysis 118

7.5.1.6 Raman analysis 118

7.5.1.7 XPS analysis 119

7.5.1.8 Summary 121

7.5.2 Catalysis 121

7.5.2.1 Effect of the reaction temperature 121

7.5.2.2 Effect of the catalyst mass 122

7.5.2.3 Effect of hydrogen flow rate 123

7.5.2.4 Catalyst stability test 124

7.5.2.5 Summary on the catalyst activity.....125

7.6 Hydrogenation of CALD using carbon dots reduced Pd catalyst supported on hollow carbon spheres.....128

7.6.1 Synthesis of 5 wt. % Pd/CDs/HCSs catalyst.....128

7.6.2 Catalyst characterization.....128

7.6.3 Catalyst performance evaluation.....129

7.7 Comparison of the catalytic activity of the synthesized catalysts.....130

7.8 Conclusions.....131

7.9 References.....131

Chapter 8: General conclusions and recommendations.....134

8.1 Conclusions.....134

8.2 Recommendations.....137

Appendix A: Supporting information.....139

LIST OF FIGURES

Chapter 1

Figure 1.1: Reaction pathway for the selective hydrogenation of CALD……...…….1

Chapter 2

Figure 2.1: Representation of chemical structure of CDs [7]…….…….10

Figure 2.2: Schematic representation of different types of carbon dots [18]……...….11

Figure 2.3: Scheme of two approaches used in the synthesis of CDs [18]……...…….12

Figure 2.4: (a) Reaction set-up for the synthesis of CDs, digital image of CDs (b) before treatment, (c) after treatment, (d) particle size distribution of CDs, (e) TEM image of CDs, and (f) HRTEM image of CDs [21]…….13

Figure 2.5: TEM images of GQDs synthesized at 90 °C by using oxidation at 1 V for (a) 15 h, (c) 11 h, (e) 7 h with their corresponding particle size distribution (b, d, f) respectively. (g) The HRTEM image of GQDs and (h) SAED pattern of GQDs [22]…….13

Figure 2.6: HRTEM images of CDs synthesized using different laser pulse widths (a) 0.3 ms, (b) 0.9 ms, and (c) 1.5 ms with their corresponding particle size distribution (d, e, and f) respectively [23]……...14

Figure 2.7: TEM images of CDs passivated using TTDDA derived from (a) CAC, (b) WAC, and (c) CNAC with their corresponding particle size distribution. (d) The size distribution of TTDDA passivated CDs derived from CAC measured using a Malvern NanoZS zetasizer, (inset- CDs solution under UV light (365 nm)) [24]……..15

Figure 2.8: (a) TEM image, (b) AFM image, and (c) particles size distribution of CDs [25]…….15

Figure 2.9: TEM image of CDs and the inset is the particle size distribution of the CDs [26]…....16

Figure 2.10: (a) TEM image of CDs [27]…….….16

Figure 2.11: (a) TEM image and (b) particle size distribution of CDs [28]……....17

Figure 2.12: (a) TEM image (inset-HRTEM) and (b) particle size distribution of CDs [29]…….18

Figure 2.13: HRTEM images of CDs synthesize using different carbon precursors and their corresponding magnified HTREM images inset (a) TMB, (b) DBA, (c) PY, and (d) PHA [30]…19

Figure 2.14: Model showing the arrangement of carbon layers of a single carbon black particle with concentric layers [58]……23

Figure 2.15: Schematic representation showing polymerization of RF resin using the extended Stöber process [63]……...……24

Figure 2.16: SEM images showing the effect of temperature using different precursors in the synthesis of CSs [67]…….26

Figure 2.17: (a) Changes in the pH solution during HTC of the glucose at 200 °C and yield of the SCSs with reaction time, SEM images of the SCSs synthesized after (b) 3h, and (c) 24h [68]……...27

Figure 2.18: Schematic representation of the hard-core templating method for the synthesis of HCSs……..……29

Chapter 4

Figure 4.1: TEM images of CDs (a-c) and their corresponding particle size distributions (d-f)……...54

Figure 4.2: TEM images of N-CDs (a-e) and their corresponding particle size distributions (f-i)……..……55-56

Figure 4.3: PXRD of (a) sucrose and (b) the synthesized CDs and NCDs with different concentration……...…….57

Figure 4.4: FTIR of the synthesized (a) CDs and (b) NCDs from different sucrose concentration……58

Figure 4.5: TG and DTG profiles of the synthesized CDs (a) 0.1 M, (b) 0.15 M, (c) 0.3 M, and NCDs (d) 0.15 M + urea, and (e) 0.3 M + urea……..59

Figure 4.6: UV-vis spectra of the synthesized (a) CDs and (b) NCDs……61

Figure 4.7: PL spectra of the synthesized (a) CDs and (b) N-CDs…….62

Chapter 5

Figure 5.1: Reaction pathway for the selective hydrogenation of CALD……65

Figure 5.2: (a) HRTEM image and (b) particle size distribution of the CDs…….68

Figure 5.3: PXRD of (a) sucrose and (b) CDs synthesized using sucrose……68

Figure 5.4: TGA and the DTG profile of the CDs…….69

Figure 5.5 (a) FTIR spectra, (b) XPS spectra, and (c) C1s spectra of the CDs……..70

Figure 5.6: (a) UV-vis spectra and (b) PL spectra of the CDs……71

Figure 5.7: (a-b) HRTEM images and (c-d) HAAFD STEM bright and dark images of 1 wt. % Pd/CDs…….72

Figure 5.8: (a) PXRD and (b) TGA and DTG of 1 wt. % Pd/CDs catalyst……73

Figure 5.9: (a) UV-vis spectra and (b) PL spectra of the 1 wt. % Pd/CDs……..73

Figure 5.10: (a) FTIR spectra, (b) XPS spectra, and (c) C1s spectra of the 1 wt. % Pd/CDs…..74

Figure 5.11: Raman spectra of (a) CDs and (b) 1 wt. % Pd/CDs……75

Figure 5.12: The conversion of CALD over CDs catalyst at 40 °C and 60 °C (50 mg CDs, 50 mL/min = H_2 flow rate, 100 ml ethanol, and 1.32 g CALD)…….75

Figure 5.13: Conversion of CALD over CDs and fCDs catalysts at 40 °C. Reference conditions: mcatalyst = 50 mg, t = 7 h, 50 mL/min = H_2 flow rate, 100 ml ethanol, and 1.32 g CALD……77

Figure 5.14: The conversion of CALD over Pd/CDs catalyst. Reference conditions: T = 60 °C, t = 7 h, 50 mL/min = H_2 flow rate, 100 ml ethanol, and 1.32 g CALD……78

Figure 5.15: Effect of temperature on the activity of the Pd/CDs catalyst…….78

Figure 5.16: The conversion of CALD over Pd/CDs catalyst at different hydrogen flow rate. Reference conditions: T = 60 °C, 50 mg catalyst, 100 ml ethanol, and 1.32 g CALD……79

Figure 5.17: TEM images of the Pd/CDs catalyst after first cycle…….80

Chapter 6

Figure 6.1: TEM images of (a) RF spheres, (c) fSCSs, and their corresponding particle size distributions (b and d)……...91

Figure 6.2: (a) TGA and (b) DTG profiles of SCSs and fSCSs……92

Figure 6.3: (a) PXRD profiles and (b) Raman spectra of SCSs and fSCSs……92

Figure 6.4: N_2 adsorption-desorption isotherms of the (a) SCSs and (b) fSCSs……93

Figure 6.5: (a) XPS spectra, (b) C1s spectra, and (c) O1s spectra of the fSCSs……94

Figure 6.6: FTIR of the (a) pristine SCSs and (b) functionalized SCSs……95

Figure 6.7: TEM images of (a) Pd/SCSs, and (c) Pd/fSCSs, and (b,d) particle size distribution of Pd NPs……95-96

Figure 6.8: TGA and DTG profiles of (a) Pd/SCSs and (b) Pd/fSCSs……...96

Figure 6.9: PXRD profiles of the Pd/SCSs and Pd/fSCSs……97

Figure 6.10: (a and b) XPS spectra and (c and d) Pd $3d_{5/2}$ spectra of Pd/SCSs and Pd/fSCSs catalysts respectively……99

Figure 6.11: Conversion of CALD over Pd/SCSs. Reference conditions: 6 h, 100 mg catalyst, 50 mL/min = H_2 flow rate, 100 ml ethanol, T = 60 °C, and 1.32 g CALD……101

Figure 6.12: The influence of temperature on the (a) CALD conversion and (b) selectivity and (c) Arrhenius plot for CALD hydrogenation over the Pd/fSCSs……103

Figure 6.13: The influence of the catalyst mass on the (a) CALD conversion and (b) selectivity……...104

Figure 6.14: (a) The effect of H_2 flow rate on the (a) activity and (b) selectivity of the Pd/fSCSs catalyst, and (c) the effect of the removal of dissolved traces of oxygen (A; removal; (B) ; no removal) on the CALD conversion on the Pd/fSCSs catalyst……105

Figure 6.15: Effect of CALD concentration on the (a) conversion and (b) selectivity on the hydrogenation of CALD over the Pd/fSCSs catalyst……...106

Figure 6.16: Influence of the stirring speed on (a) CALD conversion and (b) selectivity over 5 wt. % Pd/fSCSs catalyst……..106

Figure 6.17: Recycling of (a) Pd/fSCSs and (b) Pd/SCSs over five cycles at 60 °C and 50 mL/min H_2 flow rate……...107

Chapter 7

Figure 7.1: (a) TEM image, (b) particle size distribution, (c) SEM image, and (d) TGA and DTA profiles of the as-synthesized PSSs……115

Figure 7.2: TEM images of (a) HCSs, (c) 5 wt. % Pd/HCSs catalyst, and their respective size distributions (b, d)……...116

Figure 7.3: PXRD pattern of the HCSs and 5 wt. % Pd/HCSs catalyst……117

Figure 7.4: TGA and DTG profiles for (a) HCSs and (b) 5 wt. % Pd/HCSs catalyst……117

Figure 7.5: Raman spectra of the HCSs and 5 wt. % Pd/HCSs……119

Figure 7.6: (a) XPS spectra survey, and deconvoluted spectrum of (b) C1s, (c) O1s, and (d) Pd3d……120

Figure 7.7: The influence of the reaction temperature on the (a) CALD conversion and (b-d) selectivity over the 5 wt. % Pd/HCSs. Reference conditions: t = 6 h, $mass_{catalyst}$ = 150 mg, 50 mL/min = H_2 flow rate, 100 ml ethanol, and 1.32 g CALD……122

Figure 7.8: The influence of the catalyst amount on the (a) CALD conversion and (b-d) selectivity over the 5 wt. % Pd/HCSs. Reference conditions: t = 6 h, T= 60 °C, 50 mL/min = H_2 flow rate, 100 ml ethanol, and 1.32 g CALD……..123

Figure 7.9: Influence of the hydrogen gas flow rate on the (a) CALD conversion and (b-d) selectivity over Pd/HCSs catalyst……...124

Figure 7.10: (a) Recycling of Pd/HCSs catalyst over five runs at 60 °C and (b) TEM images of Pd/HCSs after recycling……..125

Figure 7.11: (a) TEM image, (b) PXRD pattern, and (c) TGA and DGA profiles of Pd/CDs/HCSs catalyst……129

Figure 7.12: (a) CALD conversion, (b, c) selectivity over Pd/CDs/HCSs catalyst at 40 and 60 °C……130

LIST OF SCHEMES

Scheme 4.1: Synthesis of (a) CDs and (b) NCDs using sucrose as carbon source and urea as nitrogen dopant via hydrothermal treatment…….52

Scheme 6.1: Reaction pathway for the selective hydrogenation of CALD……86

LIST OF TABLES

Chapter 2

Table 2.1: Summary of work done on the hydrogenation of CALD using noble metals supported on CNMs…….31-33

Chapter 4

Table 4.1: Summary of the reaction conditions along with the particle size of the synthesized CDs and NCDs and % yield……..……53

Table 4.2: Summary of the maximum decomposition temperature and % weight loss of the synthesized CDs and NCDs…….….60

Table 4.3: Optical properties of the synthesized CDs and NCDs…….….61

Chapter 5

Table 5.1: CDs and Pd/CDs activity and selectivity for the hydrogenation of CALD……..…77

Chapter 6

Table 6.1: Properties of the carbon supports and the catalyst supported on the carbon spheres……..98

Table 6.2: Elemental quantification of Pd/CSs catalysts using XPS analysis……99

Table 6.3: Binding energy and % of Pd, PdO, and PdO_2 content of the Pd/CSs catalysts from XPS…….100

Table 6.4: CALD conversion and selectivity of Pd/fSCSs and Pd/SCSs……101

Chapter 7

Table 7.1: Summary of the textual properties of the HCSs and Pd/HCSs catalyst……118

Table 7.2: Summarizes the D and the G band positions, and I_D/I_G ratios obtained from the HCSs and Pd/HCSs catalyst……..119

Table 7.3: Elemental quantification of Pd/HCSs catalysts using XPS analysis……..….120

Table 7.4: Summary of the work done using Pd catalysts supported on CNMs in the selective hydrogenation of CALD…….126

APPENDIX A: SUPPLEMENTARY INFORMATION

List of figures

Figure S5.1: TEM images of Pd/CDs catalyst…….139

Figure S5.2: TEM images of CDs conversion to (a) aggregates and (b) carbon sheets via annealing at 190 and 300 °C respectively……139

Figure S5.3: (a) FTIR spectra and (b) DTG profile of the as-synthesized CDs and fCDs……140

Figure S5.4: The conversion of CALD over Pd/CDs catalyst at different reaction temperatures. Reference conditions: $m_{catalyst}$ = 100 mg, t = 8 h, 50 mL/min = H_2 flow rate, 100 ml ethanol, and 1.32 g CALD……142

Figure S5.5: The CALD conversion over Pd/CDs catalyst at various CALD concentrations (T = 60 °C, $m_{catalyst}$ = 50 mg, t = 8 h, 50 mL/min = H_2 flow rate, and 100 ml ethanol)……...……142

Figure S5.6: Effect of the catalyst mass on the activity of the Pd/CDs catalyst……143

List of tables

Table S5.1: Comparison of the position of the oxygenated functional groups…….140

Table S5.2 shows a comparison of different characterization techniques used in this study with those from the literature similar to this work……..……141

ABBREVIATIONS

CDs	**Carbon dots**
FCDs	**Surface passivated carbon dots**
SCSs	**Solid carbon spheres**
fSCSs	**Functionalized solid carbon spheres**
HCSs	**Hollow carbon spheres**
Pd/CDs	**Carbon dots reduced palladium nanoparticles**
Pd/SCSs	**Palladium nanoparticles supported on solid carbon spheres**
Pd/fSCSs	**Palladium nanoparticles supported on functionalized solid carbon spheres**
Pd/HCSs	**Palladium nanoparticles supported on hollow carbon spheres**
CALD	**Cinnamaldehyde**
CA	**Cinnamyl alcohol**
HCALD	**Hydrocinnamaldehyde**
3P1P	**3-phenyl-1-propanol**
H_2PdCl_4	**Dihydrogen tetrachloropalladate**
TEM	**Transmission electron microscopy**
HRTEM	**High-resolution transmission electron microscopy**
HAADF	**High-angle annular dark-field imaging**
STEM	**Scanning transmission electron microscopy**
FTIR	**Fourier transform infrared spectrometer**
CNTs	**Carbon nanotubes**
AC	**Activated carbon**
CNFs	**Carbon nanofibers**
CVD	**Chemical vapour deposition**
PL	**Photoluminescence**

TGA	**Thermogravimetric analysis**
BET	**Brunauer-Emmet and Teller**
PXRD	**Powder X-ray diffraction**

Chapter 1: Introduction: Hydrogenation of cinnamaldehyde

1.1 Background

Selective hydrogenation of α,β-unsaturated aldehydes into their corresponding unsaturated alcohols has been studied intensively in both industrial and academic arenas [1-6]. This enormous attention is due to the application of the unsaturated alcohols in the production of pharmaceuticals, fine chemicals, and spices [1, 2]. Cinnamaldehyde (CALD) is one of the members of the α,β-unsaturated aldehyde family with the formula $C_6H_5CH=CHCHO$. The selective hydrogenation of CALD has been widely studied because of the great fundamental and industrial value of the products obtained in this process [2, 7]. Hydrogenation of CALD can proceed via the reduction of the C=C bond forming hydrocinnamaldehyde (HCALD) and the reduction of the C=O bond forming cinnamyl alcohol (CA) [1, 2, 7-9]. Both HCALD and CA are the intermediate products and they can both be further hydrogenated to give 3-phenyl-1-propanol (3P1P) [1, 2, 7-9]. Figure 1.1 shows the schematic representation of the selective hydrogenation of CALD.

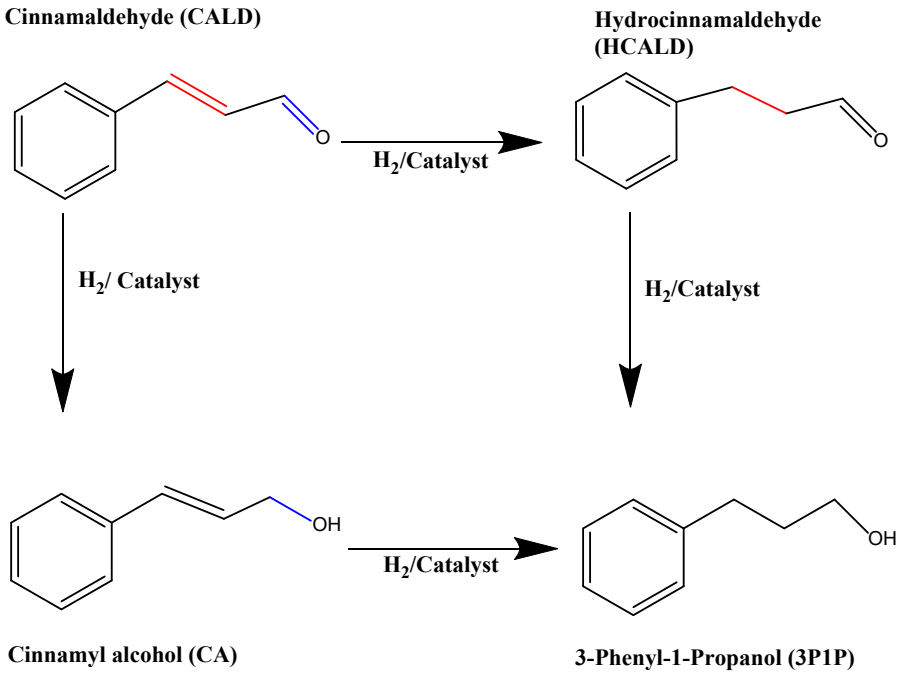

Figure 1.1: Reaction pathway for the selective hydrogenation of CALD (adapted from Zeng *et al.* [2]).

Selective hydrogenation of CALD is still a challenge, as the hydrogenation of the C=C bond is kinetically and thermodynamically favoured compared to the cleavage of the C=O bond as the latter reaction requires more energy [2, 7, 10-21]. All the products formed from this process are of practical value. HCALD has been used in the synthesis of an intermediate reagent of an antiviral pharmaceutical (i.e. HIV protease inhibitor) [1, 4, 14, 22]. CA has found use in the synthesis of perfumes, pharmaceuticals, fixatives, modifiers, cosmetics, and fungicides [2, 4, 9, 12, 22-24]. 3P1P has been used in the field of medicine and has been used as a fragrance reagent in the production of cosmetics, shampoos, detergents, and toilet soaps [8, 9].

The conjugation effect between the C=C and C=O bonds poses difficulty in the selective control of the hydrogenation reaction of the C=O bond [2]. The conversion of CALD to CA has been commercially achieved in high yields by the process named the Meerwein-Ponndorf-Verley reaction, which uses aluminium triisopropoxide as a reagent [7]. The problem with this process is the disposal of aluminium salts. This has led to an interest in finding an alternative catalytic hydrogenation process that does not use stoichiometric reagents [7].

Studies based on heterogeneous metallic catalysts have been conducted in order to find a better way to control the selectivity of the reaction by means of alloying, ligand modification, and support optimization [25]. Among the different types of supports used in heterogeneous catalysis, carbon materials have been useful, although there are also certain limitations for their use as a support [26]. Carbon materials cannot be used in hydrogenation reactions at temperatures exceeding 700 °C (formation of methane) and in the presence of oxygen, at temperatures higher than 500 °C (gasification to form CO_2) [26]. Besides the aforementioned limitations, carbon materials have advantages as catalyst supports such as the facile recovery of precious materials for recycling from metal supported catalysts and weak metal-support interactions [26, 27]. In addition, carbon materials supported catalysts have been reported to have a greater resistance to poisoning [28].

In this study, carbon dots (CDs) will be explored as either a reducing agent or as a "support" to establish metal-to-support interactions between the carbon dot and palladium i.e. a Pd/CDs composite. CDs are a new class of carbon-based nanomaterials with sizes of less than 10 nm [29-34]. The CDs were accidentally discovered as by-products in 2004 by Xu and colleagues in the process of separation and purification of single-walled CNTs from arc-discharged soot [29-31, 35]. Further analysis on this by-product was carried out as they exhibited fluorescent properties. Analysis conducted of the fluorescent material showed that they comprised of very

small particles of a carbonaceous material [36]. Upon their discovery, they were termed fluorescent carbon nanoparticles until 2006 when they received their name "carbon quantum dots" from Sun *et al*. who proposed a synthetic route to produce CDs with much-enhanced fluorescence emission via surface passivation [36, 37].

In previous studies, spherically shaped carbon nanomaterials such as hollow carbon spheres (HCSs) and solid carbon spheres (SCSs) have been used as a catalyst support in the hydrogenation reaction of CALD [38, 39]. HCSs and SCSs belong to a class of zero-dimensional carbon materials due to their spherical shape [40]. Due to the unique properties of these carbon materials such as high surface-to-volume ratios, and excellent thermal and chemical stability, both HCSs and SCSs have found use in catalysis [41-43]. Manikai *et al.* studied the hydrogenation of CALD reaction using nitrogen-doped carbon spheres (N-CSs) as a support for Pd catalyst [38]. Nongwe *et al*. looked at the hydrogenation of CALD using platinum (Pt) supported nitrogen-doped HCSs (Pt/N-HCSs) [39]. In both cases the carbon spheres were doped with nitrogen to improve the metal-carbon interaction, enhancing the catalytic activity of the catalysts. For comparison purposes, we will use Pd catalysts supported on both HCSs and SCSs to look at the effect of different carbon supports on the catalytic activity of the Pd catalysts.

1.2 Problem statement

Reducing and stabilizing agents (citric acid, hydrazine hydrate, sodium borohydride, etc.) are often required in the preparation of metal nanoparticles with high hydrogenation activity [44]. Some these reducing agents used are toxic and the reduced metal NPs tend to form aggregates due to their high surface energy [44]. The use of these reducing agents limits the process of hydrogenation, hence it is important to find environment-friendly reducing agents that can prevent metal nanoparticle agglomeration by stabilizing the metal nanoparticles [44-46]. It is proposed to use CDs as a reducing agent. The surface of the CDs contains many "electrons and holes" which allows them to serve either as reducing agents or as oxidizing agents [45, 46]. In addition, various functional groups on the surface of the carbon dots can coordinate with metal ions and stabilize metal nanoparticles [45, 46].

Other approach that has been looked at in trying to solve the issue of particle agglomeration is restricting metal nanoparticles inside nano-reactors (i.e. HCSs, carbon nanotubes, mesoporous silica shells etc.) [47-50]. This approach is used as a way of minimizing the extent of particle agglomeration as metal NPs are in isolated cavities or tubes [47, 49]. The porosity of the nano-reactors can be tuned using surfactants. Due to the porosity of these nano-reactors, catalytic

reactions can still take place inside as they allow migration of reactants to the nanoparticle surface [47].

1.3 The motivation of the study

Carbon has often been used as a catalyst support due to its specific electronic and mechanical properties. Most important is the ability of a scientist to manipulate and vary the surface of carbon by simple procedures. This allows for the surface of the carbon to interact differently with metals attached to its surface. Composites comprising of carbonaceous materials with metallic nanoparticles are technologically important and they have found use in catalysis, fuel cells, and optoelectronics [34]. For example, in catalysis metal nanoparticles embedded in carbon nanotubes and graphene as support act as excellent heterogeneous catalysts for organic transformations [34].

Carbon dots have functionalized groups on their surface, and they might act as excellent supports to control the nucleation and growth of nanoparticles. CDs can play a role in the prevention of metal nanoparticle aggregate due to their interaction with metal nanoparticles enhancing the catalytic activity of the metal nanoparticles [34, 51]. The functional groups on the surface of CDs endow them with a reducing property that enables them to be used for the reduction of metal salts to the corresponding nanoparticles [34]. Metal nanoparticles show great potential as catalysts due to their large surface area and size-dependent properties, different from bulk metals. The metal nanoparticles can be used in an organic or aqueous solution in the presence of a capping agent to prevent agglomeration and/or coalescence in different catalytic reactions, such as carbon-carbon coupling, oxidation, and hydrogenation [52]. However, recovering the metal NPs from the reaction mixture is difficult and the instability of metal nanoparticles upon exposure to high temperature, or high pressure restricts the use of these systems. To overcome this problem two approaches are widely used, i) depositing nanoparticles on high surface area substances, and ii) confining the nanoparticles in the channels or void spaces of porous materials [53]. In this project, approach (i) will be used.

1.4 Aims and objectives of the study

Aims

The aim of this project is to reduce Pd salts to metallic Pd NPs using CDs. The synthesized composite will be tested in the hydrogenation reaction of CALD to evaluate and compare the reactivity of Pd/CDs under different conditions. The surface of the CDs is known to be covered

by OH/COOH groups and the role of these functional groups on the metal binding to carbon will need to be assessed.

The objectives of the study are:

1. To synthesize carbon dots with different sizes (≤ 10 nm).
2. To reduced H_2PdCl_4 to metallic Pd nanoparticles using CDs.
3. To assess the physical and chemical properties, size, and morphology of the synthesized catalyst and support using different characterization techniques.
4. To test the catalytic activity of Pd/CDs in the hydrogenation of cinnamaldehyde.
5. To compare the catalytic activity of Pd NPs supported on CDs, SCSs, and HCSs in the hydrogenation of cinnamaldehyde.
6. To compare the effect of using CDs and sodium borohydride as reducing agents for the Pd salt.

1.5 Outline of thesis

Chapter 1: Introduction: Gives a brief detail on the hydrogenation of cinnamaldehyde and motivation of the study.

Chapter 2: Literature review on the carbon nanomaterials used in this study, Pd based catalyst and carbon nanomaterials supported catalyst on hydrogenation of CALD.

Chapter 3: Experimental methods and characterization techniques used in this study.

Chapter 4: Reports on the synthesis of CDs and NCDs via the hydrothermal treatment of sucrose and urea.

Chapter 5: Reports on the hydrogenation of cinnamaldehyde using carbon dots reduced palladium nanoparticles. We look at the catalytic effect of both the CDs and Pd on the CALD hydrogenation.

Chapter 6: Hydrogenation of cinnamaldehyde over palladium nanoparticles supported on functionalized solid carbon spheres catalyst. The effect of oxygen functional groups on the surface of the support on the activity and selectivity of the catalyst is investigated.

Chapter 7: Hydrogenation of cinnamaldehyde over palladium nanoparticles supported on hollow carbon spheres catalyst. In this chapter we also look at the effect of using different reducing agents for the reduction of Pd salt on the activity of the catalyst.

Chapter 8: General conclusions and future recommendations.

1.6 References

1. Zhao, F.; Ikushima, Y.; Chatterjee, M.; Shirai, M.; Arai, M. *Green Chemistry* **2003**, *5*, 76.
2. Zeng, L.-H.; Yan, H.-X.; Zeng, Y.-K.; Li, Y.-F.; Zhang, Z.-X.; Liu, Z.-W.; Liu, Z.-T. *The Canadian Journal of Chemical Engineering*, *0*.
3. Zhu, J.; Dou, M.; Lu, M.; Xiang, X.; Ding, X.; Liu, W.; Li, M. *Applied Catalysis A: General* **2019**, *575*, 11.
4. Zhang, L.; Chen, X.; Peng, Z.; Liang, C. *Molecular Catalysis* **2018**, *449*, 14.
5. Fujita, S.-i.; Mitani, H.; Zhang, C.; Li, K.; Zhao, F.; Arai, M. *Molecular Catalysis* **2017**, *442*, 12.
6. Chen, S.; Meng, L.; Chen, B.; Chen, W.; Duan, X.; Huang, X.; Zhang, B.; Fu, H.; Wan, Y. *ACS Catalysis* **2017**, *7*, 2074.
7. Leng, F.; Gerber, I. C.; Axet, M. R.; Serp, P. *Comptes Rendus Chimie* **2018**, *21*, 346.
8. Chang, S.; Meng, S.; Fu, X.; Zhang, S.; Zheng, X.; Chen, S. *ChemistrySelect* **2019**, *4*, 2018.
9. Martínez-Ortiz, M. J.; de la Rosa-Guzmán, M. A.; Vargas-García, J. R.; Flores-Moreno, J. L.; Castillo, N.; Guzmán-Vargas, A.; Morandi, S.; Pérez-Gutiérrez, R. M. *The Canadian Journal of Chemical Engineering* **2018**, *96*, 297.
10. Yuan, T.; Liu, D.; Pan, Y.; Pu, X.; Xia, Y.; Wang, J.; Xiong, W. *Catalysis Letters* **2019**, *149*, 851.
11. Prakash, M. G.; Mahalakshmy, R.; Krishnamurthy, K. R.; Viswanathan, B. *European Chemical Bulletin* **2017**, 6, 125.
12. Han, Q.; Liu, Y.; Wang, D.; Yuan, F.; Niu, X.; Zhu, Y. *Journal of Chemistry* **2016**, *2016*, 9.
13. Zhang, Y.; Zhang, S.; Pan, X.; Bao, M.; Huang, J.; Shen, W. *Catalysis Letters* **2017**, *147*, 102.
14. Jiang, F.; Cai, J.; Liu, B.; Xu, Y.; Liu, X. *RSC Advances* **2016**, *6*, 75541.
15. Espro, C.; Donato, A.; Galvagno, S.; Neri, G. *Reaction Kinetics, Mechanisms and Catalysis* **2016**, *118*, 223.
16. Garkhedkar, A. M.; Shingote, S. K.; Rane, V. H.; Kelkar, A. A.; Ranade, V. V. *Indian Chemical Engineer* **2015**, *57*, 219.
17. Durndell, L. J.; Wilson, K.; Lee, A. F. *RSC Advances* **2015**, *5*, 80022.

18. Durndell, L. J.; Parlett, C. M. A.; Hondow, N. S.; Isaacs, M. A.; Wilson, K.; Lee, A. F. *Scientific Reports* **2015**, *5*, 9425.
19. Gutiérrez, V.; Nador, F.; Radivoy, G.; Volpe, M. A. *Applied Catalysis A: General* **2013**, *464-465*, 109.
20. Rojas, H.; Díaz, G.; Martínez, J. J.; Castañeda, C.; Gómez-Cortés, A.; Arenas-Alatorre, J. *Journal of Molecular Catalysis A: Chemical* **2012**, *363-364*, 122.
21. Zheng, R.; Porosoff, M. D.; Weiner, J. L.; Lu, S.; Zhu, Y.; Chen, J. G. *Applied Catalysis A: General* **2012**, *419-420*, 126.
22. Das, D.; Pal, K.; Llorca, J.; Dominguez, M.; Colussi, S.; Trovarelli, A.; Gayen, A. *Reaction Kinetics, Mechanisms and Catalysis* **2017**, *122*, 135.
23. Nagpure, A. S.; Gurrala, L.; Gogoi, P.; Chilukuri, S. V. *RSC Advances* **2016**, *6*, 44333.
24. Vriamont, C.; Haynes, T.; McCague-Murphy, E.; Pennetreau, F.; Riant, O.; Hermans, S. *Journal of Catalysis* **2015**, *329*, 389.
25. Dai, Y.; Gao, X.; Chu, X.; Jiang, C.; Yao, Y.; Guo, Z.; Zhou, C.; Wang, C.; Wang, H.; Yang, Y. *Journal of Catalysis* **2018**, *364*, 192.
26. Mondal, K. C.; Cele, L. M.; Witcomb, M. J.; Coville, N. J. *Catalysis Communications* **2008**, *9*, 494.
27. Oosthuizen, R. S.; Nyamori, V. O. *Platinum Metals Review* **2011**, *55*, 154.
28. Rylander, P. *Catalytic hydrogenation over platinum metals*; Elsevier, 2012.
29. Zhou, J.; Zhou, H.; Tang, J.; Deng, S.; Yan, F.; Li, W.; Qu, M. *Microchimica Acta* **2017**, *184*, 343.
30. Dimos, K. *Current Organic Chemistry* **2016**, *20*, 682.
31. Baker, S. N.; Baker, G. A. *Angewandte Chemie International Edition* **2010**, *49*, 6726.
32. Lim, S. Y.; Shen, W.; Gao, Z. *Chemical Society Reviews* **2015**, *44*, 362.
33. Li, X.; Wang, H.; Shimizu, Y.; Pyatenko, A.; Kawaguchi, K.; Koshizaki, N. *Chemical Communications* **2011**, *47*, 932.
34. Wang, Y.; Hu, A. *Journal of Materials Chemistry C* **2014**, *2*, 6921.
35. Xu, X.; Ray, R.; Gu, Y.; Ploehn, H. J.; Gearheart, L.; Raker, K.; Scrivens, W. A. *Journal of the American Chemical Society* **2004**, *126*, 12736.
36. Jelinek, R.; *Carbon Nanostructures* **2016**, 1.
37. Sun, Y.-P.; Zhou, B.; Lin, Y.; Wang, W.; Fernando, K. A. S.; Pathak, P.; Meziani, M. J.; Harruff, B. A.; Wang, X.; Wang, H.; Luo, P. G.; Yang, H.; Kose, M. E.; Chen, B.; Veca, L. M.; Xie, S.-Y. *Journal of the American Chemical Society* **2006**, *128*, 7756.

38. Manikai, S. M.-A. *The synthesis of nitrogen doped carbon spheres as supports for palladium catalysts in the hydrogenation of cinnamaldehyde*, PhD Thesis, University of the Witwatersrand, Johannesburg, 2015.
39. Nongwe, I.; Ravat, V.; Meijboom, R.; Coville, N. J. *Applied Catalysis A: General* **2016**, *517*, 30.
40. Lu, A.-H.; Hao, G.-P.; Sun, Q.; Zhang, X.-Q.; Li, W.-C. *Macromolecular Chemistry and Physics* **2012**, *213*, 1107.
41. Friedel, B.; Greulich-Weber, S. *Small* **2006**, *2*, 859.
42. Kim, S.-W.; Kim, M.; Lee, W. Y.; Hyeon, T. *Journal of the American Chemical Society* **2002**, *124*, 7642.
43. Lu, A.-H.; Sun, T.; Li, W.-C.; Sun, Q.; Han, F.; Liu, D.-H.; Guo, Y. *Angewandte Chemie International Edition* **2011**, *50*, 11765.
44. Zhang, J.; Chen, Y.; Tan, J.; Sang, H.; Zhang, L.; Yue, D. *Applied Surface Science***2017**, *396*, 1138.
45. Jin, J.; Zhu, S.; Song, Y.; Zhao, H.; Zhang, Z.; Guo, Y.; Li, J.; Song, W.; Yang, B.; Zhao, B. *ACS Applied Materials & Interfaces***2016**, *8*, 27956.
46. Luo, P.; Li, C.; Shi, G. *Physical Chemistry Chemical Physics***2012**, *14*, 7360.
47. Pérez-Lorenzo, M.; Vaz, B.; Salgueirino, V.; Correa-Duarte, M. A. *Chemistry–A European Journal* **2013**, *19*, 12196.
48. Lee, J.; Kim, S. M.; Lee, I. S. *Nano Today* **2014**, *9*, 631.
49. Pan, X.; Bao, X. *Accounts of Chemical Research* **2011**, *44*, 553.
50. Cornelio, B.; Saunders, A.; Solomonsz, W.; Laronze-Cochard, M.; Fontana, A.; Sapi, J.; Khlobystov, A. N.; Rance, G. A. *Journal of Materials Chemistry A* **2015**, *3*, 3918.
51. Dey, D.; Bhattacharya, T.; Majumdar, B.; Mandani, S.; Sharma, B.; Sarma, T. K. *Dalton Transactions* **2013**, *42*, 13821.
52. Harada, T.; Ikeda, S.; Ng, Y. H.; Sakata, T.; Mori, H.; Torimoto, T.; Matsumura, M. *Advanced Functional Materials* **2008**, *18*, 2190.
53. Huang, X.; Guo, C.; Zuo, J.; Zheng, N.; Stucky, G. D. *Small* **2009**, *5*, 361.

Chapter 2: Literature review

2.1 Background on carbon nanomaterials

The term nanocarbon is used to indicate a broad range of carbons with at least one dimension less than 100 nm [1]. Since fullerenes were discovered in 1985, an extensive effort has been put into the synthesis of shaped nanocarbon materials [1]. This has led to the synthesis of many different shaped carbons that include tubes, onions, fibers, horns, spheres, calabashes, etc. [1-3]. Over the past two decades, carbon-based nanomaterials have attracted great interest in both academic and industrial areas due to their outstanding features such as biocompatibility, chemical stability, and low toxicity [4, 5].

Carbon nanomaterials can be classified into two general groups depending on the predominant types of a covalent bond linking their carbon atoms [6]. The first group involves carbon nanomaterials that consist of sp^2 carbon atoms that are densely packed in a hexagonal honeycomb crystal lattice and they may also contain some sp^3 carbon at defects sites or edges [6]. This group consists of graphene, graphenic nanosheets, carbon nanotubes (CNTs), nanohorns, onion-like carbon spheres, nanospheres, and carbon dots (CDs) [6]. The second group has both sp^3 and sp^2 carbon atoms in different ratios or consist mostly of sp^3 carbon atoms [6]. Nanodiamond is the only known member of this group [6]. However, some type of CDs with amorphous structures could also be regarded as members [6].

2.2 Carbon dots

2.2.1 Introduction to carbon dots

Carbon dots (CDs) are quasi-spherical nanoparticles made up of an amorphous to nano-crystalline graphite core with sizes less than 10 nm [7, 8]. Upon their discovery in 2004 during separation and purification of single-walled CNTs from arc-discharged soot further analysis was carried out [5, 9-11]. Three distinct products of carbonaceous nanomaterials were separated by gel electrophoresis. Of these three products, one displayed a fast-moving band with fluorescent properties [9]. This by-product intrigued researchers who carried out further analysis of the fluorescent material. From their results, it was shown that the fluorescent material comprised of very small particles of a carbonaceous material [9, 12].

Initially, they were termed fluorescent carbon nanoparticles until 2006 in which they received their name “carbon quantum dots” from Sun *et al*. who proposed a method to make CDs with much-enhanced fluorescence emission via surface passivation [12, 13]. The fluorescent properties of the CDs are ascribed to their quantum confinement effect and surface energy traps [14].

Figure 2.1 shows the chemical structure of CDs with carboxyl moieties on the surface [7]. The core structure of the CDs mainly consists of sp^2 carbon fused by diamond-like sp^3 hybridized carbon insertion [15]. The surface of the CDs contains multiple oxygen-containing functional groups [15]. The surface of CDs can be easily functionalized with organic molecules to introduce different heteroatoms and to tailor their wavelength emission [10]. The functional groups on the surface of the CDs stabilize the surface energy traps and make them emissive [16]. The photoluminescence properties of CDs can be affected by variation in their size and the emission is red-shifted with increasing size [17]. CDs have high solubility, robust chemical inertness, and high resistance to photobleaching. Hydrophilicity or hydrophobicity of CDs can be adjusted and they are highly soluble and can be easily dispersed in water [10].

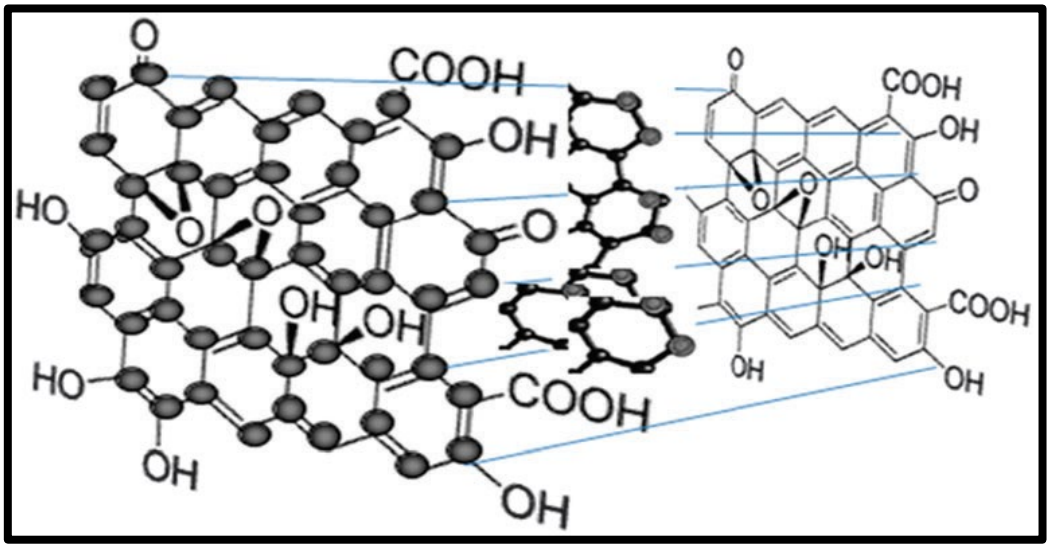

Figure 2.1: Representation of chemical structure of CDs [7].

There are three types of CDs that are known, namely; carbon nanodots (CNDs), graphene quantum dots (GQDs) and polymer dots (PDs) (Figure 2.2) [5, 18]. They have similar photoluminescence properties and differ in their core structure and surface functional groups. GQDs are defined as nanographene fragments with a single or a few layers of graphene [18]. CNDs are spherical carbon nanomaterials in the nanoscale range which can be divided into two: carbon nanoparticles with no crystal lattice and carbon quantum dots (CQDs) which have a crystal lattice [18]. PDs refer to cross-linked polymers prepared from linear polymers or

monomers [5, 18]. In particular, the optical properties and the fluorescence emissions of these materials have attracted increasing interest in recent years [7, 12]. This project will focus on the synthesis and catalytic properties of CNDs only.

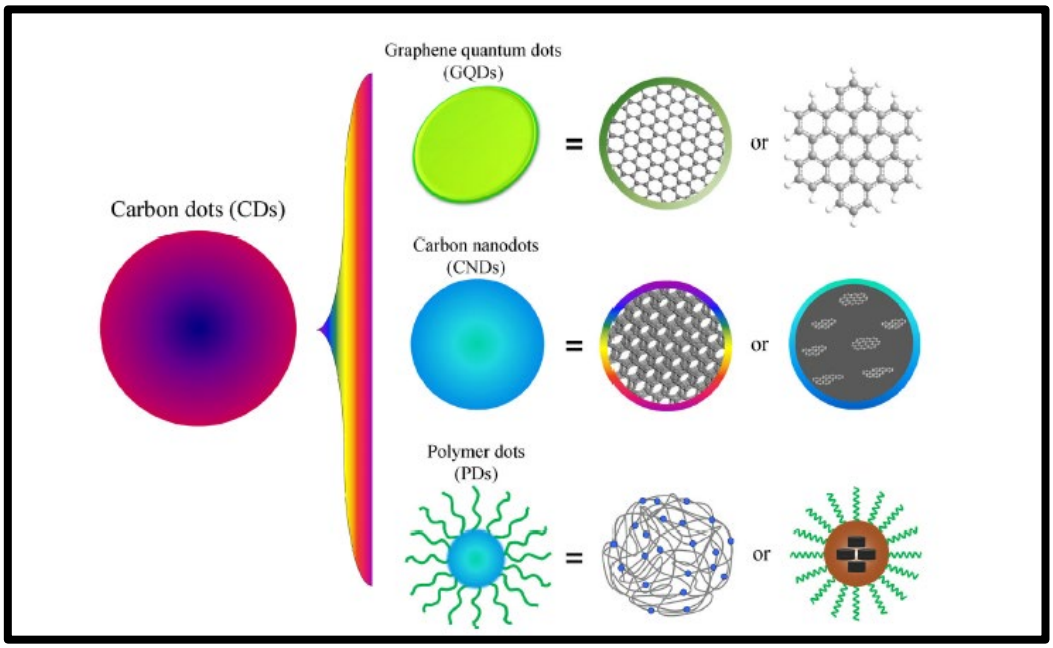

Figure 2.2: Schematic representation of different types of carbon dots [18].

2.2.2 Synthesis of carbon dots

Since the discovery of carbon dots in 2004, a significant increase in the development of physical and chemical methods to synthesize carbon dots has been achieved [11]. CDs can be synthesized either by top-down or bottom-up methods (Fig. 2.3). The top-down approach refers to the breakage of bulk carbon materials such as carbon soot, CNTs, activated carbon, and graphite by means of laser ablation, arc discharge, ultrasonic methods, and chemical and electrochemical oxidation [8, 11, 19]. These carbon sources lack an efficient band gap to give fluorescence, hence their surface chemistry and size must be modified to make them photoluminescent [18]. The bottom-up approach refers to the conversion of molecular precursors such as citrate, carbohydrates, and a diverse range of biomass materials via hydrothermal treatment, plasma treatment, thermal decomposition, microwave synthesis, and template-based routes to CDs [8, 19]. As a result of the different starting materials and processing methods used, CDs consist of amorphous to nanocrystalline cores and with a variety of functional groups [8].

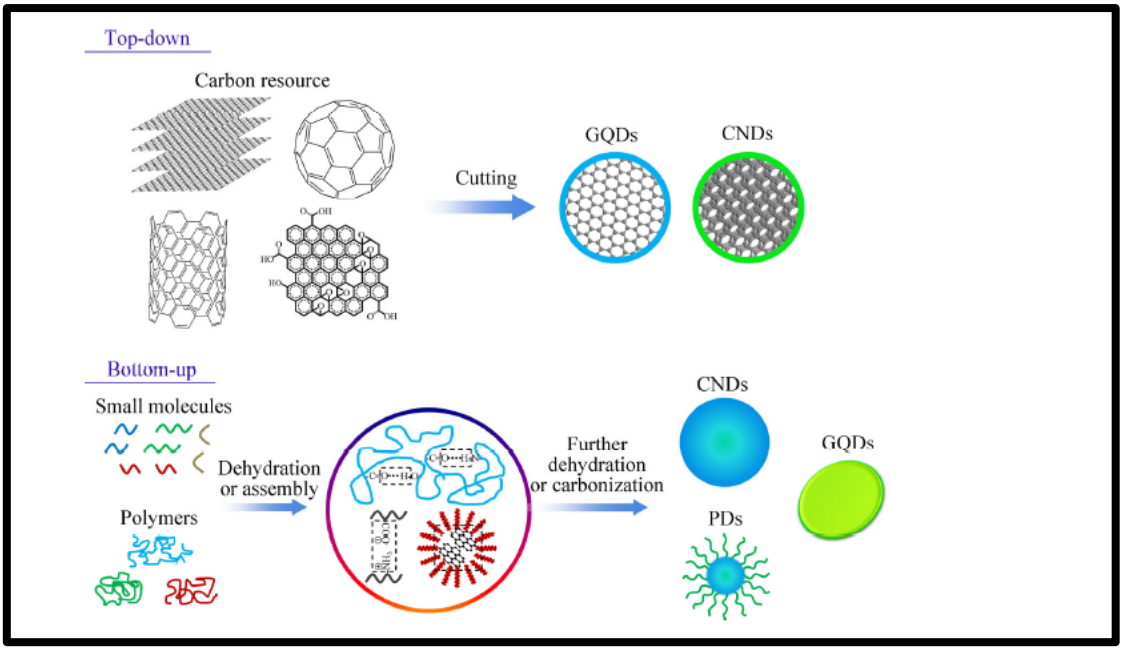

Figure 2.3: Scheme of two approaches used in the synthesis of CDs [18].

2.2.2.1 Top-down approaches

Electrochemical methods have been applied to making CDs due to their advantages such as low cost, easy manipulation and production producing adjustable emission properties by varying the synthetic conditions [20]. Ming *et al.* reported the synthesis of CDs using a one-step electrochemical approach [21]. A graphite rod inserted in ultrapure water was used as an anode that was placed parallel to the other graphite rod as the counter electrode. A direct current power supply with static potentials of 15-60 V was applied to the two electrodes (Fig. 2.4 a-b). After stirring for 120 h, the anode graphite rod started to corrode forming a dark yellow solution in the reactor (Fig. 2.4 b). The CDs were recovered by filtering the solution, which was centrifuged at 22000 rpm for 30 min to remove precipitated graphite oxide. The particle size of the obtained CDs was in the range of 3-6 nm. From HRTEM studies it was observed that the CDs exhibited a crystal lattice spacing of 0.321 nm which is in the agreement with the (002) lattice plane of graphitic carbon (Fig. 2.4 d-f).

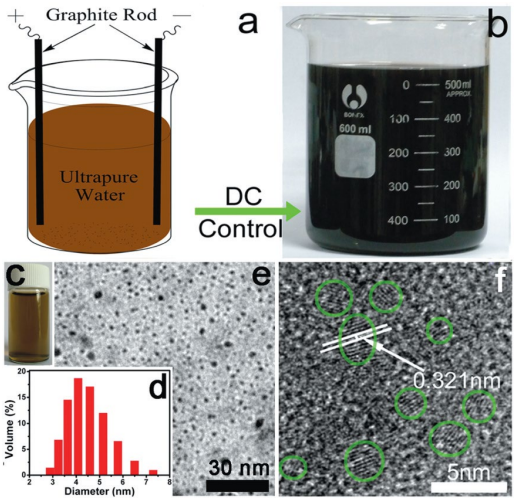

Figure 2.4: (a) Reaction set-up for the synthesis of CDs, digital image of CDs (b) before treatment, (c) after treatment, (d) particle size distribution of CDs, (e) TEM image of CDs, and (f) HRTEM image of CDs [21].

In 2012 Dhanjar *et al.* used an electrochemical method to prepare GQDs from multiwalled carbon nanotubes (MCNTs) dispersed in propylene by using $LiClO_4$ at 90 °C [22]. The reaction time was varied (7, 11, and 15 h) at a potential of 1 V. The TEM images (Fig. 2.5 a, c, and e) showed that the average particle size of GQDs decreased with an increase in oxidation time. The obtained GQDs had fringes with a crystal lattice spacing of 0.33 nm and 0.242 nm corresponding to (002) and (1120) lattice planes respectively.

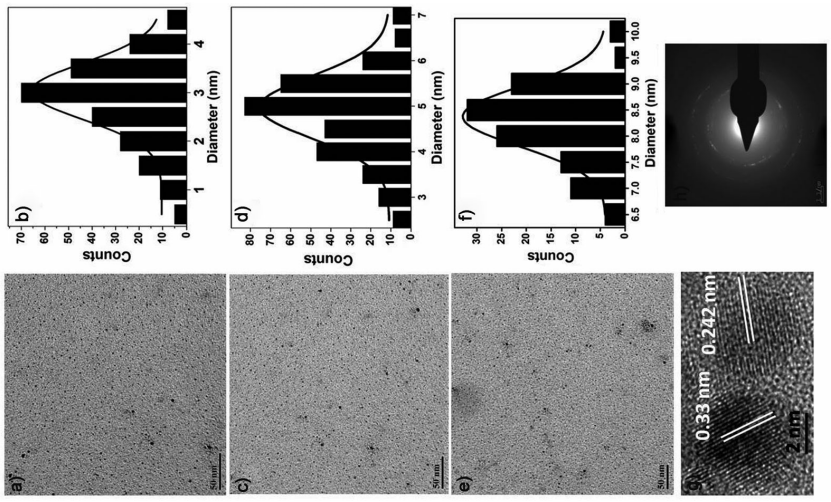

Figure 2.5: TEM images of GQDs synthesized at 90 °C by using oxidation at 1 V for (a) 15 h, (c) 11 h, (e) 7 h with their corresponding particle size distribution (b, d, f) respectively. (g) The HRTEM image of GQDs and (h) SAED pattern of GQDs [22].

Laser ablation is a physical method used to synthesize nanomaterials through laser irradiation of a solid target in a solvent [23]. Hu *et al.* reported the synthesis of CQDs from graphite flakes dispersed in PEG_{15000} solution irradiated with an Nd:YAG pulsed laser with a wavelength of 1.064 μm [23]. After 4 h the homogeneous black suspension was centrifuged (5000 rpm) and a colourful supernatant was separated from the black carbon precipitate. The authors demonstrated that the average particle size of CDs could be increased from 3.2 nm to 13.4 nm by increasing the pulse widths.

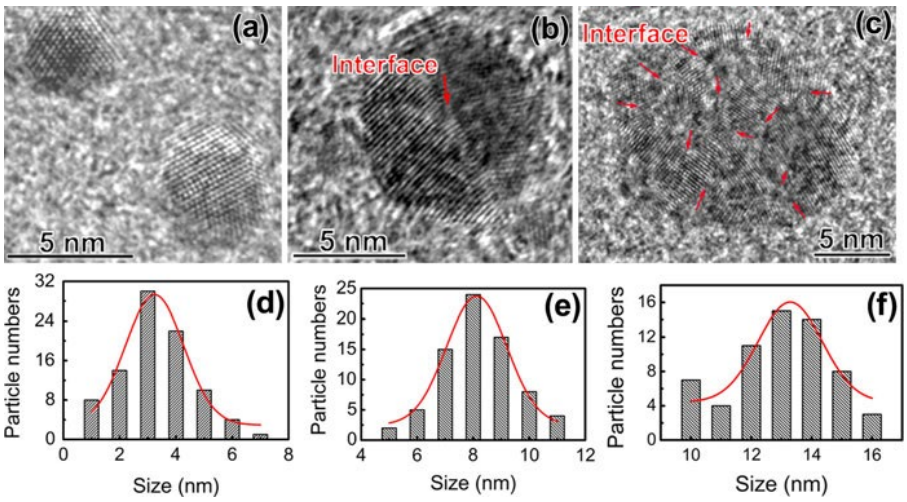

Figure 2.6: HRTEM images of CDs synthesized using different laser pulse widths (a) 0.3 ms, (b) 0.9 ms, and (c) 1.5 ms with their corresponding particle size distribution (d, e, and f) respectively [23].

Chemical oxidation is one of the most efficient and convenient methods used to synthesize CDs on a large scale [20, 24]. This approach involves oxidation of a carbon source using oxidative reagents such as nitric acid and sulphuric acid, which introduces abundant oxygen-containing functional groups [20]. Qiao e*t al.* synthesized multicolour photoluminescence CDs using chemical oxidation [24]. In this approach, three types of carbon sources were used, namely: coal activated carbon (CAC), wood activated carbon (WAC), and coconut activated carbon (CNAC). The CDs were synthesized by treating the carbon source with nitric acid followed by surface passivation using 4,7,10-trioxa-1,13-tridecanediamine (TTDDA). From the TEM images, all the samples had size distributions in the range of 2 to 6 nm.

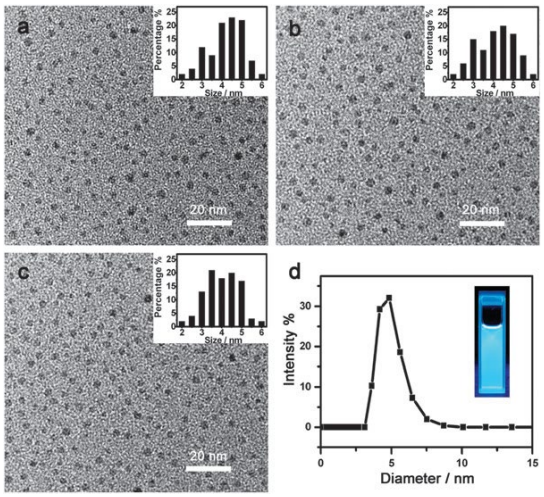

Figure 2.7: TEM images of CDs passivated using TTDDA derived from (a) CAC, (b) WAC, and (c) CNAC with their corresponding particle size distribution. (d) The size distribution of TTDDA passivated CDs derived from CAC measured using a Malvern NanoZS zetasizer, (inset- CDs solution under UV light (365 nm)) [24].

Park *et al.* reported the synthesis of CDs by treating food wastes in ethanol solution (10% ethanol) with ultrasound at 40 kHz [25]. To remove the larger particles the solution was centrifuged (4500 rpm, 5 min). The supernatant was filtered twice using a 0.22 µm membrane and the solution was oven-dried at 45 °C to get CDs in solid form. The TEM and AFM images revealed that the average particle size of the CDs was 4.6 nm (Fig. 2.8).

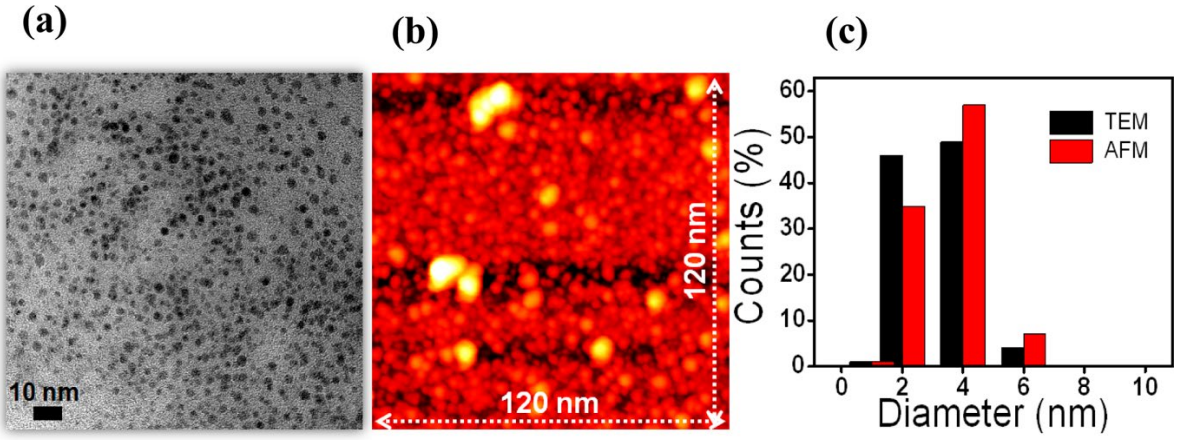

Figure 2.8: (a) TEM image, (b) AFM image, and (c) particles size distribution of CDs [25].

2.2.2.2 Bottom-up approaches

The bottom-up approaches use various molecular carbon sources to make CDs. Some examples are listed below. Guo *et al.* reported the synthesis of CDs using sodium citrate as a carbon

source [26]. A mixture of sodium citrate, ammonium bicarbonate, and water was transferred into a Teflon-lined stainless-steel autoclave and placed inside a drying oven at 180 °C for 4 h. The CDs were purified using a dialysis tube (1 KDa, MWCO) for 24 h. The TEM image (Fig. 2.9) shows CDs with particle size of 1.59 nm.

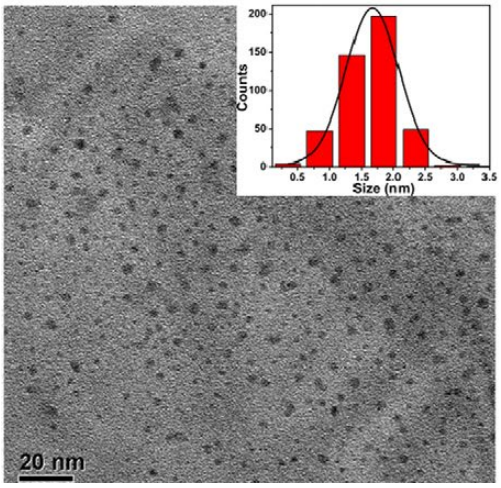

Figure 2.9: TEM image of CDs and the inset is the particle size distribution of the CDs [26].

In 2016 Liu *et al.* used a pyrolysis method to synthesize N-doped CDs [27]. A chemical vapour deposition (CVD) method was used to carbonize chitosan at 300 °C for 2 h at a heating rate of 5 °C/min under a flow of N_2 gas. The obtained powder was dispersed in water, and then filtered to separate CDs from larger particles. Figure 2.10 shows the TEM image of the CDs with particle size ranging from 1-6 nm. From HRTEM studies (inset) the CDs displayed crystallinity with an interlayer spacing of 0.18 nm.

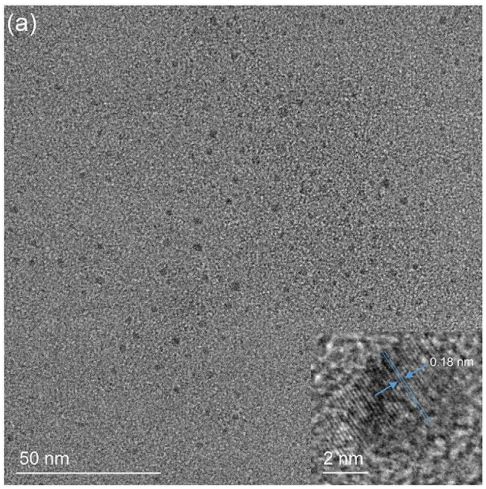

Figure 2.10: (a) TEM image of CDs [27].

Gong *et al.* prepared CDs using a microwave-assisted hydrothermal method [28]. A certain amount of Vitamin C was dissolved in water, which was then placed in a microwave digestion container and heated at 180 °C for 5 minutes at 900 W power. The resultant solution was centrifuged (14000 rpm, 10 min) and CDs were obtained from the supernatant. From the TEM image (Fig. 2.11) the CDs had an average particle size of 3 nm.

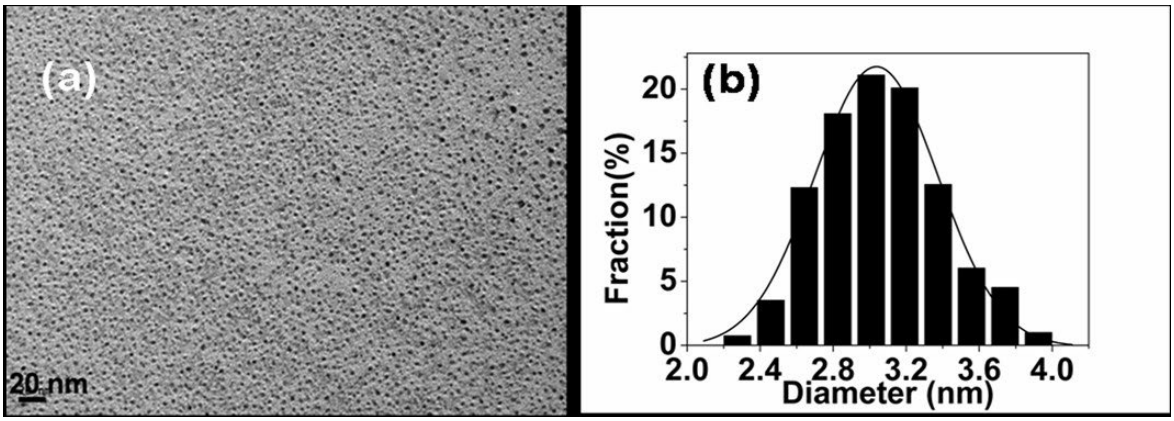

Figure 2.11: (a) TEM image and (b) particle size distribution of CDs [28].

Chen *et al.* reported the synthesis of CDs in high yield (41.8%) using the hydrothermal method [29]. A mixture of sucrose and oleic acid was heated at 215 °C for 5 min while vigorously stirring the mixture under a N_2 atmosphere. The brownish solid obtained was dispersed in water and the remaining oil acid was extracted using hexane. By-products were removed using a dialysis membrane (0.5 kDa) and the final product was freeze-dried to obtain CDs in solid form. The TEM image (Fig. 2.12) showed well-dispersed CDs with an average diameter of 1.84 ± 0.8 nm. The HRTEM image of the CDs did not show any crystallinity indicating that the synthesized CDs were amorphous.

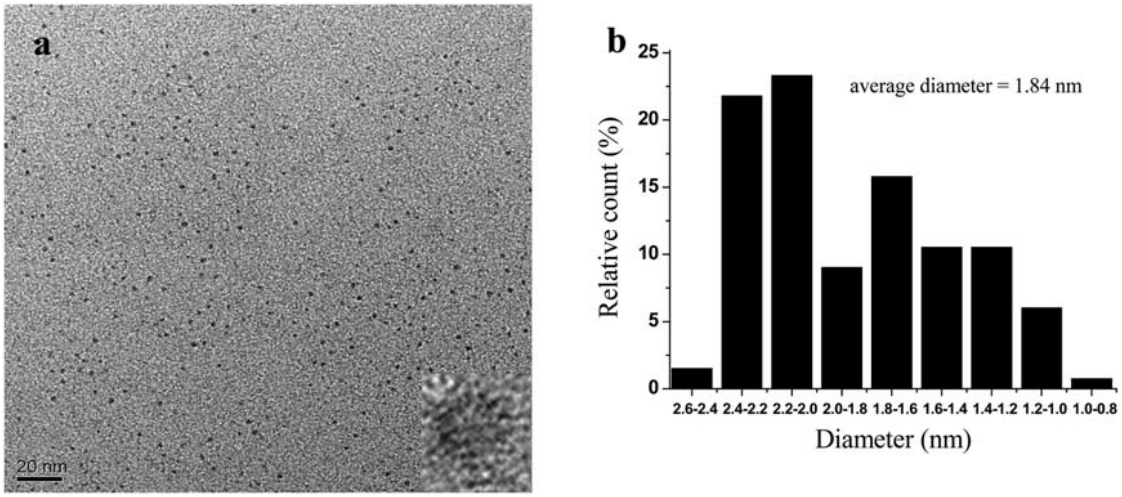

Figure 2.12: (a) TEM image (inset-HRTEM) and (b) particle size distribution of CDs [29].

Yang *et al.* synthesized CDs using the copolymer Pluronic P123 as a soft template and ordered mesoporous silica (OMS), SBA-15, as a hard template [30]. After synthesis of P123 in silica, different carbon precursors (1,3,5-trimethylbenzene (TMB), pyrene (PY), and o-diaminobenzene (DAB)) were added into the mixture of P123 in silica and stirred at 40 °C for 24 h. The reaction mixture was transferred into a hydrothermal reactor which was heated at 100 °C for 24 h. The obtained product was air-dried after filtration and washing steps. After air-drying the product was calcined under a N_2 atmosphere at 900 °C for 2 h. CDs were obtained by etching the CDs@OMS composites using 2 M NaOH solution at 40 °C for 48 h. To neutralize the excess NaOH, nitric acid was used and then removed by dialysis of the suspension against milli-Q water through a dialysis membrane (MWCO 3500) to give the CDs. The morphology of the CDs was studied using HRTEM (Fig. 2.13). The average particle size was calculated to be 3.1 ± 0.6, 3.0 ± 0.4, 3.8 ± 0.8, and 4.4 ± 0.4 nm for CDs synthesized using TMB, DBA, PY, and PHA respectively. From the magnified HRTEM (inset) only CDs synthesized from PY and PHA were shown to have lattice fringes.

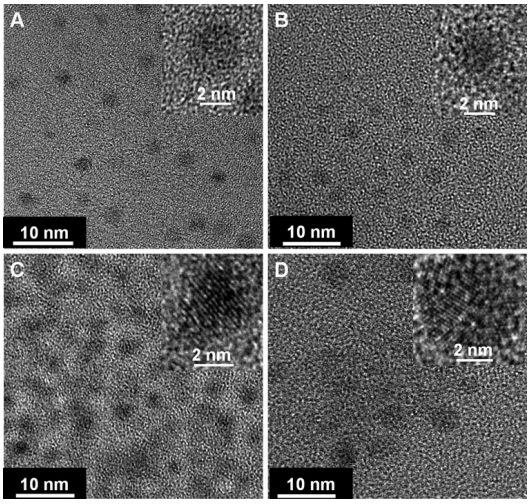

Figure 2.13: HRTEM images of CDs synthesize using different carbon precursors and their corresponding magnified HTREM images inset (a) TMB, (b) DBA, (c) PY, and (d) PHA [30].

In summary, CDs synthesis usually involves a bottom-up process, which uses small carbon molecular precursors to make carbon dots [11]. Both the bottom-up and top-down approaches have two steps in common, the functionalization step and passivation step [11]. The characteristics of CDs can be modified by the choice of precursors used during synthesis, surface passivation, and functionalization [16]. The functionalization step gives the CDs their water solubility properties and general reactivity properties [31]. The passivation step not only protects the CDs from contamination but also prevents functional groups on the surface of CDs from reacting with organic molecules, which may cause the disappearance of the optoelectrical properties of CDs [10]. This step can enhance the quantum yields of CDs and is important for the extended lifetime of CDs [17].

2.2.3 Surface modification of carbon dots

CDs mainly consist of C, O, and H elements that relate to the presence of hydroxyl, carbonyl, and carboxylic acid functional groups attached to a carbon-based core [20]. Depending on the surface chemistry, CDs can be hydrophilic or hydrophobic [32, 33]. The presence of functional groups can improve the dispersibility of the CDs in different solvents and it also allows for the surface modification of the CDs via functionalization or doping with molecules containing heteroatoms [5, 8, 20, 32]. It has been reported that the incorporation of functional groups, such as carboxyls and amines, can create various defects on the surface of the CDs [7].These defects lead to a broad variation in fluorescence emission as they function as excitation energy traps [7]. Functionalization of CDs is done to improve the physical and chemical properties of CDs which enables them to be applied in various applications [34]. For example, in sensor

applications, it has been reported that the as-synthesized CDs lack sensitivity towards the target species, an effect associated with the functional groups present on their surface [35]. Hence, most research has focused on surface modification of the CDs via functionalization or passivation to improve sensitivity, selectivity and to enhance the fluorescence intensities of sensors [35].

There are two main methods for surface functionalization of CDs, namely a multi-step synthesis and a one-step synthesis [5]. In the multi-step functionalization synthesis, the reactive functional groups on the surface of the as-synthesized carbon dots are further modified through surface chemistry. This method is widely used for doping the CDs with heteroatoms to tune the conduction/valence band position that results in the enhanced fluorescent property of the CDs. The one-step synthesis method involves the formation of the CDs with functional groups in a one-pot process [5]. This is achieved by using starting materials that already have functional groups.

Functionalized or as-prepared CDs have a relatively low emission frequency compared to semiconductor quantum dots; hence, it is still a challenge to enhance the fluorescence properties of CDs [36, 37]. CDs doping is another popular method used to modify the optical and electron transfer properties of the CDs [36]. The doping approach can be classified in terms of the dopant used; these could be metal atoms or heteroatoms. Metal doping can be used to tune the optical properties of the CDs by modifying the band structure [34]. The challenge with a metal atom doping approach is that the process leads to an increase in toxicity of the doped CDs [36]. Hence, heteroatom-doping has attracted much more attention in recent years [36]. Nitrogen is widely used to improve the photoluminescence properties of CDs due to the close similarity of the atomic size of N and C and the strong bonding between them [36, 38]. Alternate dopants such as sulfur, silicon, boron, phosphorus or a combination of different dopants can also be used [36, 37].

2.2.4 Application of carbon dots

The good biological properties of CDs relative to quantum dots such as their low toxicity and good biocompatibility, endow them with potential applications in bioimaging, drug delivery, and biosensors [31]. The unique electronic and optical properties of CDs ensure their wide potential in optronics, sensors, and catalysis [31]. Scialabba *et al.* reported the synthesis of heteroatom doped Red-emissive CDs functionalized with biotin-terminated polyethylene glycol (PEG_{2000}) (CDs-PEG-BT) [39]. The CDs-PEG-BT were shown to have a high potential as

cancer theranostic tools as they were found to incorporate more than 16 % of anticancer drugs which can later be released inside tumours by a near-infrared-triggered photothermal effect.

The possible use of CDs in solar energy devices has been explored as they have light-absorbing properties [12]. Ghann *et al.* reported the use of CDs as sensitizing agents to enhance the photoanodic properties for dye-sensitized solar cells [40]. Amato *et al.* reported nitrogen-doped CDs as promising photoluminescent dopants that can be used to enhance properties of luminescent solar concentrators [41]. The authors prepared poly(methyl methacrylate)/nitrogen doped CDs hybrids to increase the efficiency of silicon solar cells.

Due to the photoluminescence properties of CDs, mercury ion detection in environmental and biological samples has been among the most widely studied of their chemical sensing applications [12, 42]. Although there have been some drawbacks in using CDs for sensor applications such as unsatisfactory sensitivity towards target species, researchers have found ways of improving their selectivity and sensitivity by modifying the surface of the CDs [43]. Yan *et al.* prepared sensors using two kinds of CDs, one functionalized with an amino group and a carboxylic group, and the second one capped with a methyldimethoxysilane group and a carboxylic group [42]. The authors reported that the carboxylic groups on the CDs coordinated with the mercury ions to form non-fluorescent complexes. Both the sensors were reported to have high selectivity and sensitivity towards trace mercury ions in aqueous media (20 μM).

The use of CDs as a photocatalyst in the degradation of organic dyes has also been studied intensively [44-47]. CDs have been reported as promising semiconductor photocatalyst due to their ability to generate electron hole pairs under light irradiation [44-47]. For example, Peng *et al.* reported on the use of CDs synthesized by hydrothermal treatment of citric acid and 1,2-diboranyethane on the photocatalytic degradation of methylene blue (MB) and rhodamine B (RhB) under visible light irradiation [45]. The CDs were shown to have high photocatalytic activity toward degradation of MB and RhB and their dye degradation efficiency was comparable to metal-based photocatalysts.

Metallic NPs supported on carbon nanomaterials have been used in a wide range of applications, e.g., fuel cells, optoelectronics, and catalysis [48]. In catalysis, metal nanoparticles supported on carbon nanotubes and graphene have been reported act as an excellent heterogeneous catalyst for organic transformations [48]. CDs might also act as supports for the reduction of noble metal ions and help prevent agglomeration of the metal nanoparticles [48]. For example, Dey *et al*. used CDs as a reducing and stabilizing agent for the reduction of the

H_2PdCl_4 salt to Pd nanoparticles [48]. The Pd@CDs composite was used as a catalyst for the Heck and Suzuki coupling reactions. This composite was found to have high catalytic activity for C-C bond formation reactions.

However, little is known about the catalytic behaviour of metals placed outside the CDs in hydrogenation reactions. So far, only one publication has been reported. This involved the preparation of Rh/CDs applied in a hydrogenation reaction. *Zhang et al.* reported the preparation of Rh NPs by using CDs as a reducing and stabilizing agent for NPs [49]. The Rh/CDs composite was applied in the hydrogenation of hydroxyl-terminated polybutadiene (HTPB) and hydroxy-terminated butadiene-acrylonitrile (HTBN) at various temperatures (80, 100, and 120 °C). The catalyst was found to be highly active in the hydrogenation of HTBN and HTPB at 80 °C. In this project, CDs will be used to investigate metal support interaction between carbon dots and Pd NPs in the hydrogenation reactions.

2.3 Carbon spheres

2.3.1 Introduction to carbon spheres

The uniqueness of carbon as an element arises from carbon being able to form C-C bonds and to form covalent bonds with other elements [50]. Carbon atoms can form heptagonal, pentagonal, and hexagonal rings due to the use of different hybrid orbitals [50]. Synthesis of spherical shaped carbon materials dates back to thousands of years [51]. For instance, carbon blacks were produced from partial combustion or thermal decomposition of hydrocarbons in early combustion reaction [52-54]. Carbon blacks have been commercially used as a pigment in black ink, for the reinforcement of rubber, and for its electronically conductive properties [53, 54]. After the discovery of fullerenes in 1985, studies based on spherical carbon materials emerged focusing on developing new and efficient methods that can be used to synthesize spherical carbon materials [51].

Carbon spheres (CSs) were observed in the 1980s during the carbonization of polyethylene (PE) and polyvinyl chloride (PVC) under pressure and also the decomposition of β-SiC powder via conically converging shock-wave processes by Inagaki *et al.* and Yamada *et al.* respectively [52, 55, 56]. As one of carbon allotropes, CSs are classed as zero-dimensional carbon materials due to their spherical shape [50]. CSs can have a solid, hollow or core-shell morphology [50, 51, 57]. Secondly, CSs can be categorized into (i) concentric, (ii) radial, and (iii) or randomly oriented carbon layers [55]. Thirdly, CSs can be classed according to their size: (i) fullerenes family and

graphitic carbon onions having diameters ranging from 2-20 nm, (ii) less graphitic spheres with diameters in the range of 50 nm-1 μm, (iii) carbon beads with diameters from one to several microns [58].

CSs tend to form aggregates as a result of Van der Waals forces and their accretion has been attributed to long reaction times and cooling from synthesis temperature to room temperature [55]. It has been proposed that CSs are formed from graphene sheets that are normally unclosed shells having wavy flakes that are arranged to give the curvature of the sphere, which creates open edges at the surface (Fig.2.14) [59]. CSs have attracted a lot of interest due to their unique properties which led to their use in many applications such as electrodes, catalyst supports, encapsulating magnetic nanoparticles, drug and enzyme delivery, water treatment, gas storage, and conversion media, etc. [60, 61].

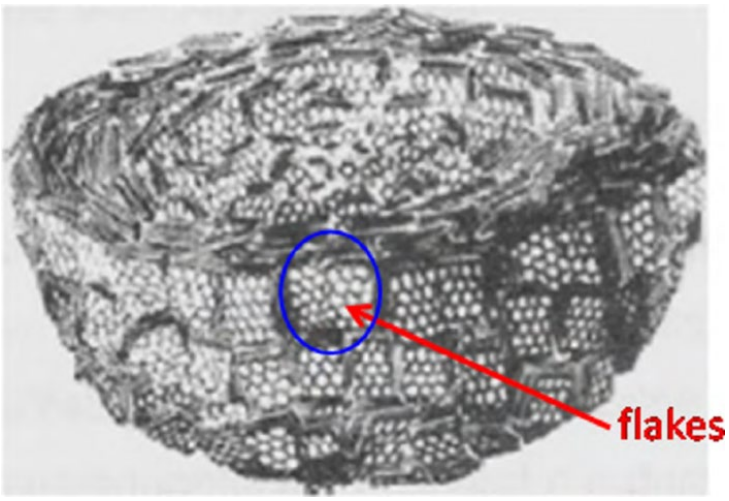

Figure 2.14: Model showing the arrangement of carbon layers of a single carbon black particle with concentric layers [59].

2.3.2 Solid carbon spheres

Solid carbon spheres (SCSs) can be prepared by pyrolysis of polymer analogs at high temperatures resulting in the formation of a carbon residue [62]. This approach utilizes phenolic resins that are thermally stable and can give a high carbon conversion. The phenolic resins can be made by the polymerization of phenols (e.g. phenol, resorcinol, phloroglucinol) and aldehyde (e.g. formaldehyde and furfuraldehyde) [62]. The method for the synthesis of these phenolic resins has been adapted from the Stöber process [63, 64]. The Stöber process has been used to synthesize monodispersed silica spheres and it was later extended by researchers to synthesize phenolic resins [63]. The Stöber process attracted a lot of interest because the synthesis

of highly monodispersed silica spheres with a narrow size distribution, control of particle size and surface chemistry such as pore size has been achieved [63]. Hence, this has raised a lot of interest in extending the Stöber process to the synthesis of phenolic resins [63].

Friedel *et al.* prepared monodispersed SCSs with the size range of 100-1000 nm from the carbonization of melamine and formaldehyde (MF) resin [65]. The synthesized MF resin spheres had an average size of 1600 nm and were carbonized at temperatures between 400 and 1000 °C. The authors observed that the MF resins shrank when exposed to heat treatment under non-oxidizing conditions. The shrinkage was attributed to (i) loss of water and (ii) decomposition reactions of the MF resin (i.e. loss of functional groups which was supported by the FTIR data).

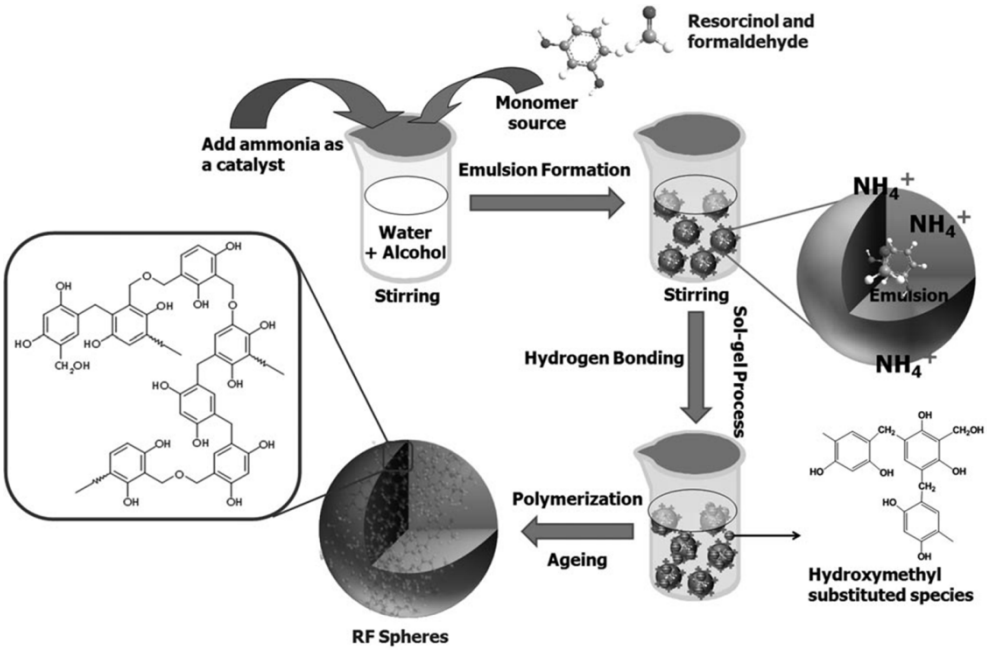

Figure 2.15: Schematic representation showing polymerization of RF resin using the extended Stöber process [63].

Liu and his colleagues prepared monodispersed SCSs from the polymerization of resorcinol and formaldehyde (RF) resin (Fig. 2.15) [63]. The synthesized RF resin spheres had diameters ranging from 200 to 1000 nm depending on the reactant molar ratio and the synthesis temperature used. To obtain the SCSs, RF resin spheres with an average particle size of 520 nm were carbonized at 600 °C under an inert atmosphere. The obtained SCSs preserved the spherical morphology of the RF resin spheres and resin spheres and had an average diameter size of 410 nm.

Another approach that has been studied intensively in the synthesis of SCSs is the hydrothermal carbonization (HTC) of biomass reaction [62]. This method is considered to be a most facile, cheap, and environmentally friendly route as it utilizes biomass e.g. fructose, glucose, xylose, maltose, etc. as a carbon precursor [62, 66]. The HTC method has been used to synthesize SCSs from carbohydrate sources in the temperature range of 160-200 °C. The formation of SCSs has been reported to form in four steps that include dehydration, condensation, polymerization, and aromatization. The porous structure and functional surface groups on the as-synthesized SCSs has led to their use in applications such as biomedicine, catalysis, and nanodevices [62].

Romeo-Anaya *et al.* prepared SCSs using the HTC approach [67]. Solutions of three different carbohydrates were hydrothermally treated using an autoclave in the temperature range of 180-240 °C. From the three-carbon precursors, it was noted, using SEM, that only glucose and a disaccharide solution formed CSs at 180 °C (Fig 2.16 1d-f). For the cellulose solution, the formation of SCSs was observed at temperatures above 200 °C. The formation of SCSs with larger particle sizes was favoured when using a disaccharide as a carbon precursor.

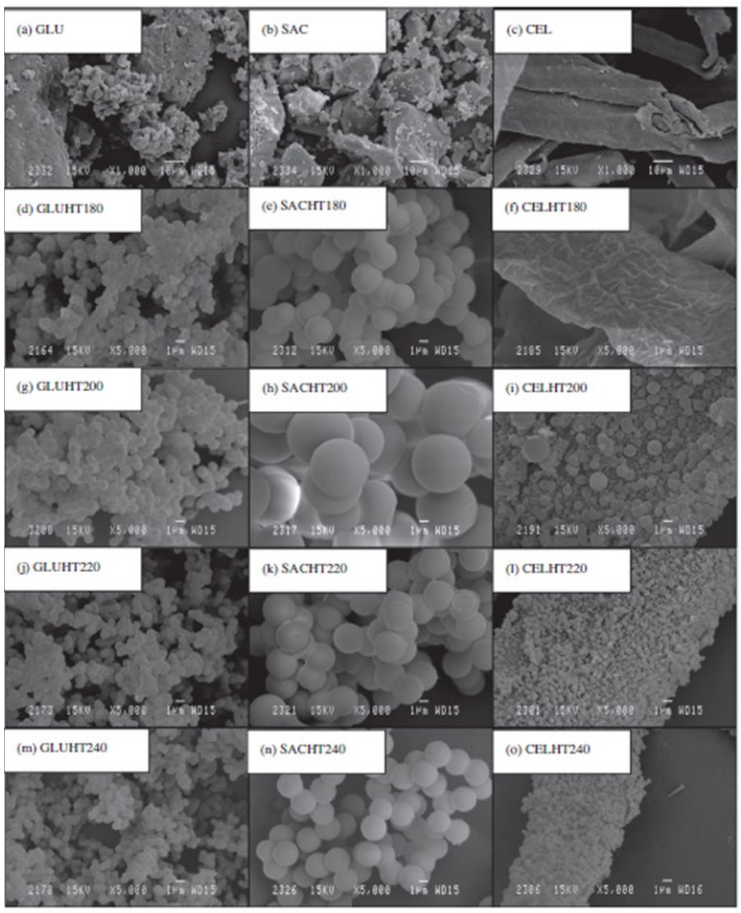

Figure 2.16: SEM images showing the effect of temperature using different precursors in the synthesis of CSs [67].

Inada *et al*. reported the synthesis of SCSs from HTC of a 1 M solution of glucose at 200 °C while varying the reaction time from 3-24 hours [68]. The average diameter of the SCSs obtained varied from 50-200 nm with reaction time (Fig. 2.17 b and c). The authors noted a change in the pH of the glucose solution and an increase in the yield of the SCSs with an increase in the reaction time (Fig. 2.17 a).

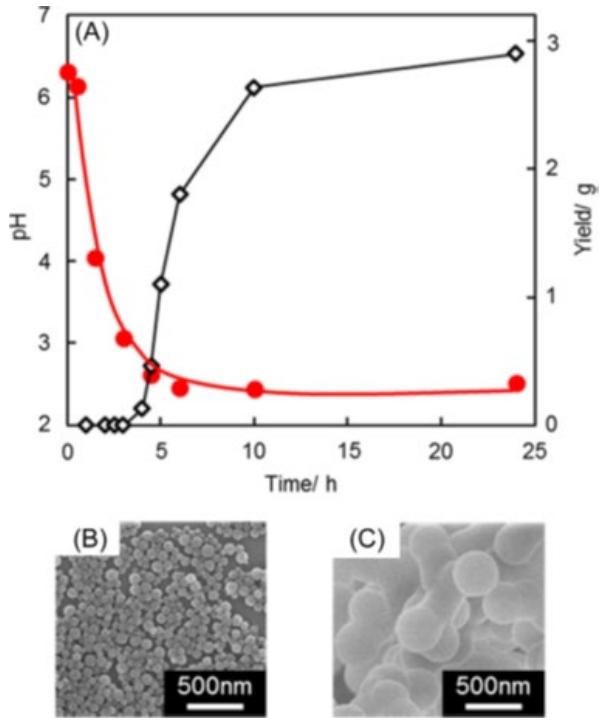

Figure 2.17: (a) Changes in the pH solution during HTC of the glucose at 200 °C and yield of the SCSs with reaction time, SEM images of the SCSs synthesized after (b) 3h, and (c) 24h [68].

Other methods that can be used to synthesize SCSs include the use of chemical vapour deposition (CVD). In this approach, SCSs are formed by pyrolysis of hydrocarbons at elevated temperatures with or without the presence of a catalyst [69, 70]. Wang *et al.* synthesized monodispersed SCSs with an average diameter of 210 nm using a mixed-valent oxide-catalytic carbonization process [70]. In this procedure, methane gas was flowed through a quartz tube in the presence of transition and/or rare earth metal oxides with mixed valences and heated in a furnace at 1100 °C.

Jin *et al.* prepared SCSs with diameters ranging from 50 nm to 1 μm using the CVD method [71]. In their approach, different liquid hydrocarbons (styrene, benzene, cyclohexane, toluene, and hexane) were carbonized using a double stage furnace reactor. The liquid was vaporized in the first stage furnace (T= 215 °C) under flowing argon gas. The vapour was then carbonized in the second stage furnace (T= 900-1200 °C). Styrene was used to look at the effect of flow rate and the reaction time on the diameter of the spheres. The authors showed that there were no significant changes in the diameter of the SCSs when varying the reaction time at temperatures between 900 and 1200 °C. Also, it was noted that increasing the flow rate of the carbon source resulted in an increase in the diameter of the SCSs.

2.3.3 Hollow carbon spheres

Hollow carbon spheres (HCSs) have attracted great interest due to their intriguing structure and properties [72]. The unique properties of HCSs include tunable porosity, high surface-volume ratio, surface functionality, interior void, and excellent chemical and thermal stabilities [72-75]. These properties have led to an intensive study of HCSs in different applications such as catalysis, adsorption/separation, microreactors, synthesis templates, energy storage and conversion [72-74, 76].

Different methods to produce HCSs have been developed by researchers. The developed synthetic routes can be classed into two approaches. The hard-core templating method and the soft-core templating method, based on the types of templates used to create the hollow core [72, 74]. The most widely used method is the hard-core templating method which uses a sacrificial-core-based approach (Fig. 2.18a). In this process, a robust core material (i.e. silica spheres, metal oxides, and polystyrene spheres (PSSs) having monodispersed size and spherical shape is coated with a carbon precursor which forms a core-shell structure followed by the carbonization of the shell [54, 74, 75, 77]. The carbon precursors often used are resorcinol formaldehyde resin [78, 79], glucose [81, 82], dopamine [83, 84], methane [74], and petroleum pitch [73]. The core template can be removed either by thermal decomposition, acid/alkaline etching or dissolution to form a hollow carbon structure. The hard-core templating method allows for the production of monodispersed HCSs with controllable size and shell thickness [72, 76]. As mentioned before the HCSs can be used as a nanoreactor and noble nanoparticles can be encapsulated inside the HCSs (Fig. 2.18b). This reduces the extent of particle agglomeration during catalysis reactions by providing the catalysts with an isolated and protected environment from the neighbouring catalyst particles, and molecules in the surrounding solution [72, 84].

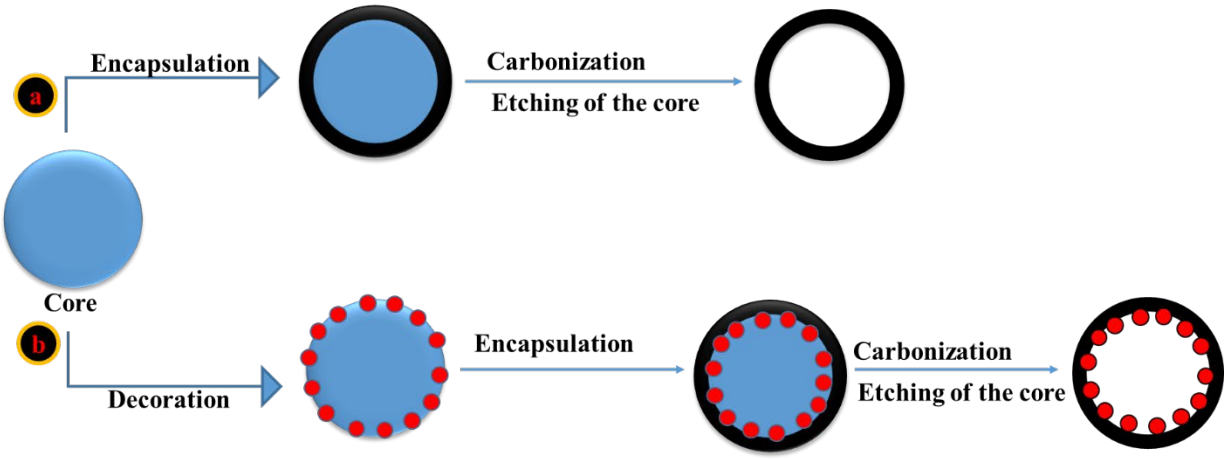

Figure 2.18: Schematic representation of the hard-core templating method for the synthesis of HCSs.

The soft-core templating method involves self-assembly of the precursor molecules and the colloidal systems to form a core template. This approach uses a soft and flexible core such as a surfactant or polymer micelle, gas bubble, emulsion droplet, or supramolecule [76, 85]. In comparison, the soft-core templating method is advantageous to use because the template can be easily removed through pyrolysis or extraction but the morphology and the monodispersity of the HCSs are difficult to control because the soft templates are highly susceptible to environmental changes [76, 77]. Also, some of the carbon precursors used are corrosive, toxic, or expensive as they are highly dependent on carbon-rich polymers or fossil-based compounds [72].

2.4 Catalysts supported on carbon nanomaterials

Metal NPs or metal oxide catalysts can be supported on conventional oxide supports (e.g. silica, alumina) or conventional carbon supports in order to improve catalytic activity and durability of the catalyst [86]. Catalysts supported on conventional carbon supports have been studied over the past few decades and have found use in many different applications in catalysis [87]. Among other reasons why conventional carbon supports are preferred over conventional oxide supports include their unique properties such as (i) large surface area, (ii) high thermal stability, (iii) facile recovery of noble metals, and (iv) ability to tune their surface chemistry or porosity [86-88].

Our research group has synthesized various-shaped carbon nanomaterials (e.g. SCSs, HCSs, CNTs, CNFs, and graphene oxide). Some of these CNMs have been used to support catalysts (e.g. Pt, Pd, Ru, Co, Os, and Fe) and were applied in the Fischer-Tropsch process, carbon monoxide methanation, and hydrogenation of CALD to name a few [89-95]. For example, Phaahlamohlaka *et al.* studied the hydrogen spillover process using mesoporous HCSs as a

model catalyst support [91]. The interior of the MHCSs allowed the authors to create both primary (Ru and Co_3O_4 were in close contact) and secondary (Ru and Co_3O_4 were separated by the mesoporous carbon shell) spillover effects. When Ru and Co_3O_4 were in close contact (Ru/Co/MHCS) a higher F-T activity and greater reducibility at lower temperatures were reported. In contrast to Ru/Co/MHCS, when Ru and Co_3O_4 (Ru@MHCS@Co) were separated, lower reducibility at higher temperatures and low F-T activity was reported.

Manikai, in her Ph.D. study looked at the effect of nitrogen-doped SCSs as Pd catalyst support in the hydrogenation CALD [90]. It was reported that N-doping resulted in a catalyst with Pd particle size ranging from 4.15 to 4.82 nm compared to Pd NPs supported on oxygen functionalized SCSs (4.68-7.51 nm). The catalytic activity of Pd NPs supported on N-SCSs was significantly enhanced as a CALD conversion of 91 % was obtained compared to a non-doped catalyst (CALD conversion of 48%). Different shaped CNMs have been used as Pd catalyst supports in the selective hydrogenation of CALD and their effect will be discussed in section 2.4.2.

2.4.1 Application of metals supported on carbon nanomaterials in the hydrogenation of cinnamaldehyde

Selective hydrogenation of α,β-unsaturated aldehydes is widely studied for the production of valuable fine chemicals [96]. For an example, the selective hydrogenation of cinnamaldehyde (CALD) is one of the most studied reactions in the synthesis of commercial fine chemicals [96]. The selective hydrogenation of CALD proceeds via different pathways to allow hydrogenation of the C=C forming hydrocinnamaldehyde (HCALD) and the hydrogenation of the C=O bond forming cinnamylalcohol (CA) [96-98]. Both CA and HCALD can be further hydrogenated to form 3-phenyl-1-propanol [96-98]. Supported noble (e.g. Pd, Pt, Ir and Ru) and non-noble (e.g. Ni, Cu, Fe, and Co) metals have been used in the selective hydrogenation of CALD [99, 100]. In the selective hydrogenation of CALD, Pd, Rh, Mo, and Cu have been reported to be more selective towards the hydrogenation of C=C bond, whereas Pt, Ir, Ru and Co are effective in the hydrogenation of C=O bond [101].

Carbon nanomaterials (CNMs) such as graphene, carbon nanotubes (CNTs), and carbon nanofibers (CNFs) have found use as supports for metals in the selective hydrogenation of CALD [98, 102-104]. The ease of surface modification of these CNMs have an impact on metal dispersion thus affecting the catalyst performance [96]. The properties of CNMs such as good electronic transfer and hydrophobic surface have been reported to enhance the reaction rate as

these properties enables the adsorption of organic compounds with weak polarity on their surface [104]. The metal NPs distribution and size are mostly affected by the interaction between the active metal NPs and the carbon support [96, 105]. The use of CNMs is advantageous because of the weak interaction between the carbon support and metal NPs which provides facile recovery of precious metals [105]. However, the use of the pristine CNMs as metal NPs support has some drawbacks. Due to the weak carbon to metal interaction, the metal NPs can leach out or form aggregates which results in the deactivation of the catalyst [96, 105]. To overcome this problem the surface of the CNMs can be modified by heteroatoms (e.g. nitrogen, phosphorus, and sulphur) doping or functionalization to introduce oxygen-containing functional groups via oxidation with acid treatment [96, 105]. The surface modification of the CNMs improves the interaction between the carbon support and metal NPs [96, 105]. Table 2.1 summarizes some of the work done on the hydrogenation of CALD using noble metal based catalysts supported on CNMs.

Table 2.1: Summary of work done on the hydrogenation of CALD using noble metals supported on CNMs.

Catalysts	CALD hydrogenation conditions	Results	Refere-nces
0.4 wt. % Pt/graphite 2 wt. % Pt/graphite 4 wt. % Pt/graphite	80 mg catalyst, 0.038 mol CALD, 10 mL isopropanol, 0.5 MPa H_2, 60 °C, 4 h.	The first catalyst showed no activity. The catalyst with 4 wt. % had the highest conversion of CALD (97.3 %) and 97.2 % 3P1P, 1.7 % CA, and 1.1 propyl benzene selectivity.	103
3.5 wt. % Pt/CNTs 3.5 wt. % Pt/RGO@SiO_2	50 mg catalyst, 1 g CALD, 30 mL isopropanol, 10 bar H_2, 60 °C, 2 h.	CALD conversion of 39 % was obtained when using Pt/CNTs catalyst and 23 % HCALD, 9 % 3P1P, 62 % CA, and 6 % by-products selectivity. Similar CALD conversion (38%) was obtained with Pt/RGO@SiO_2	100

		catalyst. A selectivity of 8 % HCALD, 48 % CA, 11 % 3P1P, and 6 % by-products was reported.	
3.4 wt. % Ru/CNTs 3.04 wt. % Ru@CNTs	10 mg catalyst, 1 g CALD, 100 mL isopropanol, 2 MPa H_2, 100 °C, 2h.	The Ru/CNTs catalyst had 100 % HCALD selectivity whereas Ru@CNTs formed three products (HCALD, CA, and 3P1P) with comparable selectivity.	106
3 wt. % Pt/CNTs-1 (CNTs inner diameter less than 10 nm. 3 wt. % Pt/CNTs-2 (CNTs-2 inner diameter ranges between 60 and 100 nm)	0.3 g catalyst, 5 mL CALD, 35 mL isopropanol, 3 MPa H_2, 80 °C, 12 h.	3 wt. % Pt/CNTs-1 attained 100 % conversion in 4 hours compared to 8 hours from 3 wt. % Pt/CNTs-2 catalyst. The 3 wt. % Pt/CNTs-1 catalyst hydrogenated both the C=O and C=C bond forming 3P1P. The 3 wt. % Pt/CNTs-2 catalyst had 60 % CA.	107
5 wt. % Ru/CNF (CNF oxidized only) Ru/CNF pretreated and annealed at various temperatures of 300, 500, and 700 °C.	0.5-1 g catalyst, 9 g CALD, 100 mL isopropanol, 4.5 MPa H_2, 110 °C, 50 min.	At a conversion of 60 %, the 5 wt. % Ru/CNF catalyst was more selective to CA whereas 5 wt. % Ru/CNF973 catalyst showed an increase in HCALD selectivity from 34 % to 73 % respectively. Annealing the catalyst at higher temperature increased the activity of the catalyst by a factor of 22.	108
Pt/AC-H_2O Pt/AC-2%KOH Pt/AC-8%KOH Pt/AC-10%KOH	5.0 mg catalyst, 1.0 mL CALD, 1.0 mL ethanol, 3.0 MPa, 80 °C, 2 h.	Pretreatment of AC with KOH from 2 to 10 % showed an increase in CALD conversion (38.7 to 62.88 %) when	96

Pt/AC-15%KOH		compared to Pt/AC-H_2O catalyst (32.0 %). Increasing the concentration of KOH to 15 % let to a drastic decrease in the CALD conversion (16.0 %). An increase in the selectivity to CA was observed with an increase in KOH % in the catalyst (51.7 to 73.4 %).	
15 wt. % Ni/P25 15 wt. % Ni/Hombilcat 15 wt. % Ni/Rutile 15 wt. % Ni/SiO_2 15 wt. % Ni/Al_2O_3	150 mg catalyst, 1.2 g CALD, 16 mL methanol, 20 Kg/cm^2 H_2, 120 °C, 1 h.	Ni/P25 had 91 % CALD conversion with 61 % selectivity to CA. Ni/Hombilcat converted 57 % CALD and a selectivity of 66 % to HCALD was observed. Ni/Rutile had 51 % conversion with 72 % selectivity to HCALD. Ni/SO_2 had 38 % CALD conversion and 79 % selectivity to HCALD. Ni/Al_2O_3 had the lowest CALD conversion (18 %) and a selectivity of 78 % to HCALD.	109

2.4.2 Carbon nanomaterials as catalysts (carbocatalysis)

Carbon materials are known to act as catalysts, a phenomenon known as carbocatalysis [110, 111]. Carbocatalysis studies date back as early as 1925 when charcoal was discovered as an active component in the oxidation of oxalic acid by Rideal and Wright [112]. The rapid development of carbon nanomaterials (CNMs) such as fullerene, CNTs, graphene, nanodiamonds, and mesoporous carbon has led to an enormous interest in the use of these CNMs as carbocatalysts in various catalytic applications [113]. Functional groups on the surface of these CNMs have been identified as one of the catalytic sites [113].

Wu *et al.* reported the reduction of nitrobenzene to form aniline using acid treated CNTs (oCNTs) [114]. The conversion of about 40 % was obtained. The oCNTs were thermally treated at 500 and 800 °C to partially remove some of the oxygen functional groups and they were labelled oCNTs500 and oCNTs800. When the oCNTs500 catalyst was used nitrobenzene conversion of 95.5 % was obtained. The selectivity to aniline of 97.5 to 91.9 % was reported for oCNTs and oCNT500 catalysts respectively. Increasing the annealing temperature to 800 °C resulted in the deactivation of the catalyst (22 % conversion was reported). The decrease in the catalyst activity with increasing annealing temperature was attributed to a decrease in the total content of oxygen and carbonyl groups.

Primo *et al.* reported on the use of graphene as carbocatalyst in the selective hydrogenation of acetylene and alkene [115]. The authors reported that the conversion of acetylene in the presence of graphene as catalyst increased along with the reaction temperature. At room temperature acetylene conversion of 16 % was obtained. When the reaction temperature was increased to 110 and 120 °C the catalyst resulted in the acetylene conversion of 99 % and 21 % conversion of ethylene. However, there are no literature reports on the use of CNMs as catalyst in the hydrogenation of CALD.

2.4.3 Hydrogenation of cinnamaldehyde using carbon nanomaterials supported palladium catalysts

Sairanen *et al.* prepared multi-walled carbon nanotubes (MWCNTs) supported Pd catalysts using three different deposition methods (dry-impregnation, wet-impregnation, and atomic layer deposition (ALD)) [116]. The synthesized Pd/MWCNTs catalysts were labelled as wet-impregnated, dry-impregnated, and ALD-prepared catalysts and tested them for the hydrogenation of CALD. The wet-impregnated catalyst produced HCALD and 3P1P as major products with a small amount of propylbenzene as a by-product. Using both dry-impregnated and ALD-prepared catalysts only 3P1P and propylbenzene were produced. The synthesized catalysts did not produce CA. The difference in the product distribution of these catalysts was attributed to a difference in metal particle sizes and dispersion.

Xu *et al.* reported the synthesis of oxygen functionalized graphite felt (OGF) supported Pd catalyst (Pd/OGF) for liquid-phase hydrogenation of CALD [117]. To study the effect of oxygen containing functional groups on the support, Pd/GF was used for comparison. Different parameters, such as stirring rate, initial CALD concentration ([CALD]), reaction temperature, and hydrogen flow rate were used to evaluate the catalyst activity. The influence of the stirring

speed was carried out at 80 °C using different stirring speed (250 to 500) rpm. It was observed that at a stirring rate of 375 rpm the hydrogenation activity increased and reached a maximum whereas at a stirring rate of 500 rpm a slight drop in the hydrogenation activity occurred. The authors concluded that the stirring rate enhanced the selectivity of the C=C hydrogenation (88 and 91 %) between 250 and 375 rpm respectively. The influence of initial CALD concentration did not have a significant impact on the selectivity of the C=C hydrogenation as it remained between 86 and 91 %. The effect of the reaction temperature was conducted between 40 and 80 °C. It was observed that increasing the reaction temperature resulted in an increase in CALD conversion and C=C hydrogenation selectivity (88 to 91 %).

To compare the activity of Pd/OGF and Pd/GF catalysts, the influence of hydrogen flow rate and catalyst stability was studied. The influence of hydrogen flow rate was carried out under similar conditions (i.e. H_2 flow rate of 50 mL/min and [CALD] of 0.08 mol/L) for the two catalysts. Both the catalysts had similar activity. When the hydrogen flow rate was lowered to 12.5 ml/min and initial [CALD] increased to 0.32 mol/L, the Pd/OGF catalyst hydrogenated CALD much quicker than the Pd/GF catalyst. This was attributed to poor Pd particle dispersion on the surface of the GF support and a larger Pd particle size which resulted in a slower rate of hydrogen dissociation. The catalyst stability was tested up to fifteen cycles and it was shown that the Pd/OGF catalyst was highly stable as no deactivation was observed after fifteen cycles. The Pd/GF catalyst CALD conversion decreased to 40 % after the fourth cycle as a result of severe catalyst deactivation. The authors concluded that the oxygen containing functional groups and the defects created on the OGF support provided strong anchoring sites for dispersing Pd NPs. These anchoring sites stabilized the Pd NPs and prevented the Pd nanoparticle agglomeration. The strong metal-support interaction resulted in endurance of the Pd/OGF catalyst as this was observed during cycling test.

Nagpure *et al.* reported the synthesis of Pd NPs supported on nitrogen-doped mesoporous carbon (Pd-NMC) [118]. The Pd-NMC catalyst attained 100 % CALD conversion within 3 hours with high selectivity (93 %) to the hydrogenation of C=C forming HCALD. For comparison nitrogen free Pd-MC catalyst was used to hydrogenate CALD, and the selectivity to HCALD dropped to 66 %. The authors concluded that N-doping resulted in well-dispersed Pd NPs, improved metal-support interaction between Pd and NMC, and generated small Pd NPs which enhanced the catalytic activity of the catalyst. On the other hand, the use of a nitrogen free catalyst had poor Pd NPs dispersion along with a larger Pd particle size. The stability of the

Pd-NMC catalyst was tested and it was found that the catalyst gave 100 % CALD conversion after six cycles without any significant drop in the HCALD selectivity.

2.5 Conclusions

Different properties of shaped CNMs has led to their extensive use in diverse applications. The use of CNMs as a catalyst support for the hydrogenation of CALD has been well documented in the literature. The carbon-metal interaction has been shown to have a great impact on the catalytic activity of the catalyst. Functionalization of the CNMs with oxygen-containing functional groups or doping CNMs with heteroatoms has been reported as the key in improving metal dispersion on the surface of the carbon support. Also, surface modification helped in minimizing the extent of metal particle agglomeration during application.

Carbon dots (CDs) as recent members of CNMs are intriguing and their unique properties have allowed their use in various applications. C-C formation reactions are amongst different applications in which a CDs composite has found use. Developing a catalyst that is highly selective, stable, and active is often challenging in chemoselective hydrogenation reactions. Our goal was to investigate and understand the use of CDs as reducing agent for Pd ions and to "support" the Pd NPs for use in the hydrogenation of CALD. From the literature review, Pd based catalysts have been shown to be highly selective towards the reduction of the C=C bond, hence, part of our goal was to determine if the selectivity to the reduction of C=O bond by incorporating highly functionalized CDs was feasible. Many CNMs used as catalyst support are inert and thus do not have any intrinsic catalytic activity. However, the small size and surface properties of the CDs suggest that the catalytic activity of the CDs in the hydrogenation of CALD could be different to that observed using a more standard carbon support.

The use of HCSs and SCSs as support for Pd catalyst for hydrogenation of CALD is not well documented in the literature. Since both HCSs and SCSs are inert [91, 119], they were used as a support for Pd NPs in order to be able to make comparisons with the Pd/CDs catalyst.

2.6 References

1. Su, D. S.; Perathoner, S.; Centi, G. *Chemical Reviews* **2013**, *113*, 5782.
2. Wang, F.-L.; Pang, L.-L.; Jiang, Y.-Y.; Chen, B.; Lin, D.; Lun, N.; Zhu, H.-L.; Liu, R.; Meng, X.-L.; Wang, Y.; Bai, Y.-J.; Yin, L.-W. *Materials Letters* **2009**, *63*, 2564.
3. Deshmukh, A. A.; Mhlanga, S. D.; Coville, N. J. *Materials Science and Engineering: R: Reports* **2010**, *70*, 1.

4. De, B.; Karak, N. *Journal of Materials Chemistry A* **2017**, *5*, 1826.
5. Zhou, J.; Zhou, H.; Tang, J.; Deng, S.; Yan, F.; Li, W.; Qu, M. *Microchimica Acta* **2017**, *184*, 343.
6. Georgakilas, V.; Perman, J. A.; Tucek, J.; Zboril, R. *Chemical Reviews* **2015**, *115*, 4744.
7. Lim, S. Y.; Shen, W.; Gao, Z. *Chemical Society Reviews* **2015**, *44*, 362.
8. Shen, L.-M.; Liu, J. *Talanta* **2016**, *156*, 245.
9. Xu, X.; Ray, R.; Gu, Y.; Ploehn, H. J.; Gearheart, L.; Raker, K.; Scrivens, W. A. *Journal of the American Chemical Society* **2004**, *126*, 12736.
10. Dimos, K. *Current Organic Chemistry* **2016**, *20*, 682
11. Baker, S. N.; Baker, G. A. *Angewandte Chemie International Edition* **2010**, *49*, 6726.
12. Jelinek, R.; *Carbon Nanostructures* **2016**, 1.
13. Sun, Y.-P.; Zhou, B.; Lin, Y.; Wang, W.; Fernando, K. A. S.; Pathak, P.; Meziani, M. J.; Harruff, B. A.; Wang, X.; Wang, H.; Luo, P. G.; Yang, H.; Kose, M. E.; Chen, B.; Veca, L. M.; Xie, S.-Y. *Journal of the American Chemical Society* **2006**, *128*, 7756.
14. Biswas, A.; Paul, S.; Banerjee, A. *Journal of Materials Chemistry A* **2015**, *3*, 15074.
15. Gwebu, S. S.; Nomngongo, P. N.; Maxakato, N. W. In *Nanocatalysts*; IntechOpen: 2019.
16. Wang, X.; Qu, K.; Xu, B.; Ren, J.; Qu, X. *Journal of Materials Chemistry* **2011**, *21*, 2445.
17. Bayati, M.; Dai, J.; Zambrana, A.; Rees, C.; Fidalgo de Cortalezzi, M. *Journal of Environmental Sciences* **2017**.
18. Zhu, S.; Song, Y.; Zhao, X.; Shao, J.; Zhang, J.; Yang, B. *Nano Research* **2015**, *8*, 355.
19. Wang, R.; Lu, K.-Q.; Tang, Z.-R.; Xu, Y.-J. *Journal of Materials Chemistry A* **2017**, *5*, 3717.
20. Wu, Z. L.; Liu, Z. X.; Yuan, Y. H. *Journal of Materials Chemistry B* **2017**, *5*, 3794.
21. Ming, H.; Ma, Z.; Liu, Y.; Pan, K.; Yu, H.; Wang, F.; Kang, Z. *Dalton Transactions* **2012**, *41*, 9526.
22. Shinde, D. B.; Pillai, V. K. *Chemistry – A European Journal* **2012**, *18*, 12522.
23. Hu, S.; Liu, J.; Yang, J.; Wang, Y.; Cao, S. *Journal of Nanoparticle Research* **2011**, *13*, 7247.
24. Qiao, Z.-A.; Wang, Y.; Gao, Y.; Li, H.; Dai, T.; Liu, Y.; Huo, Q. *Chemical Communications* **2010**, *46*, 8812.

25. Park, S. Y.; Lee, H. U.; Park, E. S.; Lee, S. C.; Lee, J.-W.; Jeong, S. W.; Kim, C. H.; Lee, Y.-C.; Huh, Y. S.; Lee, J. *ACS Applied Materials & Interfaces* **2014**, *6*, 3365.
26. Guo, Y.; Wang, Z.; Shao, H.; Jiang, X. *Carbon* **2013**, *52*, 583.
27. Liu, X.; Pang, J.; Xu, F.; Zhang, X. *Scientific Reports* **2016**, *6*, 31100.
28. Gong, J.; Lu, X.; An, X. *RSC Advances* **2015**, *5*, 8533.
29. Chen, B.; Li, F.; Li, S.; Weng, W.; Guo, H.; Guo, T.; Zhang, X.; Chen, Y.; Huang, T.; Hong, X. *Nanoscale* **2013**, *5*, 1967.
30. Yang, Y.; Wu, D.; Han, S.; Hu, P.; Liu, R. *Chemical Communications* **2013**, *49*, 4920.
31. Wang, Y.; Hu, A. *Journal of Materials Chemistry C* **2014**, *2*, 6921.
32. Yao, B.; Huang, H.; Liu, Y.; Kang, Z. *Trends in Chemistry* **2019**, *1*, 235.
33. Zhao, P.; Zhu, L. *Chemical Communications* **2018**, *54*, 5401.
34. Chen, B. B.; Liu, M. L.; Li, C. M.; Huang, C. Z. *Advances in Colloid and Interface Science* **2019**, *270*, 165.
35. Radhakrishnan, K.; Panneerselvam, P.; Marieeswaran, M. *Analytical Methods* **2019**, *11*, 490.
36. Xu, Q.; Kuang, T.; Liu, Y.; Cai, L.; Peng, X.; Sreenivasan Sreeprasad, T.; Zhao, P.; Yu, Z.; Li, N. *Journal of Materials Chemistry B* **2016**, *4*, 7204.
37. Park, Y.; Yoo, J.; Lim, B.; Kwon, W.; Rhee, S. W. *Journal of Materials Chemistry A* **2016**, *4*, 11582.
38. Song, Y.; Zhu, C.; Song, J.; Li, H.; Du, D.; Lin, Y. *ACS Applied Materials & Interfaces* **2017**, *9*, 7399.
39. Scialabba, C.; Sciortino, A.; Messina, F.; Buscarino, G.; Cannas, M.; Roscigno, G.; Condorelli, G.; Cavallaro, G.; Giammona, G.; Mauro, N. *ACS Applied Materials & Interfaces* **2019**, *11*, 19854.
40. Ghann, W.; Sharma, V.; Kang, H.; Karim, F.; Richards, B.; Mobin, S. M.; Uddin, J.; Rahman, M. M.; Hossain, F.; Kabir, H.; Uddin, N. *International Journal of Hydrogen Energy* **2019**, *44*, 14580.
41. Amato, F.; Cacioppo, M.; Arcudi, F.; Prato, M.; Mituo, M.; Fernandes, E.; Carreno, M.; Pereyra, I.; Bartoli, J. *Chemical Engineering Transactions* **2019**, *74*, 1105.
42. Yan, F.; Zou, Y.; Wang, M.; Mu, X.; Yang, N.; Chen, L. *Sensors and Actuators B: Chemical* **2014**, *192*, 488.
43. Radhakrishnan, K.; Panneerselvam, P.; Marieeswaran, M. *Analytical Methods* **2019**, *11*, 490.

44. Long, C.; Jiang, Z.; Shangguan, J.; Qing, T.; Zhang, P.; Feng, B. *Chemical Engineering Journal* **2021**, *406*, 126848.
45. Peng, Z.; Zhou, Y.; Ji, C.; Pardo, J.; Mintz, K. J.; Pandey, R. R.; Chusuei, C. C.; Graham, R. M.; Yan, G.; Leblanc, R. M. *Nanomaterials* **2020**, *10* (8), 1560.
46. Safardoust-Hojaghan, H.; Salavati-Niasari, M. *Journal of Cleaner Production* **2017**, *148*, 31–36.
47. Zaib, M.; Akhtar, A.; Maqsood, F.; Shahzadi, T. *Arab J Sci Eng* **2021**, *46* (1), 437–446.
48. Dey, D.; Bhattacharya, T.; Majumdar, B.; Mandani, S.; Sharma, B.; Sarma, T. K. *Dalton Transactions* **2013**, *42*, 13821.
49. Zhang, J.; Chen, Y.; Tan, J.; Sang, H.; Zhang, L.; Yue, D. *Applied Surface Science* **2017**, *396*, 1138.
50. Lu, A.-H.; Hao, G.-P.; Sun, Q.; Zhang, X.-Q.; Li, W.-C. *Macromolecular Chemistry and Physics* **2012**, *213*, 1107.
51. Deshmukh, A. A.; Mhlanga, S. D.; Coville, N. J. *Materials Science and Engineering: R: Reports* **2010**, *70*, 1.
52. Yamada, K.; Tobisawa, S. *Carbon* **1989**, *27*, 845.
53. Wang, M. J.; Gray, C. A.; Reznek, S. A.; Mahmud, K.; Kutsovsky, Y. *Kirk-Othmer Encyclopedia of Chemical Technology* **2000**.
54. Li, S.; Pasc, A.; Fierro, V.; Celzard, A. *Journal of Materials Chemistry A* **2016**, *4*, 12686.
55. Nieto-Márquez, A.; Romero, R.; Romero, A.; Valverde, J. L. *Journal of Materials Chemistry* **2011**, *21*, 1664.
56. Inagaki, M.; Kuroda, K.; Sakai, M. *Carbon* **1983**, *21*, 231.
57. Coville, N. J.; Mhlanga, S. D.; Nxumalo, E. N.; Shaikjee, A. *South African Journal of Science* **2011**, *107*, 01.
58. Serp, P.; Feurer, R.; Kalck, P.; Kihn, Y.; Faria, J. L.; Figueiredo, J. L. *Carbon* **2001**, *39*, 621.
59. Wissler, M. *Journal of Power Sources* **2006**, *156*, 142.
60. Wang, F.-L.; Pang, L.-L.; Jiang, Y.-Y.; Chen, B.; Lin, D.; Lun, N.; Zhu, H.-L.; Liu, R.; Meng, X.-L.; Wang, Y.; Bai, Y.-J.; Yin, L.-W. *Materials Letters* **2009**, *63*, 2564.
61. Khodabakhshi, S.; Kiani, S.; Niu, Y.; White, A. O.; Suwaileh, W.; Palmer, R. E.; Barron, A. R.; Andreoli, E. *Carbon* **2021**, *171*, 426.

62. Lu, A.-H.; Hao, G.-P.; Sun, Q.; Zhang, X.-Q.; Li, W.-C. *Macromolecular Chemistry and Physics* **2012**, *213*, 1107.
63. Liu, J.; Qiao, S. Z.; Liu, H.; Chen, J.; Orpe, A.; Zhao, D.; Lu, G. Q. *Angewandte Chemie International Edition* **2011**, *50*, 5947.
64. Zhao, J.; Gilani, M. R. H. S.; Lai, J.; Nsabimana, A.; Liu, Z.; Luque, R.; Xu, G. *Macromolecules* **2018**, *51*, 5494.
65. Friedel, B.; Greulich-Weber, S. *Small* **2006**, *2*, 859.
66. Titirici, M.-M.; Antonietti, M. *Chemical Society Reviews* **2010**, *39*, 103.
67. Romero-Anaya, A. J.; Ouzzine, M.; Lillo-Ródenas, M. A.; Linares-Solano, A. *Carbon* **2014**, *68*, 296.
68. Inada, M.; Enomoto, N.; Hojo, J.; Hayashi, K. *Advanced Powder Technology* **2017**, *28*, 884.
69. Qian, H.-s.; Han, F.-m.; Zhang, B.; Guo, Y.-c.; Yue, J.; Peng, B.-x. *Carbon* **2004**, *42*, 761.
70. Wang, Z. L.; Kang, Z. C. *The Journal of Physical Chemistry* **1996**, *100*, 17725.
71. Jin, Y. Z.; Gao, C.; Hsu, W. K.; Zhu, Y.; Huczko, A.; Bystrzejewski, M.; Roe, M.; Lee, C. Y.; Acquah, S.; Kroto, H.; Walton, D. R. M. *Carbon* **2005**, *43*, 1944.
72. Liu, X.; Song, P.; Hou, J.; Wang, B.; Xu, F.; Zhang, X. *ACS Sustainable Chemistry & Engineering* **2018**, *6*, 2797.
73. Du, J.; Liu, L.; Liu, B.; Yu, Y.; Lv, H.; Chen, A. *Carbon* **2019**, *143*, 467.
74. Li, X.; Chi, M.; Mahurin, S. M.; Liu, R.; Chuang, Y.-J.; Dai, S.; Pan, Z. *Carbon* **2016**, *101*, 57.
75. Zhao, X.; Li, Y.; Gong, Q.; Huang, Y.; Gong, M.; Du, K.; Guo, Y.; Bai, J.; Gan, J.; Zhao, M.; Zhao, Y.; Zhuang, D. *Carbon* **2021**, *183*, 158.
76. Lee, J.; Kim, S. M.; Lee, I. S. *Nano Today* **2014**, *9*, 631.
77. Chen, A.; Wang, Y.; Yu, Y.; Sun, H.; Li, Y.; Xia, K.; Li, S. *Journal of Materials Science* **2017**, *52*, 3153.
78. Zhang, Z.; Zhang, J.; Wang, Y.; Tong, Y.; Zhang, L. *Talanta* **2017**, *167*, 428.
79. Zhang, L.; Liu, L.; Liu, M.; Yu, Y.; Hu, Z.; Liu, B.; Lv, H.; Chen, A. *Journal of Alloys and Compounds* **2019**, *778*, 294.
80. Fang, X.; Liu, S.; Zang, J.; Xu, C.; Zheng, M.-S.; Dong, Q.-F.; Sun, D.; Zheng, N. *Nanoscale* **2013**, *5*, 6908.
81. Tang, K.; Fu, L.; White, R. J.; Yu, L.; Titirici, M.-M.; Antonietti, M.; Maier, J. *Advanced Energy Materials* **2012**, *2*, 873.

82. Wang, F.-L.; Pang, L.-L.; Jiang, Y.-Y.; Chen, B.; Lin, D.; Lun, N.; Zhu, H.-L.; Liu, R.; Meng, X.-L.; Wang, Y.; Bai, Y.-J.; Yin, L.-W. *Materials Letters* **2009**, *63*, 2564.
83. Bian, S.-W.; Liu, S.; Guo, M.-X.; Xu, L.-L.; Chang, L. *RSC Advances* **2015**, *5*, 11913.
84. Cai, T.; Xing, W.; Liu, Z.; Zeng, J.; Xue, Q.; Qiao, S.; Yan, Z. *Carbon* **2015**, *86*, 235.
85. Pérez-Lorenzo, M.; Vaz, B.; Salgueiriño, V.; Correa-Duarte, M. A. *Chemistry – A European Journal* **2013**, *19*, 12196.
86. Zhai, Y.; Zhu, Z.; Dong, S. *ChemCatChem* **2015**, *7*, 2806.
87. Gerber, I. C.; Serp, P. *Chemical Reviews* **2019**, *120*, 1250.
88. Fu, T.; Li, Z. *Chemical Engineering Science* **2015**, *135*, 3.
89. Nongwe, I.; Ravat, V.; Meijboom, R.; Coville, N. J. *Applied Catalysis A: General* **2016**, *517*, 30.
90. Manikai, S. M.-A. *The synthesis of nitrogen doped carbon spheres as supports for palladium catalysts in the hydrogenation of cinnamaldehyde*, PhD Thesis, University of the Witwatersrand, Johannesburg, **2015**.
91. Phaahlamohlaka, T. N.; Kumi, D. O.; Dlamini, M. W.; Jewell, L. L.; Coville, N. J. *Catalysis Today* **2016**, *275*, 76.
92. Kumi, D. O.; Phaahlamohlaka, T. N.; Dlamini, M. W.; Mangezvo, I. T.; Mhlanga, S. D.; Scurrell, M. S.; Coville, N. J. *Applied Catalysis B: Environmental* **2018**, *232*, 492.
93. Phaahlamohlaka, T. N.; Dlamini, M. W.; Mogodi, M. W.; Kumi, D. O.; Jewell, L. L.; Billing, D. G.; Coville, N. J. *Applied Catalysis A: General* **2018**, *552*, 129.
94. Molefe, T.; Forbes, R. P.; Coville, N. J. *Catalysis Letters* **2020**, 1.
95. Dlamini, M. W.; Coville, N. J.; Scurrell, M. S. *RSC Advances* **2016**, *6*, 22222.
96. Zeng, L.-H.; Yan, H.-X.; Zeng, Y.-K.; Li, Y.-F.; Zhang, Z.-X.; Liu, Z.-W.; Liu, Z.-T. *The Canadian Journal of Chemical Engineering*, *0*.
97. Cabiac, A.; Delahay, G.; Durand, R.; Trens, P.; Coq, B.; Plée, D. *Carbon* **2007**, *45*, 3.
98. Solhy, A.; Machado, B. F.; Beausoleil, J.; Kihn, Y.; Gonçalves, F.; Pereira, M. F. R.; Órfão, J. J. M.; Figueiredo, J. L.; Faria, J. L.; Serp, P. *Carbon* **2008**, *46*, 1194.
99. Jiang, F.; Cai, J.; Liu, B.; Xu, Y.; Liu, X. *RSC Advances* **2016**, *6*, 75541.
100. Han, Q.; Liu, Y.; Wang, D.; Yuan, F.; Niu, X.; Zhu, Y. *Journal of Chemistry* **2016**, *2016*, 9.
101. Martínez-Ortiz, M. J.; de la Rosa-Guzmán, M. A.; Vargas-García, J. R.; Flores-Moreno, J. L.; Castillo, N.; Guzmán-Vargas, A.; Morandi, S.; Pérez-Gutiérrez, R. M. *The Canadian Journal of Chemical Engineering* **2018**, *96*, 297.

102. Lamme, W. S.; Zečević, J.; de Jong, K. P. *ChemCatChem* **2018**, *10*, 1552.

103. Chang, S.; Meng, S.; Fu, X.; Zhang, S.; Zheng, X.; Chen, S. *ChemistrySelect* **2019**, *4*, 2018.

104. Zhu, J.; Dou, M.; Lu, M.; Xiang, X.; Ding, X.; Liu, W.; Li, M. *Applied Catalysis A: General* **2019**, *575*, 11.

105. Xu, Z.; Duong-Viet, C.; Liu, Y.; Baaziz, W.; Li, B.; Nguyen-Dinh, L.; Ersen, O.; Pham-Huu, C. *Applied Catalysis B: Environmental* **2019**, *244*, 128.

106. Ma, H.; Yu, T.; Pan, X.; Bao, X. *Chinese Journal of Catalysis* **2017**, *38*, 1315.

107. Ma, H.; Wang, L.; Chen, L.; Dong, C.; Yu, W.; Huang, T.; Qian, Y. *Catalysis Communications* **2007**, *8*, 452.

108. Toebes, M. L.; Prinsloo, F. F.; Bitter, J. H.; van Dillen, A. J.; de Jong, K. P. *Journal of Catalysis* **2003**, *214*, 78.

109. Prakash, M. G.; Mahalakshmy, R.; Krishnamurthy, K. R.; Viswanathan, B. *Catalysis Science & Technology* **2015**, *5*, 3313.

110. Navalon, S.; Dhakshinamoorthy, A.; Alvaro, M.; Garcia, H. *Chemical Reviews* **2014**, *114*, 6179.

111. Gordeev, E. G.; Pentsak, E. O.; Ananikov, V. P. *Journal of the American Chemical Society* **2020**.

112. Rideal, E. K.; Wright, W. M. *Journal of the Chemical Society, Transactions* **1925**, *127*, 1347.

113. Su, D. S.; Wen, G.; Wu, S.; Peng, F.; Schlögl, R. *Angewandte Chemie International Edition* **2017**, *56*, 936.

114. Wu, S.; Wen, G.; Wang, J.; Rong, J.; Zong, B.; Schlögl, R.; Su, D. S. *Catalysis Science & Technology* **2014**, *4*, 4183.

115. Primo, A.; Neatu, F.; Florea, M.; Parvulescu, V.; Garcia, H. *Nature Communications* **2014**, *5*, 5291.

116. Sairanen, E.; Karinen, R.; Borghei, M.; Kauppinen, E. I.; Lehtonen, J. *ChemCatChem* **2012**, *4*, 2055.

117. Xu, Z.; Duong-Viet, C.; Liu, Y.; Baaziz, W.; Li, B.; Nguyen-Dinh, L.; Ersen, O.; Pham-Huu, C. *Applied Catalysis B: Environmental* **2019**, *244*, 128.

118. Nagpure, A. S.; Gurrala, L.; Gogoi, P.; Chilukuri, S. V. *RSC Advances* **2016**, *6*, 44333.

119. Dlamini, M. W.; Kumi, D. O.; Phaahlamohlaka, T. N.; Lyadov, A. S.; Billing, D. G.; Jewell, L. L.; Coville, N. J. *ChemCatChem* **2015**, *7*, 3000.

Chapter 3: Experimental methods and characterization techniques

3.1 Introduction

This chapter gives details on the methodology used to prepare different carbon nanomaterials (CNMs), Pd supported catalysts, and the catalytic evaluation of the synthesized catalysts, along with the characterization techniques used. The morphology, size, and structure of the synthesized materials were studied using transmission electron microscopy (TEM), high-resolution TEM (HRTEM), and scanning electron microscopy (SEM). UV-vis and photoluminescence (PL) spectroscopy were used to determine the optical properties of the synthesized CDs and Pd/CDs composite. Raman spectroscopy was used to determine the degree of graphitization of the synthesized CNMs. Fourier transform infrared (FTIR) spectrometer and X-ray photoelectron spectroscopy (XPS) were used to study the surface properties and elemental composition of the synthesized materials. Powder X-ray diffraction (PXRD) was used to determine the phase composition and crystallinity of the materials. The thermal stability of the prepared materials was analyzed using thermogravimetric analysis (TGA). Brunauer-Emmet and Teller (BET) was used to determine the surface area and porosity of the synthesized CNMs and Pd supported catalysts.

3.2 Synthesis of carbon nanomaterials

3.2.1 Materials

The chemicals used were of technical and analytical grade. Sucrose, oleic acid (90 %), CALD (98 %), CA (98 %), 3P1P (98 %, FCC), HCALD (90 %), PVP (MW 40000), CTAB (≥ 98 %), resorcinol (99 %), $NaBH_4$ (96 %), formaldehyde (34.5 wt. %), and $PdCl_2$ (99 %) were purchased from Sigma-Aldrich. The absolute ethanol was purchased from MK chemical. Hexane fraction and HCl (32 %), sulphuric acid (98 %), nitric acid (55 %), and acetic acid glacial CP were purchased from Associated Chemical Enterprise. Urea was purchased from Promark chemicals. KPS (95 %) was purchased from Eimer and Amend chemicals.

3.2.2 Synthesis of carbon dots

CDs were synthesized using the bottom-up approach through hydrothermal treatment. The synthesis of the CDs was achieved using sucrose and oleic acid/urea as carbon precursors. The synthesis of the CDs was modified from the methods reported in the literature [1-3].

3.2.2.1 Reflux method

CDs were synthesized by refluxing 20 g of sucrose and 20 mL of oleic acid for 2½ h at 215 °C under a controlled nitrogen environment [1]. After cooling, the supernatant liquid was discarded and the brown solid product at the bottom of the flask was dispersed in 40 mL distilled water. The CDs were then extracted using hexane and water to remove the remaining oleic acid. The final product was oven-dried for 72 h at 100 °C. The yield of the CDs (brown solid) obtained was 41 %.

Surface passivation of the CDs was carried out as follows: A mass of 500 mg of the as-synthesized CDs was dispersed in 100 mL acetic acid (90 %). The resulting solution was refluxed at 90 °C for 1 h. After refluxing the solvent was evaporated at 70 °C and then washed with water. The resulting product was dried in the oven at 100 °C for 24 h and labelled as fCDs.

3.2.2.2 Autoclave method

The solution of sucrose (40 mL) was prepared with various concentrations (0.1, 0.15, and 0.3 M). [2, 3] The prepared sucrose solution was transferred into a Teflon cup and placed inside a Teflon-lined autoclave. The solution was heated at 190 °C at a rate of 5 °C/min for 12 h. For the synthesis of N-doped CDs, a mass of 0.4 g of urea was added to the prepared sucrose solution (0.15 and 0.3 M) and heated at 190 °C. The reaction time was varied between 1 and 12 h. After the hydrothermal treatment, acetone was added, and the product was centrifuged at 18000 rmp for 15 min. The supernatant liquid was collected and filtered several times using a 0.22 μm filtering membrane. The solvent was evaporated at 70 °C using a rotary evaporator and the obtained dark brown solid was dried inside the oven at 100 °C for 72 h. The obtained yield below 40 %.

3.2.3 Synthesis of functionalized solid carbon spheres

An amount of 0.5 mL ammonia solution (25 %) was added to an ethanolic solution made of distilled water (60 mL) and absolute ethanol (24 mL) and stirred for an hour in a 500 mL Schott bottle [4, 5]. After an hour, a mass of 0.6 g resorcinol was added, and the solution was stirred for 30 minutes. This was followed by the addition of 0.80 mL formaldehyde and the mixture was

stirred for 24 hours at room temperature. The mixture inside a Schott bottle was hydrothermally treated in an oil bath at 100 °C for 24 h. After hydrothermal treatment, the reddish powder was recovered by centrifuging at 18000 rpm for 20 min, followed by washing using ethanol and distilled water and then dried at 100 °C for 4 h. The resorcinol/formaldehyde (RF) spheres were carbonized at 900 °C for 4 h under nitrogen gas (20 ml/min) to obtain solid carbon spheres. The yield of the SCSs was calculated to be 42 %.

The as-synthesized SCSs were treated in acid. A mass of 1 g of SCSs was added to a mixture of nitric acid (55 %, 11.24 mL) and sulphuric acid (98 %, 3.76 mL) in a 500 mL round bottom flask. The mixture was refluxed at 110 °C for 2 h. The acid treated SCSs were washed with distilled water until a pH of 7 was reached. The obtained product was dried at 100 °C for 4 h and labelled fSCSs.

3.2.4 Synthesis of hollow carbon spheres

HCSs were synthesized using a (**3.2.3.1**) hard template method and the template (polystyrene spheres) was then coated with (**3.2.3.2**) resorcinol (R) and formaldehyde (F) polymer followed by carbonization of RF using hydrothermal method followed by decomposition of the template and carbonization of RF polymer [6, 7].

3.2.4.1 Synthesis of polystyrene spheres (PSSs)

A mass of 0.1 g PVP (mw 40000) and styrene (8 mL) were dispersed in 250 mL ethanolic solution (200 mL ethanol and 50 mL distilled H_2O). The mixture was sonicated for 30 minutes. Potassium persulfate (0.15 g) was dissolved in 20 mL distilled water and added to the first mixture. The solution was sonicated for 10 min. The mixture was then refluxed at 80 °C for 24 h. The PSSs were centrifuged at 18000 rpm for 15 min and washed with ethanol and distilled water followed by oven drying at 60 °C overnight.

3.2.4.2 Synthesis of HCSs

The synthesized PSSs template was coated with RF polymer using the following procedure: PSSs (2 g) were added into a mixture of ethanol (100 mL), ammonia solution (25 %, 1 mL), and distilled water (50 mL) in a 500 mL Schott bottle. To disperse the PSSs template, the mixture was sonicated for 30 min. In a separate bottle, resorcinol (0.75 g), CTAB (1 g), and formaldehyde (1.5 mL) were added to 50 mL of ethanol. The second mixture was added to the first mixture and stirred for 24 h at room temperature, followed by hydrothermal treatment inside an oil bath at 100 °C for 24 h. The resulting brownish product was filtered and washed

several times using ethanol/water. The obtained product was then dried at 100 °C for 4 h and crushed into fine powder. The product was labelled PSSs@RF.

For the synthesis of HCSs, the PSSs@RF was carbonized using a horizontal CVD furnace under the flow of N_2 gas (50 mL/min). A mass of 0.6 g of PSSs@RF was placed inside a quartz boat which was placed in the middle of a quartz tube and inserted inside the CVD furnace. The carbonization of the HCSs was done in two consecutive steps, firstly the template (PSSs) was decomposed at 350 °C (10 °C/min) for an hour followed by carbonization of RF polymer into HCSs at 600 °C for 2 h. The calculated yield for the HCSs was 26 %.

3.3 Synthesis of the catalysts

3.3.1 Synthesis of Pd/CDs composite

A mass of 100 mg CDs was dispersed in distilled water (100 mL) followed by the addition of 3.75 mL of 2 mM H_2PdCl_4. The mixed solution was refluxed at 100 °C for 6 h. The resultant solution was evaporated using a rotary evaporator at 70 °C. The product was washed several times using ethanol. The nanoparticles were oven-dried for 48 h at 100 °C.

3.3.2 Synthesis of Pd/CSs

The procedure for the impregnation of Pd NPs on the support was modified from the method reported by Zhu *et al.* [8].

A mass of 0.6 g carbon support was added to 141 mL of 2 mM H_2PdCl_4 solution and the mixture was stirred overnight. A mass of 0.1895 g of sodium borohydride dissolved in ethanol was slowly added to the mixture with continuous stirring for 2 h to reduce the metal salt into metallic Pd NPs. The supported catalyst was filtered and washed using distilled water and absolute ethanol. The obtained black solid was dried at 100 °C for 4 h.

3.4 Characterization techniques

3.4.1 HRTEM, TEM, STEM, and SEM

TEM and HRTEM were used to study the morphology, size, atomic structure, and crystal structure of the synthesized carbon materials and Pd catalysts [9, 10]. TEM analysis was done using a FEI Technai G2 spirit electron microscope operating at 120 keV. The HRTEM images were taken using a Tecnai G2 30ST operating at 200 kV. High-angle annular dark-field imaging (HAADF) and scanning transmission electron microscopy (STEM) images were acquired using a JEOL ARM-200F operating at 200 kV. For analysis, the powder sample was dispersed in ethanol and/ distilled water and sonicated for 30 minutes. The prepared sample

was transferred dropwise onto a copper grid three times. The copper grid was air dried before analysis. The particle sizes and diameter of the synthesized materials were measured using Image J software by counting > 100 particles from TEM images obtained. The morphology of PSSs was determined using SEM. SEM analysis was done using ZEISS SIGMA 03-39 FESEM operating at 20 kV. A small amount of sample powder was spread on a carbon tape placed on a carbon stap. The sample was then coated with layers of carbon and gold/palladium alloy before analysis.

3.4.2 Powder X-ray diffraction (PXRD)

To determine the crystallinity, crystalline grain size, and phases of the prepared samples [9], a D2 phaser equipped with a Lynxene detector using Cu-K_α radiation at 30 kV was used with a scan range from $5° \leq 2\Theta \leq 90°$ in 0.026 steps. For sample preparation, the synthesized sample was ground to a fine powder and then placed on a zero-background sample holder and flattened for analysis. The crystalline grain size was estimated using Eva diffraction software by applying the Scherrer equation using the broadening of the most intense peak of an XRD pattern.

3.4.3 Thermogravimetric analysis

The thermal stability of the prepared samples was analyzed using a Perkin Elmer TGA 4000 instrument. TGA technique is used to monitor a change of mass of a sample as a function of increasing temperature under a controlled oxidizing atmosphere. A mass of ± 9 mg sample inside a ceramic pan was placed inside the instrument furnace and heated in the temperature range of 35 to 900 °C at a rate of 10 °C/min under a flow of air (20 ml/min) gas while monitoring the change in mass.

3.4.4 UV-vis and PL spectroscopy

The optical properties of the CDs and the Pd/CDs composite were determined using UV-vis and PL spectrophotometers. UV-vis absorption measurements were carried out using a Varian Cary Eclipse (Cary 50) UV-vis absorption spectrophotometer. Photoluminescence characteristics were measured using an Agilent Cary Eclipse fluorescence spectrometer.

3.4.5 Fourier transform infrared spectrometer

A Brüker Tensor 27 FTIR spectrometer was used to determine the presence of functional groups on the surface of the synthesized samples. The measurements of the absorption of electromagnetic radiation were between 600 to 4000 cm^{-1}.

3.4.6 X-ray photoelectron spectroscopy

For surface chemical analysis XPS was used to determine the elemental composition of the synthesized samples. In the measurement the surface of the sample is irradiated with a beam of X-ray (at a depth of 2-10 nm) while measuring the kinetic energy and the number of electrons escaping from the surface of the sample [11]. From the information gathered an XPS spectrum is generated from the corresponding elements present on the surface of the sample. In this study, the XPS spectra of the samples were obtained using a Thermo ESCAlab 250Xi equipped with a monochromatic Al K_α X-ray source operating at 1486.7 eV.

3.4.7 Brunauer-Emmet and Teller (BET) analysis

BET technique was used to determine the surface area and porosity of the prepared carbon nanomaterials. A Micromeritics Tristar 3000 surface area and porosity analyzer was used to conduct N_2 adsorption-desorption experiments at -195 °C. Before analysis, the samples were degassed at 150 °C for 4 h under N_2 gas.

3.4.8 Laser Raman spectroscopy

To determine the crystallinity and disorder of the obtained samples a Brüker Senterra Raman spectrophotometer with a laser excitation wavelength of 532 nm using Opus 7.1 software was used. For analysis, the sample was placed on a glass slide and the spectrum was recorded in dark field mode.

3.4.9 Calculation of product yield

$$\%\,\boldsymbol{Yield} = \frac{\boldsymbol{mass\ of\ carbon\ produced}}{\boldsymbol{mass\ of\ carbon\ source\ used}} * \mathbf{100} \quad \textbf{..... equation 3.1}$$

3.5 Catalyst testing and product analysis

3.5.1 Catalytic hydrogenation of CALD

The selective hydrogenation of CALD was carried out under atmospheric pressure in a three-neck round bottom flask (100 mL) equipped with a condenser, magnetic stirrer, gas inlet, and

sampling port. The three-neck round bottom flask was placed inside an oil bath with a thermocouple to maintain the desired temperature of the bath. The reaction mixture consisted of 100 mg catalyst, 1.32 g CALD, and 100 mL absolute ethanol. To remove traces of dissolved oxygen, N_2 gas was bubbled into the reaction mixture while the temperature was ramped to 60 °C (2 °C/min). Once the oil bath reached 60 °C, N_2 was switched with H_2 (50 mL/min) gas to allow for hydrogenation of CALD. The reaction was carried out for 7 or 8 h while taking samples from the reaction periodically for analysis.

3.5.2 Product analysis

Product analysis was carried out using an offline Varian 3700 GC with a flame ionization detector (FID) and a capillary column (Phenomenex Zebron, 30 m L. x 0.53 mm I.D. x 1.5 µ F.T.). The conditions for analysis were as follows: the temperatures of the column, detector, and injector were set to 300, 250, and 200 °C respectively, with N_2 (5 mL/min) as the carrier gas.

3.5.3 Calculations of CALD conversion and selectivity (%)

The CALD conversion and product selectivity were calculated according to the following equations (eq.):

$$\text{Conversion (\%)} = \frac{[CALD]_0 - [CALD]_t}{[CALD]_0} \times 100 \quad \text{.....eq. (3.2)}$$

$$\text{Selectivity (\%)} = \frac{[X]_t}{\sum [X]_t} \times 100 \quad \text{.....eq. (3.3)}$$

$$\text{Activity (mol/g}_{Pd}\text{.h)} = \frac{n_t}{m_{pd}.h} \quad \text{.....eq. (3.4)}$$

Where $[CALD]_0$ represents the initial concentration of CALD, $[CALD]_t$ represents CALD concentration at a specific time t, $[X]_t$ represents the concentration of the product obtained at a given time t, n_t represents the number of moles of CALD converted, m_{pd} represents the mass of Pd in the catalyst, and h represents the reaction time.

3.6 References

1. Chen, B.; Li, F.; Li, S.; Weng, W.; Guo, H.; Guo, T.; Zhang, X.; Chen, Y.; Huang, T.; Hong, X.; You, S.; Lin, Y.; Zeng, K.; Chen, S. *Nanoscale* **2013**, *5*, 1967.
2. Sadhanala, H. K.; Khatei, J.; Nanda, K. K. *RSC Advances* **2014**, *4*, 11481.
3. Gan, Z.; Hao, Y.; Shan, Y. *ChemNanoMat* **2016**, *2*, 171.

4. Dlamini, M.W. *Spherical carbons as model supports for Fe, Co and Fe-Co Fischer-Tropsch catalysts*, PhD Thesis, University of the Witwatersrand, Johannesburg, **2016**.
5. Shin, Y.-R.; Jung, S.-M.; Jeon, I.-Y.; Baek, J.-B. *Carbon* **2013**, *52*, 493.
6. Magubane, A. *Synthesis of copper nanoparticles contained in mesoporous hollow carbon spheres as potential catalysts for growing helical carbon nanofibers,* MSc Dissertation, University of the Witwatersrand, Johannesburg, **2017**.
7. Buthelezi, T.I. *Carbon with different functionalities as a hydrogen transport layer in ruthenium promoted Fischer -Tropsch catalysts,* MSc Dissertation, University of the Witwatersrand, Johannesburg, **2019**.
8. Zhu, J.; Dou, M.; Lu, M.; Xiang, X.; Ding, X.; Liu, W.; Li, M. *Applied Catalysis A: General* **2019**, *575*, 11.
9. Mourdikoudis, S.; Pallares, R. M.; Thanh, N. T. *Nanoscale* **2018**, *10*, 12871.
10. Lin, P.-C.; Lin, S.; Wang, P. C.; Sridhar, R. *Biotechnology advances* **2014**, *32*, 711.
11. Hu, M.; Yao, Z.; Wang, X. *AIMS Mater. Sci* **2017**, *4*, 755.

Chapter 4: Synthesis of carbon dots using hydrothermal treatment of sucrose

4.1 Introduction

Carbon dots (CDs) can be synthesized from different carbon precursors using the bottom-up and top-down approaches [1-5]. The bottom-up approach uses molecular precursors to generate CDs whereas the top-down approach involves the cleavage of carbon materials (i.e. activated carbon, carbon nanotubes, and graphite) using chemical, physical or electrochemical methods [1-5]. The use of the bottom-up approach is advantageous because it uses precursors that already have heteroatoms, hence this procedure does not require further functionalization of the synthesized CDs [1-6]. The bottom-up approach has been studied intensively because it is considered cheaper and "greener" than other methods [4, 5].

Hydrothermal synthesis is one of the methods that is often used in the synthesis of the CDs using organic precursors (saccharides, organic acids, juice, waste peels, etc.) in water [3, 5-7]. In this procedure, the polymerization and/or carbonization of the organic molecules occurs in the presence of water in a sealed vessel at high temperature and pressure [8]. Carbohydrates (monosaccharides and disaccharides) have been used as starting materials in the synthesis of the CDs because of their low carbonization temperature and availability [2, 9-12].

In this study, we investigated the synthesis of CDs using the hydrothermal treatment of sucrose at 190 °C in a Teflon-lined autoclave. The concentration of the sucrose was varied while monitoring the changes in the properties of the synthesized CDs. Sucrose is rich in oxygen-containing functional groups. The introduction of nitrogen into the CDs was achieved by a reaction between urea and sucrose. The synthesized CDs and NCDs with different functional groups and particle sizes can later be used as potential reducing agent for metal salt precursor. This can be useful in studying the interaction between CDs/NCDs and metal nanoparticles (NPs) and how those interactions can influence the catalytic activity and selectivity of the metal NPs in the hydrogenation of cinnamaldehyde.

4.2 Experimental procedure

4.2.1 Materials

Sucrose was purchased from Sigma-Aldrich. The absolute ethanol and acetone were purchased from MK chemical. Urea was purchased from Promark chemicals. Distilled water was used in this study.

4.2.2 Synthesis of the CDs

The synthesis of the CDs was modified from the methods reported in the literature [10-12]. The experimental procedure used make the CDs was reported in section **3.2.2.2**. The CDs were prepared using different concentrations of sucrose solution using hydrothermal treatment at 190 °C for 12 h in an autoclave. For the synthesis of nitrogen-doped CDs (NCDs), urea was used as a dopant and the mole ratio of sucrose and urea was varied from 1:1 to 2:1.

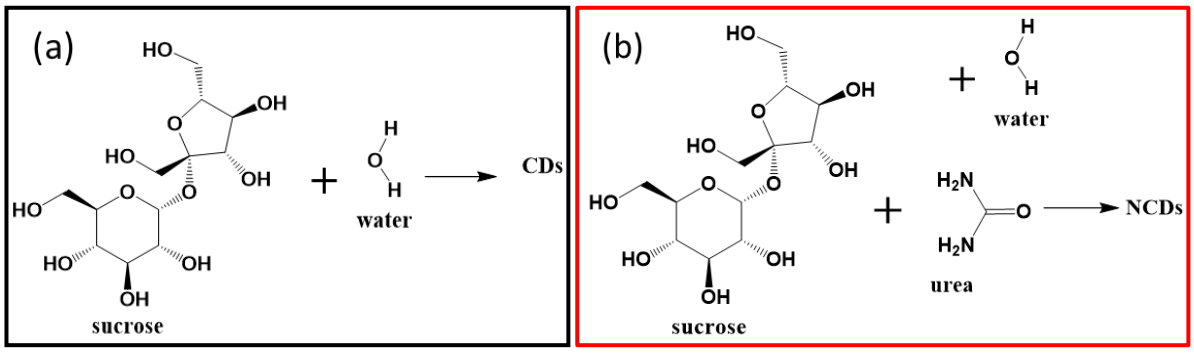

Scheme 4.1: Synthesis of (a) CDs and (b) NCDs using sucrose as carbon source and urea as nitrogen dopant via hydrothermal treatment.

4.3 Characterization techniques

Characterization techniques (TEM, PXRD, FTIR, TGA, UV-vis, and PL) used in this study are reported in chapter 3.

4.4 Results and discussion

4.4.1 TEM analysis

Table 4.1 summarizes the reaction conditions, average particle size, and % yield of the CDs and NCDs. The % yield of the CDs increased with an increase in the concentration of the sucrose solution. The TEM images of the CDs synthesized using different sucrose concentrations are shown in Fig. 4.1a-c with their corresponding particle size distributions (Fig. 4.1d-f). The synthesized CDs were quasi-spherical in shape with different particle sizes. The

calculated average particle size of the CDs was 8.4 ± 2.0, 2.2 ± 0.5, and 1.9 ± 0.5 nm for 0.3, 0.15, and 0.1 M sucrose solution, respectively. The particle size of the CDs decreased with a decrease in the concentration of sucrose. The average particle size of the synthesized CDs was quite different when compared to the CDs reported by Gan *et al.* (2.6 nm; prepared using 1.5 M sucrose at 190 °C for 5 h) [11].

Table 4.1: Summary of the reaction conditions along with the particle size of the synthesized CDs and NCDs and % yield.

Sample	Reaction time (h)	Particle size (nm)[a]	Yield (%) [b]	Reference
0.1 M	12	1.9 ± 0.5	11	This work
0.15 M	12	2.2 ± 0.5	20	This work
0.3 M	12	8.4 ± 2.0	38	This work
0.3 M + urea	12	51.5 ± 12.7	-	This work
0.3 M + urea	6	42.3 ± 13.8	-	This work
0.3 M + urea	1	30.2 ± 5.8 and 1.0 ± 0.4	59	This work
0.15 M + urea	12	4.1 ± 1.2	27	This work
1.5 M	5	2.6	-	11

[a] calculated from TEM images and [b]calculated using equation 3.1.

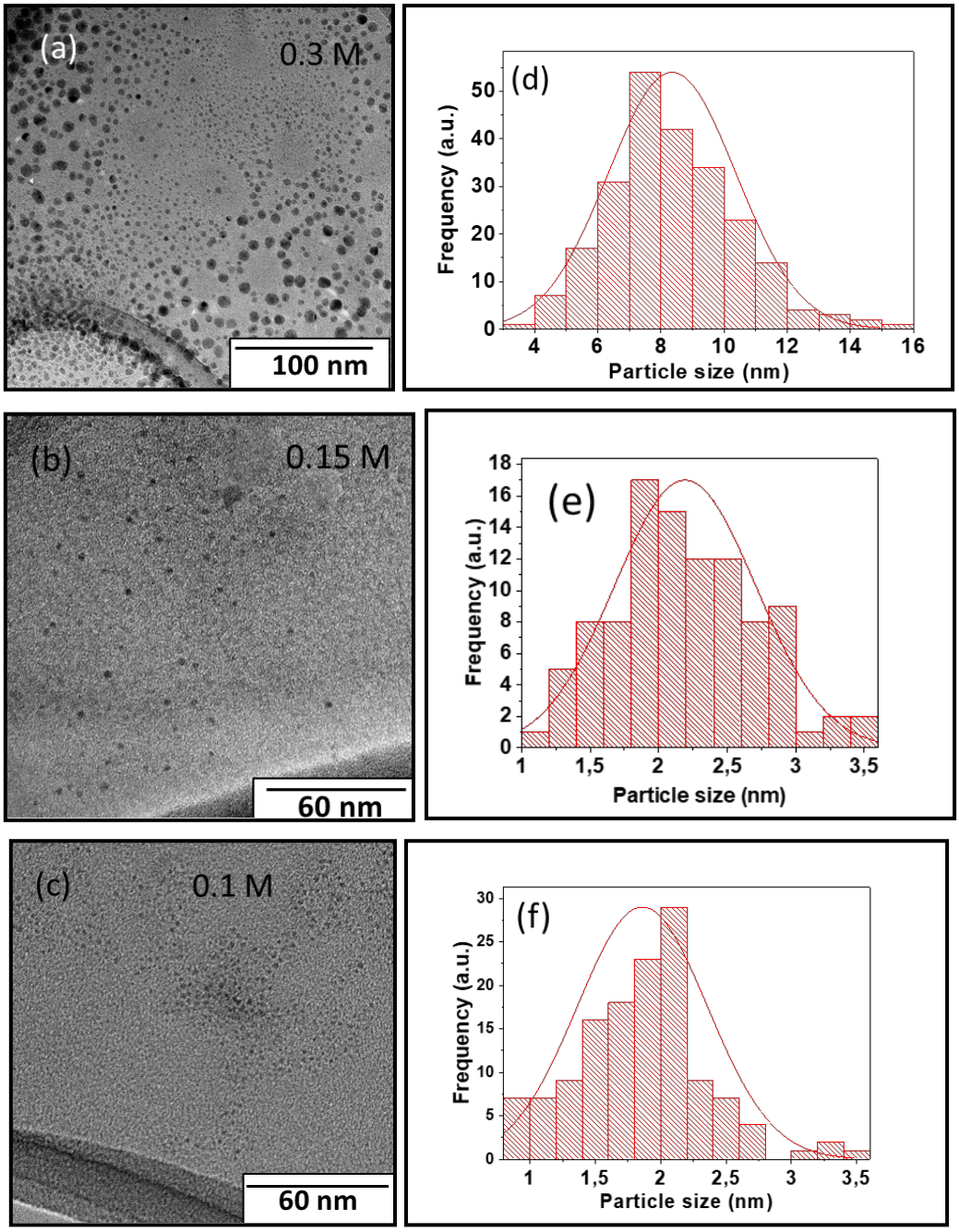

Figure 4.1: TEM images of CDs (a-c) and their corresponding particle size distributions (d-f).

TEM images and their corresponding particle size distributions of the NCDs and carbon nanoparticles (CNPs-size range between 10-100 nm) are shown in Fig. 4.2 a-e. For the N-doped CDs (0.15 M + urea), the average particle size was determined to be 4.1 ± 1.2 nm. The formation of CNPs with an increase in the reaction time was observed for NCDs (0.3 M + urea) samples. The particle size of the CNPs decreased from 51.5 ± 12.7 to 42.3 ± 13.8 nm for the reaction time of 12 and 6 h, respectively. When the reaction time was further reduced to an hour, the size of the CNPs decreased and the formation of NCDs was observed. The average

diameter of the carbon spheres and NCDs were determined to be 30.2 ± 0.2 and 1.0 ± 0.4 nm respectively.

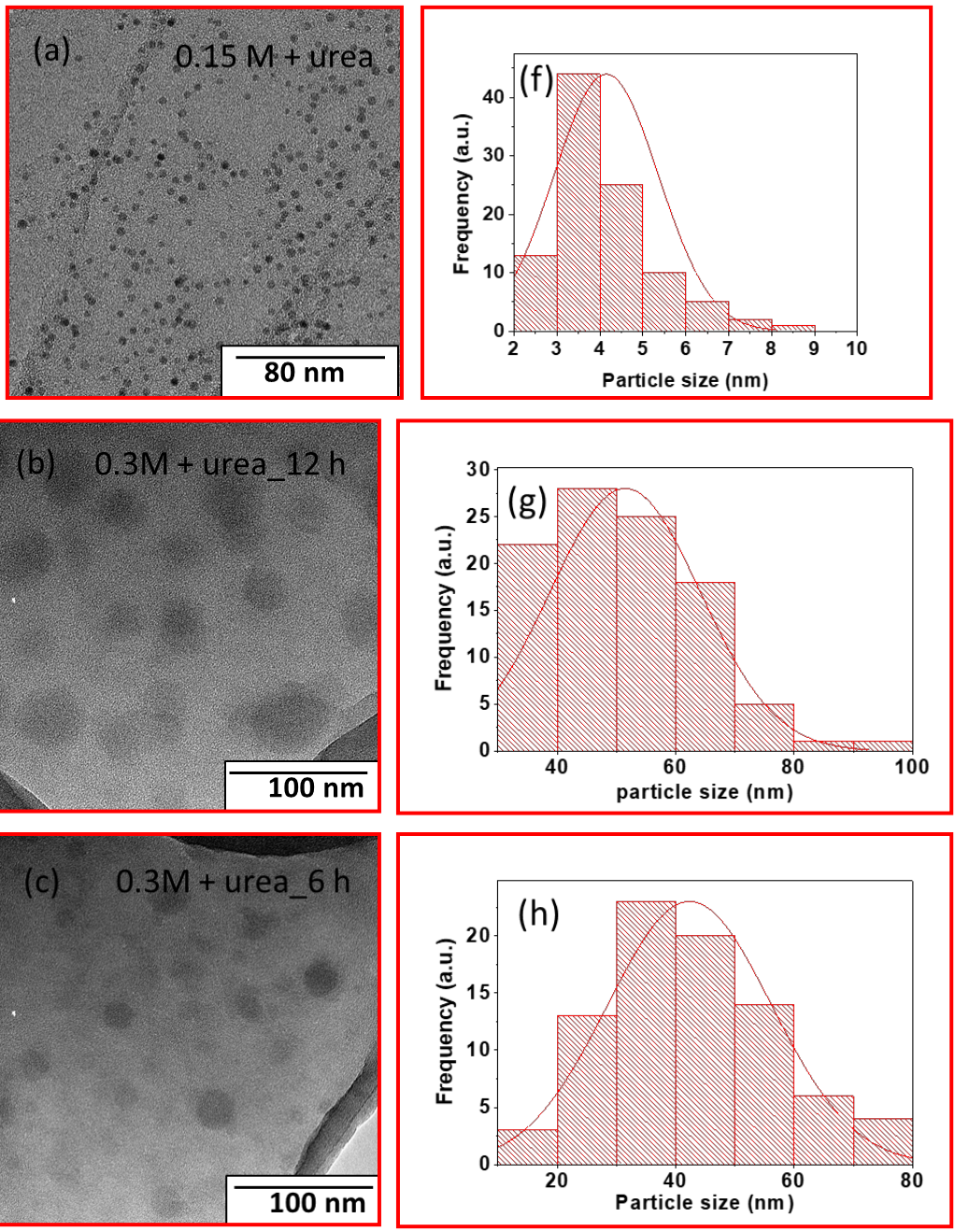

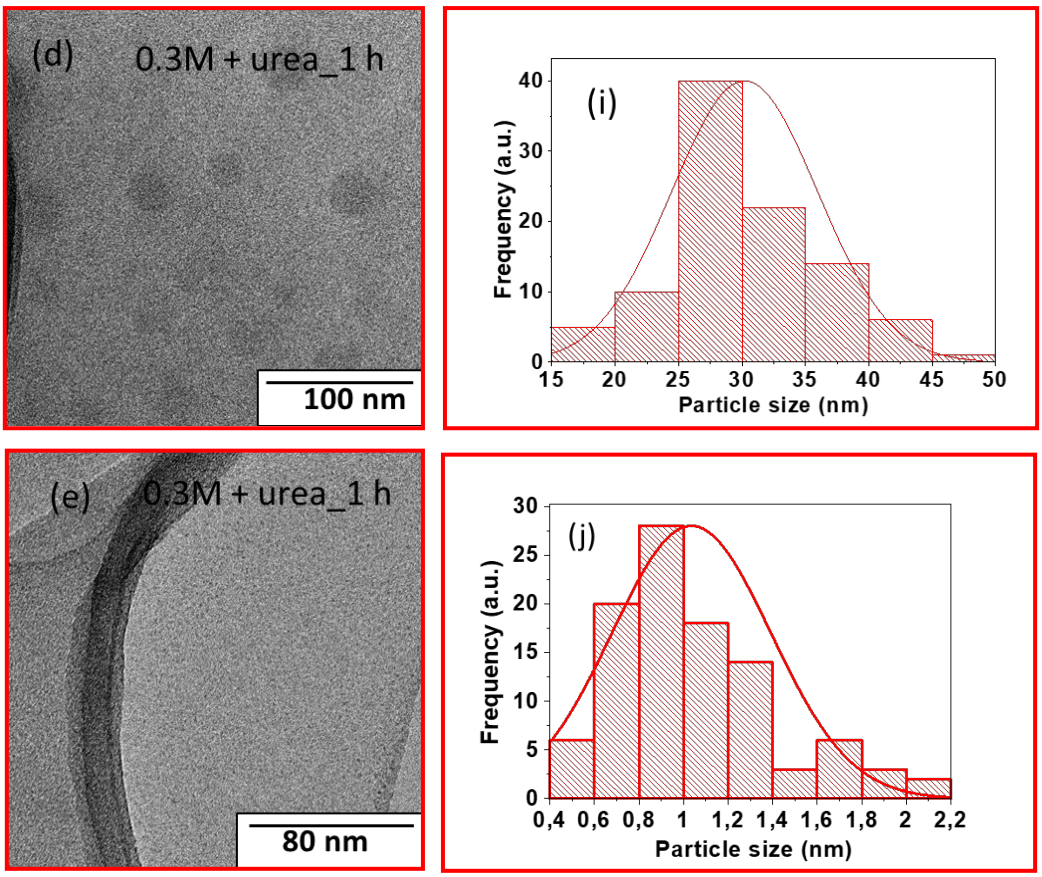

Figure 4.2: TEM images of N-CDs (a-e) and their corresponding particle size distributions (f-i).

4.4.2 PXRD analysis

Figure 4.3 shows the PXRD pattern of the carbon precursor and that of the synthesized CDs and NCDs. The XRD pattern (Fig.4.3b) shows that the sucrose was fully carbonized in all the reactions; a comparison with the crystalline XRD pattern (Fig. 4.3a) of the sucrose is quite different. The samples exhibited a broad diffraction peak at 2Θ *ca.* 19.2-20.1 °. The broadness of the diffraction peak is associated with disordered carbon atoms [13] and small CDs particle size [10]. There was no significant change in the XRD pattern between the CDs and N-doped CDs. The peak position of the diffraction peak decreased from a 2Θ value of 20.1 to 19.7 ° for 0.1 M and 0.3 M CDs respectively. For the NCDs (0.3 M) the diffraction peak decreased to a 2Θ value of 19.2 ° when compared to CDs. This suggests that there were some minor structural changes of the NCDs due to the addition of the nitrogen-containing functional groups [10].

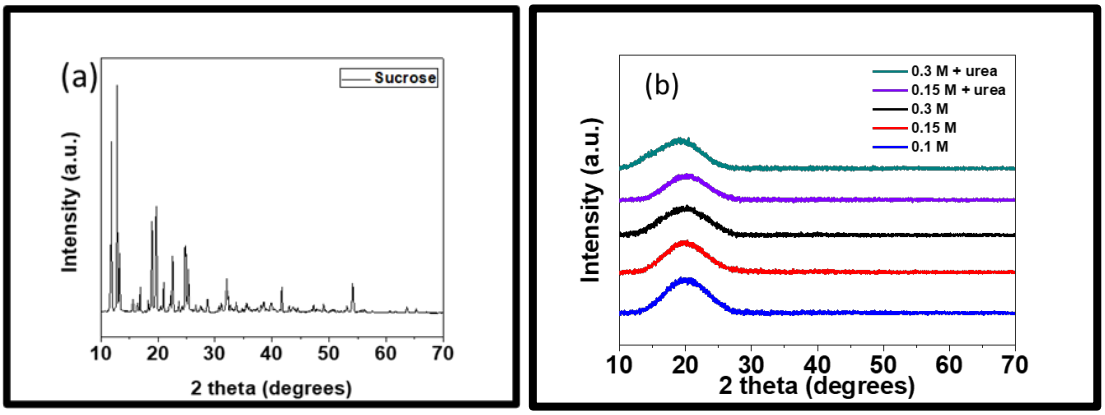

Figure 4.3: PXRD of (a) sucrose and (b) the synthesized CDs and NCDs with different concentration.

4.4.3 FTIR analysis

To study the surface properties, FTIR spectroscopy was used to determine the functional groups present on the surface of the CDs and NCDs. Generally, CDs are composed of C, H, and O elements and they can be doped with heteroatoms such as nitrogen, sulfur, boron, and phosphorus [14]. Figure 4.4 shows the FTIR spectra of the CDs (a) and NCDs (b). From the FTIR of the CDs, the broad absorption band at 3301-3326 cm^{-1} corresponds to the stretching mode O-H [10, 12]. the absorption band at 2924-2929 cm^{-1} can be attributed to C-H stretches [10, 12]. The absorption peak at *ca.* 1704 and 1618 cm^{-1} correspond to stretching vibrations of C=O, and the C=C bending mode of aromatic rings [15]. The peak at 1163 cm^{-1} can be assigned to the bending mode of the C-O-C group [10, 12]. The FTIR spectra (Fig.4.4b) of the N-doped CDs showed similar functionalities as those found in the CDs. The absorption peak at 1671 cm^{-1} can be attributed to the bending vibration mode of N-H [16]. The disappearance of the absorption band corresponding to the stretching vibration of the C=O bond was observed. A shift to the higher wavelength of the broad absorption band of O-H stretching mode was observed for the NCDs (i.e., 0.15M CDs (3326 cm^{-1}) to N-CDs (3346 cm^{-1}) and 0.3 M CDs (3264 cm^{-1}) to NCDs (3277 cm^{-1}). The change in the absorption band position can be associated with the presence of the O-H and N-H stretching [15].

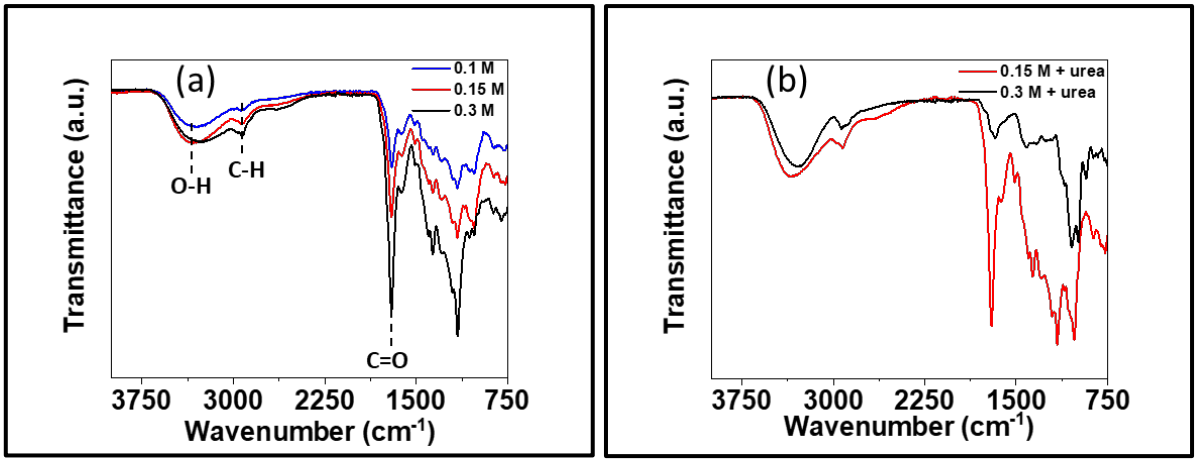

Figure 4.4: FTIR of the synthesized (a) CDs and (b) NCDs from different sucrose concentration.

4.4.4 Thermal stability analysis

The thermal stability of the five samples was studied using TG analysis while monitoring the weight loss of the sample in the temperature range of 35-900 °C. Figure 4.5 shows the TGA and DTG graphs of the five samples. The maximum decomposition temperature of the CDs and their corresponding weight loss are summarized in Table 4.1. All the TG graphs shows that the samples fully decompose in air as indicated by the observation that no sample was left at T > 650 °C. The small peaks at below 100 °C are due to the loss of the absorbed moisture as it is well known that CDs are hygroscopic [17]. The prominent DTG peak at *ca.* 202, 204, 218, 201, and 211 °C (0.1 M, 0.15 M, 0.3 M, 0.15 M + urea, and 0.3 M + urea respectively) with the corresponding weight loss of 26.2, 32.4, 32.1, 32.2, and 41.9 % are due to the loss of functional groups on the surface of the carbon dots. This is consistent with the data obtained from the FTIR spectra. This mass loss at a lower temperature (< 300 °C) in the DTG of oxidized activated carbon was also observed by Soni *et al.* and this was attributed to volatile organic compounds [18].

The small DTG peak at *ca* 351, 349, 343, 358, and 333 °C with corresponding weight loss of 10.6, 10.2, 6.8, 9.8, and 17 % respectively can be attributed to the loss of amorphous carbon attached to the functional groups. The loss of the carbogenic core of the CDs was recorded at c*a* 527, 536, 448, 518, and 573 °C with corresponding weight loss of 62, 56.8, 49.4, 57.3, and 38.6 % respectively. The sample prepared using 0.3 M sucrose had an additional peak at *ca.* 569 °C with the corresponding weight loss of 10.2 %. This could be attributed to the difference in the graphitic nature of the CDs (0.3 M) leading to the additional weight loss of the carbogenic

core at temperatures above 500 °C. The CDs (0.3 M) were slightly more thermally stable compared to other samples. Compared to other samples, the DTG profile (Fig. 4.5 e) of the NCDs (0.3 M + urea) had a weight loss of about 38.6 % at a maximum temperature of 573 °C which is smaller. However, there was a significant increase in the weight loss of functional groups at a maximum temperature of 211 °C.

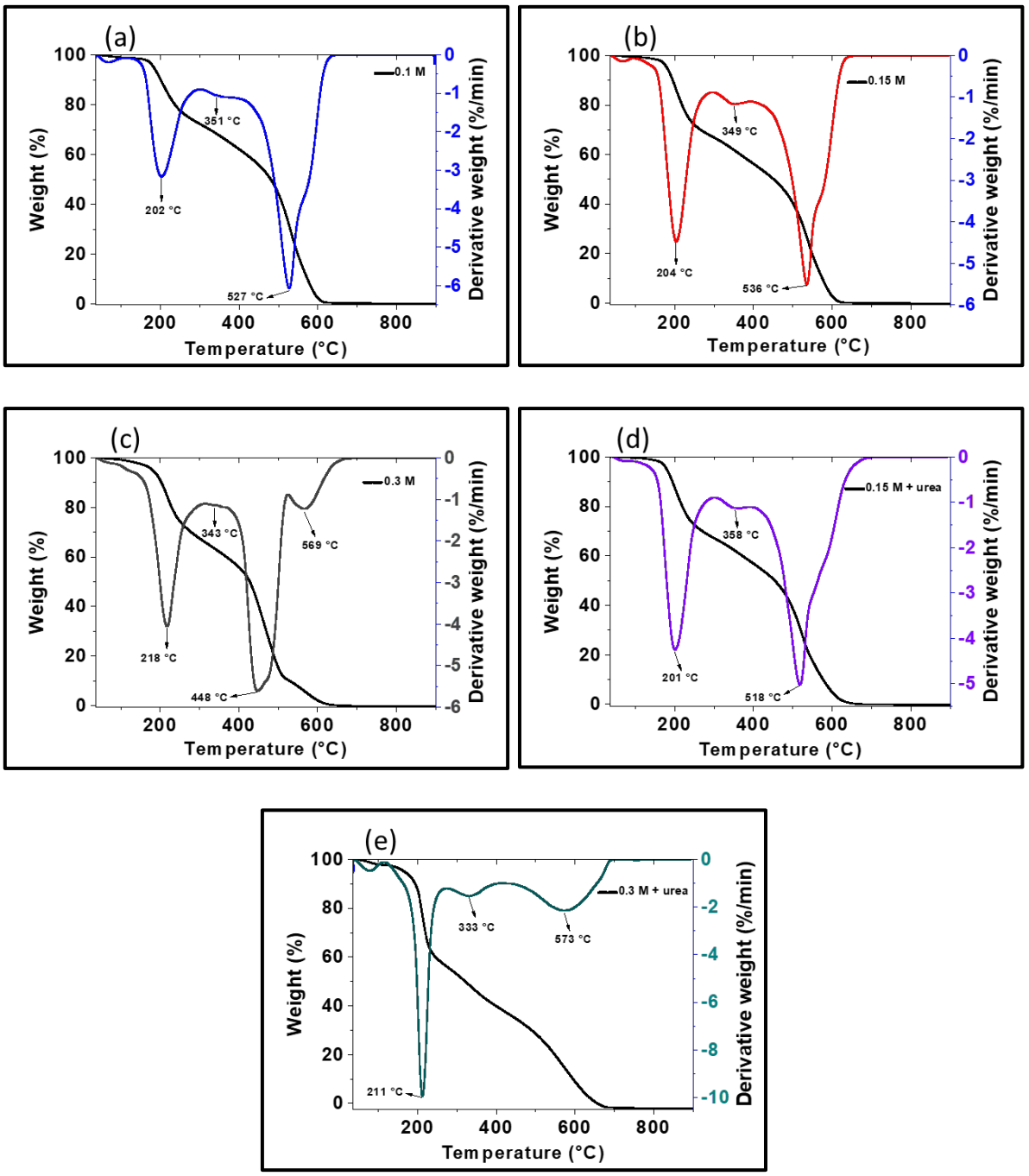

Figure 4.5: TG and DTG profiles of the synthesized CDs (a) 0.1 M, (b) 0.15 M, (c) 0.3 M, and NCDs (d) 0.15 M + urea, and (e) 0.3 M + urea.

Table 4.2: Summary of the maximum decomposition temperature and % weight loss of the synthesized CDs and NCDs.

Sample	Maximum decomposition temperature (°C) and % weight loss									
	Peak 1		Peak 2		Peak 3		Peak 4		Peak 5	
0.1 M	68 °C	1.2 %	202 °C	26.2 %	351 °C	10.6 %	527 °C	62 %	-	-
0.15 M	66 °C	0.6 %	204 °C	32.4 %	349 °C	10.2 %	536 °C	56.8 %	-	-
0.15 M + urea	71 °C	0.7 %	201 °C	32.2 %	358 °C	9.8 %	518 °C	57.3 %	-	-
0.3 M	36-130 °C	1.5 %	218 °C	32.1 %	343 °C	6.8 %	448 °C	49.4 %	569 °C	10.2 %
0.3 M + urea	77 °C	2.5 %	211 °C	41.9 %	333 °C	17 %	573 °C	38.6 %	-	-

4.4.5 Optical properties

The optical properties of the CDs and NCDs were studied using UV-vis and PL spectroscopy and the results summarized in Table 4.2. The UV-vis spectra (Fig. 4.6a) of the CDs show two absorption bands at 223-227 and 293-296 nm corresponding to polyaromatic chromophores and π -π^* transition of C=C bonds of the CDs [11, 12, 19, 20]. A slight blue shift in the absorption band (Fig. 4.6b) of the NCDs compared to CDs was observed (290 to 289 nm; 0.15 M: 0.15 M + urea) and (296 and 275 nm; 0.3 M: 0.3 M + urea) [21]. The NCDs had a strong absorption band of π -π^* transition as opposed to CDs.

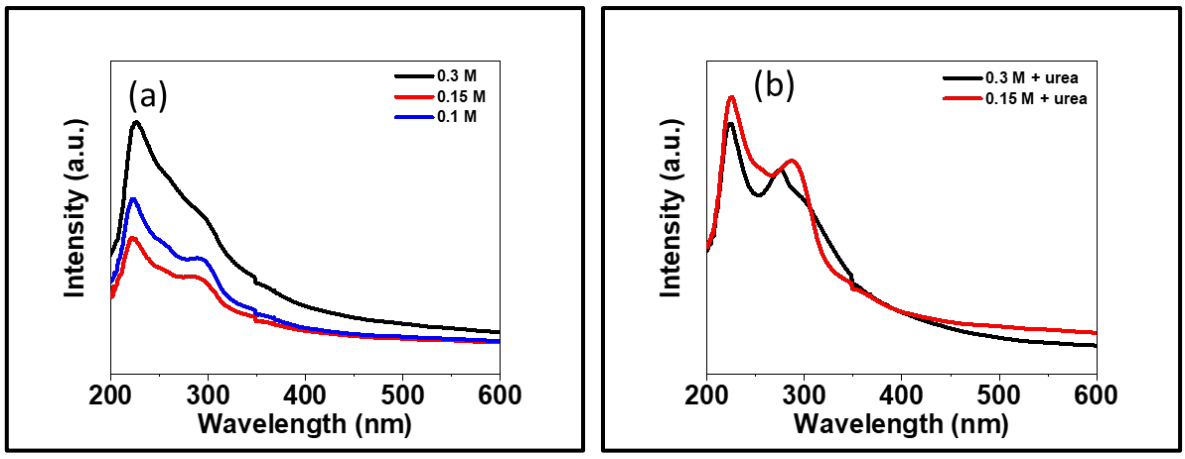

Figure 4.6: UV-vis spectra of the synthesized (a) CDs and (b) NCDs.

Table 4.3: Optical properties of the synthesized CDs and NCDs.

Sample	UV-vis absorption (nm)	UV-vis absorption (nm)	PL maximum emission wavelength (nm) (Exc. λ = 300 nm)
0.1 M	223	293	405
0.15 M	223	290	406
0.15 M + urea	226	289	406
0.3 M	227	296	410
0.3 M + urea	224	275	369 and 408

The PL spectra of the CDs at an excitation wavelength of 300 nm is shown in Figure 4.7a. From the PL spectra, it can be noted that an increase in the concentration of sucrose resulted in the red shift of the maximum emission wavelength (405 to 410 nm). In the literature there are several theories regarding the reason for explaining the presence of PL peaks generated by CDs which includes: the quantum confinement effect, the defective state emission, fluorophores, the recombination of electron-hole pairs etc. [1, 8, 22, 23]. Sadhanala *et al.* reported that the emission wavelength of the CDs does not only depend on the excitation wavelength but also on the particle size of the CDs due to a quantum confinement effect [10]. When the mole ratio of sucrose: urea was increased from 1:1 to 2:1 a dual-band emission (369 and 408 nm) was observed (Fig.4.7b). In the literature, the dual-band emission is associated with unequal

levels of emissive electronic transitions which is usually caused by surface defects on the CDs [24]. Sarkar *et al.* reported double peaks in the PL spectra of the CDs synthesized using a hydrothermal treatment of sucrose, and the observed peaks were attributed to the size distribution of the sample [12]. The sample contained small size CDs (< 6 nm) attached to bigger spheres (50 nm). This is consistent with what we observed in the TEM images (Fig. 4.2d-e) of the NCDs (0.3 M + urea_1h). The NCDs (0.15 M + urea) had the same maximum emission as the CDs (0.15 M).

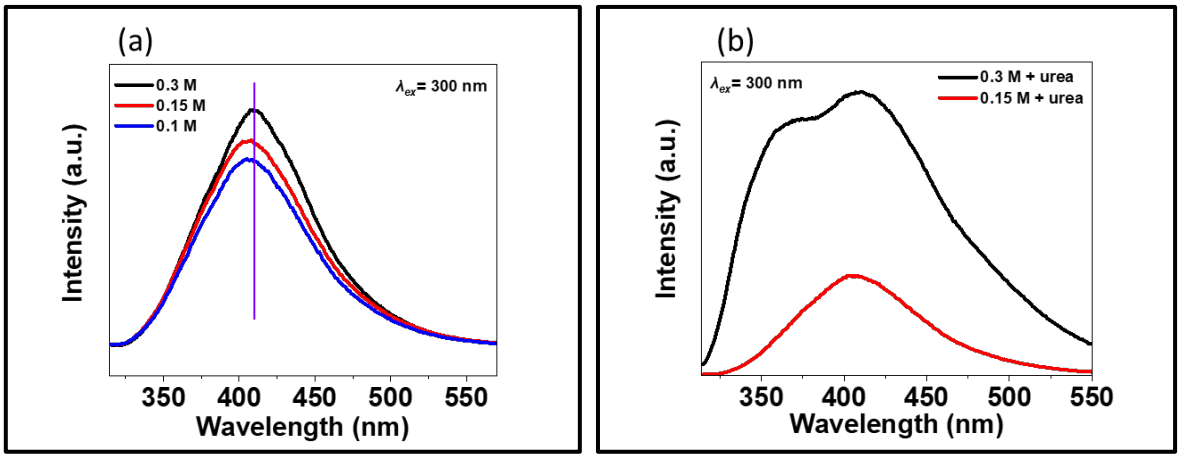

Figure 4.7: PL spectra of the synthesized (a) CDs and (b) N-CDs.

4.5 Conclusions

In conclusion, CDs were synthesized using sucrose as a carbon source. The FTIR spectra of the samples showed the presence of oxygen-containing functional groups. This was further supported by TGA in which we observed a weight loss at temperatures below 250 °C. With the NCDs (0.3 M + urea) an increase of 9.8 % weight loss was observed and this can be attributed to the addition of nitrogen-containing functional groups. The UV-vis of the N-CDs showed a strong absorption peak in the UV region compared to CDs. The PL spectra of the CDs showed a slight red shift (5 nm) in the emission wavelength which is associated with a change in the particle size of the CDs. The chemical and optical properties of the NCDs (0.3 M + urea) were quite different to the properties of undoped CDs which is an indication of the structural changes induced by N-doping.

4.6 References

1. Tuerhong, M.; Yang, X.; Xue-Bo, Y. *Chinese Journal of Analytical Chemistry* **2017**, *45*, 139.
2. Hill, S.; Galan, M. C. *Beilstein journal of organic chemistry* **2017**, *13*, 675.

3. Zhou, J.; Zhou, H.; Tang, J.; Deng, S.; Yan, F.; Li, W.; Qu, M. *Microchimica Acta* **2017**, *184*, 343.
4. Lim, S. Y.; Shen, W.; Gao, Z. *Chemical Society Reviews* **2015**, *44*, 362.
5. Wang, R.; Lu, K.-Q.; Tang, Z.-R.; Xu, Y.-J. *Journal of Materials Chemistry A* **2017**, *5*, 3717.
6. Yang, P.; Yang, Z. *Journal of Energy Chemistry* **2020**, *50*, 365.
7. Liu, X.; Yang, C.; Zheng, B.; Dai, J.; Yan, L.; Zhuang, Z.; Du, J.; Guo, Y.; Xiao, D. *Sensors and Actuators B: Chemical* **2018**, *255*, 572.
8. De, B.; Karak, N. *Journal of Materials Chemistry A* **2017**, *5*, 1826.
9. Emanuele, A.; Cailotto, S.; Campalani, C.; Branzi, L.; Raviola, C.; Ravelli, D.; Cattaruzza, E.; Trave, E.; Benedetti, A.; Selva, M. *Molecules* **2020**, *25*, 101.
10. Sadhanala, H. K.; Khatei, J.; Nanda, K. K. *RSC Advances* **2014**, *4*, 11481.
11. Gan, Z.; Hao, Y.; Shan, Y. *ChemNanoMat* **2016**, *2*, 171.
12. Sarkar, S.; Banerjee, D.; Ghorai, U. K.; Das, N. S.; Chattopadhyay, K. K. *Journal of Luminescence* **2016**, *178*, 314.
13. Liu, X.; Pang, J.; Xu, F.; Zhang, X. *Scientific reports* **2016**, *6*, 1.
14. Bhattacharyya, S.; Ehrat, F.; Urban, P.; Teves, R.; Wyrwich, R.; Döblinger, M.; Feldmann, J.; Urban, A. S.; Stolarczyk, J. K. *Nature communications* **2017**, *8*, 1.
15. Liu, X.; Liu, J.; Zheng, B.; Yan, L.; Dai, J.; Zhuang, Z.; Du, J.; Guo, Y.; Xiao, D. *New Journal of Chemistry* **2017**, *41*, 10607.
16. Miao, X.; Qu, D.; Yang, D.; Nie, B.; Zhao, Y.; Fan, H.; Sun, Z. *Advanced materials* **2018**, *30*, 1704740.
17. Baker, S. N.; Baker, G. A. *Angewandte Chemie International Edition* **2010**, *49*, 6726.
18. Soni, N.; Singh, S.; Sharma, S.; Batra, G.; Kaushik, K.; Rao, C.; Verma, N. C.; Mondal, B.; Yadav, A.; Nandi, C. K. *Chemical Science* **2021**, *12*, 3615.
19. Chen, B.; Li, F.; Li, S.; Weng, W.; Guo, H.; Guo, T.; Zhang, X.; Chen, Y.; Huang, T.; Hong, X.; You, S.; Lin, Y.; Zeng, K.; Chen, S. *Nanoscale* **2013**, *5*, 1967.
20. Wu, Z. L.; Liu, Z. X.; Yuan, Y. H. *Journal of Materials Chemistry B* **2017**, *5*, 3794.
21. Basu, N.; Mandal, D. *Photochemical & Photobiological Sciences* **2019**, *18*, 54.
22. Park, Y.; Yoo, J.; Lim, B.; Kwon, W.; Rhee, S.-W. *Journal of Materials Chemistry A* **2016**, *4*, 11582.
23. Wang, Y.; Hu, A. *Journal of Materials Chemistry C* **2014**, *2*, 6921.
24. Zhu, P.-p.; Cheng, Z.; Du, L.-l.; Chen, Q.; Tan, K.-j. *Langmuir* **2018**, *34*, 9982.

Chapter 5: Hydrogenation of cinnamaldehyde using carbon dots reduced palladium nanoparticles

5.1 Introduction

Carbon dots (CDs) are a more recent class of carbon nanomaterials with excellent electronic properties and they can act as electron donors and or acceptors [1]. The CDs were accidentally discovered in 2004 by Xu and colleagues, as by-products formed during the separation and purification of single-walled CNTs from arc-discharge soot [2, 3-5]. CDs are defined as quasi-spherical nanoparticles made up of an amorphous to nano-crystalline graphite core with sizes less than 10 nm [2-4, 6-9].

Composites made with metallic nanoparticles and generic nanocarbon based materials have been used in a wide range of applications [7]. Metal nanoparticles supported on CNTs and graphene have been shown to act as excellent heterogeneous catalysts in organic transformation studies [7]. In many reactions the metal must be in a reduced state and thus the preparation of metal nanoparticles for use in hydrogenation reactions involve the use of both reducing and stabilizing agents such as citric acid, hydrazine hydrate, sodium borohydride, etc. [1]. Some of the reducing agents used are toxic (e.g. hydrazine hydrate/sodium borohydride) can also lead to metal particle agglomeration [6]. The use of these reducing agents can limit reactant hydrogenation, hence it is necessary to find reducing agents that are environmentally friendly and can stabilize metal nanoparticles to prevent their aggregation [1, 10].

The CD surface has been reported to act as both a "ligand" (capping agent) to stabilize small metal particles as well as a reducing agent to generate metal agglomerates from metal ions [11-14, 16]. Since the CDs are small (< 10 nm), this means that the interaction between the carbon and the metal will be unusual since both will have similar sizes. This can lead to the possibility of inverse catalyst-support interactions where the catalyst particle can be larger than the support particle [15]. Further, the CDs can also act as catalysts or nanocomposite catalysts due to their ability to act as an electron donor or electron acceptor [16, 17].

To further investigate the dual effect of a metal and a CD, in particular when the metal particle is larger than the CD particle, we have synthesized Pd/CDs and studied their behaviour (as well as that of the CDs) in the hydrogenation of cinnamaldehyde (CALD). Figure 5.1 shows the

schematic representation of the selective hydrogenation of CALD. Hydrogenation of CALD results in the formation of three different products with hydrocinnamaldehyde (HCALD) and cinnamyl alcohol (CA) as intermediate products and 3-phenyl-1-propanol as a final product [18-20]. The products produced from this process are all industrially valuable and are used for the synthesis of fine chemicals [19, 20]. Selective hydrogenation of CALD is a challenge even though the hydrogenation of the C=C bonds relative to the C=O bonds is kinetically and thermodynamically more favourable [21, 22].

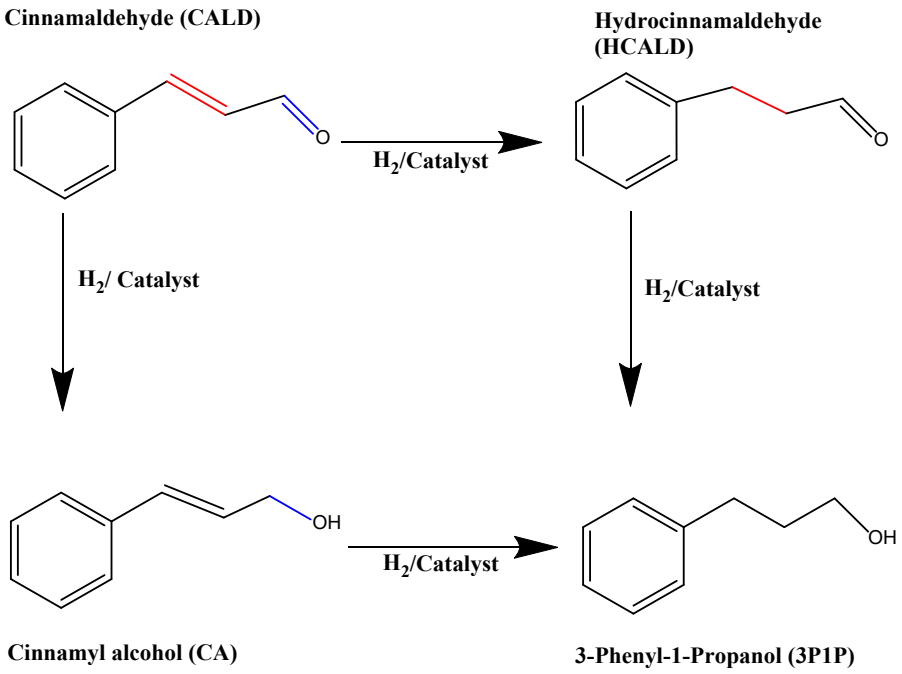

Figure 5.1: Reaction pathway for the selective hydrogenation of CALD.

We chose to generate a metal-CD complex with Pd, as the Pd catalyst has been studied intensively in different organic transformation reactions [19, 23, 24]. Among these reactions, the use of Pd based catalysts for hydrogenation of cinnamaldehyde has been well documented and provides a good model reaction for the study [25-30]. Studies have shown that the Pd catalyst is mostly selective towards the reduction of the C=C bond [31, 32]. The reduction of a Pd salt using CDs has been reported and the synthesized composites have been tested in different applications. Dey *et al.* investigated the catalytic effect of carbon dot reduced palladium nanoparticles (Pd@CD) for Suzuki-Miyuara and Heck coupling reactions [12]. The authors found that the CDs did not have much impact on the prevention of Pd nanoparticle agglomeration. The catalytic activity of Pd@CD nanoparticles during the coupling of phenylboronic acid and bromobenzene reached a maximum conversion of 45 % biphenyl after 10 h. The catalyst started to deactivate and precipitation of a Pd@CD composite was observed during the reaction. When

a co-stabilizer (polyvinylpyrrolidone (PVP)) was added to the Pd@CDs composite an increase in the catalytic activity was observed and the conversion of biphenyl increased to 95 % within 12 h. Wei and Chen synthesized Pd nanoparticles supported on carbon dots (Pd/CD) [13]. The Pd/CD composite was applied as an anode catalyst for methanol oxidation in alkaline fuel cells. From the electrochemical measurements, the Pd/C catalyst displayed high electrochemical activity for methanol oxidation in alkaline electrolyte. It was also noted that the catalyst provided non-blocked active surfaces for the organic molecular fuel oxidation.

The present work reports for the first time the use of CDs and Pd/CDs catalysts in the liquid phase hydrogenation of CALD. The catalytic activity and selectivity of the two catalysts were investigated. It was found that the two catalysts had different activity and selectivity in the hydrogenation of CALD. It was further observed that the catalyst deactivation was related to the conversion of CDs to carbon flakes.

5.2 Experimental procedure

The methods used to synthesize CDs and Pd/CDs composite were modified from the methods reported in the literature by Chen *et al.* and Dey *et al.* respectively [33, 12].

5.3 Characterization of materials

The catalyst loading was determined by inductively coupled plasma-emission spectroscopy (ICP-OES), which was carried out using a Spectro Arcos ICP-OES. The morphology of the CDs and Pd/CDs composite was analysed by high resolution transmission electron microscopy (HRTEM) using a Tecnai G2 30ST operating at 200 kV and high-angle annular dark field imaging (HAADF). The Pd and CDs particle sizes were measured using Image J software by counting > 100 particles from TEM images obtained. Scanning transmission electron microscopy (STEM) images were acquired using a JEOL ARM-200F operating at 200 kV. The phase composition of the prepared samples was determined using, a Bruker D_2 phaser PXRD equipped with a Lynxene detector using Cu-K_α (λ = 1.54184 Å) radiation at 30 kV with a scan range from $5° \leq 2\Theta \leq 90°$ in 0.026 steps. The thermal stability of the samples was determined using a Perkin Elmer thermogravimetric analyser (TGA 4000) in air in the temperature range of 35-900 °C (10 °C/min). The presence of functional groups on the surface of the samples was determined using a Brüker Tensor 27 Fourier transform infrared (FTIR) spectrometer. UV-vis absorption measurements were carried out using a Varian Cary Eclipse (Cary 50) UV-vis absorption spectrophotometer. Photoluminescence characteristics were measured using an Agilent Cary Eclipse fluorescence spectrometer. The Raman spectra were recorded using a

Bruker Senterra Raman spectrophotometer with a laser wavelength of 532 nm using Opus 7.1 software. The elemental composition of the samples was determined using X-ray photoelectron spectroscopy (XPS) using a Thermo ESCAlab 250Xi equipped with a monochromatic Al K_α X-ray source operating at 1486.7 eV.

5.4 Catalytic tests

The selective hydrogenation of CALD was carried under atmospheric pressure in a three-neck round bottom flask (100 mL) equipped with a condenser, magnetic stirrer, gas inlet, and sampling port. The three-neck round bottom flask was placed inside an oil bath with a thermocouple to maintain the desired temperature. The reaction mixture consisted of 100 mg catalyst, 1.32 g CALD, and 100 mL absolute ethanol. To remove traces of dissolved oxygen, N_2 gas was bubbled into the reaction mixture while the temperature was ramped to 60 °C (2 °C/min). Once the oil bath reached 60 °C, N_2 was switched with H_2 (50 mL/min) gas to allow for hydrogenation of CALD. The reaction was carried out for 7 or 8 h while taking samples of the reaction periodically for analysis.

Product analysis was carried out using an offline Varian 3700 GC with a flame ionization detector (FID) and a capillary column (Phenomenex Zebron, 30 m L. x 0.53 mm I.D. x 1.5 µ F.T.). The conditions for analysis were as follows: the temperatures for column, detector and injector were set to 300, 250, and 200 °C respectively, with N_2 (5 mL/min) as the carrier gas.

5.5 Results and discussion

5.5.1 Characterization of the CDs

5.5.1.1 TEM and PXRD analysis

The synthesis of the CDs was performed using a variation of a classical procedure to make very small CDs [33]. The CDs were fully characterized by HRTEM, TGA, XRD, FTIR, XPS, UV-vis and PL spectroscopy and their properties are comparable to the CDs made by Chen and co-workers [33] (Fig. 5.2-5.6). Figure 5.2a shows the high magnification TEM image of the CDs with an average particle size of 0.9 ± 0.4 nm (1.84 nm in ref 34) (Fig. 5.2b). The PXRD of pure sucrose is shown in Fig. 5.3a reveals that the sucrose was fully carbonized when compared to the PXRD pattern of the CDs. The PXRD (Fig. 5.3b) data of the CDs shows a broad peak at 2Θ =18.77 ° which correspond to the (002) crystal plane of the CDs which further support that the CDs are amorphous.

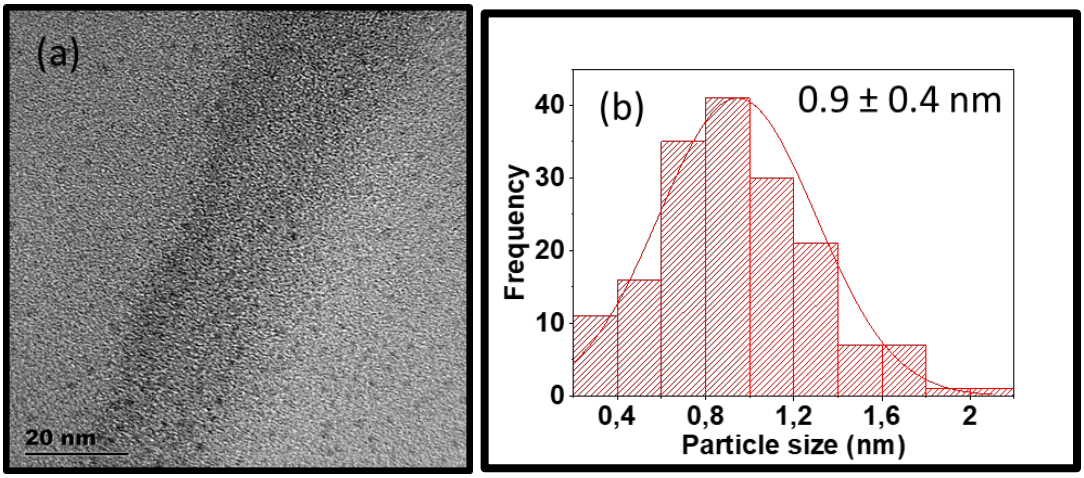

Figure 5.2: (a) HRTEM image and (b) particle size distribution of the CDs.

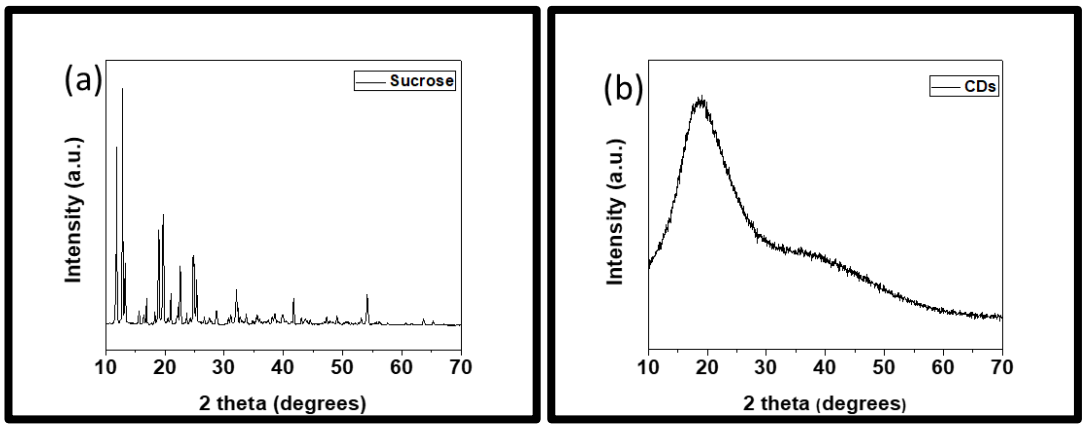

Figure 5.3: PXRD of (a) sucrose and (b) CDs synthesized using sucrose.

5.5.1.2 Thermal stability (TG analysis)

The thermal stability of the CDs was determined by using TGA and the CDs gave a classic weight loss expected for CDs (Fig. 5.4). The first and second small decomposition peaks at around 95-155 °C can be attributed to the loss of adsorbed moisture as the CDs are known to be hygroscopic [4, 34]. The onset decomposition temperature of the oxygen-containing functional groups and amorphous carbon was 223 °C with a maximum loss in the derivative curve at 308 °C. The weight percentage of amorphous carbon containing surface functional groups was estimated to be 56.6 %. The decomposition peak of the core carbon of the CDs was observed in the TG derivative curve at *ca.* 611 °C. This indicates that the core carbon of the CDs is a graphitic type of carbon.

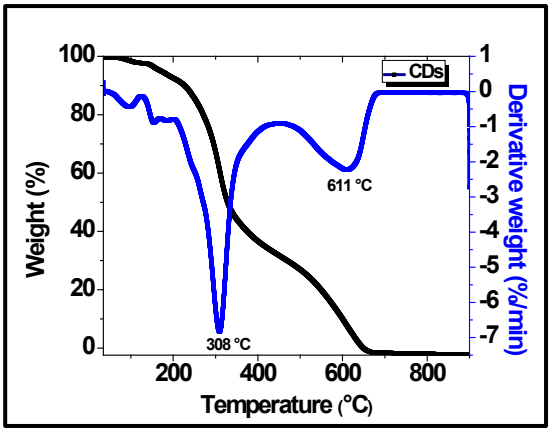

Figure 5.4: TGA and the DTG profile of the CDs.

5.5.1.3 FTIR and XPS analysis

FTIR spectroscopy was used to identify the functional groups on the surface of the CDs. FTIR spectra (Fig. 5.5a) showed prominent peaks at 1016, 1656, 2925, and a broad peak at 3317 cm^{-1} which corresponds to C-O-C, C=O, C-H, and C-OH functionalities respectively. Characterization of the surface composition and elemental analysis of the CDs were done using XPS (Fig. 5.5b). Two peaks at 285.0 eV and 532.6 eV are attributed to C1s and O1s. The third peak at 101.6 eV (0.5 atomic %) is from Si2p contamination, from scraping the sample off the glass beaker after drying the sample in an oven or due to dust. The deconvolution of the C1s XPS spectrum (Fig.5. 5c) of the CDs showed 5 types of carbon species with peaks in the spectrum corresponding to C-C sp^2 (284.4 eV), C-C sp^3 (285.0 eV), C-O (286.1 eV), C=O (287.3 eV), O-C=O (288.5 eV), indicating the presence of carboxylic, hydroxyl, and carbonyl functional groups on the surface of the CDs.

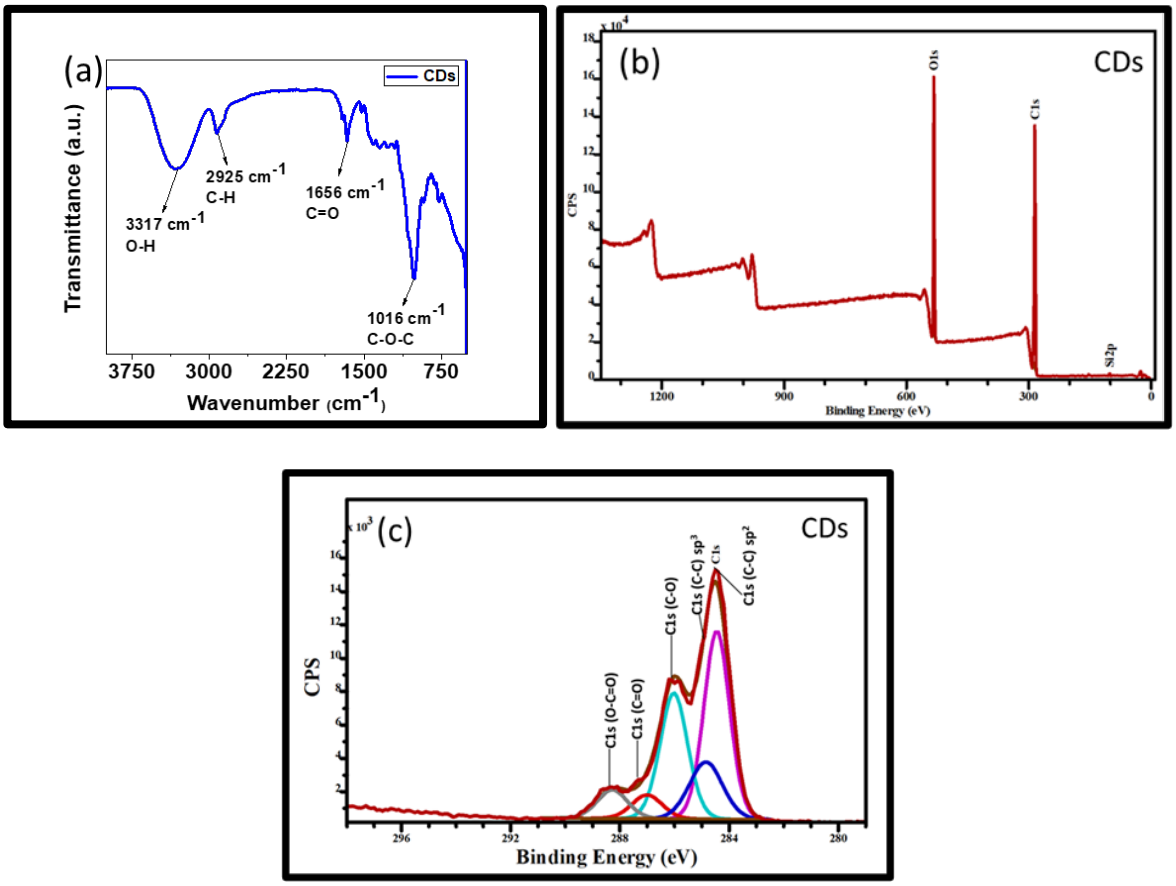

Figure 5.5 (a) FTIR spectra, (b) XPS spectra, and (c) C_{1s} spectra of the CDs.

5.5.1.4 Optical properties

The optical properties of the CDs were investigated using UV-vis and PL spectroscopy. The UV-vis spectra (Fig. 5.6a) of the CDs showed two peaks in the 200-300 nm region and a tail extending to the visible region. The peak at 226 nm is due to the presence of multiple polyaromatic chromophores, while the peak at 284 nm is attributed to the $\pi - \pi^*$ transition of the CDs [33]. When the CDs were excited at a wavelength of 365 nm, a maximum emission peak at 471 nm was observed (Fig. 5.6b). The optical properties of the pristine CDs are similar to the ones reported by Chen and co-workers [33]. The reported UV-vis spectra showed two absorption peaks at 225 and 280 nm [33]. From the PL spectra, the CDs showed a maximum emission peak at 461 nm when excited at a wavelength of 365 nm [33]. A small shift in the PL maxima from 471 nm to 461 nm [33] is consistent with smaller particles produced in this study [7].

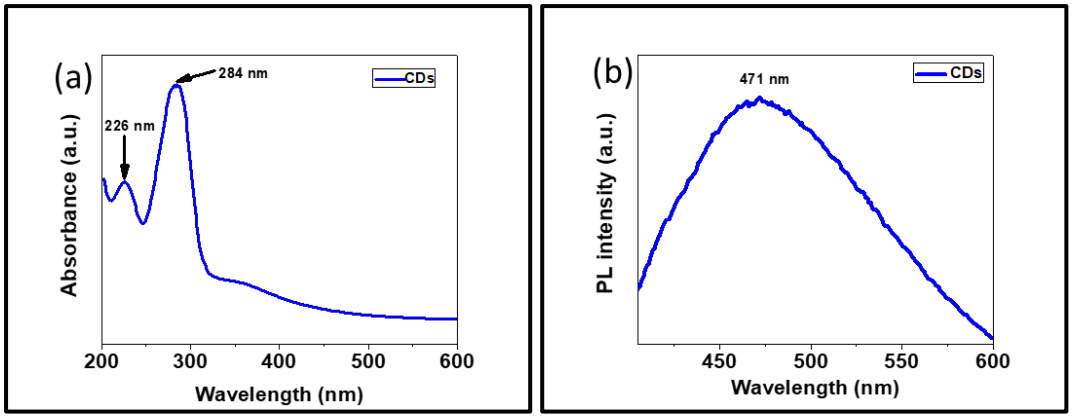

Figure 5.6: (a) UV-vis spectra and (b) PL spectra of the CDs.

5.5.2 Characterization of the Pd/CDs composite

5.5.2.1 Morphology analysis

The Pd/CDs were made by adding a Pd salt to the CDs without the addition of a reducing agent. The Pd metal content on the synthesized Pd/CDs catalyst was determined using ICP-OES and was found to be 0.81 % Pd. A TEM image of the Pd NPs is shown in Fig. 5.7a and the NPs have variables sizes (5.5-13.7 nm). To show if there is any interaction between the Pd/CDs composite, TEM images of the catalyst was taken at slightly lower magnification and it was noted that some of the Pd NPs are covered with a carbon layer (Fig. S5.1a (red circle), b) whereas some of the NPs are not coated (blue circle). It appears that the Pd is seen on/in a carbon overlayer, similar to that described by Dey *et al.* [12], Dhenadhayalan *et al.* [35], and Chandrasekaran *et al.* [36]. The HRTEM image in Fig. 5.7b shows one of the large nanoparticles in the Pd/CDs composite. Here a multi-twinned Pd nanoparticle (d = 11.6 nm) with high crystallinity and a lattice *d*-spacing of 0.22 nm is seen. This lattice *d*-spacing corresponds to the (111) plane of Pd (0) and indicates that the Pd has been reduced by the CDs. A HAADF STEM image (bright and dark field) of the sample (Fig. 5.7c and d) confirmed the presence of Pd and that the Pd NPs had variable diameters. Thus, the TEM data reveals that a Pd-carbon catalyst has been made, but that the expected inverse catalyst support interaction was not observed; the CDs have been modified by the Pd.[15, 37] The use of Pd in the transformation of carbon nanotubes to few-layer graphene sheets was also reported by Janowska *et al.* [37]. The authors reported on Pd catalyzed few-layer graphene sheets via unzipping of carbon nanotubes in an oxygen-containing liquid medium under microwaves radiation. A similar conversion of the CDs to a layered carbon has occurred here.

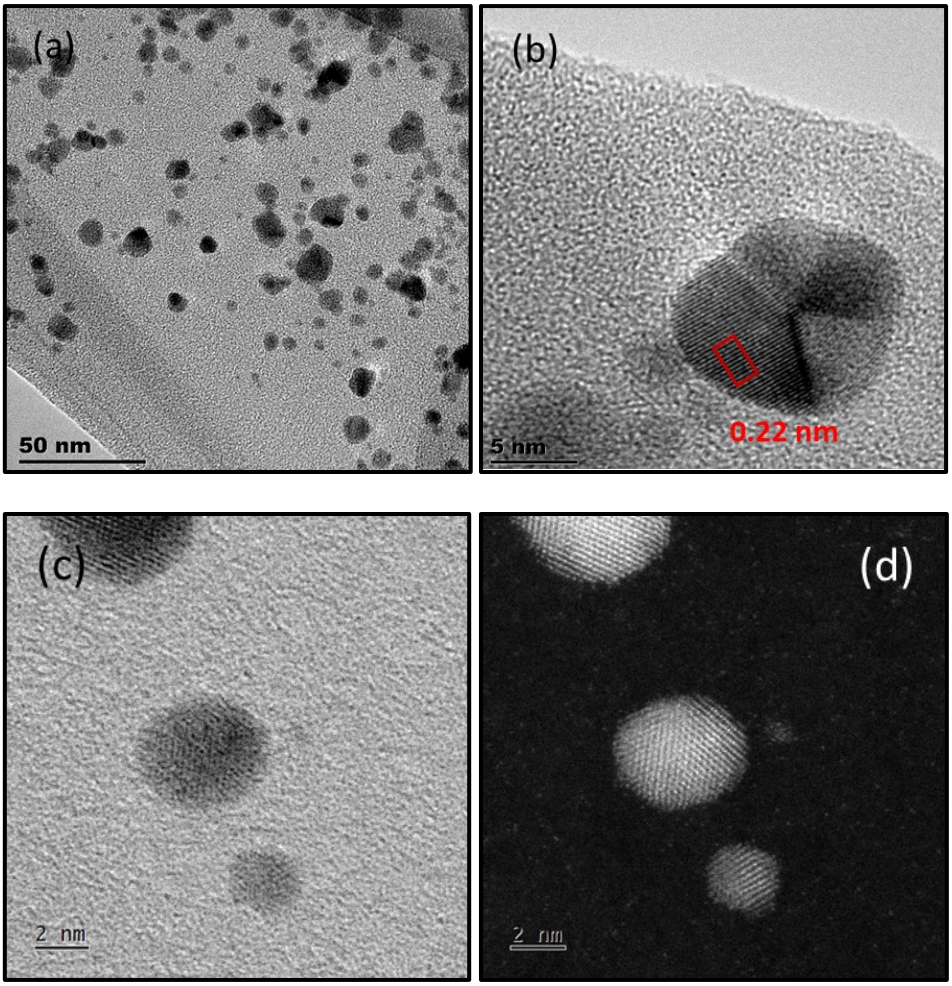

Figure 5.7: (a-b) HRTEM images and (c-d) HAADF STEM bright and dark images of 1 wt. % Pd/CDs.

5.5.2.2 PXRD and thermal stability analysis

The PXRD data for the Pd/CDs composite also confirmed that the H_2PdCl_4 salt had been reduced to metallic Pd. The PXRD (Fig. 5.8a) peaks at *ca.* 39.7°, 46.3°, 67.1°, and 81.1° corresponds to the Pd nanoparticle crystal planes: (111), (200), (220), and (311) [38]. The Pd nanoparticle plane (111) was more prominent than other phases which correlates to the lattice *d*-spacing obtained from HRTEM images of the Pd/CDs. The Pd crystallite size measured using the Scherrer equation gave d = 9.7 nm, a value similar to that found from TEM measurements. The thermal stability of Pd/CDs was studied using TGA (Fig. 5.8b). From the TGA, a residue of 0.45 weight % (due to oxidized Pd) was observed. Compared to the TGA of the CDs, it was observed that the addition of the Pd catalyst decreased the thermal stability of the CDs. The presence of Pd also affected the removal of the functional groups with the maximum peak position reduced from 308 °C (see Fig. 5.4) to 186 °C. A small peak at *ca.* 300 °C is thought

to be due to CDs that did not interact with Pd. The decomposition of the CDs core was observed in the derivative curve at *ca.* 424 °C, much lower than seen in the CDs. The early onset oxidation of the carbon can be attributed to the ability of the Pd nanoparticles to catalyze the oxidation of carbon [39]. The content of surface functional groups was also lower in the Pd/CDs as indicated by the ratio of the functional group/core carbon peaks (from 57 % to 23.2 %).

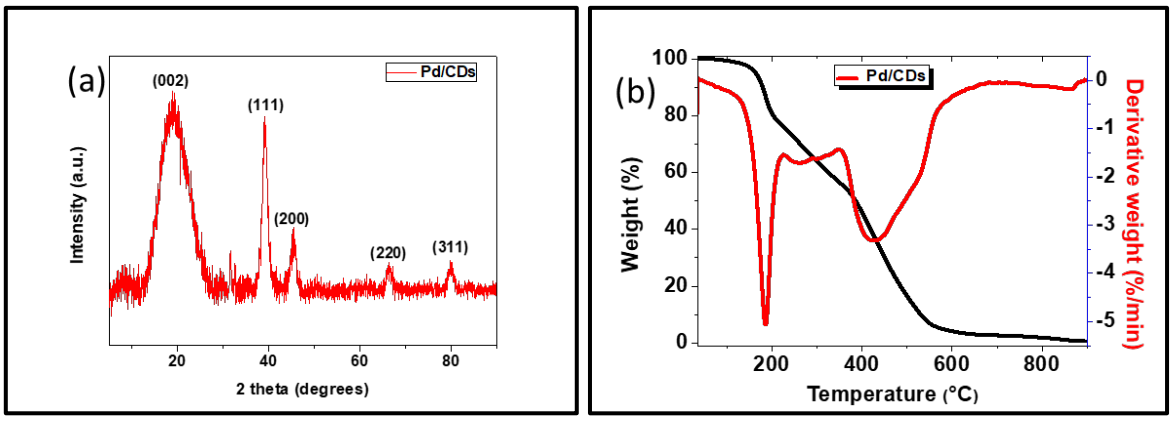

Figure 5.8: (a) PXRD and (b) TGA and DTG of 1 wt. % Pd/CDs catalyst.

5.5.2.3 Optical properties

The UV-vis spectra (Fig. 5.9a) of the Pd/CDs composite is similar to that of the CDs with a slight blue shift in the two absorption peaks (226 to 222 nm and 284 to 283 nm, CDs → Pd/CDs respectively). The absence of the plasmonic peaks for Pd(II) at 325 and 440 nm shows that a complete reduction of Pd(II) to Pd has occurred [40, 41]. The addition of Pd to the CDs led to quenching of the photoluminescence of the CDs and shifted the peak maximum from 471 nm to 456 nm (Fig. 5.9b). This phenomenon can be attributed to possible aggregation of CDs, the removal of the CD functional groups, and photoinduced electron transfer from the CD shells to metal cores [42].

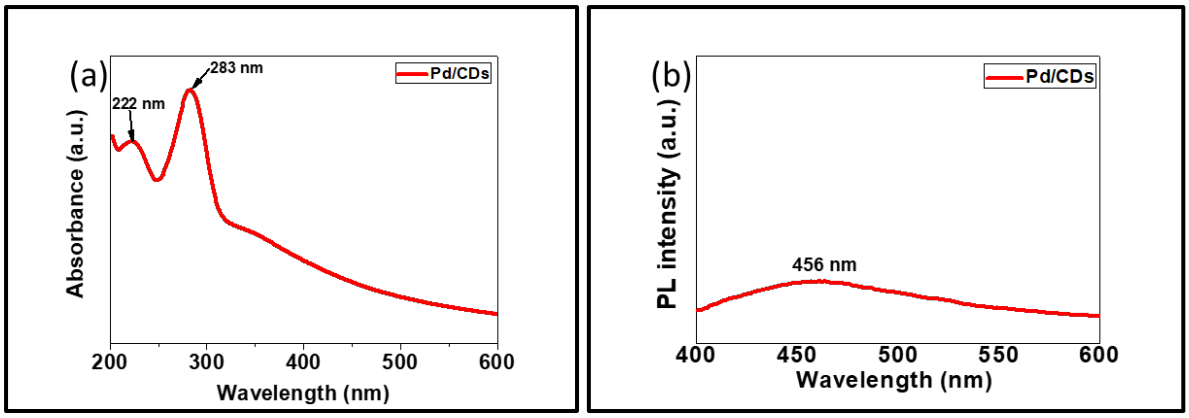

Figure 5.9: (a) UV-vis spectra and (b) PL spectra of the 1 wt. % Pd/CDs.

5.5.2.4 FTIR and XPS analysis

The FTIR spectrum (Fig. 5.10a) of the Pd/CDs showed little change from the CDs spectrum. However, XPS data (Fig. 5.10b) of the Pd/CDs showed that after the reduction of H_2PdCl_4 there was a decrease in the O1s atomic % of Pd/CDs composite from 26.8 to 22.4 % when compared to the CDs (Fig S5.5.b). The C/O atomic ratio of Pd/CDs composite was calculated to be 3.0 and this value is higher than that of the CDs (2.7). The deconvolution of the C1s XPS spectrum (Fig. 5.10c) of the Pd/CDs composite, as with the CDs, showed 5 types of carbon species which peaks in the spectrum correspond to C-C sp^2 (284.1 eV), C-C sp^3 (285.0 eV), C-O (285.9 eV), C=O (287.1 eV), O-C=O (288.4 eV) indicating that the composite still has oxygenated functional groups . A decrease in the intensity of the oxygenated peaks (C=O, O-C=O, and C-O) on the surface of the CDs was also observed. This reduction in the intensity of the oxygenated peaks was also observed by Dey and co-workers [12].

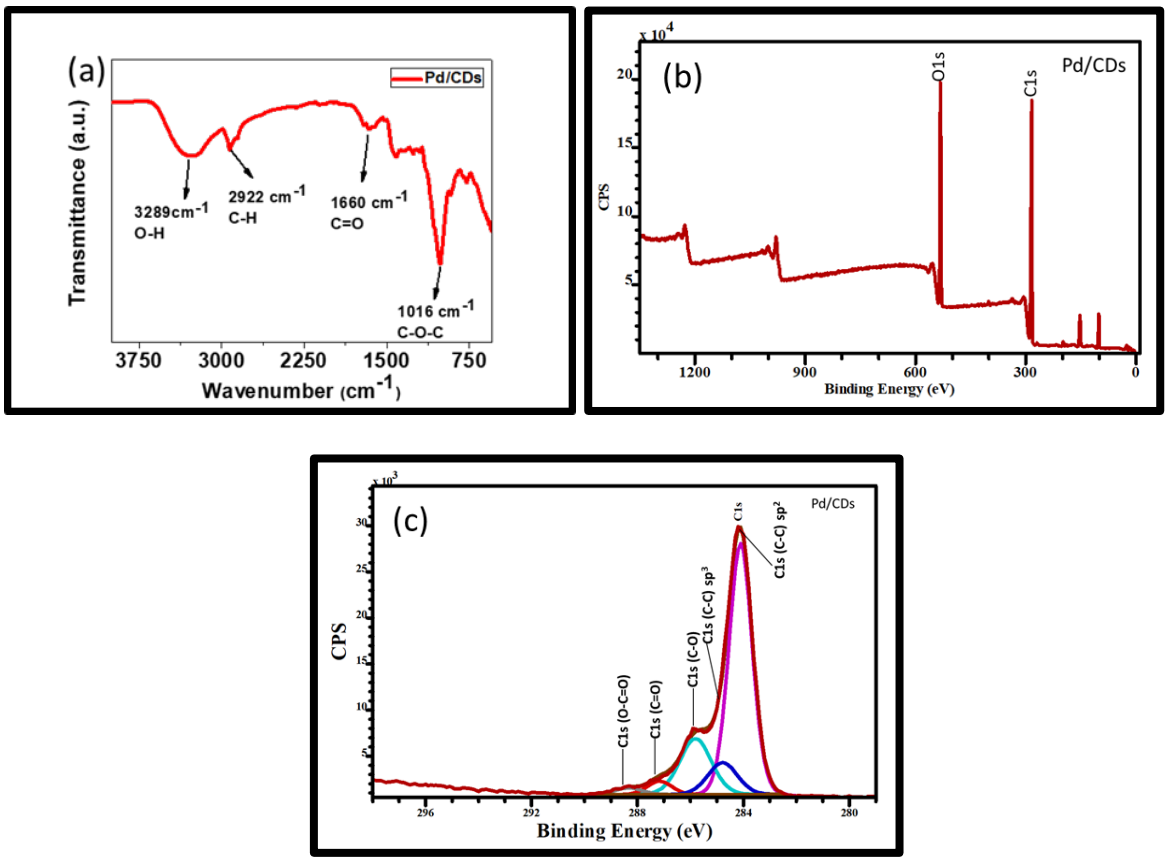

Figure 5.10: (a) FTIR spectra, (b) XPS spectra, and (c) C_{1s} spectra of the 1 wt. % Pd/CDs.

5.5.2.5 Raman analysis

The Pd/CDs composite showed Raman signals as shown in Fig. 5.11b whereas no Raman signal was observed for CDs due to their high fluorescence property (Fig. 5.11a). The Pd/CDs

Raman spectra depicts the two classic peaks at ca. 1383 cm^{-1} (D band) and 1584 cm^{-1} (G band). The D band is characteristic of disordered graphite and the G band is associated with a vibration of sp^2 carbon atoms [43]. The Raman results are in agreement with PL spectral data for the Pd/CDs. The intensity ratio of the D and G band (I_D/I_G) can be used to estimate the graphitization of carbon nanomaterials and was estimated to be 0.81, which is consistent with a partially graphitic carbon material.

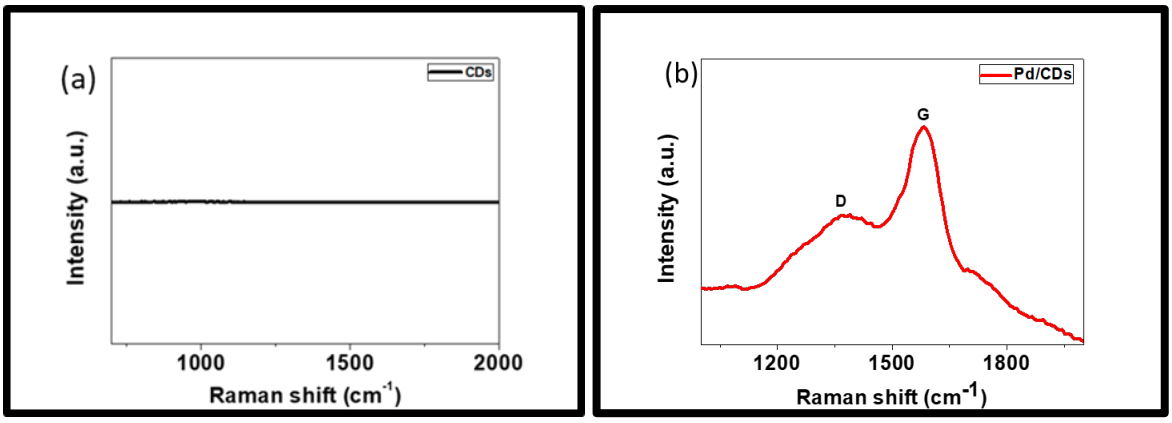

Figure 5.11: Raman spectra of (a) CDs and (b) 1 wt. % Pd/CDs.

5.5.3 Summary

In summary, the method used in the synthesis of the Pd/CDs resulted in the Pd being reduced by the CDs and that some interaction between the CDs and Pd was shown (TGA, UV-vis, PL spectroscopy). Further, interaction of the CDs with the Pd led to partial removal of surface groups by the Pd and conversion of the CDs to a carbon layered material.

The observation of the conversion of CDs to carbon sheets has been described before, but in this report the reaction occurred thermally at temperatures > 300 °C [44]. In other studies CDs conversion into porous 3D carbon framework thermally at *ca.* 800 °C has also been mentioned [45]. It appears from our study that this reaction to convert CDs to other carbon shapes can also occur at lower temperatures (100 °C) in the presence of the Pd acting as a catalyst. The reaction resulted in coverage/embedding of the Pd with a carbon overlayer that was generated from the CDs, as seen by others [12, 35, 36]. The conversion of CDs to carbon sheets without the presence of Pd was undertaken and this conversion occurred at temperature of *ca.* 300 °C (Fig. S5.2). Not unexpectedly this conversion of the CDs impacted on the catalytic behaviour of the Pd.

5.5.4 Hydrogenation of CALD using CDs and Pd/CDs composite

5.5.4.1 Catalytic reactions of CDs

Carbon materials are known to act as catalysts, a phenomenon known as carbocatalysis [46, 47]. The development of carbon nanomaterials (CNMs) such as fullerene, CNTs, graphene, nanodiamonds, and mesoporous carbon has led to an enormous interest in the use of these CNMs as carbocatalysts in various catalytic applications [48]. Functional groups on the surface of these CNMs have been identified as one of the catalytic sites [48].

The CALD hydrogenation reaction was carried out in the liquid phase. The catalytic activity of the CDs towards the hydrogenation of CALD was evaluated at 40 and 60 °C (Fig. 5.12). The reaction is in general rapid and the reaction terminated prior to conversion of all the CALD. For example, at 60 °C within 4 h 40 % CALD conversion was obtained, and after that no further reaction took place. In terms of selectivity, the CDs catalyst was completely selective to the hydrogenation of the C=O bond forming CA, and no HCALD and 3P1P were detected. This is consistent with the ability of the carbon π-electrons to donate electrons to the CALD, as observed for Pt which also hydrogenates the C=O bond [49].

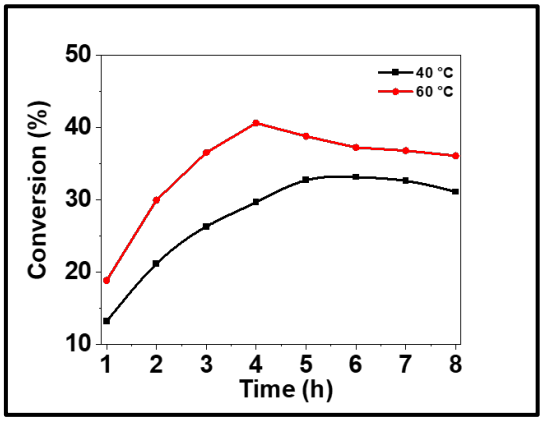

Figure 5.12: The conversion of CALD over CDs catalyst at 40 °C and 60 °C (50 mg CDs, 50 mL/min = H_2 flow rate, 100 ml ethanol, and 1.32 g CALD).

In an attempt to modify the activity of the CDs, a surface reaction with acetic acid (to give fCDs) was undertaken to generate potential reaction sites. The FTIR (Fig.S5.3a) spectrum of the fCDs indeed showed the growth of peaks at 3366, 1711, and 1018 cm^{-1} which corresponds to O-H, C=O, and C-O-C functional groups when compared to the FTIR spectrum of the CDs. There was also a slight red shift in the peaks suggesting stronger bond formation (Table S5.1). The fCDs were used in the cinnamaldehyde reduction reaction, but unexpectedly the fCDs gave

a reduction in catalyst activity indicating that the acid functional groups were not the major contributor to the reaction (Figure 5.13). The selectivity to C=O reduction was maintained.

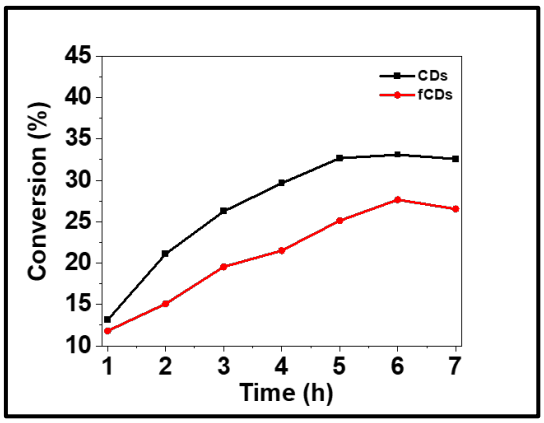

Figure 5.13: Conversion of CALD over CDs and fCDs catalysts at 40 °C. Reference conditions: $m_{catalyst}$ = 50 mg, t = 7 h, 50 mL/min = H_2 flow rate, 100 ml ethanol, and 1.32 g CALD.

5.5.4.2 Catalytic activity of Pd/CDs

The catalytic activity of the Pd/CDs catalysts was determined. The activity was found to be higher for the Pd/CDs than for the CDs but also, significantly, the product distributions were entirely different (it is to be noted that the Pd content was < 1%). For example, after 1 h reaction using similar reaction conditions (60 °C) the conversion of CALD was higher for the Pd/CDs (64.3 %) than for the CDs (18.8 %) (Table 5.1). Thus, the Pd/CD catalyst completely overwhelmed the catalytic reaction of the CDs. This suggests that the reduction of the Pd by the CDs removed the active surface groups responsible for the hydrogenation of the CALD to CA.

Table 5.1: CDs and Pd/CDs activity and selectivity for the hydrogenation of CALD.

Catalysts	Conversion (%)	Selectivity (%)		
		HCALD	3P1P	CA
CDs	18.8	0	0	100
Pd/CDs	64.3	100	0	0

Reference conditions: 1 h, 50 mg catalyst, 50 mL/min = H_2 flow rate, 100 ml ethanol, T = 60 °C, and 1.32 g CALD.

The catalytic activity of Pd/CDs catalyst was further studied, using different reaction conditions. The effect of the Pd/CDs catalyst mass on the hydrogenation of CALD was tested at 60 °C (Fig. 5.14). A relatively good linear correlation between the catalyst activity and the

amount of catalyst used was observed. The conversion of CALD increased from 46 to 73 % with an increase in the catalyst mass.

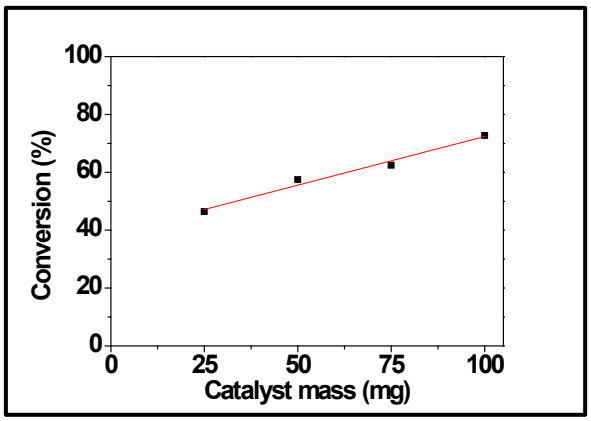

Figure 5.14: The conversion of CALD over Pd/CDs catalyst. Reference conditions: T = 60 °C, t = 7 h, 50 mL/min = H_2 flow rate, 100 ml ethanol, and 1.32 g CALD.

The effect of reaction temperature on the CALD conversion and product selectivity was also studied by varying the temperature between 40 and 80 °C (Fig. S5.4). The activity (mol/g_{Pd}.h) based on CALD conversion towards the Pd mass on the Pd/CDs catalyst was calculated. Figure 5.15 shows the effect of temperature on the catalyst activity after 1 h. The catalyst activity increased from 7.2 to 8.2 mol/g_{Pd}.h with increasing reaction temperature. As the reaction temperature increased the turnover number of the effective active sites of the catalyst slightly increased. The catalyst was 100 % selective toward the reduction of the C=C bond, forming only hydrocinnamaldehyde.

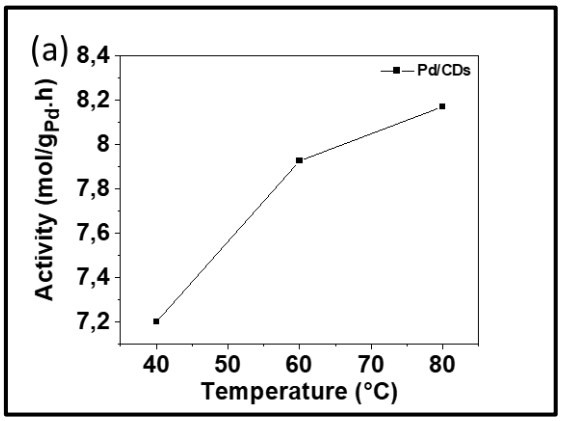

Figure 5.15: Effect of temperature on the activity of the Pd/CDs catalyst.

While good conversions were achieved with the Pd/CDs catalyst, our observations were quite different from the ones reported by Dey *et al.* [12] on the coupling of phenylboronic acid and

bromobenzene reaction. It was noted that in the Dey *et al*. study that the Pd/CDs catalyst precipitated during the reaction leading to Pd nanoparticle agglomeration (and catalyst deactivation) and that to improve the efficiency of the catalyst a co-stabilizer had to be added.

Figure 5.16 shows the influence of H_2 flow rate on the hydrogenation of the CALD over the Pd/CDs catalyst. An increase in the hydrogen flow rate did not have a significant influence on the activity of the catalyst and did not change the selectivity of the catalyst. This suggests that the reaction is not limited by the amount of H_2 in the reaction.

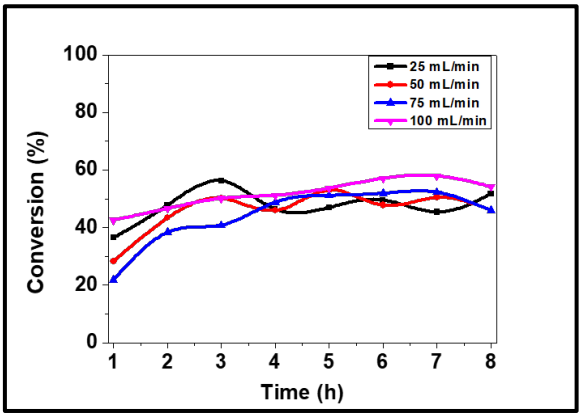

Figure 5.16: The conversion of CALD over Pd/CDs catalyst at different hydrogen flow rate. Reference conditions: T = 60 °C, 50 mg catalyst, 100 ml ethanol, and 1.32 g CALD.

Recyclability studies were undertaken; the catalyst from a previous reaction was separated from the reaction medium using a centrifuge and washed using ethanol. The obtained catalyst was dried at 100 °C for 2 h. To reactivate the catalyst, it was reduced at 190 °C using a CVD furnace under a flow of H_2 (50 ml/min) and N_2 as a carrier gas. The data indicated that the catalysts lost activity completely after the first cycle.

TEM images were recorded on the catalyst after the reaction (Fig. 5.17). A comparison of Fig 5.7a and S5.1 with Fig. 5.17 indicates that three effects have occurred: i) the Pd particles have agglomerated further ii) the carbon particles have now formed thicker sheets and iii) the carbon appears to have encapsulated the Pd. These multiple effects led to the deactivation of the catalyst. It is clear that the CDs thus play no role in stabilizing the Pd particles as was also observed in the study conducted by Dey *et al.* [12].

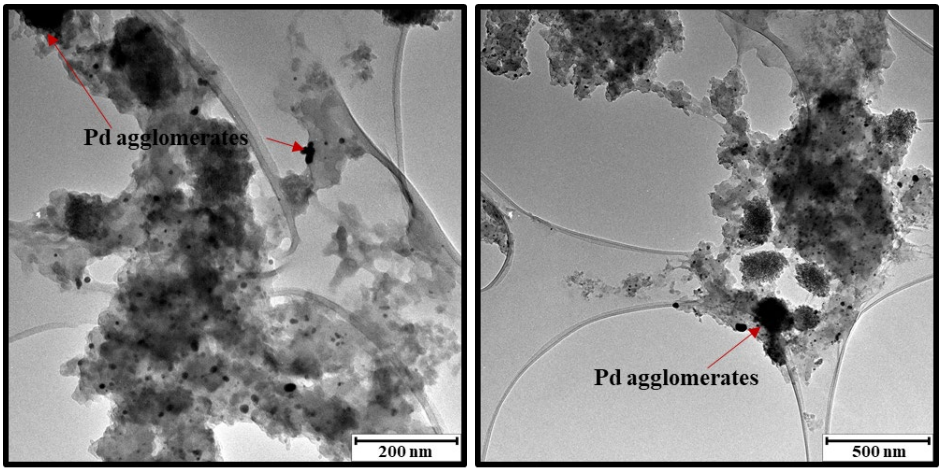

Figure 5.17: TEM images of the Pd/CDs catalyst after first cycle.

5.5.4.3 Comments of the mechanism

In the literature, the product selectivity of metal catalysts has been associated with the metal d-band width [26, 49]. The metal d-band width can be arranged in the following increasing order: Pd < Pt < Ir ≈ Os [26]. The chances of the metal surface interacting with the conjugated C=C bond increases with a narrower d-band metal width suggesting that Pd would catalyse the C=C bond in CALD [26].

Our initial objective was to investigate the role of Pd supported on CDs to study an inverse catalyst support effect ($d_{Pd} > d_{support\ particle}$) and to study the selectivity of this type of catalyst. The first step was to evaluate the CDs in the CALD hydrogenation reaction. Here studies showed that the C=O bond was selectively hydrogenated. Functionalization of the CDs with acetic acid further revealed that the acid C=O groups were not the dominant groups required to hydrogenate the C=O CALD bond.

The Pd/CDs were then investigated for the CALD hydrogenation. After reaction with Pd, some changes in the surface chemistry of the CDs were noted. TEM data indicated some interaction between the Pd and CDs to give reduced Pd, and that the CDs were converted to larger structures. This was unexpected and suggested that the activity of the CDs would be modified by this process by i) loss of surface area and ii) loss of functional groups. The study indicated that the Pd (< 1 %) dominated the catalytic reaction. We assume that the active functional groups responsible for selectivity towards C=O were removed from the CDs during the reduction of the Pd salt. Toebes *et al.* has also reported that the removal of the oxygenated functional groups present on a Pt/CNF catalyst resulted in an enhanced selectivity towards the reduction of the C=C bond in the hydrogenation of CALD [51].

5.6 Conclusions

The data presented from this study shows that CDs can be used as a reducing agent for Pd salts thus avoiding the use of strong and toxic reducing agents. From HRTEM studies, it was shown that highly crystalline Pd NPs were formed after reaction of a Pd salt with the CDs. The UV-vis spectra of the Pd/CDs is similar to that of CDs and no plasmonic peaks of Pd (II) were observed. The PL and Raman spectra of the Pd/CDs catalyst has shown that CDs have electron transfer properties indicated by quenching of the photoluminescence of the CDs. The interaction between CDs and Pd NPs is similar to reactions with other nano carbons in which the Pd salts are reduced by the carbon. The use of the Pd/CDs catalyst for the reduction of CALD led to a conversion of 78 % at 80 °C. The presence of the CDs in the Pd/CDs composite did not influence the selectivity of Pd NPs. It was observed that the CDs and Pd/CDs catalysts favoured different adsorption modes (C=O or C=C respectively) leading to different product distributions. The reaction of the Pd with the CDs also led to CDs conversion to carbon sheets. As the result this effect led to the catalyst deactivation observed in the reaction.

5.7 References

1. Zhang, J.; Chen, Y.; Tan, J.; Sang, H.; Zhang, L.; Yue, D. *Applied Surface Science* **2017**, *396*, 1138.
2. Zhou, J.; Zhou, H.; Tang, J.; Deng, S.; Yan, F.; Li, W.; Qu, M. *Microchimica Acta* **2017**, *184*, 343.
3. Dimos, K. *Current Organic Chemistry* **2016**, *20*, 682.
4. Baker, S. N.; Baker, G. A. *Angewandte Chemie International Edition* **2010**, *49*, 6726.
5. Xu, X.; Ray, R.; Gu, Y.; Ploehn, H. J.; Gearheart, L.; Raker, K.; Scrivens, W. A. *Journal of the American Chemical Society* **2004**, *126*, 12736.
6. Lim, S. Y.; Shen, W.; Gao, Z. *Chemical Society Reviews* **2015**, *44*, 362.
7. Wang, Y.; Hu, A. *Journal of Materials Chemistry C* **2014**, *2*, 6921.
8. Li, X.; Wang, H.; Shimizu, Y.; Pyatenko, A.; Kawaguchi, K.; Koshizaki, N. *Chemical Communications* **2011**, *47*, 932.
9. Shen, L.-M.; Liu, J. *Talanta* **2016**, *156*, 245.
10. Sun, J.-K.; Xu, Q. *ChemCatChem* **2015**, *7*, 526.
11. Wang, X.; Long, Y.; Wang, Q.; Zhang, H.; Huang, X.; Zhu, R.; Teng, P.; Liang, L.; Zheng, H. *Carbon* **2013**, *64*, 499.
12. Dey, D.; Bhattacharya, T.; Majumdar, B.; Mandani, S.; Sharma, B.; Sarma, T. K. *Dalton Transactions* **2013**, *42*, 13821

13. Wei, W.; Chen, W. *Journal of Power Sources* **2012**, *204*, 85.
14. Im, H.; Noh, S.; Shim, J. H. *Electrochimica Acta* **2020**, *329*, 135172.
15. Zhang, J.; Medlin, J. W. *Surface Science Reports* **2018**, *73*, 117.
16. Dhenadhayalan, N.; Lin, K. C.; Saleh, T. A. *Small* **2020**, *16*, 1905767.
17. Dhenadhayalan, N.; Lin, K.-C. *ACS Applied Materials & Interfaces* **2020**, *12*, 13759.
18. Galvagno, S.; Capannelli, G.; Neri, G.; Donato, A.; Pietropaolo, R. *Journal of Molecular Catalysis* **1991**, *64*, 237.
19. Zhao, F.; Ikushima, Y.; Chatterjee, M.; Shirai, M.; Arai, M. *Green Chemistry* **2003**, *5*, 76.
20. Zeng, L.-H.; Yan, H.-X.; Zeng, Y.-K.; Li, Y.-F.; Zhang, Z.-X.; Liu, Z.-W.; Liu, Z.-T. *The Canadian Journal of Chemical Engineering* **2019**, *97*, 2505.
21. Yuan, T.; Liu, D.; Pan, Y.; Pu, X.; Xia, Y.; Wang, J.; Xiong, W. *Catalysis Letters* **2019**, *149*, 851.
22. Prakash, M. G.; Mahalakshmy, R.; Krishnamurthy, K. R.; Viswanathan, B. *European Chemical Bulletin* **2017**, 6, 125.
23. Bewana, S.; Ndolomingo, M. J.; Carleschi, E.; Doyle, B. P.; Meijboom, R.; Bingwa, N. *ACS Applied Materials & Interfaces* **2019**, *11*, 32994.
24. Harada, T.; Ikeda, S.; Miyazaki, M.; Sakata, T.; Mori, H.; Matsumura, M. *Journal of Molecular Catalysis A: Chemical* **2007**, *268*, 59.
25. Sairanen, E.; Karinen, R.; Borghei, M.; Kauppinen, E. I.; Lehtonen, J. *ChemCatChem* **2012**, *4*, 2055.
26. Nagpure, A. S.; Gurrala, L.; Gogoi, P.; Chilukuri, S. V. *RSC Advances* **2016**, *6*, 44333.
27. Pham-Huu, C.; Keller, N.; Ehret, G.; Charbonniere, L. c. J.; Ziessel, R.; Ledoux, M. J. *Journal of Molecular Catalysis A: Chemical* **2001**, *170*, 155.
28. Zhu, J.; Dou, M.; Lu, M.; Xiang, X.; Ding, X.; Liu, W.; Li, M. *Applied Catalysis A: General* **2019**, *575*, 11.
29. Tessonnier, J.-P.; Pesant, L.; Ehret, G.; Ledoux, M. J.; Pham-Huu, C. *Applied Catalysis A: General* **2005**, *288*, 203.
30. Xu, Z.; Duong-Viet, C.; Liu, Y.; Baaziz, W.; Li, B.; Nguyen-Dinh, L.; Ersen, O.; Pham-Huu, C. *Applied Catalysis B: Environmental* **2019**, *244*, 128.
31. Martínez-Ortiz, M. J.; de la Rosa-Guzmán, M. A.; Vargas-García, J. R.; Flores-Moreno, J. L.; Castillo, N.; Guzmán-Vargas, A.; Morandi, S.; Pérez-Gutiérrez, R. M. *The Canadian Journal of Chemical Engineering* **2018**, *96*, 297.

32. Das, D.; Pal, K.; Llorca, J.; Dominguez, M.; Colussi, S.; Trovarelli, A.; Gayen, A. *Reaction Kinetics, Mechanisms and Catalysis* **2017**, *122*, 135.
33. Chen, B.; Li, F.; Li, S.; Weng, W.; Guo, H.; Guo, T.; Zhang, X.; Chen, Y.; Huang, T.; Hong, X.; You, S.; Lin, Y.; Zeng, K.; Chen, S. *Nanoscale* **2013**, *5*, 1967.
34. He, Y.; He, J.; Yu, Z.; Zhang, H.; Liu, Y.; Hu, G.; Zheng, M.; Dong, H.; Zhuang, J.; Lei, B. *Journal of Materials Chemistry C* **2018**, *6*, 2495.
35. Dhenadhayalan, N.; Hsin, T.-H.; Lin, K.-C. *Advanced Materials Interfaces* **2019**, *6*, 1900361.
36. Chandrasekaran, P.; Jebakumar Immanuel Edison, T. N.; Sethuraman, M. G. *International Journal of Hydrogen Energy* **2020**, *45*, 28800.
37. Janowska, I.; Ersen, O.; Jacob, T.; Vennégues, P.; Bégin, D.; Ledoux, M.-J.; Pham-Huu, C. *Applied Catalysis A: General* **2009**, *371*, 22.
38. Huang, Q.; Lin, X.; Zhu, J.-J.; Tong, Q.-X. *Biosensors and Bioelectronics* **2017**, *94*, 507.
39. Moyo, M.; Motchelaho, M. A. M.; Xiong, H.; Jewell, L. L.; Coville, N. J. *Applied Catalysis A: General* **2012**, *413-414*, 223.
40. Chen, L.-J.; Wan, C.-C.; Wang, Y.-Y. *Journal of Colloid and Interface Science* **2006**, *297*, 143.
41. D'Souz, L.; Sampath, S. *Langmuir* **2000**, *16*, 8510.
42. Luo, P.; Li, C.; Shi, G. Physical Chemistry Chemical Physics 2012, 14, 7360.
43. Ferrari, A. C.; Basko, D. M. *Nature Nanotechnology* **2013**, *8*, 235.
44. Mokoloko, L. L.; Matsoso, B. J.; Forbes, R. P.; Barrett, D. H.; Moreno, B. D.; Coville, N. J. *Carbon Trends* **2021**, *4*, 100074.
45. Hou, H.; Banks, C. E.; Jing, M.; Zhang, Y.; Ji, X. *Advanced Materials* **2015**, *27*, 7861.
46. Navalon, S.; Dhakshinamoorthy, A.; Alvaro, M.; Garcia, H. *Chemical Reviews* **2014**, *114*, 6179.
47. Gordeev, E. G.; Pentsak, E. O.; Ananikov, V. P. *Journal of the American Chemical Society* **2020**.
48. Su, D. S.; Wen, G.; Wu, S.; Peng, F.; Schlögl, R. *Angewandte Chemie International Edition* **2017**, *56*, 936.
49. Ma, H.; Wang, L.; Chen, L.; Dong, C.; Yu, W.; Huang, T.; Qian, Y. *Catalysis Communications* **2007**, *8*, 452.
50. Lan, X.; Wang, T. *ACS Catalysis* **2020**, *10*, 2764.

51. Toebes, M. L.; Zhang, Y.; Hájek, J.; Alexander Nijhuis, T.; Bitter, J. H.; Jos van Dillen, A.; Murzin, D. Y.; Koningsberger, D. C.; de Jong, K. P. *Journal of Catalysis* **2004**, *226*, 215.

Chapter 6: Hydrogenation of cinnamaldehyde over palladium nanoparticles supported on a functionalized solid carbon spheres catalyst

6.1 Introduction

Chemoselective hydrogenation of α,β-unsaturated aldehydes is one of the most important reactions from an academic and industrial point of view. This reaction is used in the production of fine chemicals, spices, and pharmaceutical intermediates [1-3]. One of the model α,β-unsaturated aldehydes compounds is cinnamaldehyde (CALD). The immense interest in the selective hydrogenation of CALD arises because (i) the products produced in this reaction are of economic value in both the pharmaceutical and fragrance industries and (ii) conjugation exists between the C=C bond and C=O bond in CALD which impacts on their chemistry [1]. The selective hydrogenation of CALD can occur through different pathways (Scheme 6.1) via hydrogenation of the C=C bond to form hydrocinnamaldehyde (HCALD) or hydrogenation of the C=O bond to form cinnamyl alcohol (CA). Both HCALD and CA can be further hydrogenated to form 3-phenyl-1-propanol (3P1P) [1-3]. The reduction of the C=C bond occurs more easily than that of the C=O bond as it is both the kinetically and thermodynamically favoured product. Depending on the solvent used (i.e. ethanol or isopropanol) by-products such as acetals, propyl benzene, and β-methyl styrene can be formed as well [4-7]. The formation of the acetals has been attributed to the reaction of saturated aldehydes with the alcohol solvent through an aldol condensation reaction[7].

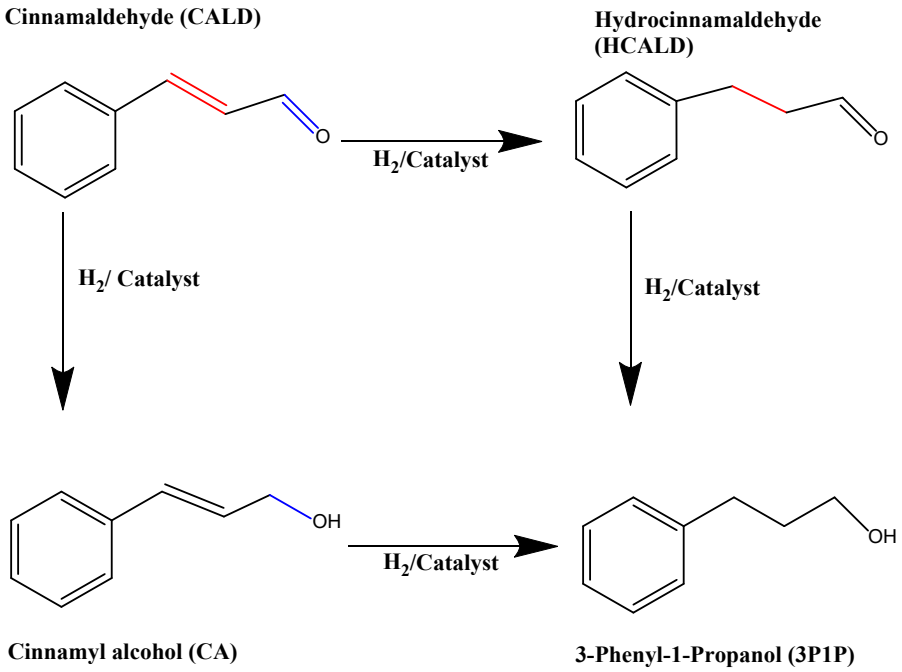

Scheme 6.1: Reaction pathway for the selective hydrogenation of CALD.

Several supported noble metals (i.e. Au, Pd, Pt, Ru, and Ir) and non-noble metals (i.e. Fe, Co, and Ni) have been used in the selective hydrogenation of CALD [8, 9]. Research work has shown that Pt, Ir, Co, Ru, and Au are relatively more selective for the hydrogenation of the C=O bond as opposed to Pd, Cu, and Ni [9]. Various factors such as metal particle size, solvent effects, the active metal, and catalyst support properties have been reported to influence the selectivity and activity of the reaction [2]. For example, Li *et al.* investigated the role played by different organic solvents on the selective hydrogenation of CALD over 5 wt. % Pd/C catalyst [10]. The organic solvents used had different physicochemical properties and those studied included protic (2-propanol and 1-butanol), aprotic polar (triethylamine, tetrahydrofuran, N,N′-dimethylformamide, diethyl ether, 4-methylpyridine, and pyridine), and aprotic apolar (n-hexane, toluene, and benzene) solvents. In their findings the CALD conversion decreased in the following order: aprotic > protic >> apolar. A selectivity of 80 % to HCALD was reported in most solvents used. However, the use of 4-methylpyridine and pyridine solvents enhanced the catalyst selectivity toward the reduction of the C=O bond, and selectivity of about 60 % to CA was reported.

One of the ways used by researchers to enhance the catalyst selectivity and activity in the selective hydrogenation of CALD is by modifying the electronic properties of the catalyst [11]. This can be done by placing the metal on a support and by the use of different supports,

different metal-support interactions will occur that will influence the course of reaction. Carbon nanomaterials (CNMs) are one example of a support that has been used to enhance the rate of a reaction by influencing the electron transfer from the CNM to the metal active site [2, 11]. The CNMs have been reported to favour the adsorption of organic compounds with weak polarity on their surface to improve the reaction rate [2, 11-13]. Metals supported on CNMs such as carbon nanotubes (CNTs), carbon nanofibers (CNFs), activated carbon (AC), graphene, and graphene oxide have all been used as a catalyst support in the selective hydrogenation of CALD [2, 7, 12, 14].

Pd supported on CNMs have been shown as promising catalysts for the selective hydrogenation of CALD. Numerous studies have reported on the role of the metal deposition and activation method [10], carbon support surface chemistry [2, 14], poison tolerance [7], confinement effect [15], and solvent effect [12] on the selectivity and activity of Pd supported on different CNMs catalyst. For example, Zhu *et al.* modified the surface of CNTs using a thermo-responsive polymer (poly(N-isopropylacrylamide); PNIPAM) and the prepared hybrid catalyst (Pd/CNT-PNIPAM) was compared to a Pd/CNTs catalyst [2]. The authors reported that surface modification of the CNTs enhanced the CALD catalytic activity while maintaining similar CA selectivity as found for a Pd/CNTs catalyst. The enhanced activity was due to a higher Pd dispersion on the hybrid catalyst. Xu *et al.* investigated the effect of oxygen functionalized graphite felt (OGF) as a Pd catalyst support (Pd/OGF) and compared the catalyst to a Pd/GF catalyst for the selective hydrogenation of CALD [9]. The Pd/OGF catalyst had a higher hydrogenation activity and it was resistant to sintering as the catalyst displayed high stability after fifteen recycling tests.

Oxygen-containing functional groups have been introduced to CNMs to improve the interaction between the carbon support and metal NPs. However, reports have indicated that the presence of polar functional groups on the carbon support can alter the selectivity and activity of the catalyst (i.e. the CALD phenyl group is repelled from adsorption on the metal surface) [1, 16]. Zeng *et al.* investigated the effect of a pre-treated AC support on the activity and selectivity of Pt NPs in the hydrogenation of CALD [1]. The AC was pre-treated with different concentrations of KOH under microwave radiation. An increase in the % of KOH used on the AC activation led to an increase in the particle size of the Pt NPs. The activity of the pre-treated catalyst increased with an increase in the concentration of KOH (2-10 %) but decreased when 15 % KOH was used. The % selectivity to CA decreased in the following order: Pt/AC-10 % KOH (73.4) > Pt/AC-8 % KOH (67.6) > Pt/AC-15 % KOH (61.5) > Pt/AC-2 % KOH (51.7 %). The enhancement in the selectivity to CA was attributed to the increase in the oxygen-

containing functional groups on the surface of the support. The oxygen-containing functional groups reduced the CALD adsorption mode via the benzene ring which reduced the distance of the C=O bond from the metal surface. In this current study, the Pd particle size and the presence of the oxygen-containing functional groups can similarly be used to explain the selectivity of the Pd/functionalized solid carbon spheres (fSCSs) catalyst.

Herein we report on the liquid phase selective hydrogenation of cinnamaldehyde as a model reaction to study the effect of surface chemistry of fSCSs when used as a support for a Pd catalyst. The use of solid carbon spheres (SCSs) as a Pd catalyst support on the hydrogenation reaction of CALD has been rarely reported in the literature. Acid treatment of CNMs has been reported to enhance the interaction between the support and the metal due to the presence of defects and oxygenated groups [1, 4]. The SCSs were treated with nitric and sulfuric acid (fSCSs) and the prepared catalyst was compared to a Pd/SCSs catalyst. The two catalysts were tested in the hydrogenation of CALD and the activity and selectivity were measured. The Pd/SCSs catalyst favoured the complete hydrogenation of CALD forming 3P1P whereas the Pd/fSCSs catalyst produced CA as a major product.

6.2 Experimental procedure

The method used to synthesize SCSs was modified from the method reported in the literature by Dlamini *et al.* [17].

6.2.1 Materials

The chemicals used were of technical and analytical grade. CALD (98 %), CA (98 %), 3P1P (98 %, FCC), HCALD (90 %) and $PdCl_2$ (99%) were purchased from Sigma-Aldrich. The absolute ethanol was purchased from MK chemical. HCl (32%), nitric acid (55 %), and sulphuric acid (98 %) were purchased from Associated Chemical Enterprise (PTY) LTD.

6.2.2 Synthesis of solid carbon spheres

An amount of 0.5 mL ammonia solution (25 %) was added to an ethanolic solution made of distilled water (60 mL) and absolute ethanol (24 mL) and the solution was stirred for one hour. After 1 h, a mass of 0.6 g resorcinol (R) was added and the solution was stirred for 30 minutes. This was followed by the addition of 0.80 mL formaldehyde (F) and the mixture was then stirred for 24 h at room temperature. The mixture, inside a Schott bottle, was hydrothermally treated in an oil bath at 100 °C for 24 h. After hydrothermal treatment, the reddish powder was recovered by centrifugation at 18000 rpm for 20 min, followed by washing using ethanol and

distilled water and then dried at 100 °C for 4 h. The RF resin spheres were carbonized at 900 °C for 4 h under nitrogen gas (20 mL/min) to obtain solid carbon spheres. The yield of the SCSs was calculated to be 42 %.

6.2.3 Acid treatment of SCSs

The as-synthesized SCSs were functionalized using an acid treatment method [18]. A mass of 1 g of SCSs was added to a mixture of nitric acid (55 %, 11.24 mL) and sulphuric acid (98 %, 3.76 mL) in a 500 mL round bottom flask. The mixture was refluxed at 110 °C for 2 h inside the fumehood. The acid-treated SCSs were washed with distilled water until a pH of 7 was reached. The obtained fSCSs were oven-dried at 100 °C for 4 h.

6.2.4 Synthesis of 5 wt. % Pd/SCSs or Pd/fSCSs catalysts

The procedure for the impregnation of Pd NPs on the support was modified from the method reported by Zhu *et al.* [2]. A mass of 0.6 g carbon support was added to 141 mL of 2 mM H_2PdCl_4 solution and the mixture was stirred overnight. A mass of 0.1895 g of sodium borohydride dissolved in ethanol was slowly added to the mixture with continuous stirring for 2 h to reduce the metal salt into metallic Pd NPs. The catalyst was filtered and washed using distilled water and absolute ethanol. The obtained black solid (Pd/fSCSs or Pd/SCSs) was oven-dried at 100 °C for 4 h.

6.3 Characterization techniques

The morphologies of the RF resin spheres, SCSs and Pd/SCSs or Pd/fSCSs were analyzed by transmission electron microscopy (TEM; FEI Tecnai spirit (T12) operating at 120 kV). The Pd particle size and spheres diameter were measured using Image J software by counting >100 particles from TEM images. The phase composition of the prepared samples was determined using, a Bruker D2 phaser PXRD equipped with a Lynxene detector using Cu-Kα ($\lambda = 1.54184$ Å) radiation at 30 kV with a scan range from $5\ ^\circ \leq 2\ \Theta \leq 90\ ^\circ$ in 0.026 steps. The thermal stability of the samples and catalyst loading were determined using a Perkin Elmer thermogravimetric analyzer (TGA 4000) in air in the temperature range of 35-900 °C (10 °C/min). A Micromeritics Tristar 3000 surface area and porosity analyzer was used to conduct N_2 adsorption-desorption experiments at -195 °C. Before analysis, the samples were degassed at 150 °C for 4 h under N_2 gas. The Raman spectra were recorded using a Bruker Senterra Raman spectrophotometer with a laser wavelength of 532 nm using Opus 7.1 software. The elemental composition of the samples was determined using X-ray photoelectron spectroscopy

(XPS) using a Thermo ESCAlab 250Xi equipped with a monochromatic Al Kα X-ray source operating at 1486.7 eV.

6.4 Catalytic tests

The selective hydrogenation of CALD was carried out under atmospheric pressure in a three-neck round bottom flask (100 mL) equipped with a condenser, magnetic stirrer, gas inlet, and sampling port. The three-neck round bottom flask was placed inside an oil bath with a thermocouple to maintain the desired temperature. The reaction mixture consisted of 100 mg catalyst, 1.32 g CALD, and 100 mL absolute ethanol. To remove traces of dissolved oxygen, N_2 gas was bubbled into the reaction mixture while the temperature was ramped to 60 °C (2 °C/min). Once the oil bath reached 60 °C, N_2 was switched with H_2 (50 mL/min) gas to allow for hydrogenation of CALD. The reaction was carried out for 6 h while taking samples of the reaction periodically for analysis.

Product analysis was carried out using an offline Varian 3700 GC with a flame ionization detector (FID) and a capillary column (Phenomenex Zebron, 30 m L. x 0.53 mm I.D. x 1.5 µ F.T.). The temperatures for column, detector and injector were set to 300, 250, and 200 °C respectively, with N_2 (5 mL/min) as the carrier gas.

6.5 Results and discussion

6.5.1 Characterization of the carbon supports

6.5.1.1 TEM analysis

SCSs were successfully synthesized using a modified Stöber method. Figure 6.1a shows the TEM image of the RF resin spheres made from resorcinol and formaldehyde polymerization with an average diameter of 820 ± 84 nm (Fig. 6.1b). Annealed SCSs were obtained by carbonization of RF resin spheres at 900 °C under an N_2 atmosphere for 4 h. The obtained annealed SCSs were treated with acid (fSCSs) and are shown in Fig. 6.1c. The TEM images show that the spheres are polydispersed with a diameter ranging between 250-700 nm (Fig. 6.1d). Shrinkage in the diameter of the fSCSs (average diameter = 535 ± 73 nm) compared to the diameter of the RF resin spheres was observed. The shrinkage of the spheres is expected and can be attributed to the loss of both the carbon periphery and the functional groups during carbonization of the RF resin spheres [19, 20]. The size of the synthesized spheres was comparable to the spheres reported by Dlamini (565 nm) [17].

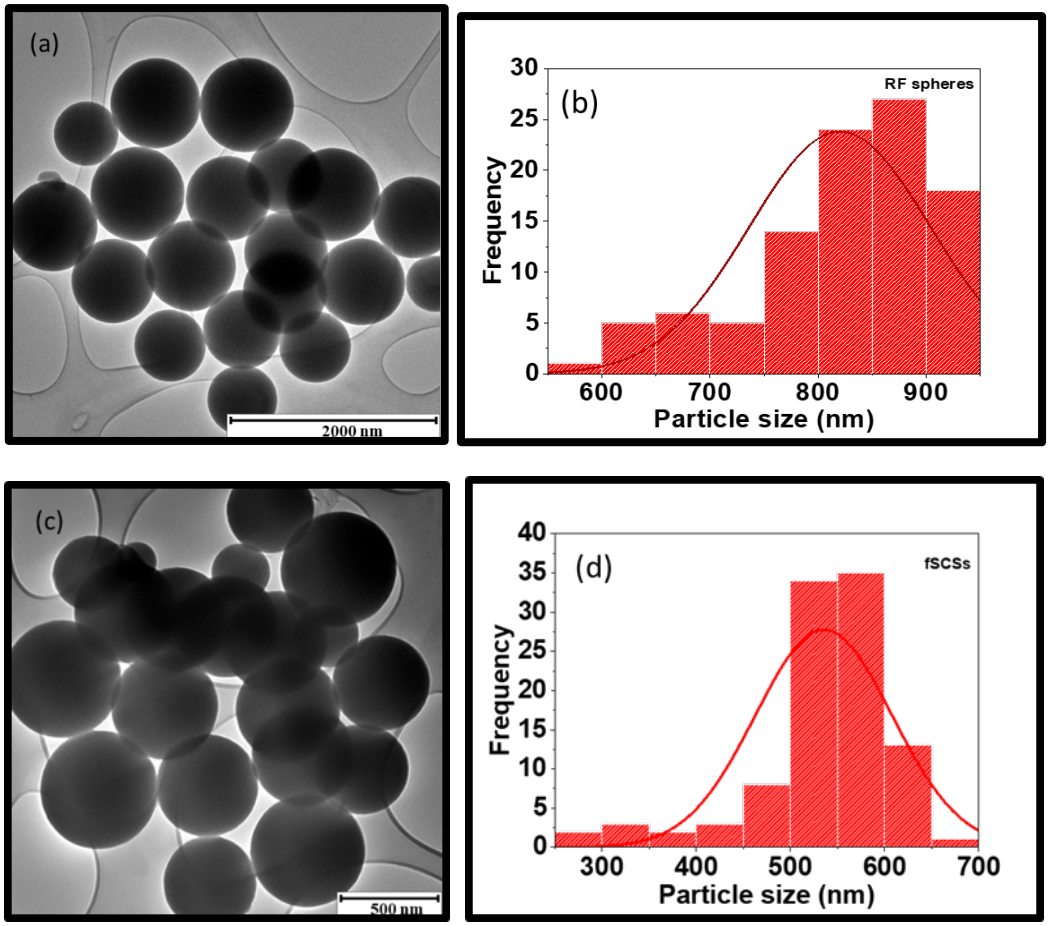

Figure 6.1: TEM images of (a) RF spheres, (c) fSCSs, and their corresponding particle size distributions (b and d).

6.5.1.2 Thermal gravimetric analysis

The thermal stability of the SCSs and fSCSs was studied using the TGA technique. The TGA and the corresponding derivative profiles of the SCSs and fSCSs are shown in Fig. 6.2a and b respectively. The acid-treated SCSs were less thermally stable than the parent SCSs. The first derivative peaks below *ca.* 100 °C can be attributed to the loss of moisture. The carbon atoms on the edges of the carbon spheres can react with oxygen upon exposure to air [21]. The derivative peak at *ca.* 241 °C in the DTG profile of the fSCSs can be attributed to the presence and thus thermal removal of the functional groups on the edges of the fSCSs. The calculated weight loss due to the functional groups was estimated to be 7 %. The onset decomposition of the SCSs was at *ca.* 420 °C whereas the fSCSs started to decompose at *ca.* 368 °C. The last derivative peaks at ~ 653 and 608 °C for SCSs and fSCSs respectively are associated with the decomposition of graphitic carbon in the core of the SCSs. The shift of the derivative peak of fSCSs to a slightly lower temperature (-45 °C) shows that acid treatment creates defects on the

structure of the SCSs resulting in less thermally stable carbon spheres. The TGA profiles show that no residues were left at 900 °C, which confirms that the samples do not have impurities.

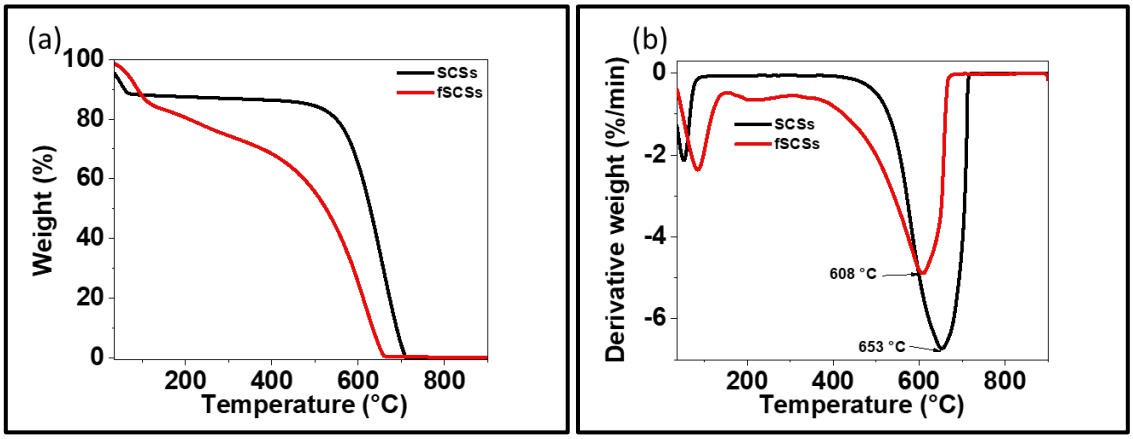

Figure 6.2: (a) TGA and (b) DTG profiles of SCSs and fSCSs.

6.5.1.3 PXRD and Raman analysis

The PXRD (Fig. 6.3a) profiles of both SCSs and fSCSs show a broad peak at 24.0 ° and another peak at 44 °. The two peaks were indexed as the (002) and (100) reflections of carbon [22]. The Raman spectra (Fig 6.3b) of the SCSs and fSCSs show two Raman peaks at (1345 and 1358 cm^{-1}) and (1594 and 1598 cm^{-1}) respectively which corresponds to the D and the G bands. The D band is associated with the breathing mode of the sp^2 and sp^3 carbon atoms and the defects in the carbon structure [23, 24]. The G band is associated with bond stretching of the sp^2 carbon atoms [23, 24]. The intensity ratio of the D and G bands was used to estimate the degree of graphitization in the carbon structure and was estimated to be 1.02 and 0.96 for the SCSs and fSCSs respectively. Acid treatment of SCSs created more defects in the carbon structure and as a result, a decrease in the I_D/I_G ratio is observed.

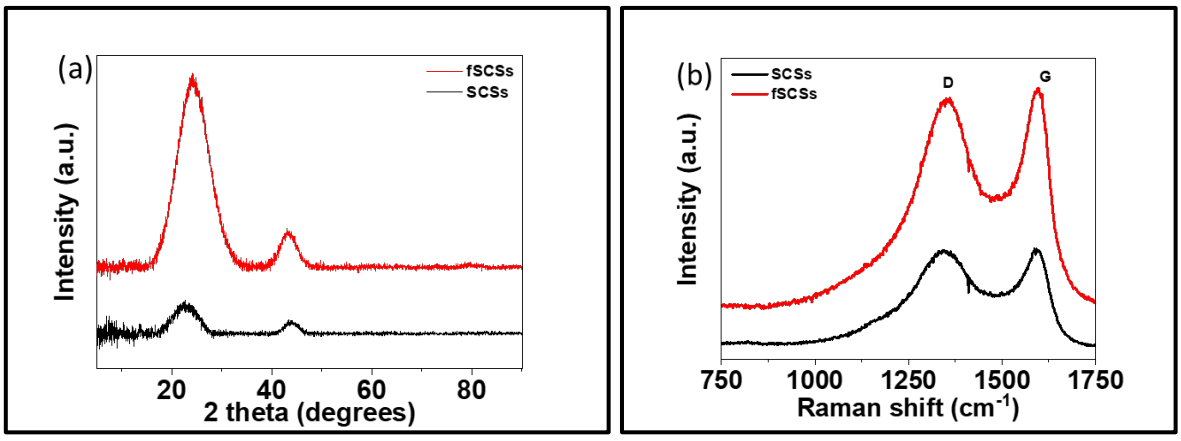

Figure 6.3: (a) PXRD profiles and (b) Raman spectra of SCSs and fSCSs.

6.5.1.4 BET surface area analysis

The surface area and the porosity of the carbon spheres were analyzed using nitrogen physisorption. Figure 6.4 shows the isotherms of the SCSs (a) and fSCSs (b). The results obtained show that acid treatment of the SCSs did not alter the physisorption properties of the carbon spheres as both samples have similar isotherms. The surface properties of the carbon spheres are shown in Table 1. The BET surface area of the SCSs and fSCSs were found to be 557 and 531 m^2/g respectively. The pore size of the carbon spheres remained the same (0.23 nm). The isotherms can be classed as a mixture of type I and IV [17, 25]. The data thus indicate that no major structural changes occurred on the SCSs surface after acid treatment.

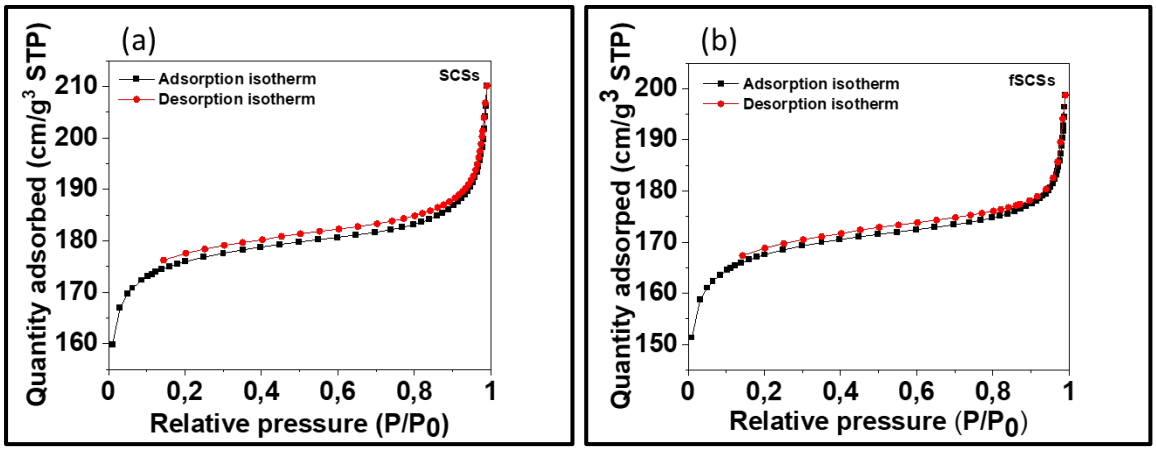

Figure 6.4: N_2 adsorption-desorption isotherms of the (a) SCSs and (b) fSCSs.

6.5.1.5 XPS and FTIR analysis

The surface and elemental composition of the fSCSs were analyzed using the XPS technique. The XPS spectra (Fig. 6.5a) shows that the fSCSs are composed of carbon, oxygen, and nitrogen with binding energy of 284.5, 532.2, and 400.1 eV respectively. The atomic % of C1s, O1s, and N1s were determined to be 80.2, 16.8, and 3.0 respectively. The presence of nitrogen can be attributed to the acid treatment of the parent SCSs. Also, Zhao *et al.* proposed that when ammonia solution is used as a catalyst in the RF polymerization it can also act as a nitrogen source [26]. The authors proposed that the N groups were incorporated into the polymer during the RF polymerization. The deconvolution of the C1s XPS spectrum (Fig. 6.5b) of the fSCSs, shows 5 types of carbon species with peaks in the spectrum that correspond to C-C sp^2 (284.2 eV), C-C sp^3 (284.6 eV), C-O (285.8 eV), C=O (288.0 eV), O-C=O (289.2 eV) indicating successful functionalization of the SCSs. The deconvoluted O1s spectra shows two peaks corresponding to C=O (532.7 eV) and C-O (531.3 eV) functional groups.

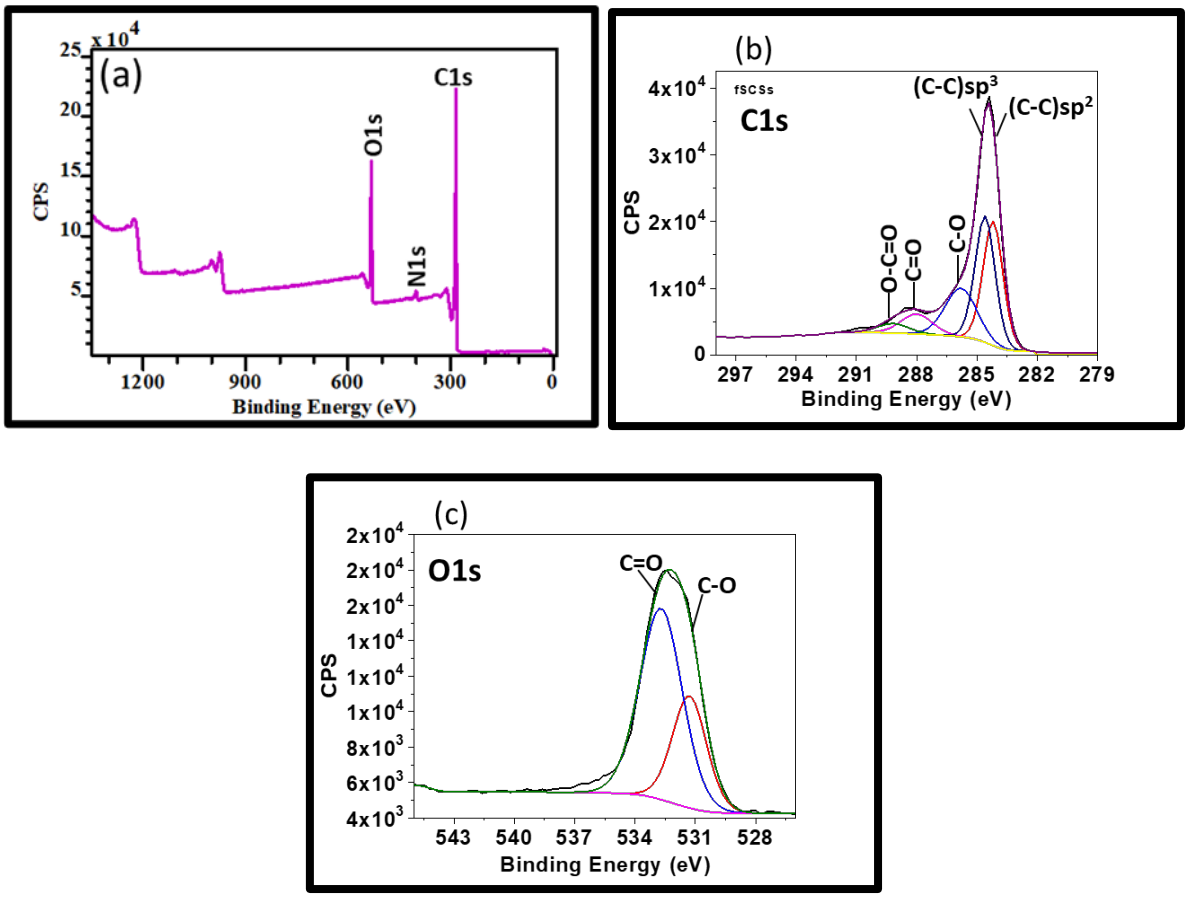

Figure 6.5: (a) XPS spectra, (b) C1s spectra, and (c) O1s spectra of the fSCSs.

In alignment with the XPS data, FTIR spectroscopy was used to confirm the presence of surface functional groups on the carbon supports. The FTIR spectra (Fig. 6.6) of the CSs, show that the oxygen-containing functional groups become visible after oxidation with acid. For the SCSs (Fig.6.6a), the band at 1058 cm^{-1} can be assigned to the stretching mode of the C-O group [27]. The acid-treated SCSs (Fig. 6.6b) show prominent bands at *ca.* 1717 and 1601 cm^{-1} corresponding to the stretching vibrations of C=O from carboxylic functional groups and the C=C stretching mode of aromatic rings [27-30]. The band at 1217 cm^{-1} can be assigned to the stretching mode of the C-O from alcohols or ether functional groups. The band at 3420 cm^{-1} can be assigned to the O-H group from residual water adsorbed on the surface of the CSs or carboxyl groups [30].

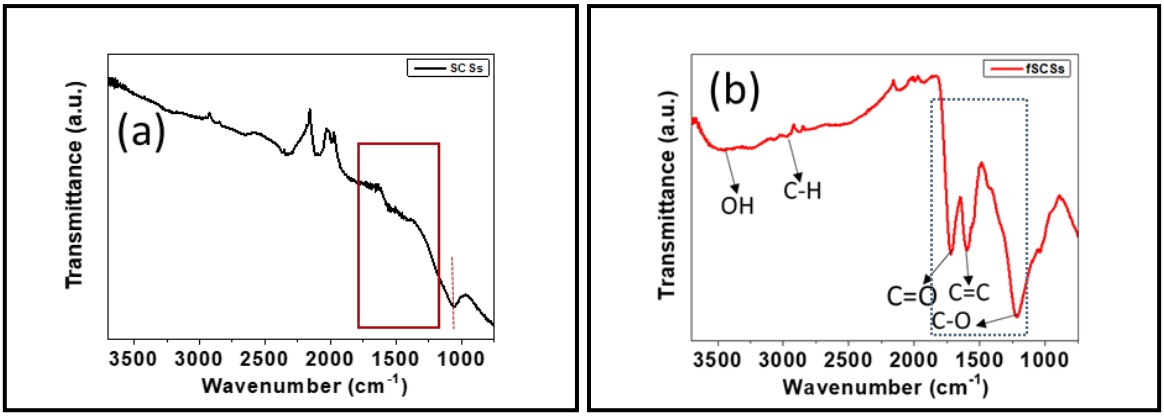

Figure 6.6: FTIR of the (a) pristine SCSs amd (b) functionalized SCSs.

6.5.2 Characterization of Pd/SCSs and Pd/fSCSs

6.5.2.1 TEM analysis

Figure 6.7 shows the TEM images of the Pd/SCSs and Pd/fSCSs and their corresponding Pd particle size distribution. The TEM images (Fig 6.7a, c) show that the Pd particles are dispersed on the surface of the carbon spheres, and agglomeration of some of the Pd particles (circled in yellow) was observed on both supports. The average particle size of the Pd particles supported on SCSs and fSCSs was determined to be 6.0 ± 2.3 and 12.0 ± 3.4 nm respectively (see Fig 6.7b, d). The Pd particles supported on the SCSs have a narrow particle size range distribution (2-13 nm) as opposed to the Pd on the fSCSs support (5-23 nm). This variation can be ascribed to the difference in the oxygen content of the supports that will be discussed later (section 6.5.2.5). In the literature, the low oxygen content on a carbon support has been reported to favour the formation of well dispersed Pd NPs (particle size < 3 nm) when using a Pd chloride precursor [31]. This is because of the weak adsorption capacity of the Pd chloride precursor on the surface carbon support with low oxygen [31, 32].

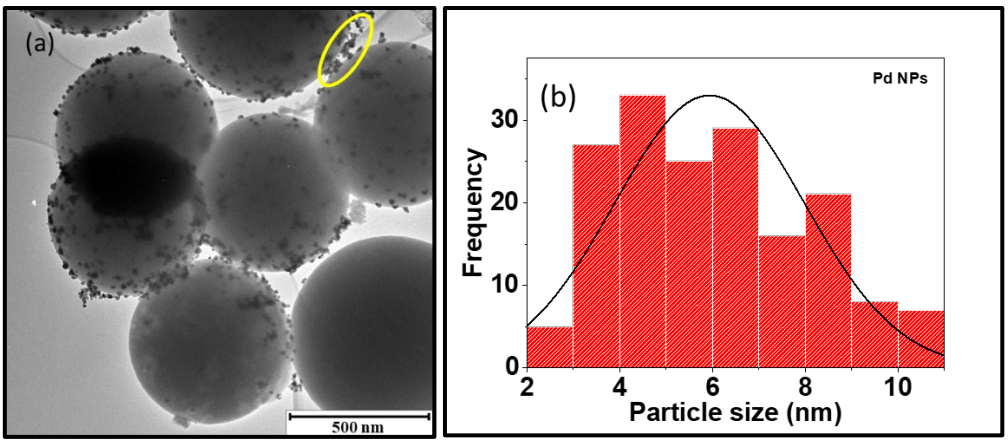

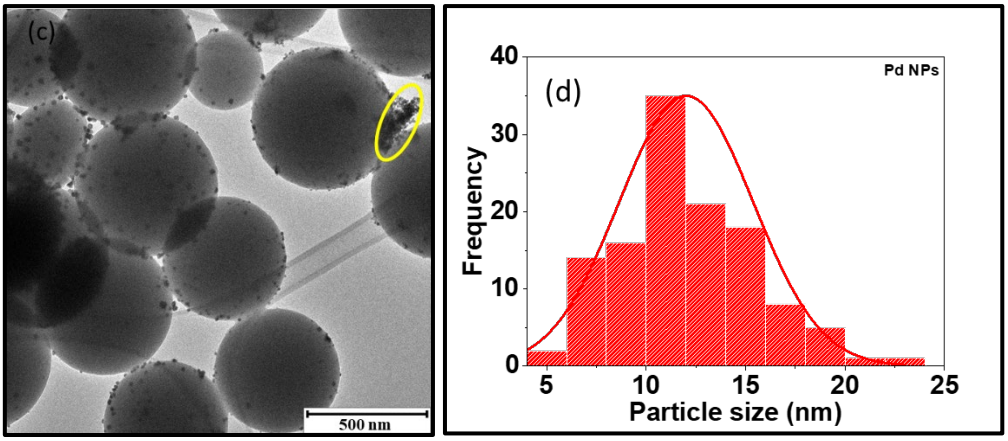

Figure 6.7: TEM images images of (a) Pd/SCSs, and (c) Pd/fSCSs, and (b,d) particle size distribution of Pd NPs.

6.5.2.2 Thermal gravimetric analysis

The percentage loading of Pd on the carbon supports was determined using the TGA technique. The TGA and DTG profiles of Pd/SCSs and Pd/fSCSs are shown in Fig. 6.8 a and b respectively. The metal residues (as PdOx) left after the decomposition of the carbon supports in an oxidative environment (air) were estimated to be 4.2 and 4.3 % for the Pd/SCSs and Pd/fSCSs catalysts to give Pd loadings of 3.6 % (Pd/SCSs) and 3.7 % (Pd/fSCSs). The Pd NPs on the carbon supports catalyzed the oxidation of the carbon as shown by a decrease in the decomposition temperature of the carbon [17]. For the Pd/SCSs catalyst the carbon decomposition temperature decreased from *ca.* 653 to 512 °C while for the Pd/fSCSs catalyst it decreased from *ca.* 608 to 469 °C (see Fig 6.2a,b). It can be noted that for the Pd/fSCSs DTG profile, there are additional peaks at c*a.* 226 and 340 °C which can be attributed to the loss of functional groups (10.6 wt. %) and carbon-containing functional groups (4.5 wt. %) respectively.

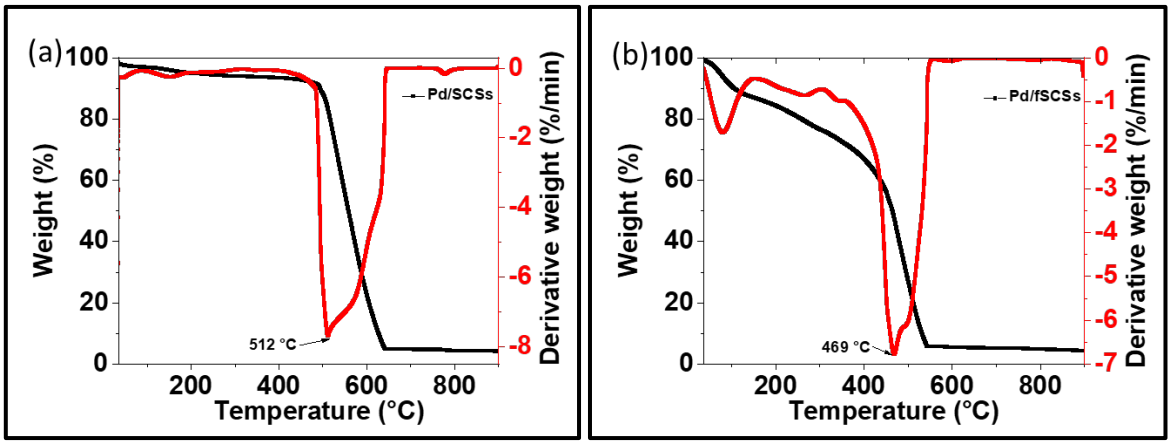

Figure 6.8: TGA and DTG profiles of (a) Pd/SCSs and (b) Pd/fSCSs.

6.5.2.3 PXRD analysis

To confirm that the reduced Pd NPs were in the metallic phase, the two catalysts were analyzed using PXRD (Fig. 6.9). The PXRD pattern of the Pd/SCSs and Pd/fSCS showed five peaks at 2Θ values of 40.5 °, 46.9 °, 68.5 °, 82.3 °, and 86.9 ° which corresponds to Pd nanoparticle crystal planes: (111), (200), (220), (311), and (222) [PDF 00-001-1201]. The Pd crystallite size was estimated using the Scherrer equation. The most intense peak of the diffraction pattern corresponding to the (111) plane was used to calculate the crystallite size and the values obtained are 6.7 and 8.9 nm for Pd/SCSs and Pd/fSCSs respectively. The PXRD data are in agreement with the TEM data and the actual (different) values for the two techniques are due to the method by which the particle sizes are measured (Table 6.1).

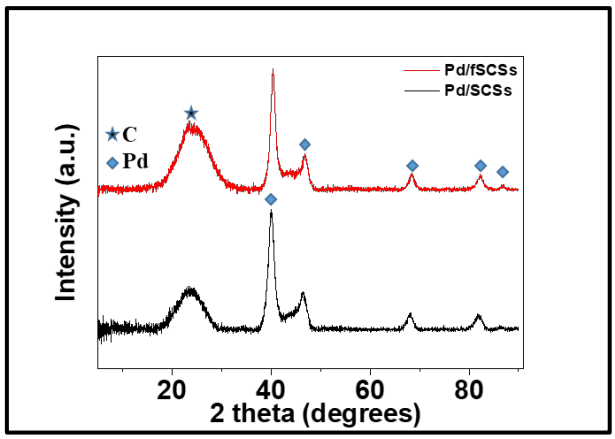

Figure 6.9: PXRD profiles of the Pd/SCSs and Pd/fSCSs.

6.5.2.4 BET analysis

Table 6.1 summarizes the surface analysis of the carbon supports and the catalysts, along with the percentage loadings of Pd and average particle/crystallite size of Pd. The BET surface area of the Pd/SCSs catalyst decreased. This could be due to the blockage of the pores of the SCSs [2].

Table 6.1: Properties of the carbon supports and the catalyst supported on the carbon spheres.

Sample	TEM Pd particle size (nm)	XRD Pd crystallite size (nm)	% Pd TGA	BET surface area (m^2/g)	Pore size (nm)	Pore volume (cm^3/g)
SCSs	-	-	-	557	2.3	0.32
Pd/SCSs	6.0 ± 2.3	6.7	3.6	390	2.4	0.23
fSCSs	-	-	-	531	2.3	0.30
Pd/fSCSs	12.0 ± 3.4	8.9	3.7	573	2.4	0.35

6.5.2.5 XPS analysis

Figure 6.10 (a and b) shows the XPS spectra of the Pd/SCSs and Pd/fSCSs catalysts. The XPS spectra of the catalysts, when compared to the carbons before Pd loading (Fig. 6.5a), show two additional peaks; for Pd 3d (335.3 and 335.5 eV) and Cl 2p (198.1 and 198.3 eV) for the Pd/SCSs and Pd/fSCSs respectively. The traces of the Cl 2p peak detected (0.2 atomic %) is residue from the metal salt used. The Pd 3d XPS spectra showed two main peaks corresponding to $3d_{3/2}$ and $3d_{5/2}$ (Fig. 6.10c and d). From the deconvolution of the Pd $3d_{5/2}$ peak, it can be noted that the Pd species exists as, Pd (335.2 and 335.0 eV), PdO (336.4 and 336,3 eV), and PdO_2 (337.8 and 337.7 eV) for the Pd/SCSs and Pd/fSCSs. The Pd in the oxide form is due to exposure of the Pd surface to air [14, 33]. The deconvolution of O1s spectra shows the presence of the Pd-O viz. O1s (C-O; Pd oxide) and O1s ((C=O) Pd 3p3) with the binding energy of (531.7 and 531.2 eV) and (532.7 and 532.8 eV) for Pd/SCSs and Pd/fSCSs catalysts respectively. The XPS data of both the catalysts shows that the electronic properties of Pd remained relatively the same regardless of the support used.

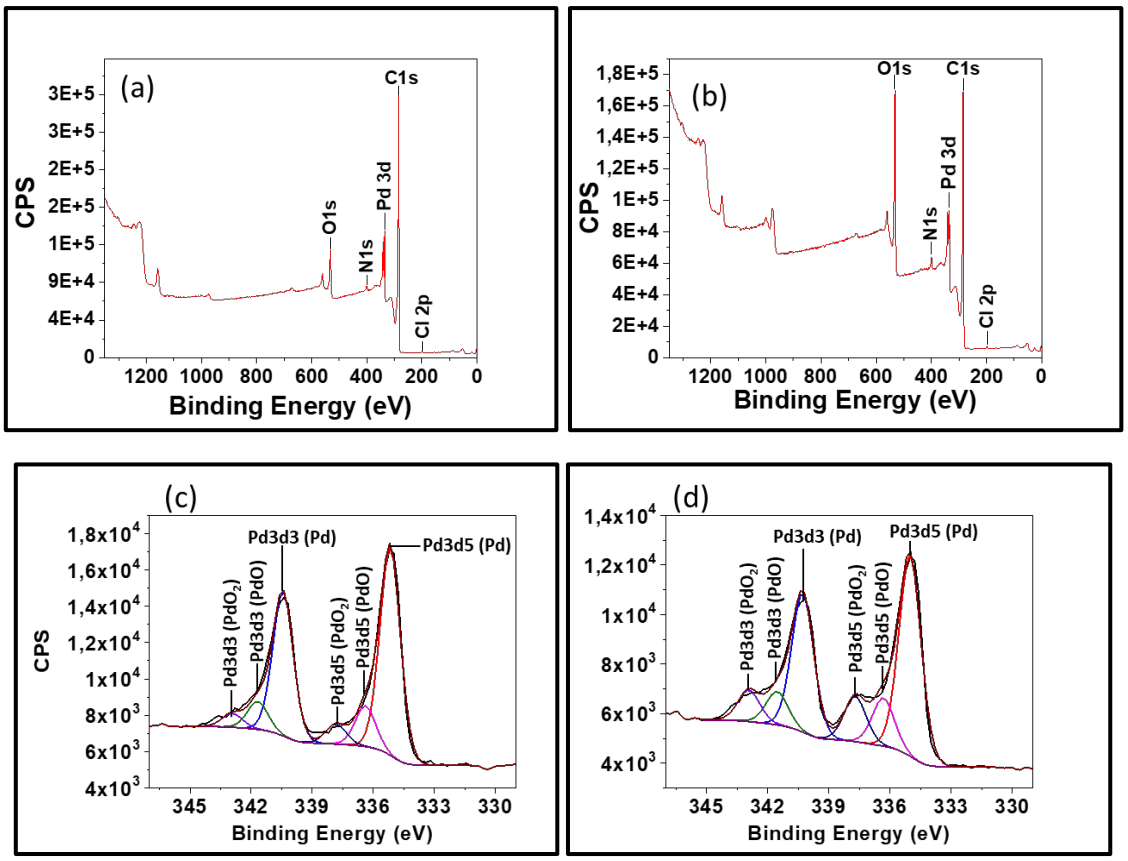

Figure 6.10: (a and b) XPS spectra and (c and d) Pd $3d_{5/2}$ spectra of Pd/SCSs and Pd/fSCSs catalysts respectively.

Table 6.2 summarizes the elemental quantification of Pd/SCSs and Pd/fSCSs from XPS analysis. From the data obtained it can be noted that C1s atomic % decreased from 87.6 to 72.4 as a result of the replacement of C by O. The atomic % of the O1s increased from 8.7 to 22.6 as an indication of successful functionalization of the carbon spheres. An increase in the atomic % of O1s could explain the observed increase in the Pd particle size from 6.0 to 12.0 nm (Fig. 6.6) due to different interaction of the CSs with H_2PdCl_4 [31, 32]. Both the carbon supports showed the presence of N1s. The increase in the N1s atomic % in the Pd/fSCSs catalyst can be attributed to acid (HNO_3) treatment of the carbon spheres [18].

Table 6.2: Elemental quantification of Pd/CSs catalysts using XPS analysis.

Catalyst	**Elemental composition (atomic %)**				
	C1s	O1s	N1s	Pd 3d	Cl 2p
Pd/SCSs	87.6	8.7	1.2	2.3	0.2
Pd/fSCSs	72.4	22.6	2.6	2.2	0.2

Table 6.3 summarizes the relative % content of the Pd (0) and Pd oxide species present in both catalysts. The content of Pd^0 species was estimated to be 76 and 68 % for Pd/SCSs and Pd/fSCSs catalysts respectively. From the data obtained it can be noted that the surface of the Pd/fSCSs catalyst is more prone to surface oxidation due to the presence of more oxygenated functional groups on the support. This is also supported by slightly higher Pd^{2+}/Pd^0 content of the Pd/fSCSs (0.24) compared to that of Pd/SCSs (0.18) which shows that the catalyst surface has more Pd^{2+}/Pd^0 species. A similar trend was also observed from the study reported by Xu *et al.* in which they reported the content of Pd^0 species of 73.1 and 61.6 % for Pd supported on GF and OGF respectively [14]. The BE of Pd^0 in both the catalysts is slightly different (± 0.2 eV), this may infer that the degree of metal-support interaction might be different [31].

Table 6.3: Binding energy and % of Pd, PdO, and PdO_2 content of the Pd/CSs catalysts from XPS.

Catalyst	BE (eV) Pd $3d_{5/2}$	Pd %	PdO %	PdO_2 %	Pd^{2+}/Pd^0
Pd/SCSs	335.2	76	14	10	0.18
Pd/fSCSs	335.0	68	16	16	0.24

6.5.3 Hydrogenation of CALD

The selective hydrogenation of CALD was carried out in a liquid phase reaction over the Pd/fSCSs and Pd/SCSs catalysts. The CALD reaction was studied using different reaction conditions including temperature, H_2 gas flow rate, stirring rate, catalyst mass, and concentration. A comparison between the catalytic activity of the Pd/fSCSs and Pd/SCSs catalysts was made. A blank test (hydrogenation in the presence of fSCSs or SCSs) was carried out in the absence of Pd and no catalytic activity was observed.

6.5.4 Optimization of conditions

6.5.4.1 Catalyst selectivity

Hydrogenation of CALD was carried out using Pd/SCSs and Pd/fSCSs under an initial set of reaction conditions (6 h, 100 mg catalyst, 50 mL/min = H_2 flow rate, 100 mL ethanol, T = 60 °C, and 1.32 g CALD) established from some preliminary studies and literature reports [34]. The results for the Pd/fSCSs catalyst are shown in sections 6.5.4.2 to 6.5.4.7. Under these conditions, the Pd/SCSs gave 100 % conversion to 3P1P i.e. total hydrogenation of both C=C and C=O bonds (Fig. 6.11; Table 6.4). In comparison, the Pd/fSCSs catalyst gave

predominantly CA i.e. only a reduction of the C=O bond. The difference in the selectivity of the two catalysts could be attributed to the difference in the particle size of Pd and/or the different oxygen content on the two supports as indicated by TEM and XPS studies (see above).

The poor selectivity of the Pd/SCSs catalyst can be attributed to the particle size and the presence of the Pd (111) plane [13, 35]. In the literature, it has been reported that if the Pd particle size is small both the CALD C=C and C=O bonds become readily accessible to the metal surface and can both be hydrogenated. A similar effect has been proposed for the adsorption of CALD on a Pd (111) plane.

Table 6.4: CALD conversion and selectivity of Pd/fSCSs and Pd/SCSs.

Sample	CALD conversion %	Selectivity (%)			
		CA	3P1P	HCALD	Other
Pd/fSCSs	98.7	92.33	3.33	0	4.34
Pd/SCSs	100	0	100	0	0

Reference conditions: 4 h, 100 mg catalyst, 50 mL/min = H_2 flow rate, 100 ml ethanol, T = 60 °C, and 1.32 g CALD.

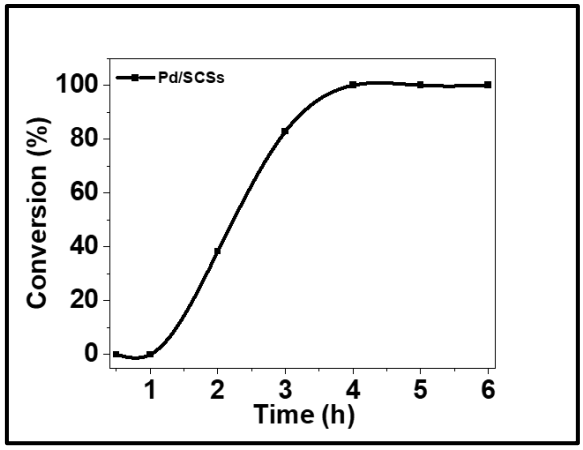

Figure 6.11: Conversion of CALD over Pd/SCSs. Reference conditions: 6 h, 100 mg catalyst, 50 mL/min = H_2 flow rate, 100 ml ethanol, T = 60 °C, and 1.32 g CALD.

6.5.4.2 Reaction temperature

Figure 6.12a shows the influence of the reaction temperature on the activity and selectivity of the Pd/fSCSs catalyst on the hydrogenation of CALD. It can be noted that CALD conversion

decreased with an increase in temperature. It is also noted that at 80 °C, the hydrogenation rate decreased with time. This observation can be ascribed to the high reaction temperature because CALD can be over-hydrogenated easily to produce by-products [1]. These by-products could result in surface poisoning of the catalyst resulting in the decrease of the catalyst activity [1]. The by-products formed can include acetals formed due to aldol condensation of CALD/HCALD with ethanol and formation β-methyl styrene due to a side reaction with CA which can be further reduced to propyl benzene [6]. This could result in surface poisoning of the catalyst resulting in the observed decrease of the catalyst activity [1]. At 40 °C, conversion of 100 % was obtained after four hours whereas at 60 °C the CALD conversion only reached 99 % after six hours. In terms of the catalyst selectivity, the catalyst was more selective to C=O bond hydrogenation, forming CA (Fig. 6.12b). All the three products (CA, HCALD, and 3P1P) were detected and it was observed that 60 °C was the optimum temperature in terms of both activity and selectivity (i.e. hydrogenation of the C=O bond).

The catalyst was less selective to C=C bond hydrogenation, which is unexpected for a Pd catalyst. By-products were also detected at all three reactions temperature studied but the reaction at 60 °C gave the least amount of by-products. The calculated catalyst activities (0.61, 1.59, and 1.30 mol/g_{Pd}.h) increased from 40 to 60 °C but slightly decreased at 80 °C, within an hour. The selectivity data (Fig 6.12b) shows that over hydrogenation to 3-P1P and 'other' products has occurred suggesting that the products poison the catalyst. Also, we noted that the reaction rates within ½ h are fast (at 60 and 80 ° C) and then decreased with reaction time. Figure 6.12c shows the Arrhenius plot for the hydrogenation of CALD catalyzed using the Pd/fSCSs catalyst. The Arrhenius plot was used to determine the activation energy of the catalyst that was calculated to be 56 kJ/mol. This value is comparable to the value (70 kJ/mol) reported by Cabiac *et al.* for the hydrogenation of CALD using 4 wt. % Pd/AC catalysts using cyclohexane as a solvent [36].

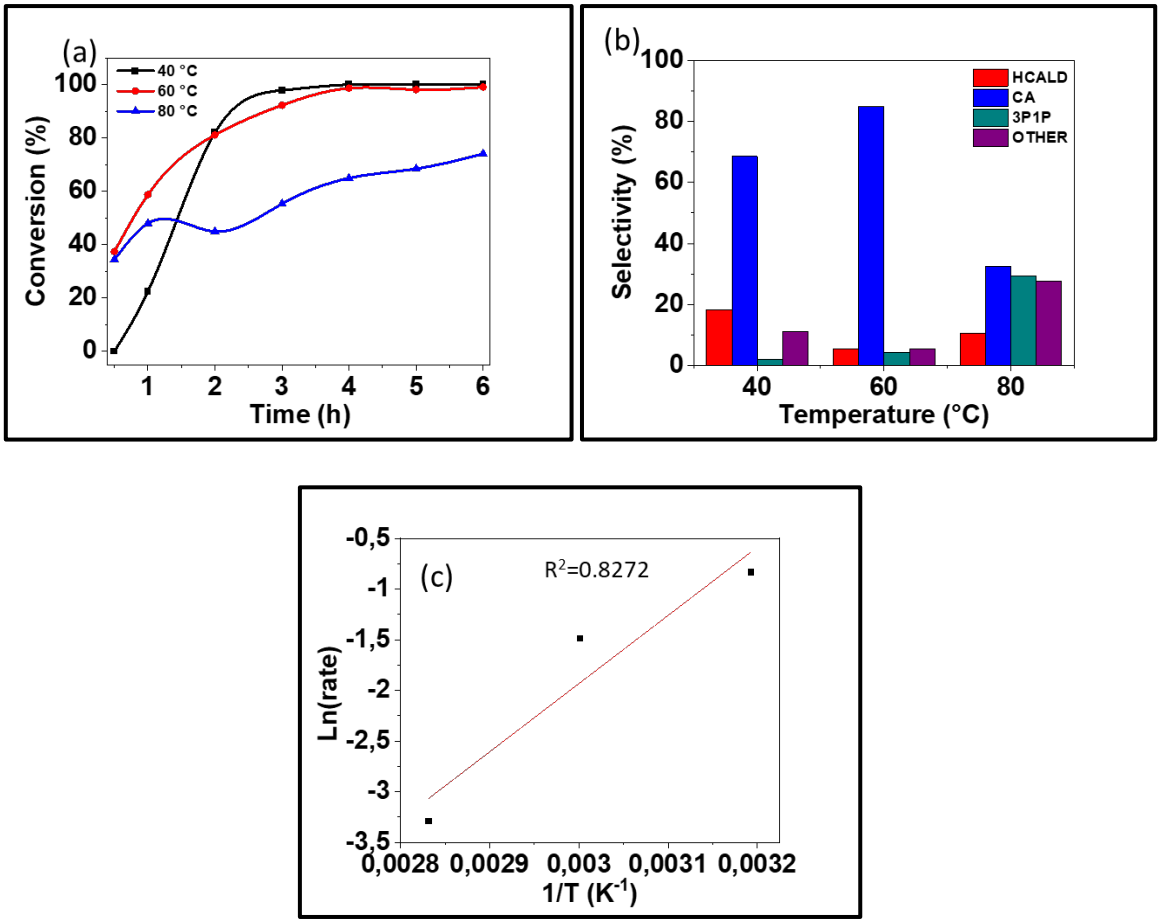

Figure 6.12: The influence of temperature on the (a) CALD conversion and (b) selectivity and (c) Arrhenius plot for CALD hydrogenation over the Pd/fSCSs.

6.5.4.3 Catalyst mass

The influence of the Pd/fSCSs catalyst amount on the conversion of CALD was studied while keeping the temperature (60 °C) and H_2 flow rate (50 mL/min) constant. Figure 6.13a shows the conversion of CALD over varying amounts of catalyst. From the data obtained it can be noted that when using 50 mg catalyst the lowest CALD conversion of 65.8 % was obtained after 6 hours. The use of larger amounts of catalyst resulted in similar activities. This again can be explained in terms of the effect of over hydrogenated products on the catalyst (see Fig 6.13b). The data reveal that CA was formed as a major product when 50 and 100 mg of the catalyst were used.

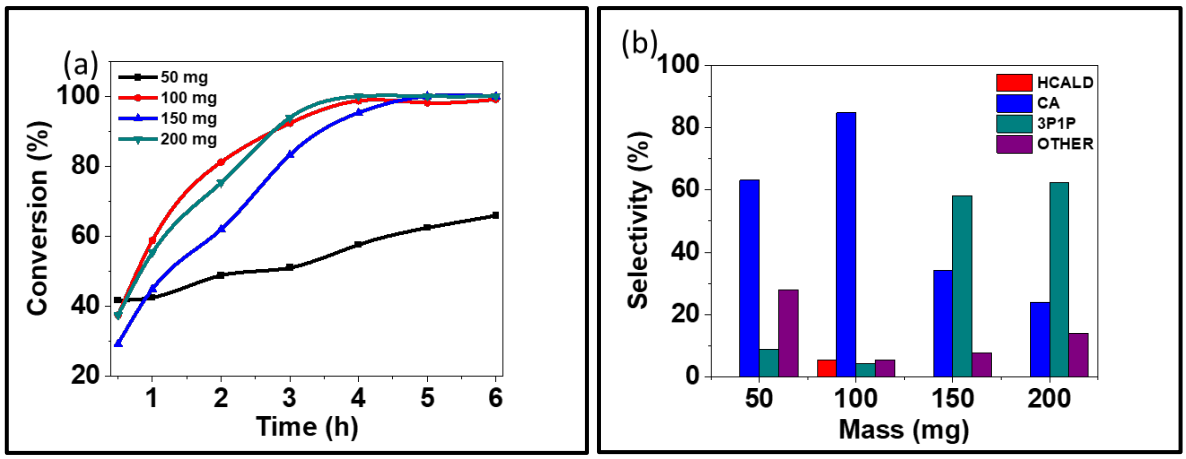

Figure 6.13: The influence of the catalyst mass on the (a) CALD conversion and (b) selectivity.

6.5.4.4 H_2 gas flow rate

The catalytic activity of the Pd/fSCSs catalyst at different hydrogen flow rates is shown in figure 6.14a. From the data presented, it can be seen that increasing the H_2 flow rate resulted in a moderate decrease in the conversion rate of the CALD. The results show that at a higher H_2 flow rate (higher H_2 concentration) there must be an increase in the adsorption of H_2 leading to (i) decreased adsorption of CALD and (ii) an increased possibility of over reduction. Both effects would lead to a decrease in activity [14]. In particular, increasing the H_2 flow rate from 75 to 100 mL/min led to an increase in the hydrogenation of both C=C and C=O bonds to form 3P1P. The selectivity to CA decreased from 85 to 45% and the formation of by-products increased with an increase in the H_2 flow rate.

The influence of O_2 on the CALD reaction was investigated, by not removing the dissolved oxygen before the CALD hydrogenation reaction was commenced. This was achieved by not flowing N_2 gas through the solution before the reaction (figure 6.14b). Indeed, the traces of dissolved oxygen did have an impact (small) on the hydrogenation of CALD. It is to be noted that the rate of CALD hydrogenation was reduced as observed by the decrease in the CALD conversion between 0.5 to 4 h. The reaction did go to completion (more slowly) indicating that any PdOx species were reduced in the reaction.

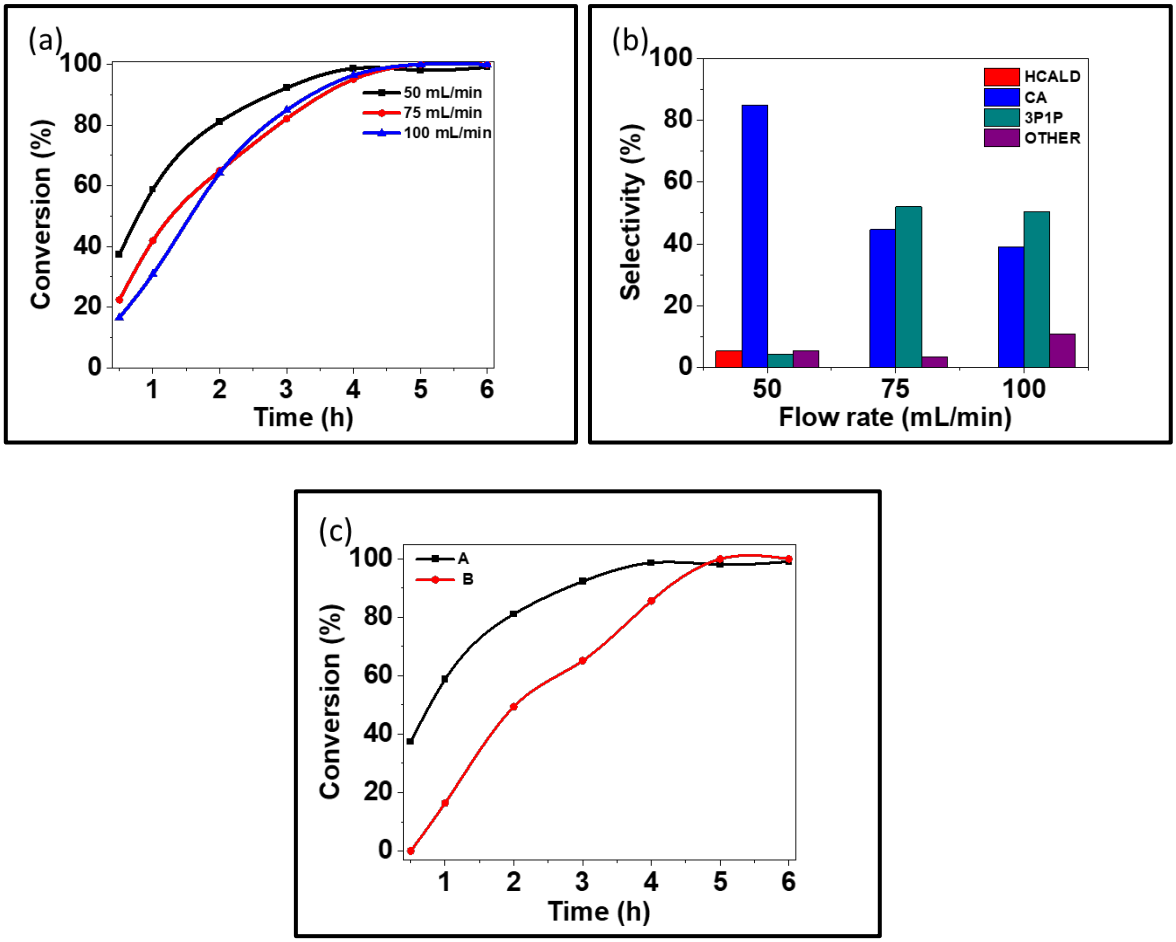

Figure 6.14: (a) The effect of H_2 flow rate on the (a) activity and (b) selectivity of the Pd/fSCSs catalyst, and (c) the effect of the removal of dissolved traces of oxygen (A; removal; (B) ; no removal) on the CALD conversion on the Pd/fSCSs catalyst.

6.5.4.5 CALD concentration

The effect of CALD concentration on the conversion (and selectivity) of the CALD reaction was carried out at 60 °C while keeping the catalyst mass (100 mg) and hydrogen flow rate (50 mL/min) the same (Fig. 6.15). Increasing the CALD concentration from 0.05 M (0.66 g) to 0.1 M (1.32 g) resulted in a slight decrease in the reaction rate. This was unexpected. However, the selectivity data revealed the problem – the ability of the Pd to interact with both the CALD and H_2. At the lower CALD concentration, the reaction is rapid but secondary reactions occurred to give 3P1P i.e. over hydrogenation of CALD. At even higher concentrations this effect became even more pronounced as the 'other' products that formed, poisoned the catalyst.

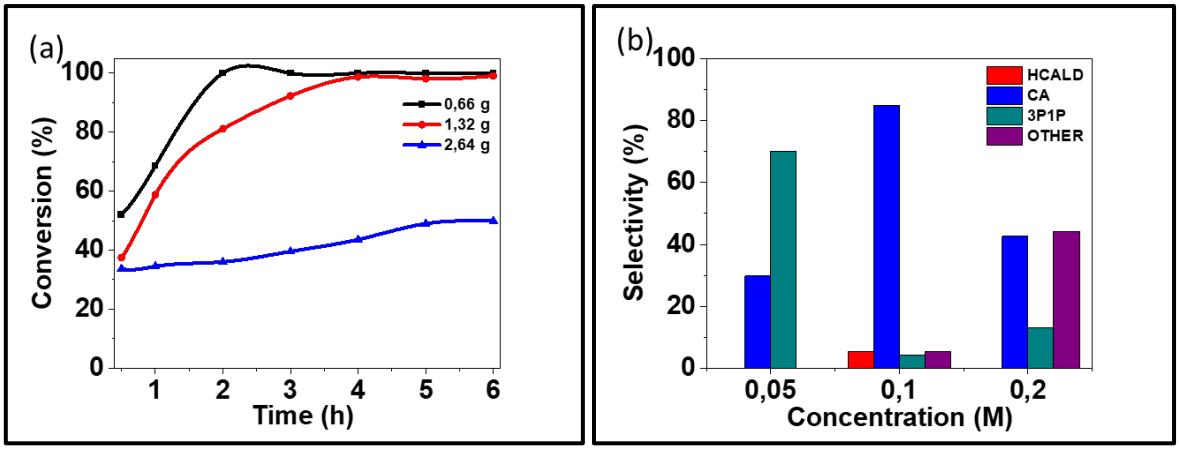

Figure 6.15: Effect of CALD concentration on the (a) conversion and (b) selectivity on the hydrogenation of CALD over the Pd/fSCSs catalyst.

6.5.4.6 Stirring rate

The hydrogenation of CALD was carried out at 60 °C with different stirring speeds (300, 600, and 900 rmp) and the results are shown in Figure 6.16a and b. It was observed that the CALD conversion occurred more rapidly with a stirring speed of 600 rmp. Even within half an hour, CALD conversions of 24, 37, and 13 % were obtained for stirring speeds of 300, 600, and 900 rmp respectively. The data parallel what was shown by the other variables. When the H_2 concentration was too low, a secondary reaction occurred and the selectivity to CA was poor. At higher H_2 concentrations the reaction is both faster and less over-reaction occurs. The optimum stirring speed of the three was thus 600 rmp.

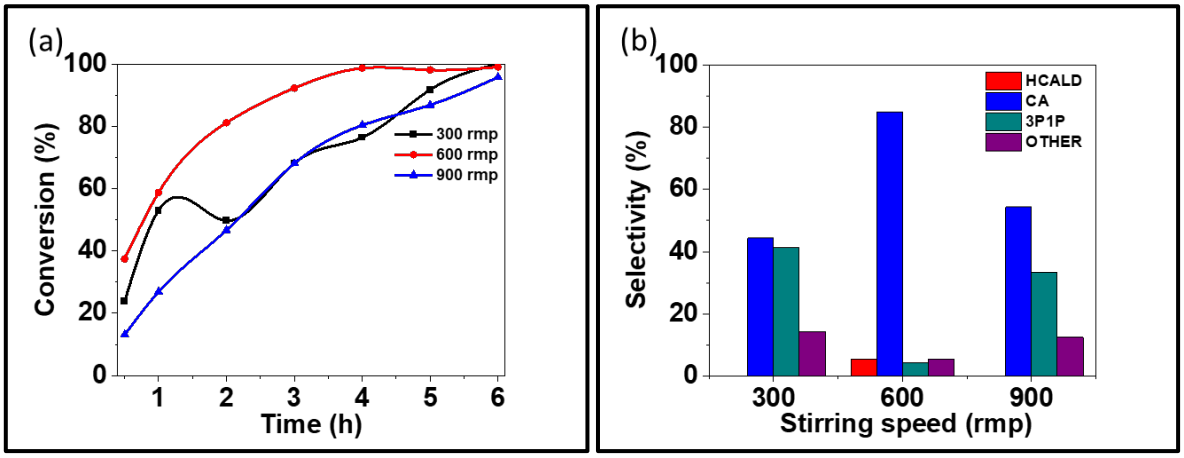

Figure 6.16: Influence of the stirring speed on (a) CALD conversion and (b) selectivity over 5 wt. % Pd/fSCSs catalyst.

6.5.4.7 Catalyst stability test

The stability of the Pd/fSCSs and Pd/SCSs catalysts were tested over five cycles. The catalyst performance and selectivity are shown in Fig. 6.17 a and b. The Pd/fSCSs catalyst maintained 100 % CALD conversion after 6 h until cycle 3. The CALD conversion then decreased substantially during cycles 4 and 5 respectively. The Pd/SCSs catalyst maintained 100 % CALD conversion throughout four runs. From cycles 4 and 5 the reaction rate started to slow down as shown by a decrease in the CALD conversion from 2 to 5 h; from the 5th cycle a maximum CALD conversion of 98 % was obtained.

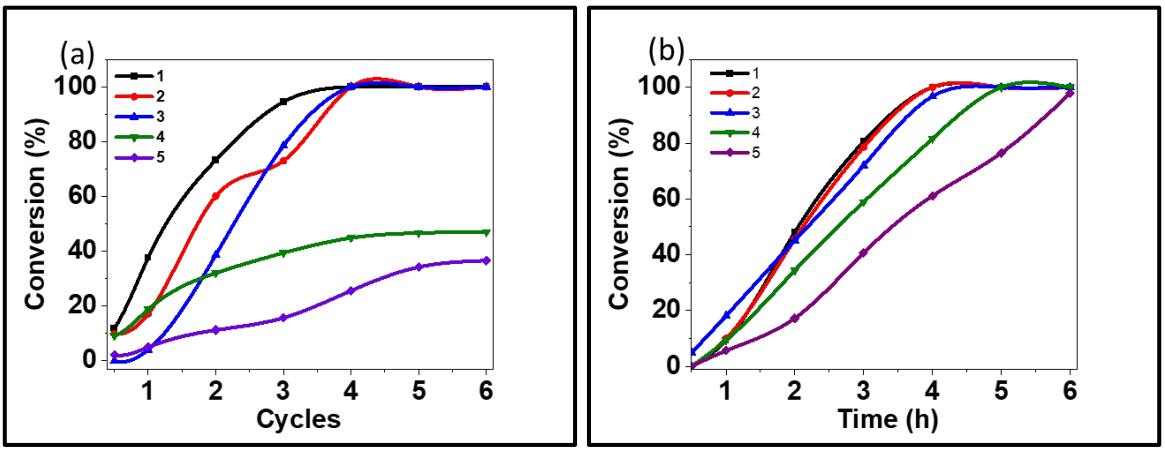

Figure 6.17: Recycling of (a) Pd/fSCSs and (b) Pd/SCSs over five cycles at 60 °C and 50 mL/min H_2 flow rate.

6.5.8 Summary on the catalyst activity and selectivity

The Pd/fSCSs catalyst was used in the selective hydrogenation of CALD. The product distribution of the catalyst varied depending on the reaction conditions used. The results obtained were unexpected as Pd metal is known to favour the reduction of the C=C bond of CALD resulting in the formation of HCALD [2, 14]. In this study, the C=O bond was reduced and CA was formed as a major product. When the reaction temperature was increased (from 60 °C to 80 °C) the CALD conversion decreased from 100 to 74 %. The formation of by-products could lead to the surface coverage of the active metal and, as a result, catalyst deactivation can occur [1, 7]. CALD over-hydrogenation (i.e. reduction of both C=C and C=O bonds) occurred when the catalyst mass was increased (150 and 200 mg) and as a result the selectivity to CA decreased from 85 to 24 %. A similar trend was observed when the hydrogen flow rate was increased (75 and 100 mL/min) and when a low concentration of CALD (0.05 M) was used.

The selectivity of the Pd/fSCSs catalyst to CA was unexpected. However, the Pd particle size and presence of polar oxygen atoms on the surface of the carbon support can be used as an explanation for this observation [1, 21]. Zeng *et al.* tuned the selectivity of Pt/AC catalyst towards CA by varying the content of oxygen-containing functional groups on the surface of the AC through pre-treatment using KOH [1]. Vatti *et al.* studied the effect of intrinsic surface electropositive sites on supported Pd catalysts in the selective hydrogenation of CALD [37]. Among the catalysts tested the selectivity toward CA decreased in the following order 1% Pd/P25-TiO_2 > Pd/SiO_2 > Pd/ γ-Al_2O_3. The increase in the selectivity to CA was correlated to an increase in the Pd^{2+}/Pd^0 ratio. It was reported that the Pd^{2+} ions might act as Lewis sites which could act as preferential adsorption sites for the C=O bond.

6.6 Conclusions

In summary, SCSs were successfully synthesized through carbonization of RF resin spheres at 900 °C. Pd particles were successfully loaded on SCSs and fSCSs. Bigger Pd particles were obtained using the functionalized SCSs. FTIR and XPS data showed that oxidation of the SCSs resulted in additional oxygen-containing functional groups being present. This was further supported by TGA data, in which the acid-treated SCSs had an early onset decomposition temperature as opposed to the as-synthesized SCSs. The Pd 3d XPS spectra of the synthesized catalysts showed that the electronic properties of the Pd were relatively the same on both carbons, indicating that little change was noted after acid treatment of the SCSs. The Pd/SCSs and Pd/fSCSs catalysts were tested in the liquid phase hydrogenation of CALD. The use of the Pd/SCSs catalyst led to complete hydrogenation of the C=C and C=O bonds without formation of by-products. The Pd/fSCSs catalyst was more selective toward the reduction of the C=O bond, followed by HCALD, then 3P1P. The activity of the Pd/fSCSs catalyst decreased with an increase in the reaction temperature (60 to 80 °C). The formation of by-products was more pronounced at a reaction temperature of 80 °C. The catalysts stability was tested in five runs. The catalytic activity of Pd/fSCSs dropped on the 4th cycle from 100 % CALD conversion to 47 % and further went down to 37 % on the fifth cycle. For the Pd/SCSs catalyst 100 % CALD conversion was maintained until the 4th cycle.

6.7 References

1. Zeng, L. H.; Yan, H. X.; Zeng, Y. K.; Li, Y. F.; Zhang, Z. X.; Liu, Z. W.; Liu, Z. T. *The Canadian Journal of Chemical Engineering* **2019**, *97*, 2505.

2. Zhu, J.; Dou, M.; Lu, M.; Xiang, X.; Ding, X.; Liu, W.; Li, M. *Applied Catalysis A: General* **2019**, *575*, 11.
3. Zhang, L.; Chen, X.; Peng, Z.; Liang, C. *Molecular Catalysis* **2018**, *449*, 14.
4. Li, R.; Yao, W.; Jin, Y.; Jia, W.; Chen, X.; Chen, J.; Zheng, J.; Hu, Y.; Han, D.; Zhao, J. *Chemical Engineering Journal* **2018**, *351*, 995.
5. Leng, F.; Gerber, I. C.; Axet, M. R.; Serp, P. *Comptes Rendus Chimie* **2018**, *21*, 346.
6. Zhang, L.; Winterbottom, J. M.; Boyes, A. P.; Raymahasay, S. *Journal of Chemical Technology & Biotechnology: International Research in Process, Environmental AND Clean Technology* **1998**, *72*, 264.
7. Chen, S.; Meng, L.; Chen, B.; Chen, W.; Duan, X.; Huang, X.; Zhang, B.; Fu, H.; Wan, Y. *ACS Catalysis* **2017**, *7*, 2074.
8. Han, Q.; Liu, Y.; Wang, D.; Yuan, F.; Niu, X.; Zhu, Y. *Journal of Chemistry* **2016**, *2016*.
9. Martínez-Ortiz, M. J.; de la Rosa-Guzmán, M. A.; Vargas-García, J. R.; Flores-Moreno, J. L.; Castillo, N.; Guzmán-Vargas, A.; Morandi, S.; Pérez-Gutiérrez, R. M. *The Canadian Journal of Chemical Engineering* **2018**, *96*, 297.
10. Li, Y.; Cheng, H.; Lin, W.; Zhang, C.; Wu, Q.; Zhao, F.; Arai, M. *Catalysis Science & Technology* **2018**, *8*, 3580.
11. Lan, X.; Wang, T. *ACS Catalysis* **2020**, *10*, 2764.
12. Lamme, W. S.; Zečević, J.; de Jong, K. P. *ChemCatChem* **2018**, *10*, 1552.
13. Sairanen, E.; Karinen, R.; Borghei, M.; Kauppinen, E. I.; Lehtonen, J. *ChemCatChem* **2012**, *4*, 2055.
14. Xu, Z.; Duong-Viet, C.; Liu, Y.; Baaziz, W.; Li, B.; Nguyen-Dinh, L.; Ersen, O.; Pham-Huu, C. *Applied Catalysis B: Environmental* **2019**, *244*, 128.
15. Tessonnier, J.-P.; Pesant, L.; Ehret, G.; Ledoux, M. J.; Pham-Huu, C. *Applied Catalysis A: General* **2005**, *288*, 203.
16. Toebes, M. L.; Prinsloo, F. F.; Bitter, J. H.; van Dillen, A. J.; de Jong, K. P. *Journal of Catalysis* **2003**, *214*, 78.
17. Dlamini, M.W. *Spherical carbons as model supports for Fe, Co and Fe-Co Fischer-Tropsch catalysts*, PhD Thesis, University of the Witwatersrand, Johannesburg, **2016**.
18. Shin, Y.-R.; Jung, S.-M.; Jeon, I.-Y.; Baek, J.-B. *Carbon* **2013**, *52*, 493.
19. Liu, J.; Qiao, S. Z.; Liu, H.; Chen, J.; Orpe, A.; Zhao, D.; Lu, G. Q. *Angewandte Chemie International Edition* **2011**, *50*, 5947.

20. Friedel, B.; Greulich-Weber, S. *Small* **2006**, *2*, 859.
21. Cattaneo, S.; Sanchez Trujillo, F. J.; Dimitratos, N.; Villa, A. *Applied Sciences* **2019**, *9*, 5061.
22. Pol, V. G.; Shrestha, L. K.; Ariga, K. *ACS Applied Materials & Interfaces* **2014**, *6*, 10649.
23. Ferrari, A. C.; Basko, D. M. *Nature Nanotechnology* **2013**, *8*, 235.
24. Ferrari, A. C.; Robertson, J. *Physical Review B* **2000**, *61*, 14095.
25. Sing, K. S. W.; Williams, R. T. *Adsorption Science & Technology* **2004**, *22*, 773.
26. Zhao, X.; Zhang, M.; Sun, X.; Li, X.; Li, J.-g. *Applied Surface Science* **2020**, *506*, 144591.
27. Jun, L. Y.; Mubarak, N. M.; Yon, L. S.; Bing, C. H.; Khalid, M.; Abdullah, E. C. *Journal of Environmental Chemical Engineering* **2018**, *6*, 5889.
28. Turgunov, M. A.; Oh, J. O.; Yoon, S. H. *Materials* **2014**, *64*, 22.
29. Taklimi, S. R.; Ghazinezami, A.; Askari, D. *Journal of Nanomaterials* **2019**, *2019*, 2836372.
30. Ye, B.; Kim, S.-I.; Lee, M.; Ezazi, M.; Kim, H.-D.; Kwon, G.; Lee, D. H. *RSC Advances* **2020**, *10*, 16700.
31. Mironenko, R. M.; Belskaya, O. B.; Likholobov, V. A. *Catalysis Today* **2020**, *357*, 152.
32. Ryndin, Y. A.; Alekseev, O. S.; Simonov, P. A.; Likholobov, V. A. *Journal of Molecular Catalysis* **1989**, *55*, 109.
33. Oliveira, R. L.; Kerstien, J.; Schomäcker, R.; Thomas, A. *Catalysis Science & Technology* **2020**, *10*, 1385.
34. Manikai, S. M.-A. *The synthesis of nitrogen doped carbon spheres as supports for palladium catalysts in the hydrogenation of cinnamaldehyde*, PhD Thesis, University of the Witwatersrand, Johannesburg, **2015**.
35. Jiang, F.; Cai, J.; Liu, B.; Xu, Y.; Liu, X. *RSC Advances* **2016**, *6*, 75541.
36. Cabiac, A.; Cacciaguerra, T.; Trens, P.; Durand, R.; Delahay, G.; Medevielle, A.; Plée, D.; Coq, B. *Applied Catalysis A: General* **2008**, *340*, 229.
37. Vatti, S. K.; Krishnamurthy, K. K. R.; Viswanathan, B. *ChemRxiv* **2020**.

Chapter 7: Hydrogenation of cinnamaldehyde using a palladium catalyst supported on hollow carbon spheres

7.1 Introduction

Spherical shaped carbon nanomaterials such as hollow carbon spheres (HCSs) have attracted a great deal of interest because of their unique properties. These properties include a tunable porosity, low density, chemical inertness, good thermal and chemical stability, and high specific surface area [1, 2]. Owing to their high specific surface area and isolated cavities, HCSs have been explored as potential support for dispersing noble metal nanoparticles (NPs) or used as nanoreactors [3-6].

In the selective hydrogenation of cinnamaldehyde (CALD) the influence of using different CNMs (e.g., graphene, graphene oxide, carbon nanotubes, carbon nanofibers, and activated carbon) as a support for metal catalysts (e.g., Pd [7-12], Pt [12-14], Ru [15, 16], Rh [12], an Au [12]) has been well documented in the literature. On the contrary, only a few studies have reported the use of the HCSs as catalyst support for use in the hydrogenation of CALD. Some examples include the use of HCSs to support Pt [17] and Co [6] catalysts for application in the liquid phase and gas phase hydrogenation of CALD, respectively. Nongwe *et al.* reported on the use of nitrogen-doped HCSs as a support for a Pt catalyst (Pt/N-HCSs) which was used in the hydrogenation of CALD [17]. The authors reported that the use of Pt/N-HCSs catalyst led to an increase in CALD conversion (80 to 99 %) and selectivity toward cinnamyl alcohol (CA, 93 to 97 %) when compared to undoped Pt/HCSs catalyst. The enhancement in the reaction rate was attributed to the change in 'polarity' of the carbon due to the presence of nitrogen atoms in the doped HCSs.

The most commonly used approach to synthesize HCSs is the hard-templating method. This method allows for fabrication of HCSs with controllable size, surface properties, and controllable morphology. Generally, spherically shaped templates such as silica spheres, metal oxide, and polymer spheres are used [1, 18]. In this study polystyrene spheres (PSSs) were used as a template, followed by coating with resorcinol-formaldehyde (RF) resin as a carbon precursor. The PSSs were used as a template because the polystyrene can easily decompose at a temperature < 400 °C under inert conditions [1, 18, 19].

Pd supported on HCSs was used in the liquid phase hydrogenation of CALD. The catalyst selectivity to hydrocinnamaldehyde (HCALD) started to decrease with an increase in the reaction time and an increase in the formation of 3-phenyl-1-propanol (3P1P) and as by-products were observed to form. The effect of using different reducing agents (i.e., carbon dots (CDs) and $NaBH_4$) on the catalyst activity, was explored using the Pd catalyst supported on the surface of the HCSs. The synthesized Pd/CDs/HCSs catalyst was tested in the liquid phase hydrogenation of CALD and preliminary results of this catalyst are presented.

7.2 Experimental procedures

The method used to synthesize PSSs and HCSs were modified from the methods reported in the literature [4, 20].

7.2.1 Materials

The chemicals used were of technical and analytical grade. CALD (98 %), CA (98 %), 3P1P (98 %, FCC), HCALD (90 %), PVP (MW 40000), CTAB (≥ 98 %), resorcinol (99 %), styrene (98 %), $NaBH_4$ (96 %), formaldehyde (34.5 wt. %), and $PdCl_2$ (99%) were purchased from Sigma-Aldrich. The absolute ethanol was purchased from MK chemical. KPS (95 %) was purchased from Eimer and Amend Chemicals.

7.2.2 Synthesis of PSSs

A mass of 0.1 g PVP (MW 40000) and styrene (8 mL) were dispersed in 250 mL ethanolic solution (200 mL ethanol and 50 mL distilled H_2O). The mixture was sonicated for 30 minutes. Potassium persulfate (0.15 g) was dissolved in 20 mL distilled water and added to the first mixture. The solution was sonicated for 10 minutes. The mixture was then refluxed at 80 °C for 24 h. The PSSs were centrifuged at 18000 rpm for 15 min and washed with ethanol and distilled water followed by oven drying at 60 °C overnight.

7.2.3 Synthesis of HCSs

The synthesized PSSs template was coated with RF polymer using the following procedure. PSSs (2 g) were added to a mixture of ethanol (100 mL), ammonia solution (25 %, 1 mL), and distilled water (50 mL) inside a 500 mL Schott bottle. To disperse the PSSs template, the mixture was sonicated for 30 min. Separately, resorcinol (R, 0.75 g), CTAB (1 g), and formaldehyde (F, 1.5 mL) were added to 50 mL of ethanol. The second mixture was added to the first mixture and stirred for 24 h at room temperature, followed by hydrothermal treatment inside an oil bath at 100 °C for 24 h. The resulting brownish product was filtered and washed

several times using ethanol/water. The obtained product was then dried at 100 °C for 4 h and crushed into a fine powder. The product was labelled as PSSs@RF.

For the synthesis of HCSs, the PSSs@RF was carbonized using a horizontal CVD furnace under a flow of N_2 gas (50 mL/min). A mass of 0.6 g of PSSs@RF was placed inside a quartz boat which was placed in the middle of a quartz tube and inserted inside the CVD furnace. The carbonization of the HCSs was done in two consecutive steps; firstly, the template (PSSs) was decomposed at 350 °C (10 °C/min) for 1 h followed by carbonization of RF polymer into HCSs at 600 °C for 2 h. The calculated yield for the HCSs was 26 %.

7.2.4 Synthesis of 5 wt.% Pd/HCSs composite

The procedure for the impregnation of Pd NPs on the support was modified from the method reported by Zhu *et al.* [7]. A mass of 0.6 g HCSs was added to 141 mL of 2 mM H_2PdCl_4 solution and the mixture was stirred overnight. A mass of 0.1895 g of sodium borohydride dissolved in ethanol was slowly added to the mixture with continuous stirring over 2 h to reduce the metal salt into metallic Pd NPs. The supported catalyst was filtered and washed using distilled water and absolute ethanol. The obtained black solid was dried at 100 °C for 4 h and labelled Pd/HCSs.

7.2.5 Synthesis of Pd/CDs/HCSs

For the synthesis of Pd/CDs/HCSs, sodium borohydride was replaced with 0.6 g of the CDs. The mixture was refluxed at 100 °C for 6 h and the resulting product was filtered and washed using water and ethanol. After filtering the Pd/CD/HCSs was dried at 100 °C for 4 h.

7.3 Characterization techniques

The morphology of the PSSs, HCSs and Pd/HCSs were analyzed by transmission electron microscopy (TEM) using an FEI Tecnai spirit (T12) operating at 120 kV. The spent Pd/HCSs catalyst and fresh Pd/CDs/HCSs catalyst were analyzed using a JEOL JEM 2100F TEM operating at 200 kV. The Pd particle size and the diameter of the spheres were measured using Image J software by counting >100 particles from the obtained TEM images. SEM analysis was done using ZEISS SIGMA 03-39 FESEM operating at 20 kV. The phase composition of the prepared samples was determined using, a Bruker D2 phaser PXRD equipped with a Lynxene detector using Cu-Kα (λ = 1.54184 Å) radiation at 30 kV with a scan range from 5 ° ≤ 2 Θ ≤ 90 ° in 0.026 steps. The thermal stability of the samples and catalyst loading were determined using a Perkin Elmer thermogravimetric analyser (TGA 4000) under an oxidative

atmosphere (air 20 mL/min) in the temperature range of 35-900 °C (10 °C/min). A Micromeritics Tristar 3000 surface area and porosity analyzer were used to conduct N_2 adsorption-desorption experiments at -195 °C. Before analysis, the samples were degassed at 150 °C for 4 h under N_2 gas. The Raman spectra were recorded using a Bruker Senterra Raman spectrophotometer with a laser wavelength of 532 nm using Opus 7.1 software. The elemental composition of the samples was determined using X-ray photoelectron spectroscopy (XPS) using a Thermo ESCAlab 250Xi equipped with a monochromatic Al Kα X-ray source operating at 1486.7 eV.

7.4 Catalytic tests

The catalytic test for CALD hydrogenation was carried using the same conditions reported in section 6.4 with the difference being the catalyst mass (150 mg).

Product analysis was carried out using an offline Varian 3700 GC with a flame ionization detector (FID) and a capillary column (Phenomenex Zebron, 30 m L. x 0.53 mm I.D. x 1.5 µ F.T.). The temperatures for the column, detector and injector were set to 300, 250, and 200 °C respectively, with N_2 (5 mL/min) as the carrier gas.

7.5 Results and discussion

7.5.1 Characterization of materials

7.5.1.1 Morphology and thermal stability analysis of the template

PSSs were synthesized via polymerization of styrene monomers in the presence of an initiator (potassium persulfate). The TEM and SEM images of the as-synthesized PSSs are shown in Fig. 7.1. The images show that the PSSs are spherical in morphology and they are monodispersed (Fig. 7.1 a, c). The size distribution of the PSSs showed that the PSSs had an average diameter of 430 ± 38 nm. From the TG analysis (Fig. 7.1d), it can be noted that the template started to decompose at *ca.* 278 °C followed by a large decomposition event at 400 °C that left no residue. The results obtained in this study are consistent with the ones reported in the literature [4, 20].

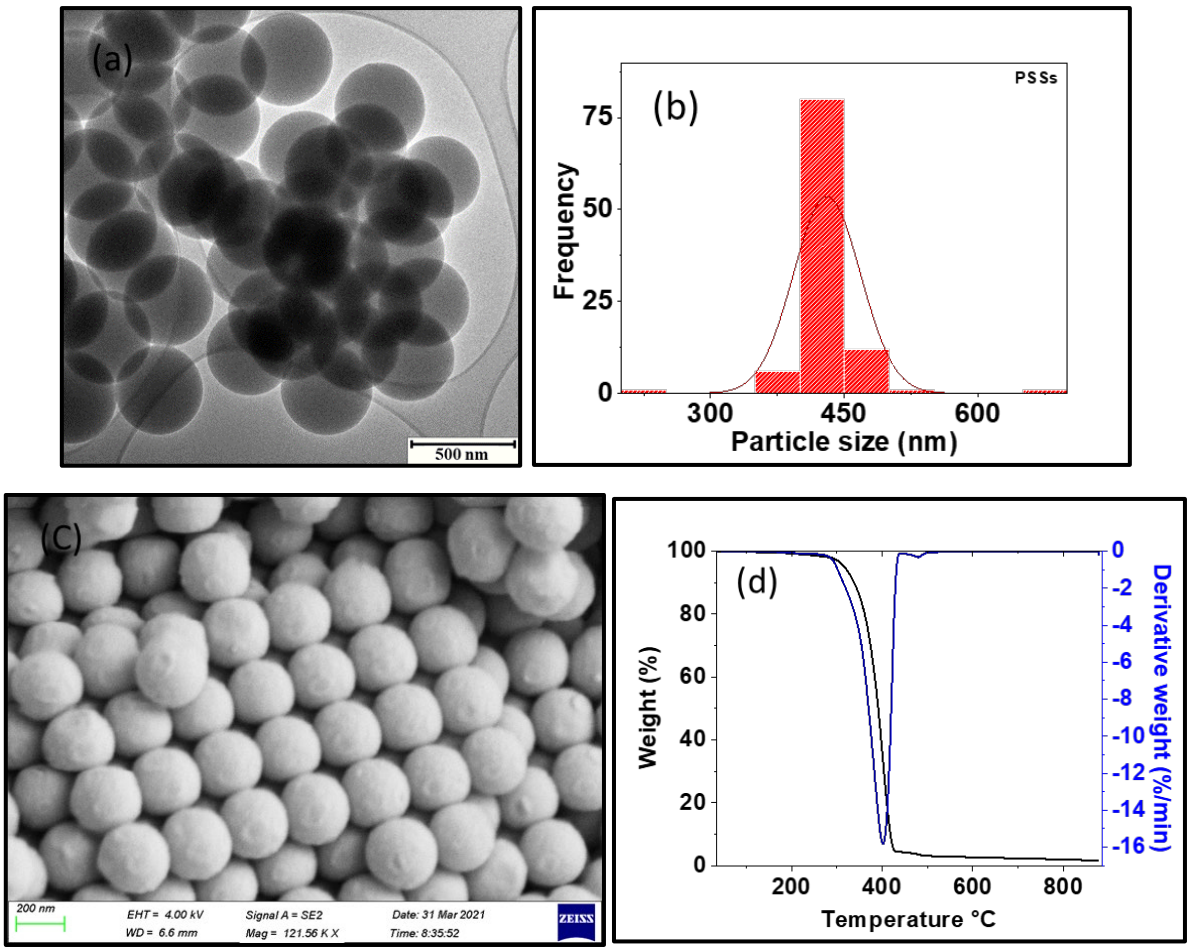

Figure 7.1: (a) TEM image, (b) particle size distribution, (c) SEM image, and (d) TGA and DTG profiles of the as-synthesized PSSs.

7.5.1.2 TEM analysis of the support and the catalyst

HCSs were obtained by coating the PSSs template with a carbon precursor, to give the RF@PSSs composite. The synthesized RF@PSSs composite was subjected to heating using the CVD method under N_2 gas to remove the template followed by annealing of the hollow carbon. From the TEM image (Fig. 7.2a) it can be seen that the obtained carbon spheres are hollow with an internal diameter of 367 ± 33 nm and shell thickness of 55 ± 7 nm. The overall average diameter of 487 ± 28 nm was obtained (Fig. 7.2b). From the data obtained it can be noted that there was a shrinkage when comparing the diameter of the PSSs (430 nm) and the internal diameter of the HCSs (367 nm). The shrinkage of the HCSs occurs during the decomposition of the PSSs as the RF polymer reacts at higher temperature [21].

The TEM image of the Pd/HCSs catalyst (Fig. 7.2c), showed that the Pd NPs were loaded on the outer surface of the HCSs. The Pd NPs were distributed on all the spheres and it is noted

that some of the NPs had formed aggregates (see red circle). The average particle size of the Pd NPs supported on the HCSs was determined to be 6.4 ± 2.9 nm (Fig. 7.2d).

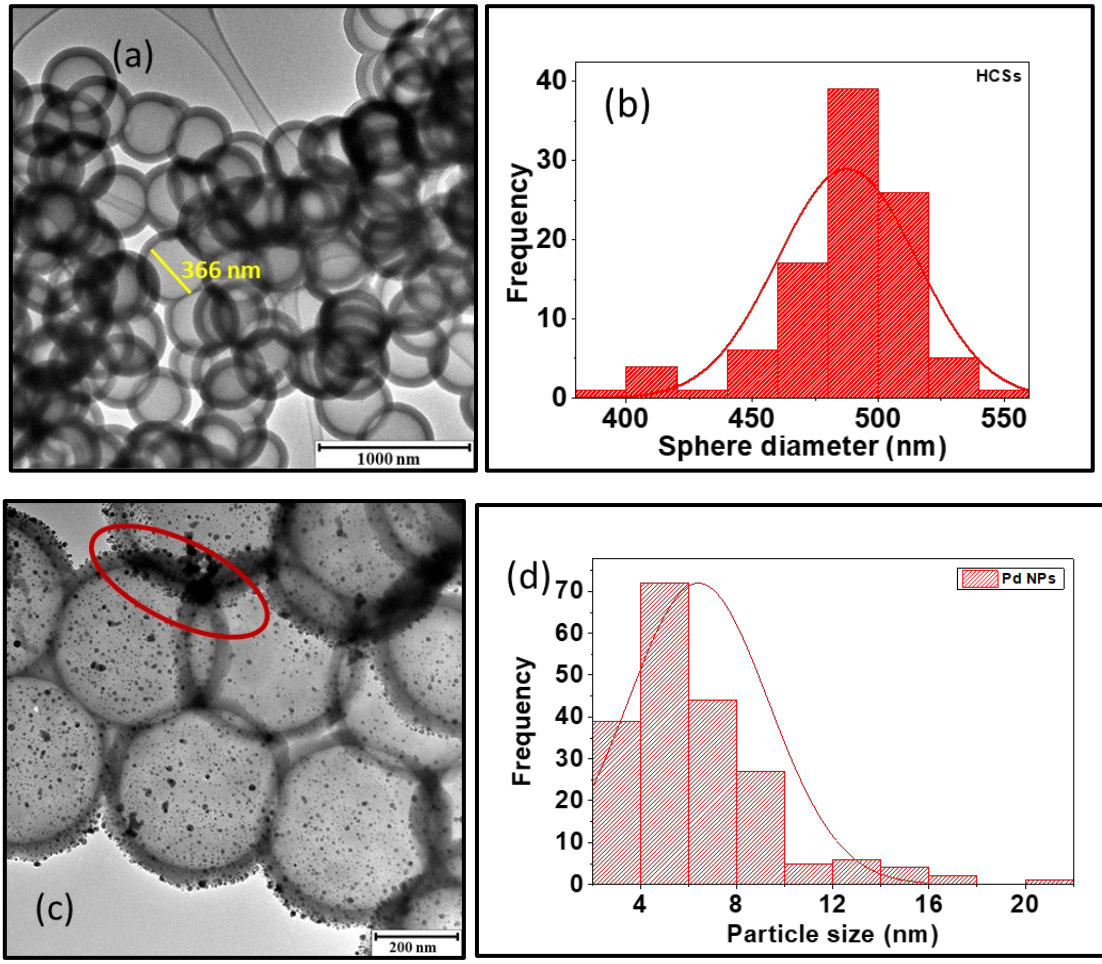

Figure 7.2: TEM images of (a) HCSs, (c) 5 wt. % Pd/HCSs catalyst, and their respective size distributions (b, d).

7.5.1.3 PXRD analysis

Fig. 7.3 shows the PXRD of the HCSs and the Pd/HCSs catalyst. The PXRD pattern of the support shows a small broad peak at a 2Θ value of 21.7 ° which corresponds to the (002) plane of carbon [5]. The PXRD pattern of the Pd/HCSs catalyst showed five additional peaks at 2Θ values of 40.1, 46.7, 68.1, 82.1, and 86.7 ° corresponding to Pd nanoparticle crystal planes: (111), (200), (220), (311), and (222) [PDF 00-005-0681].

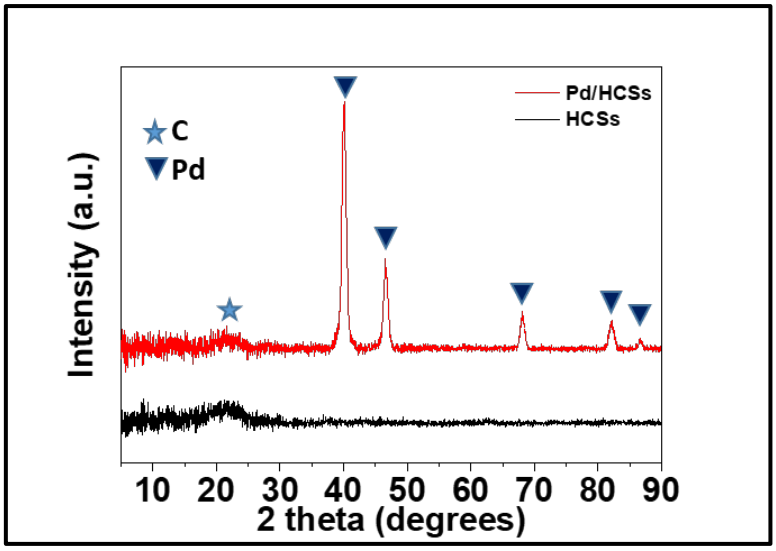

Figure 7.3: PXRD pattern of the HCSs and 5 wt. % Pd/HCSs catalyst.

7.5.1.4 Thermal stability analysis

The thermal stability of the HCSs and the effect of the Pd catalyst on the support were studied using TG analysis. The TGA derivative curve (Fig. 7.4a) of the HCSs showed that the carbon started to decompose at *ca.* 366 °C with a maximum weight loss at a temperature of *ca*. 603 °C. The TGA (Fig. 7.4b) of Pd/HCSs showed that the HCSs were less thermally stable. The derivative curve of the catalyst showed a maximum weight loss of the HCSs at a temperature *ca.* 377 °C. This is different to the maximum temperature recorded in the TGA of the HCSs, which showed that the presence of the Pd NPs catalyzed the oxidation of the HCSs. The TGA data was also used to get the percentage loading of Pd on the support. The TGA of the Pd/HCSs had a metal residue of 4.5 % (PdOx) after decomposition of carbon and the Pd loading was estimated to be 3.9 %.

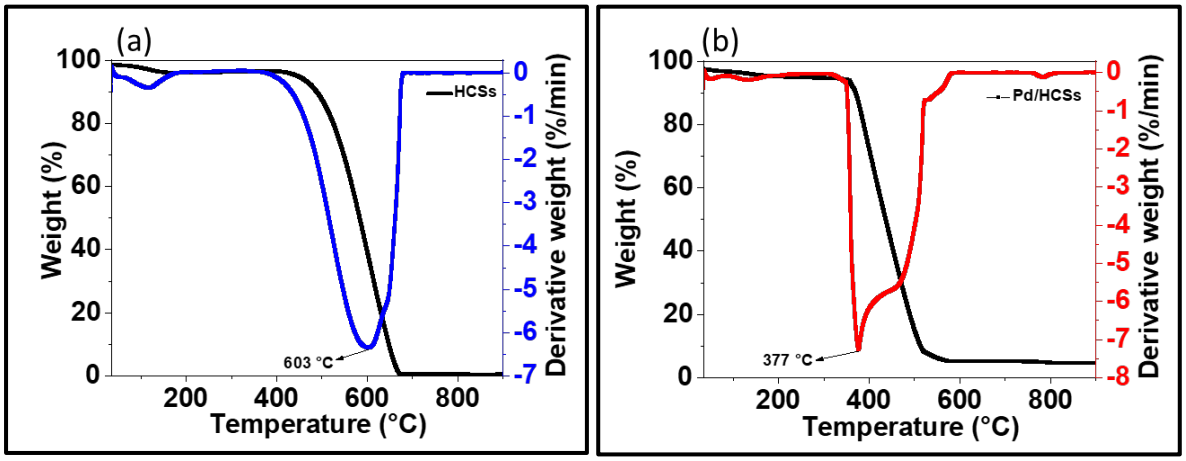

Figure 7.4: TGA and DTG profiles for (a) HCSs and (b) 5 wt. % Pd/HCSs catalyst.

7.5.1.5 BET surface area analysis

Table 7.1 gives the surface area, pore size, and pore volume of the support and the catalyst analyzed using the BET technique. The HCSs had a surface area of 392 m^2/g. Upon loading the metal on the outer surface of the HCSs, the surface area decreased to 304 m^2/g. This decrease in the surface area of the Pd/HCSs catalyst can be ascribed to the blockage of the pores of the HCS by the Pd NPs loaded on the outer surface of the HCSs [22].

Table 7.1: Summary of the textual properties of the HCSs and Pd/HCSs catalyst.

Sample Name	Surface properties		
	BET surface area (m^2/g)	Pore size (nm)	Pore volume (cm^3/g)
HCSs	392	3.5	0.34
Pd/HCSs	304	4.8	0.36

7.5.1.6 Raman analysis

To establish the graphitic nature of the materials, Raman analysis was conducted. Both the HCSs and Pd/HCSs showed two typical Raman peaks (D and G band) of carbon (Fig. 7.5, Table 7.2). The D and the G bands for the HCSs were observed at 1365 and 1595 cm^{-1} respectively. The addition of the metal to the support led to a slight shift to higher wavenumber in the D (1375 cm^{-1}) and G (1598 cm^{-1}) bands. The intensity ratio of the D and the G bands (I_D/I_G) were used to estimate the degree of graphitization of the carbon support. The I_D/I_G ratios were estimated to be 0.75 and 0.73 for the HCSs and Pd/HCSs respectively. The HCSs had a low degree of graphitization as indicated by their I_D/I_G ratio. The loading of metal NPs did not have an impact on the degree of graphitization of the HCSs.

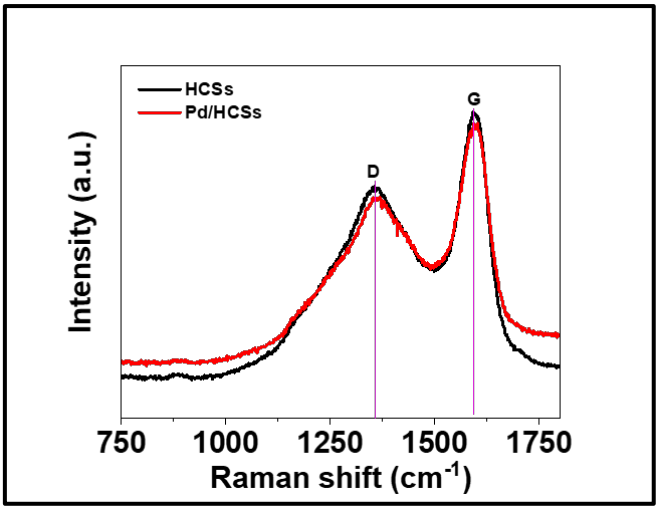

Figure 7.5: Raman spectra of the HCSs and 5 wt. % Pd/HCSs.

Table 7.2: Summarizes the D and the G band positions, and I_D/I_G ratios obtained from the HCSs and Pd/HCSs catalyst.

Sample Name	D band position (cm^{-1})	G band position (cm^{-1})	I_D/I_G ratio
HCSs	1365	1597	0.75
Pd/HCSs	1375	1598	0.73

7.5.1.7 XPS analysis

The XPS spectra showing the elemental composition and element bonding configuration of the surface atoms are shown in Fig. 7.6. Listed in table 7.3 are the atomic % of the elements. Only the Pd/HCSs were analyzed using this technique. The XPS survey spectra (Fig. 7.6a) of the Pd/HCSs catalyst showed that the supported catalyst is composed of carbon, oxygen, nitrogen, palladium, and chlorine with the corresponding binding energies of 284.1, 532.3, 399.0, 335.3, and 198.2 eV respectively. The Cl 2p peak is due to the traces of metal chloride used, whereas the N1s detected can be attributed to ammonia residues from RF polymerization or that the ammonia also acted as a nitrogen source during the polymerization reaction of the RF as reported by Zhao [23]. The bonding states of the C1s spectra were deconvoluted into five peaks centred at 284.0 (C-C sp^2), 285.0 (C-C sp^3), 285.8 (C-O), 288.0 (C=O), and 289.7 (O-C=O) eV

(Fig. 7.6b) [24, 25]. This shows that the use of RF as a carbon precursor led to HCSs with some functionalization.

The deconvolution of the O1s spectra (Fig. 7.6c) indicated that there is an interaction between the metal and the support functional groups as shown by the presence of C-O; Pd oxide (530.9 eV) and C=O + Pd3p3 (532.7 eV) peaks [25]. The deconvoluted XPS spectra (Fig. 7.6d) of Pd 3d shows two main peaks assigned to Pd $3d_{3/2}$ and $3d_{5/2}$. The core level Pd $3d_{5/2}$ area was deconvoluted into three different components assigned to Pd (335.1 eV), PdO (336.9 eV), and PdO_2 (338.1 eV) [8].

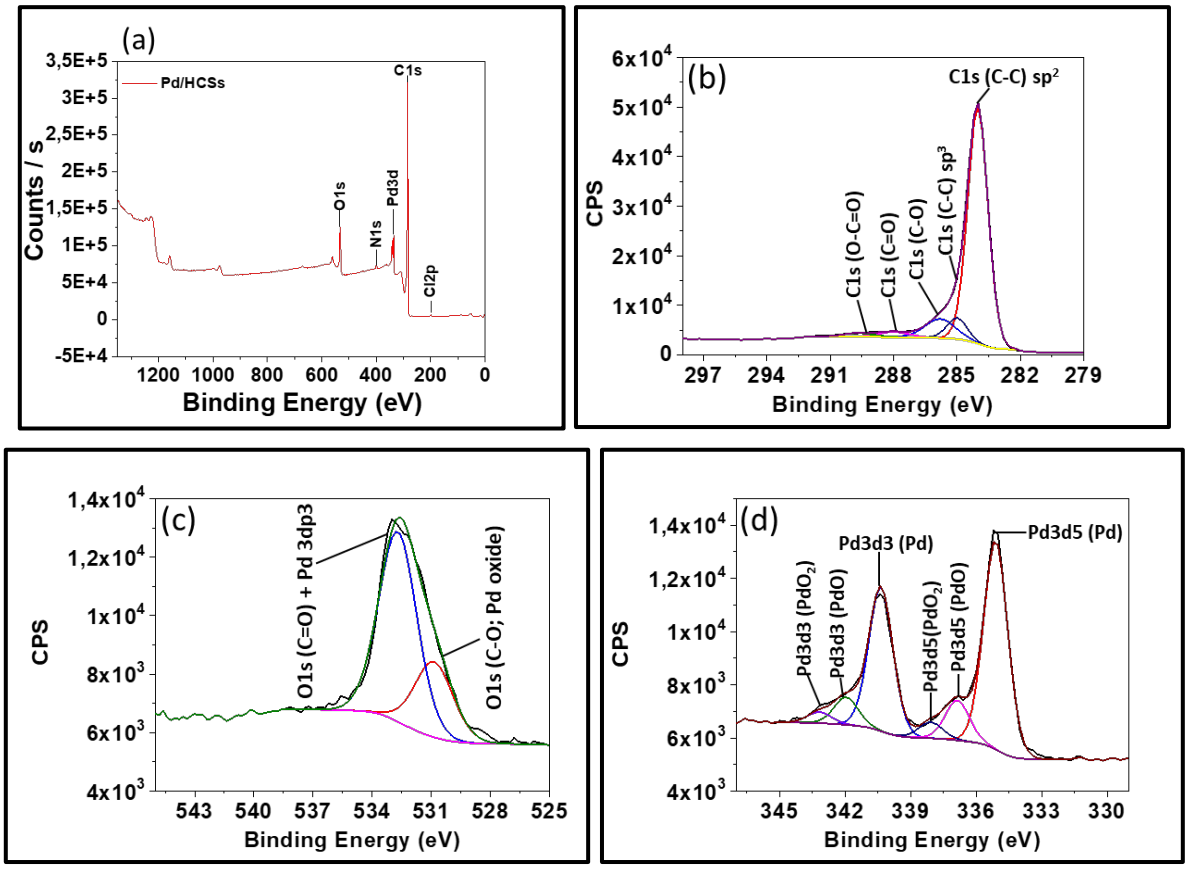

Figure 7.6: (a) XPS spectra survey, and deconvoluted spectrum of (b) C1s, (c) O1s, and (d) Pd3d.

Table 7.3: Elemental quantification of Pd/HCSs catalysts using XPS analysis.

Catalyst	**Elemental composition (atomic %)**				
	C1s	O1s	N1s	Pd 3d	Cl 2p
Pd/HCSs	87.0	9.9	1.2	1.6	0.3

7.5.1.8 Summary

HCSs were synthesized using the hard-core templating method and Pd NPs were impregnated on the outer surface using a liquid phase reduction method. The particle size of the Pd NPs (6.4 ± 2.9 nm) is similar to the one obtained when using SCSs as support (6.0 ± 2.3). From the PXRD of the Pd/HCSs catalyst, it was shown that the Pd NPs are in the metallic phase and no oxidation peaks were observed. However, the XPS data showed that the Pd/HCSs catalyst contains both metallic and oxide forms of Pd. The formation of Pd oxide can be ascribed to the surface oxidation of the Pd/HCSs catalyst upon exposure to air [26].

7.5.2 Catalysis

The liquid phase hydrogenation of CALD was carried out using a 5 wt. % Pd/HCSs catalyst. The hydrogenation of CALD was carried out using the same conditions used in chapter 6. A blank test was carried out using HCSs (without Pd NPs) as a catalyst and no catalytic activity was observed.

7.5.2.1 Effect of the reaction temperature

To study the effect of the reaction temperature on the catalytic hydrogenation of CALD over the Pd/HCSs catalyst the reaction was performed by varying the reaction temperature (40, 60, and 80 °C). Figure 7.7a shows the influence of temperature on the CALD conversion. At a reaction temperature of 40 and 60 °C total hydrogenation of CALD was observed within 4 h. The catalyst activity was slowed down when the reaction temperature was increased to 80 °C as seen with a decrease in the CALD conversion. At this temperature, CALD conversion of 29 % was observed within 4 h. From the data obtained it can be noted that the catalyst activity decreased with an increase in the reaction temperature [7, 12]. We also noted an increase in the formation of by-products with an increase in the reaction temperature. In the literature, this observation was attributed to over-hydrogenation of CALD with hydrogen to form by-products (i.e. acetals, β-methyl styrene and propyl benzene) [12]. The resulting by-products can cause surface poisoning on the active metal leading to a decrease in the catalyst activity. Figure 7.7b-d shows the catalyst selectivity while varying the reaction temperature. At the reaction temperature of 40 and 60 °C, the Pd/HCSs catalyst favoured the hydrogenation of the C=C bond yielding HCALD as a major product. The hydrogenation of the C=C bond was expected as studies on this reaction using Pd based catalyst showed a similar trend [7, 8, 27]. However, at 60 °C the selectivity to HCALD decreased faster after an hour's reaction. The sudden decrease

in the selectivity to HCALD can be attributed to further hydrogenation of the HCALD to form 3P1P. The formation of CA was not detected in this reaction.

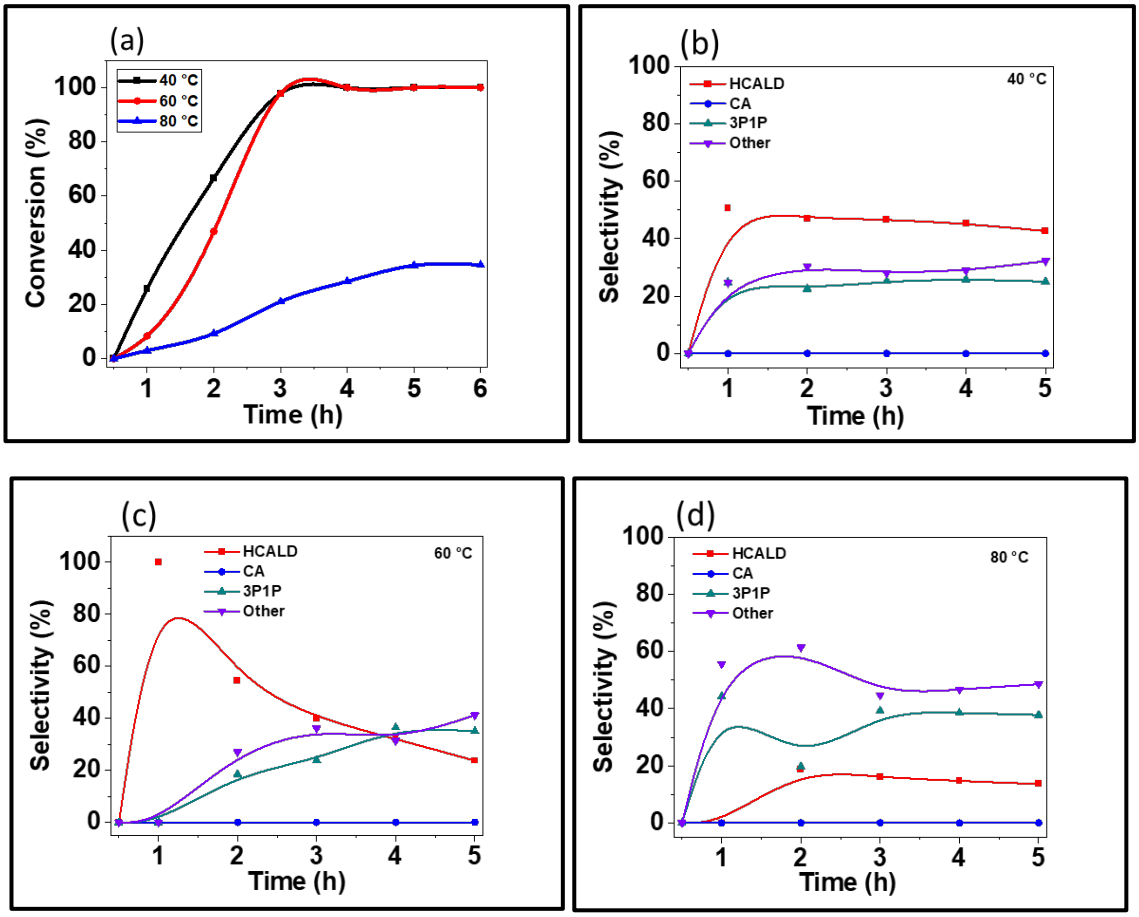

Figure 7.7: The influence of the reaction temperature on the (a) CALD conversion and (b-d) selectivity over the 5 wt. % Pd/HCSs. Reference conditions: t = 6 h, $mass_{catalyst}$ = 150 mg, 50 mL/min = H_2 flow rate, 100 ml ethanol, and 1.32 g CALD.

7.5.2.2 Effect of the catalyst mass

The effect of the catalyst mass was carried out at 60 °C while keeping the CALD concentration, hydrogen flow rate, and ethanol volume constant (Fig. 7.8a). The catalyst activity increased with increasing catalyst mass. When using 100 mg of the catalyst a CALD conversion of 36 % was achieved after 6 h, whereas increasing the catalyst mass led to 100 % CALD conversion within 4 and 3 h for 150 and 200 mg respectively. In terms of the catalyst selectivity (Fig. 7.8b-d) when 100 mg was used a significant amount of by-products was formed which can be used to explain the poor catalyst activity. The use of ethanol as a solvent in the hydrogenation of CALD has been reported to produce by-products [28, 29]. Increasing the catalyst mass to 200 mg resulted in a high selectivity toward HCALD (100 %) which rapidly decreased with an increase

in the reaction time. The HCALD formed is further hydrogenated into 3P1P and this was also observed by an increase in the formation by-products.

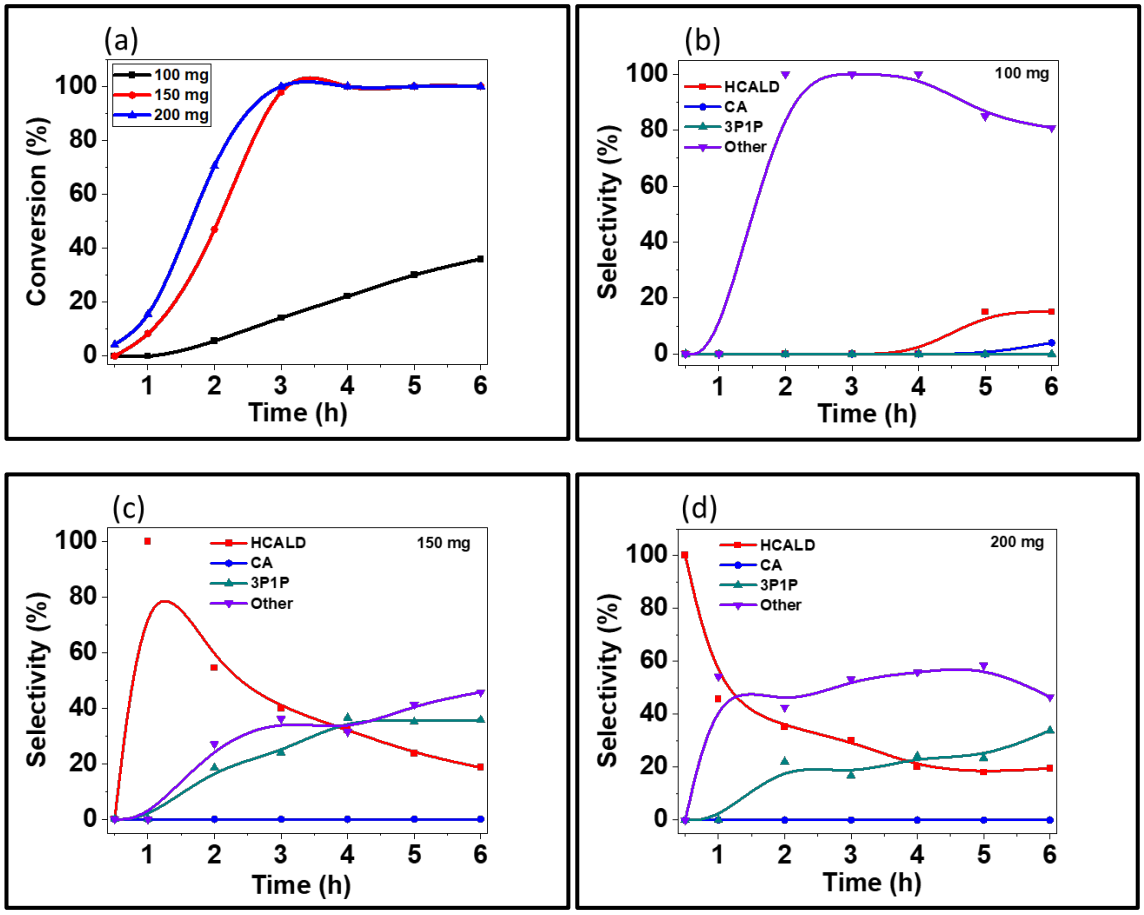

Figure 7.8: The influence of the catalyst amount on the (a) CALD conversion and (b-d) selectivity over the 5 wt. % Pd/HCSs. Reference conditions: t = 6 h, T= 60 °C, 50 mL/min = H_2 flow rate, 100 ml ethanol, and 1.32 g CALD.

7.5.2.3 Effect of hydrogen flow rate

The hydrogen flow rate effect was studied, and it was noted that the CALD conversion increased with an increase in hydrogen flow rate (Fig. 7.9a). Within half an hour the CALD conversion doubled with an increase in the hydrogen flow rate (0, 5, and 12 % for 50, 75, and 100 mL/min respectively). In terms of the catalyst selectivity (Fig. 7.9b-d), it was observed that increasing the hydrogen flow rate increased the formation of by-products. The catalyst selectivity to HCALD decreased with an increase in the hydrogen flow rate. The formation of 3P1P is the result of further hydrogenation of the C=O bond in HCALD. No CA was detected in the reaction.

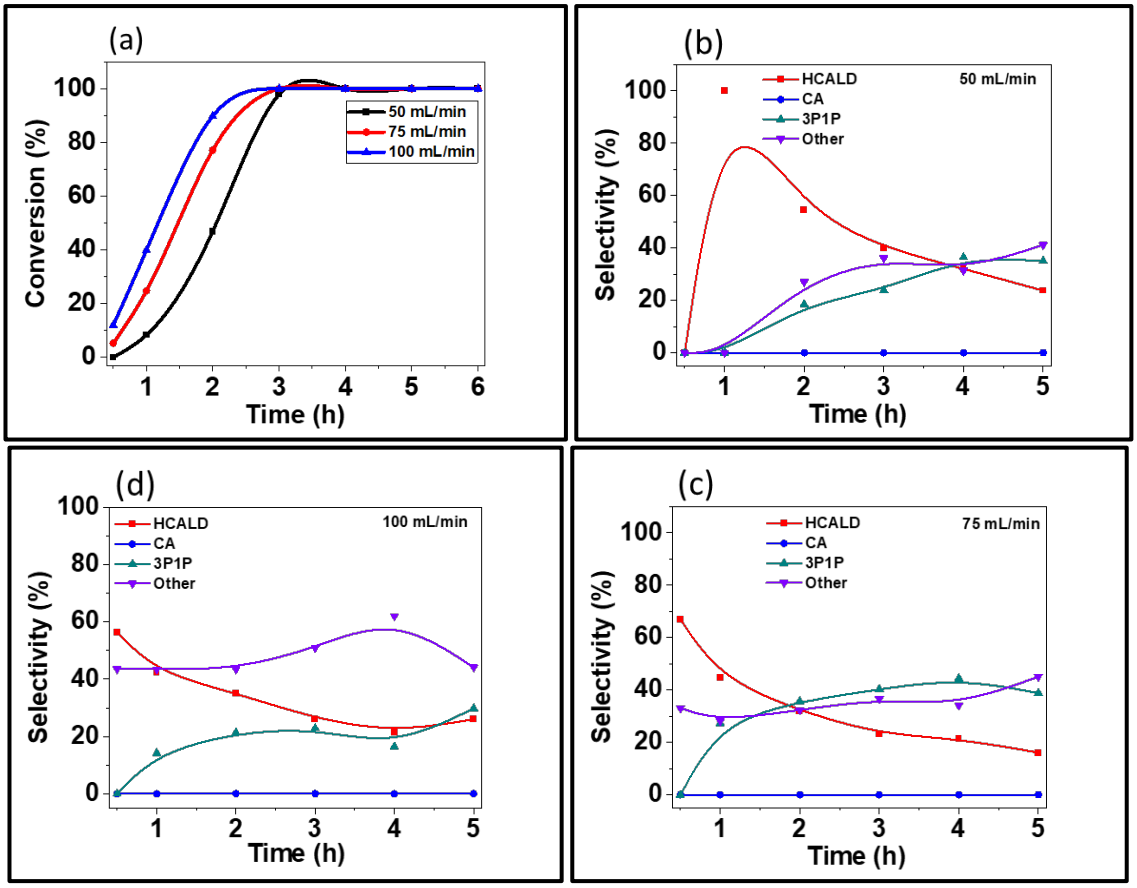

Figure 7.9: Influence of the hydrogen gas flow rate on the (a) CALD conversion and (b-d) selectivity over Pd/HCSs catalyst.

7.5.2.4 Catalyst stability test

The stability of the catalyst was tested by recycling the catalyst five times. From the data presented it can be noted that there was a rapid drop in the catalyst activity from cycle 2 to 5 (Fig. 6.10a). The CALD conversion dropped from 100 to 39 % during the first and second cycles and it further went down (< 10 %) as the number of cycles increased. To investigate the sudden drop of the catalyst activity, the spent catalyst was analyzed using TEM. From the TEM image (Fig. 10b) the Pd NP was seen to have formed aggregates (see red circle-size; range from 20 to 60 nm). The particle size of the Pd NPs had increased from 6.4 nm to 14.8 nm. The formation of particle aggregates led to a decrease in the number of effective sites resulting in the loss of the catalyst activity during catalyst recycling.

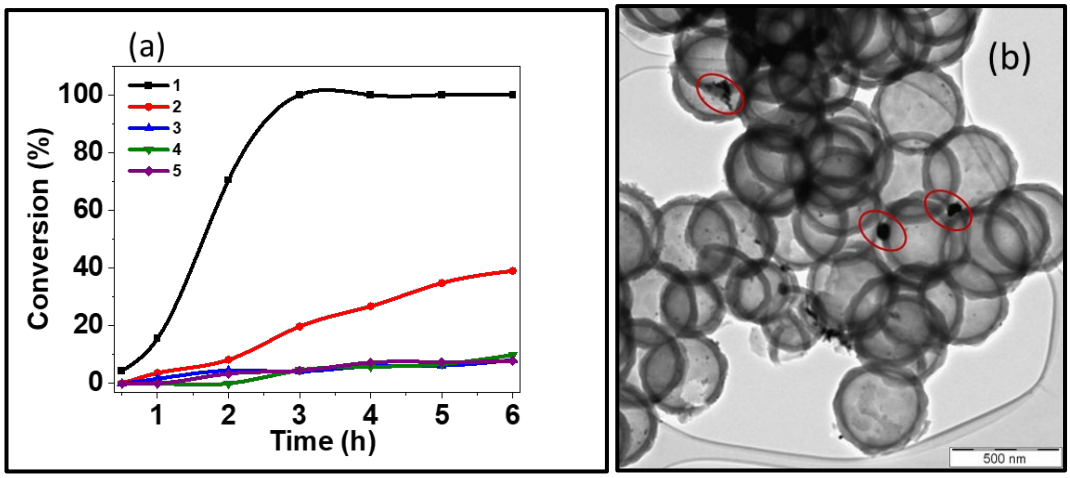

Figure 7.10: (a) Recycling of Pd/HCSs catalyst over five runs at 60 °C and (b) TEM images of Pd/HCSs after recycling.

7.5.2.5 Summary on the catalyst activity

In general, the hydrogenation of CALD using a Pd based catalyst resulted in the formation of HCALD in high yields; further reaction led to the formation of 3P1P. Table 7.4 summarizes some of the research work done on the selective hydrogenation of CALD using Pd based catalysts. The use of Pd/HCSs showed good activity in the hydrogenation of CALD. At the beginning of the reaction, the Pd/HCSs catalyst showed good selectivity to HCALD but this dropped with an increase in the reaction time. In the literature, the use of ethanol as a solvent in the hydrogenation of CALD has been reported to produce large amounts of by-products [10, 28]. This has been attributed to condensation reactions between CALD/HCALD and the ethanol solvent. For example, HCALD diethyl acetal is one of the by-products reported to be formed in equilibrium with HCALD [28]. This effect was also observed in the study conducted by Nagpure *et al.* [11]. In their study, Pd-NMC (2.05 wt. %) was used to hydrogenate CALD using ethanol as a solvent (Table 7.4). HCALD was formed as a major product followed by 3P1P. The selectivity to by-products of 4.8 % was also reported.

The product selectivity and CALD conversion can be affected by many factors such as the metal, metal particle size, reaction conditions, and catalyst support [7]. From the literature reports, the metal d-band width has been associated with catalyst selectivity [11, 30 31]. The adsorption of a C=C bond on metals with a wide d-band width is greater than those with a narrower d-band width. The metal d-band width decreases in the following order: Os ≈ Ir > Pt > Rh > Ru > Pd [11, 30]. The Pd metal has a narrower d-band width and hence the adsorption mode of the C=C bond is favourable [11, 30].

The increase in selectivity to 3P1P and a decrease in the selectivity of HCALD can be attributed to the Pd particle size and Pd (111) lattice [31, 32]. From the literature, it has been reported that the Pd particle size has an impact on selectivity. If the Pd metal is small enough both the C=C and C=O bonds of CALD can be hydrogenated [31]. Also, the Pd (111) lattice plane has been reported to favour the adsorption of both the conjugated double bonds of the CALD [31].

Table 7.4 summarizes some of the work done using Pd based catalysts on the selective hydrogenation of CALD. From the data reported, the catalysts displayed high selectivity toward HCALD (> 80 %) except for Pd/fNCSs40 (1 wt. %) catalyst [8, 11, 27, 33]. The Pd/fNCSs40 catalyst gave a selectivity of 23.2 % to HCALD and 10.1 % 3P1P [27]. A significant amount of by-products (selectivity of 66.8 %) was reported as the result of the use of ethanol as a solvent.

Table 7.4: Summary of the work done using Pd catalysts supported on CNMs in the selective hydrogenation of CALD.

Catalyst Name	CALD hydrogenation conditions	Pd particle size (nm)	Results	Refe-rence
3.9 wt. % Pd/HCSs	100 mg catalyst, 1.32 g CALD, 100 mL ethanol, 50 mL/min H_2, 60 °C, 6 h, 600 rmp.	6.4 ± 2.9	The Pd/HCSs catalyst gave 100 % CALD conversion within 4 h with selectivity of 32 % HCALD, 37 % 3P1P, and 31 % by-products.	This work
(a) 5 wt. % Pd/MWNT (b) 5 wt. % Pd/AC	100 mg catalyst, 10 mL CALD, 50 mL dioxane, 20 mL/min H_2, 80 °C, 27 h, 500 rmp.	5 ± 1 2-4	CALD conversion of 100 % was obtained after 25 h and 27 h for Pd/MWNT and Pd/AC catalysts respectively. Pd/MWNT was more selective to HCALD (90 %) 3P1P (10 %) was also observed. For the Pd/AC catalyst both HCALD and 3P1P were	33

			observed in similar proportions.	
1 wt. % Pd/fNCSs40	100 mg catalyst, 1.26 mL CALD, 100 mL ethanol, 50 mL/min H_2, 60 °C, 8 h, 40 °C.	4.68	CALD conversion of 90 % was obtained with selectivity of 23.2, 10.1, and 66.8 % corresponding to HCALD, 3P1P, and by-products.	27
2.05 wt. % Pd-NMC	25 mg catalyst, 7.5 mmol CALD, 25 mL ethanol/2-propanol, H_2 pressure 5 bar, 30 °C, 3h, 800 rmp.	2.4	When ethanol was used as a solvent a CALD conversion of 89.7 % was obtained with selectivity of 83.0, 12.2, and 4.8 corresponding to HCALD, 3P1P and by-products. Alternatively, the use of 2-propanol led to a CALD conversion of 100 % with selectivity of 93.0 % (HCALD), 4.9 % (3P1P), and 2.1 % (by-products)	11
(a) 4.3 wt. % Pd/GF (b) 4.6 wt. % OGF	0.3 g catalyst, 0.08 mol/L CALD, 100 mL dioxane, 50 mL/min H_2, 80 °C, 375 rmp and 2½ h.	13.5 3.8 ± 0.8	Both catalysts gave 100 % CALD conversion. Both catalysts had HCALD as a major product with a selectivity % of 88 and 91 for Pd/GF and Pd/OGF respectively.	8

7.6 Hydrogenation of CALD using carbon dots reduced Pd catalyst supported on hollow carbon spheres

7.6.1 Synthesis of 5 wt. % Pd/CDs/HCSs catalyst

The synthesis of Pd/CDs/HCSs was adopted from the method used for the reduction of the Pd salt reported in **chapter 5**. The CDs were used to reduce the H_2PdCl_4 solution on the surface of HCSs. After the reduction, most of the CDs were removed when filtering the catalyst, during the washing of the catalyst with water and ethanol.

7.6.2 Catalyst characterization

In this study, carbon dots were used to reduce Pd chloride salt supported on HCSs. The catalyst was labelled Pd/CDs/HCSs. Figure 7.11a shows the TEM image of the synthesized catalyst and the Pd particle size was estimated to be 45.6 ± 26.5 nm. PXRD was performed to confirm the reduction of the metal salt to metallic NPs. The PXRD pattern (Fig. 7.11b) of the Pd/CDs/HCSs catalyst showed a small broad peak at a 2Θ value of 29.9 ° associated with the (002) plane of carbon. The other additional peaks at 2Θ values of 39.7, 46.3, 67.5, 81.7, and 86.1 ° correspond to Pd nanoparticle crystal planes: (111), (200), (220), (311), and (222) [PDF 00-001-1201]. The thermal stability of the catalyst was tested using TG analysis. The derivative profile of the TG (Fig. 7.11c) shows two decomposition peaks at *ca.* 305 and 456 °C. The first derivative peak can be attributed to CDs (10.5 wt. %) that were still in contact with the support after the washing step. The decomposition of the support at a lower temperature (compared to 603 °C) is due to the presence of Pd NPs. The Pd loading (2.8 %) on the support was estimated using the TG profile and a residue of 3.2 % (PdOx) was noted.

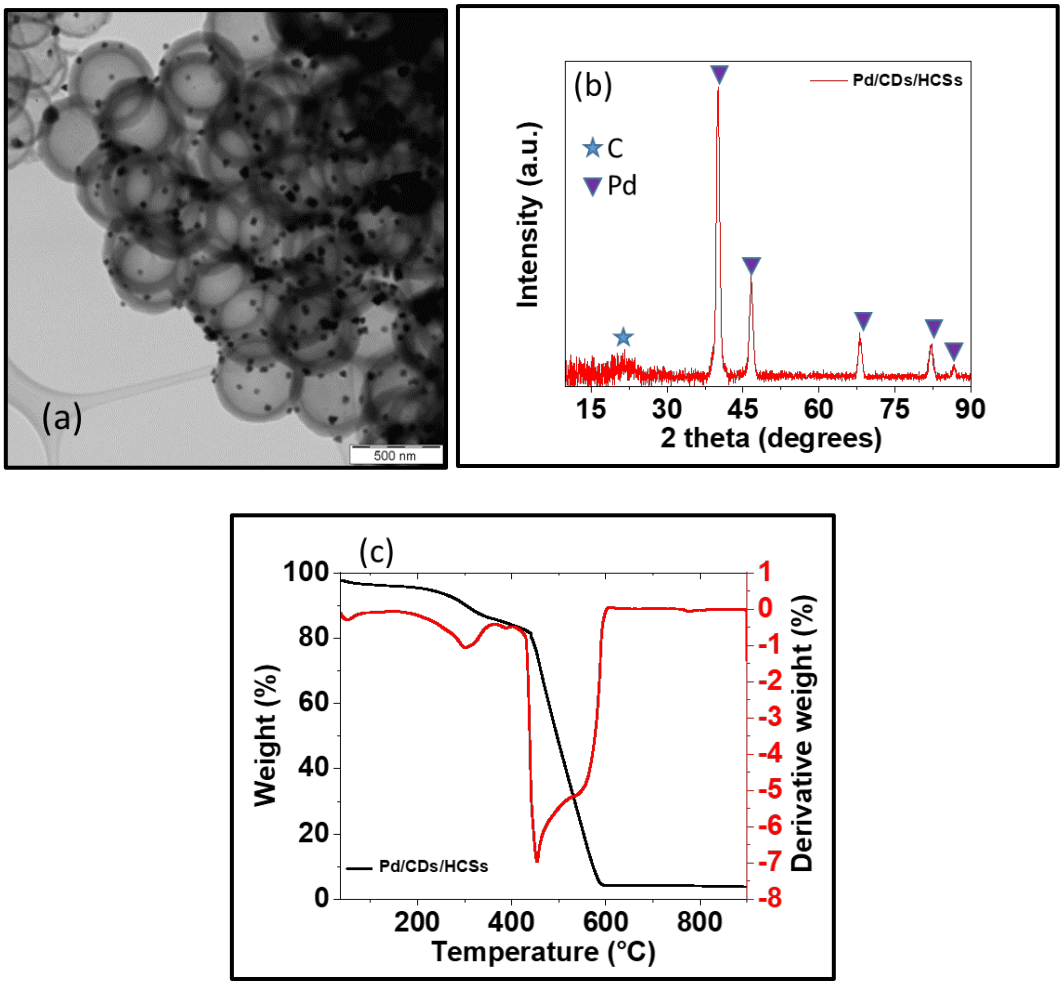

Figure 7.11: (a) TEM image, (b) PXRD pattern, and (c) TGA and DTG profiles of Pd/CDs/HCSs catalyst.

7.6.3 Catalyst performance evaluation

The catalyst activity of the Pd/CDs/HCSs was tested using different reaction temperatures (Fig.7.12a-c). The overall catalyst performance was very poor compared to Pd/HCSs catalyst. This is no surprise as TEM images indicated large particles of Pd. Increasing the reaction temperature from 40 to 60 °C resulted in a small increase in catalytic activity and CALD conversions of 13 and 15 % were obtained respectively. At 40 °C the catalyst was more selective to 3P1P (54 %) followed by HCALD (46 %). There were no by-products observed. At 60 °C the formation of by-products increased with increasing reaction time (43 %). The selectivity to HCALD (27 %) and 3P1P (30 %) were relatively the same.

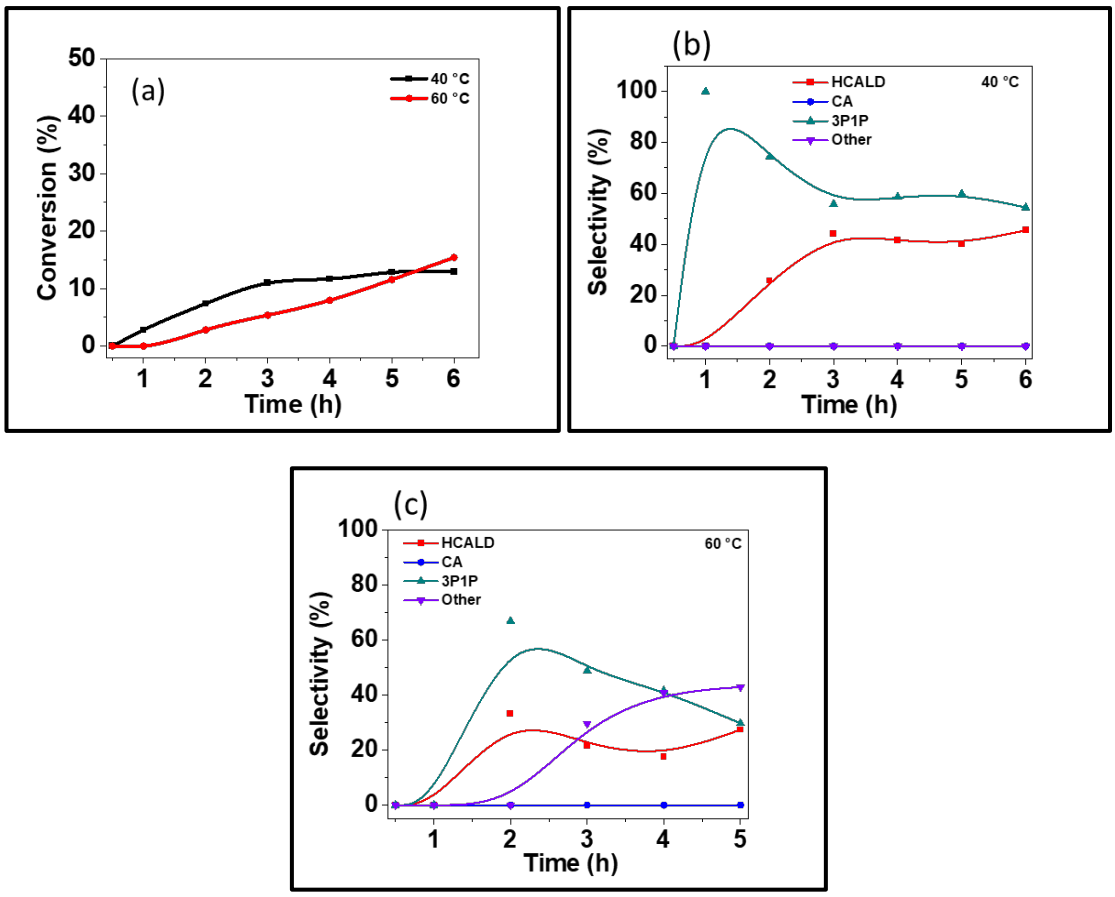

Figure 7.12: (a) CALD conversion, (b, c) selectivity over Pd/CDs/HCSs catalyst at 40 and 60 °C.

7.7 Comparison of the catalytic activity of the synthesized catalysts

The use of Pd/CDs (1 wt. %) and Pd/CDs/HCSs (5 wt. %) catalysts in the liquid phase hydrogenation of CALD both resulted in the reduction of the C=C bond to form HCALD. No by-products and CA were detected in the reaction. The reaction conditions for both catalysts were as follows (Pd/CDs-100 mg, 1.32 g CALD, 8 h, 100 mL ethanol, and 60 °C) and (Pd/CDs/HCSs-150 mg, 100 mL ethanol, 1.32 g CALD, 6 h, and 60 °C). The Pd/CDs catalyst was more efficient in the hydrogenation of CALD compared to Pd/CDs/HCSs catalyst (73 and 15 % CALD conversion respectively). The use of 5 wt. % Pd/HCSs favoured the formation of HCALD but the hydrogenation of the C=O bond to give 3P1P was noted. Total hydrogenation of CALD was observed when using 5 wt. % Pd/SCSs catalyst without the formation of any by-products although both catalysts showed similar activity. On the contrary, the use of the Pd/fSCSs (5 wt. %) catalyst led to the reduction of the C=O bond forming CA. The catalysts prepared using $NaBH_4$ had better activity than the Pd/CDs/HCSs catalyst prepared using the CDs. However, the synthesis method for the Pd/CDs/HCSs catalyst could be improved to give better dispersed Pd NPs with small size to improve the catalyst activity.

7.8 Conclusions

In summary, HCSs were synthesized using the hard-templating method and used to support a Pd catalyst. The XPS analysis showed that the support has oxygenated functional groups on the surface. As a result, the HCSs were effective in dispersing Pd NPs to give small Pd particle sizes.

- The Pd/HCSs catalyst was applied in the liquid phase selective hydrogenation of CALD. Good catalyst performance (100 % CALD) was obtained when using a reaction temperature of 40 and 60 °C, whereas a rapid drop in the catalyst activity was observed when the reaction temperature was increased to 80 °C. Increasing the catalyst mass resulted in a higher catalyst activity and a change in the catalyst selectivity was noted. The catalyst recycling led to a rapid drop in the catalyst activity due to the formation of particle aggregates and Pd sintering.
- Preliminary studies on the effect of CDs reduced Pd catalyst supported on HCSs on CALD hydrogenation was conducted. The Pd/CDs/HCSs catalyst gave poor catalyst activity and from the TEM images, it was noted that the synthesis method used still needs to be optimized to get nicely dispersed Pd NPs with small particle sizes. Optimization of the synthesis can improve the catalyst activity so that it will be possible to compare the effect of using different reducing agents.

In conclusion, our study revealed that HCSs can be used as an effective support for dispersing a Pd catalyst. The synthesized catalyst was successfully used in the selective hydrogenation of CALD.

7.9 References

1. Li, X.; Chi, M.; Mahurin, S. M.; Liu, R.; Chuang, Y.-J.; Dai, S.; Pan, Z. *Carbon* **2016**, *101*, 57.
2. Fang, X.; Liu, S.; Zang, J.; Xu, C.; Zheng, M.-S.; Dong, Q.-F.; Sun, D.; Zheng, N. *Nanoscale* **2013**, *5*, 6908.
3. Li, S.; Pasc, A.; Fierro, V.; Celzard, A. *Journal of Materials Chemistry A* **2016**, *4*, 12686.
4. Buthelezi, T.I. *Carbon with different functionalities as a hydrogen transport layer in ruthenium promoted Fischer -Tropsch catalysts,* MSc Dissertation, University of the Witwatersrand, Johannesburg, **2019**.

5. Phaahlamohlaka, T. N.; Kumi, D. O.; Dlamini, M. W.; Jewell, L. L.; Coville, N. J. *Catalysis Today* **2016**, *275*, 76.
6. Mente, P.; Mashindi, V.; Magubane, A.; Phaahlamohlaka,T.; Gangatharan, P.; Forbes, R.; Coville, N. *Canadian Journal of Chemistry* **2021**.
7. Zhu, J.; Dou, M.; Lu, M.; Xiang, X.; Ding, X.; Liu, W.; Li, M. *Applied Catalysis A: General* **2019**, *575*, 11.
8. Xu, Z.; Duong-Viet, C.; Liu, Y.; Baaziz, W.; Li, B.; Nguyen-Dinh, L.; Ersen, O.; Pham-Huu, C. *Applied Catalysis B: Environmental* **2019**, *244*, 128.
9. Lamme, W. S.; Zečević, J.; de Jong, K. P. *ChemCatChem* **2018**, *10*, 1552.
10. Chen, S.; Meng, L.; Chen, B.; Chen, W.; Duan, X.; Huang, X.; Zhang, B.; Fu, H.; Wan, Y. *ACS Catalysis* **2017**, *7*, 2074.
11. Nagpure, A. S.; Gurrala, L.; Gogoi, P.; Chilukuri, S. V. *RSC Advances* **2016**, *6*, 44333.
12. Zeng, L. H.; Yan, H. X.; Zeng, Y. K.; Li, Y. F.; Zhang, Z. X.; Liu, Z. W.; Liu, Z. T. *The Canadian Journal of Chemical Engineering* **2019**, *97*, 2505.
13. Chang, S.; Meng, S.; Fu, X.; Zhang, S.; Zheng, X.; Chen, S. *ChemistrySelect* **2019**, *4*, 2018.
14. Han, Q.; Liu, Y.; Wang, D.; Yuan, F.; Niu, X.; Zhu, Y. *Journal of Chemistry* **2016**, *2016*.
15. Ma, H.; Yu, T.; Pan, X.; Bao, X. *Chinese Journal of Catalysis* **2017**, *38*, 1315.
16. Leng, F.; Gerber, I. C.; Axet, M. R.; Serp, P. *Comptes Rendus Chimie* **2018**, *21*, 346.
17. Nongwe, I.; Ravat, V.; Meijboom, R.; Coville, N. J. *Applied Catalysis A: General* **2016**, *517*, 30.
18. Du, J.; Liu, L.; Liu, B.; Yu, Y.; Lv, H.; Chen, A. *Carbon* **2019**, *143*, 467.
19. Imhof, A. *Langmuir* **2001**, *17*, 3579.
20. Magubane, A. *Synthesis of copper nanoparticles contained in mesoporous hollow carbon spheres as potential catalysts for growing helical carbon nanofibers,* MSc Dissertation, University of the Witwatersrand, Johannesburg, **2017**.
21. Lu, A.-H.; Sun, T.; Li, W.-C.; Sun, Q.; Han, F.; Liu, D.-H.; Guo, Y. *Angewandte Chemie International Edition* **2011**, *50*, 11765.
22. Dlamini, M.W. *Spherical carbons as model supports for Fe, Co and Fe-Co Fischer-Tropsch catalysts*, PhD Thesis, University of the Witwatersrand, Johannesburg, **2016**.
23. Zhao, X.; Zhang, M.; Sun, X.; Li, X.; Li, J.-g. *Applied Surface Science* **2020**, *506*, 144591.

24. Biniak, S.; Szymański, G.; Siedlewski, J.; Świątkowski, A. *Carbon* **1997**, *35*, 1799.
25. Chen, X. Y.; Chen, C.; Zhang, Z. J.; Xie, D. H. *Industrial & Engineering Chemistry Research* **2013**, *52*, 12025.
26. Lamme, W. S.; van der Heijden, O.; Krans, N. A.; Nöllen, E.; Mager, N.; Hermans, S.; Zečević, J.; de Jong, K. P. *Journal of catalysis* **2019**, *375*, 448.
27. Manikai, S. M.-A. *The synthesis of nitrogen doped carbon spheres as supports for palladium catalysts in the hydrogenation of cinnamaldehyde*, PhD Thesis, University of the Witwatersrand, Johannesburg, **2015**.
28. Li, R.; Yao, W.; Jin, Y.; Jia, W.; Chen, X.; Chen, J.; Zheng, J.; Hu, Y.; Han, D.; Zhao, J. *Chemical Engineering Journal* **2018**, *351*, 995.
29. Zhang, L.; Winterbottom, J. M.; Boyes, A. P.; Raymahasay, S. *Journal of Chemical Technology & Biotechnology: International Research in Process, Environmental AND Clean Technology* **1998**, *72*, 264.
30. Lan, X.; Wang, T. *ACS Catalysis* **2020**, *10*, 2764.
31. Sairanen, E.; Karinen, R.; Borghei, M.; Kauppinen, E. I.; Lehtonen, J. *ChemCatChem* **2012**, *4*, 2055.
32. Jiang, F.; Cai, J.; Liu, B.; Xu, Y.; Liu, X. *RSC Advances* **2016**, *6*, 75541.
33. Tessonnier, J.-P.; Pesant, L.; Ehret, G.; Ledoux, M. J.; Pham-Huu, C. *Applied Catalysis A: General* **2005**, *288*, 203.

Chapter 8: General conclusions and recommendations

8.1 Conclusions

Fluorescent carbon dots (CDs) were synthesized using a bottom-up approach method. The CDs were synthesized from the hydrothermal treatment of sucrose, sucrose and oleic acid, and sucrose and urea, under different reaction conditions. From the TEM analysis the CDs synthesized using different sucrose solution concentrations (0.3, 0.15, and 0.1 M) had average particle sizes of 8.4 ± 2.0, 2.2 ± 0.5, and 1.9 ± 0.5 nm respectively, while those synthesized using sucrose and oleic acid had an average particle size of 0.9 ± 0.4 nm. N-doping of CDs using urea led to the formation of CNPs (size ranging between 10 and 100 nm). NCDs (0.15 M + urea) had an average particle size of 4.1 ± 1.2 nm. XPS and FTIR data confirmed the presence of functional groups on the surface of the synthesized materials. The TGA data also confirmed the presence of the functional groups by the decomposition peak observed at temperatures below 250 °C. The fluorescence properties of the materials were confirmed by UV-vis and PL spectroscopy.

The CDs were made so as to explore their use as reducing agents for Pd salts; would the CDs provide a useful method to generate metallic Pd without the use of a more typical reducing agent? The CDs indeed did reduce the Pd salt and the functional groups on the CDs were shown to play a major role in the reduction of H_2PdCl_4 to metallic Pd. This was supported by the quenching of the photoluminescence of the CDs observed in the PL spectra of the Pd/CDs composite. The XPS spectra of the Pd/CDs composite also showed a decrease in the intensity of the oxygenated peaks. PXRD and HRTEM data showed that the Pd NPs were in the metallic state.

Solid carbon spheres (SCSs) and hollow carbon spheres (HCSs) were prepared using resorcinol and formaldehyde as carbon precursors. The TEM analysis showed that the HCSs and SCSs both had a spherical morphology with a hollow and filled core, respectively. Functionalized SCSs (fSCSs) were prepared by a chemical oxidation reaction between the SCSs and an acid mixture. The thermal stability of the SCSs, fSCSs, and HCSs were similar, as shown by TGA data. Pd NPs were loaded on the outer surface of the different carbon spheres using a liquid phase reduction method in which $NaBH_4$ was used as a reducing agent. PXRD and XPS data

confirmed that the Pd was in the metallic state. The XPS data also revealed that Pd was present as Pd/PdOx on all the carbon spheres supports as confirmed by their XPS spectra. TEM images confirmed that the average particle size of Pd NPs supported on SCSs and HCSs were similar (6.0 and 6.4 nm respectively) as opposed to NPs supported on fSCSs (12.0 nm). For comparison purposes, Pd NPs supported on HCSs were prepared using CDs as a reducing agent (Pd/CD/HCSs). The loading of Pd NPs was confirmed from PXRD data and the average particle size of 45.6 ± 26.5 nm was obtained from TEM analysis.

The prepared catalysts were tested in the liquid phase hydrogenation of CALD. Different wt. % loading of Pd were used to prepare the Pd/CDs and Pd/CSs catalysts. This was found necessary as the 1 wt. % Pd/CSs catalysts did not show any activity towards the reduction of CALD. The selective hydrogenation of CALD is known to proceed by different pathways leading to the formation of different products (i.e. HCALD, CA, and 3P1P).

The carbon supports without Pd were tested in the liquid phase hydrogenation of CALD. The CDs exhibited catalytic activity and a CALD conversion of ca. 40 % was obtained. The CDs gave 100 % selectivity towards CA in the reaction. Although it is often said that CNMs are inert, literature reports have shown that CNMs can be reactive. This applies to CDs and they have been explored in different catalytic reactions as carbocatalysts. The CSs did not show any activity.

The prepared catalysts showed different selectivity in the CALD reaction. The use of the 1 wt. % Pd/CDs catalyst gave 100 % selectivity to HCALD and a CALD conversion of about 78 % (reference conditions: T = 80 °C, t = 7 h, 50 mL/min = H_2 flow rate, 100 ml ethanol, mass = 100 mg and 1.32 g CALD). In contrast, the use of Pd/SCSs and Pd/fSCSs resulted in the complete hydrogenation of CALD. The Pd/SCSs catalyst gave 100 % selectivity to 3P1P, whereas the use of 5 wt. % Pd/fSCSs catalyst, resulted in the formation CA as a major product followed by 3P1P, HCALD, and by-products. No attempt was made to identify the by-products.

The 5 wt. % Pd/HCSs gave 100 % CALD conversion and the selectivity towards HCALD decreased with an increase in the reaction time. The complete hydrogenated product (3P1P) was observed and a significant amount of different by-products were detected in the reaction. This observation could be attributed to metal poisoning due to the formation of the by-products that could cover the surface of the active metal sites. In an attempt to load Pd NPs on the surface of the HCSs using CDs as a reducing agent a Pd/CDs/HCSs catalyst was made. Very little of

the CDs remained after the washing step, while the unreacted metal precursor was removed. The 5 wt. % Pd/CDs/HCSs catalyst showed poor activity because of the larger Pd particle sizes (45.6 nm) and HCALD and 3P1P were the resulting products.

The catalyst stability was tested in five runs and the catalyst activity decreased in the following order Pd/SCSs > Pd/fSCSs > Pd/HCSs > Pd/CDs ≈ Pd/CDs/HCSs. Pd/CDs and Pd/CDs/HCSs were the least stable catalysts, and as a result no catalytic activity was observed during a second catalyst recycling. The deactivation of the Pd/CDs catalyst was attributed to the formation of a carbon layer over the Pd NPs and agglomeration of the catalyst. The use of Pd/CDs/HCSs catalyst led to a CALD conversion of around 15 % due to the larger Pd particle size and hence it was no surprise that the catalyst could not be recycled. The Pd/HCSs catalyst stability started to drop in the second cycle and the CALD conversion dropped from 100 % to < 10 % after five cycles. A decrease in the activity of Pd/fSCSs catalyst was also observed and CALD conversion dropped from 100 % to 37 % after the fifth cycle. The Pd/SCSs was the most stable catalyst as only a small change in the CALD conversion (100 to 98 %) was observed after five runs.

The selectivity in the reaction was determined by the adsorption of the CALD (i.e., C=O or C=C bond) on the catalyst sites. In this study, we have demonstrated that there are many factors (i.e. Pd particle size, solvent used, Pd support, and reaction conditions used) that contribute to the adsorption mode of the reactant onto the catalyst which in turn affects the selectivity. For example, the optimum conditions for the Pd/fSCSs catalyst were: 100 mg catalyst, 0.1 M CALD concentration, temperature of 60 °C, H_2 flow rate of 50 mL/min, and a stirring speed of 600 rmp. The use of these conditions led to a high selectivity toward the reduction of the C=O bond, forming CA as a major product. We also noted that the formation of other products (3P1P and HCALD) was minimized under these conditions (< 10 %). Also, the formation of by-products was minimized (< 6 %). The formation of larger amount of by-products was observed when using Pd/HCSs catalyst.

It was noted that the use of the carbon support with a high content of oxygen-containing functional groups contributed to the tuning of the selectivity of Pd catalyst to CA which has also been observed when using a Pt/Ru catalyst. Based on theoretical calculations from the literature, the d-band width of the metal is one of the factors affecting the adsorption mode of the reactant on the metal sites. The Pd metal has a narrower d-band width hence it is expected to be less selective to the C=O bond.

8.2 Recommendations

- Use of CDs as reducing agent:

The synthesis of CDs with larger particle size (> 3 nm) using the hydrothermal treatment of sucrose can be explored further as a reducing agent for the Pd metal salt. This can be useful in controlling the inverse 'metal-support' effect. Also, it would be beneficial to study the effect of nitrogen doping in the Pd/CDs composite in the hydrogenation of CALD. The reduction method used can be further improved to get Pd NPs with particle sizes in the range of 1 to 10 nm and to test the composites in the hydrogenation of CALD.

- The use of $NaBH_4$ as a reducing agent:

The synthesis of Pd NPs supported on carbon spheres with small particle size (< 3 nm) can be explored to enhance the selectivity of the catalyst. For comparison purposes, it would be ideal to improve the reduction method using CDs to get Pd/CDs/HCSs catalyst with well dispersed small particle size in order to improve the catalyst activity of the CALD hydrogenation reaction.

- Carbon support

Synthesis of SCSs using the carbonization of acetylene via chemical vapour deposition can be useful in eliminating/studying the effect of oxygen-containing functional groups on the Pd catalyst (supported on solid carbon spheres) in the hydrogenation of CALD. For the catalyst supported on HCSs, it would be interesting to load the Pd NPs inside the HCSs to see how that would affect the catalyst selectivity and activity in the hydrogenation of CALD.

- Use of bimetallic catalysts

To improve the selectivity of the Pd/fSCSs catalyst towards the reduction of C=O bond, a second metal with a larger d-band (e.g. Os) can be used. The Os catalyst has been reported to be highly selective to CA. This metal can be used to modify the electronic properties of the Pd metal.

- Solvents

To eliminate the formation of by-products, solvents like toluene, dioxane, pyridine, *etc.* can be used as a substitute for ethanol. The use of these solvents has been reported to produce the wanted products (HCALD, CA, 3P1P) without the formation of by-products. Solvents like

pyridine have been used to enhance the selectivity of a Pd/C catalyst towards the reduction of the C=O bond.

Appendix A: Supporting information

(i) Characterization on the Pd/CDs and annealed CDs

TEM analysis

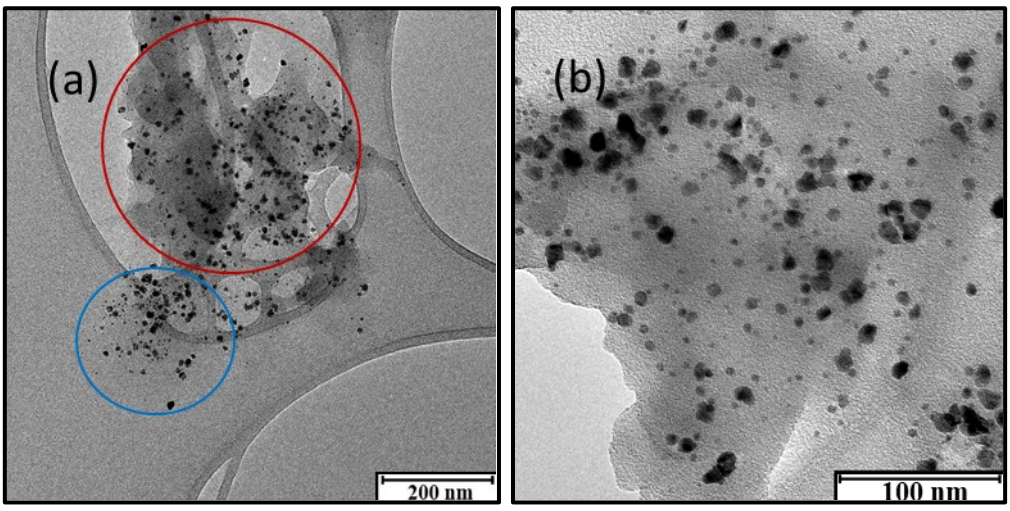

Figure S5.1: TEM images of Pd/CDs catalyst.

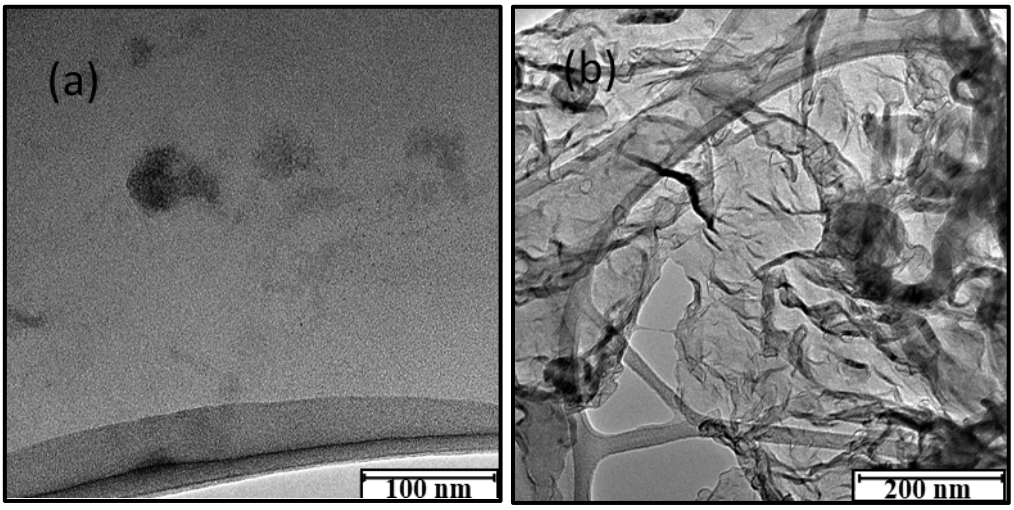

Figure S5.2: TEM images of CDs conversion to (a) aggregates and (b) carbon sheets via annealing at 190 and 300 °C respectivley.

(ii) Characterization data on the fCDs

FTIR and TGA

To identify the surface functionalities present of the synthesized fCDs FTIR was used. FTIR (Fig.S5.3a) of the fCDs showed prominent peaks at 1018, 1711, and a broad peak at 3366 cm^{-1} which corresponds to C-O-C, C=O, and C-OH functionalities respectively. The peaks of the CDs functionalized with 90 % acetic acid were more prominent than those of the as-synthesized CDs.

Figure S5.3b shows the DTG profile comparison of the CDs and fCDs. According to the data, the fCDs was the least thermally stable sample. The DTG profile shows a loss of moisture adsorbed on the surface of the CDs and fCDs at ca. less than 200 °C. The derivative peak at ca. 308 and 310 °C for the CDs and fCDs respectively can be attributed to the loss of oxygen-containing functional groups and amorphous carbon. Most of the core carbon of the CDs and fCDs decomposed at 611 and 494 °C respectively.

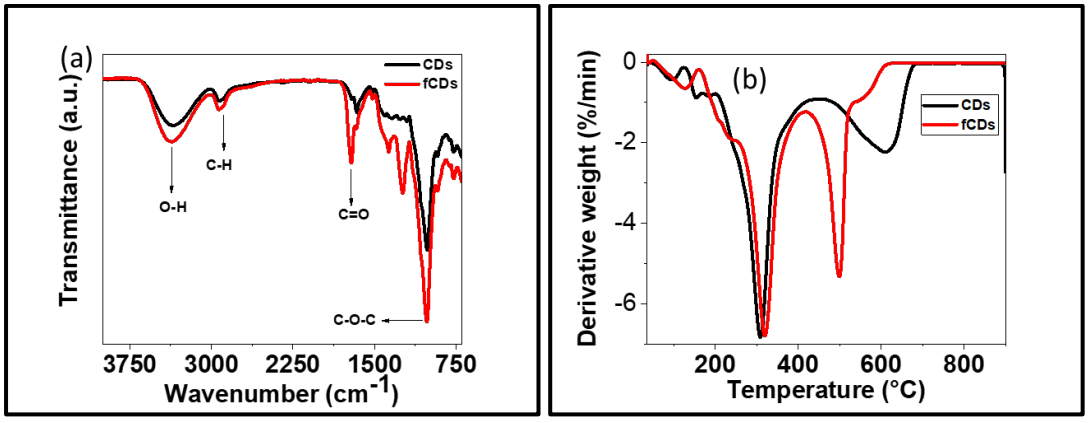

Figure S5.3: (a) FTIR spectra and (b) DTG profile of the as-synthesized CDs and fCDs.

Table S5.1: Comparison of the position of the oxygenated functional groups.

Sample	C-O-H (cm^{-1})	C=O (cm^{-1})	C-O-C (cm^{-1})
CDs	3317	1656	1016
fCDs	3366	1711	1018

(iii) Comparative literature studies

Table S5.2 shows a comparison of different characterization techniques used in this study with those from the literature similar to this work.

Sample	Method	CDs or Pd particle size (nm) [a]	Other techniques		Ref
CDs	Sucrose/oleic acid refluxed at 215 °C for 150 min	0.9 ± 0.4 nm	PXRD peak	18.77 °	This study
			FTIR	Similar oxygenated functional groups	
			XPS (C_{1s})	5 types of carbon (C-C sp^2, C-C sp^3, C-O, C=O, and O-C=O)	
			UV-vis	Peaks allocated at 226 and 284 nm	
			PL (excitation λ of 365 nm)	Emission peak at 471 nm	
CDs	Sucrose/oleic acid refluxed at 215 °C for 5 min	1.84 ± 0.8 nm	PXRD peak	18.06 °	33
			FTIR	Similar oxygenated functional groups	
			XPS (C_{1s})	3 types of carbon (C=C, C-O, and C=O)	
			UV-vis	Peaks allocated at 225 and 280 nm	
			PL (excitation λ of 365 nm)	Emission peak at 461 nm	
Pd/CDs	CDs/H_2PdCl_4 refluxed at 100 °C for 6 h	9.1 ± 1.6 nm	HRTEM observation	No carbon layer over Pd NP	This work
			PL	Photoluminescence of the CDs was quenched	
			XPS	The intensity of the oxygenated peaks was reduced	
Pd/CDs	❖ CDs extracted from clotted cream ❖ CDs/H_2PdCl_4 refluxed at 100 °C for 6 h	❖ 6.6 nm ❖ -	HRTEM observation Ultrathin carbon layer over Pd NP		12
			PL	Photoluminescence of the CDs was quenched	
			XPS	The intensity of the oxygenated peaks was reduced	

[a] HRTEM

iii) Catalytic data

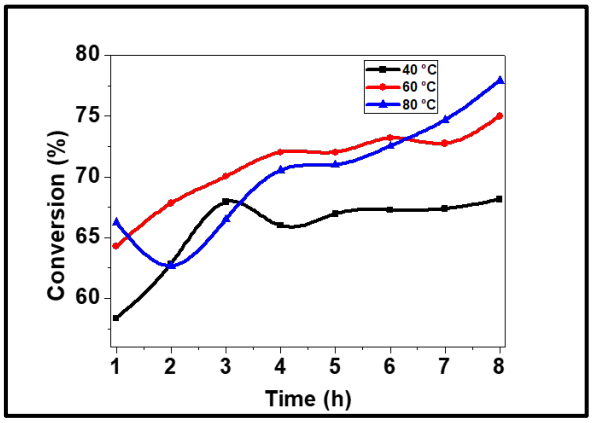

Figure S5.4: The conversion of CALD over Pd/CDs catalyst at different reaction temperatures. Reference conditions: $m_{catalyst}$ = 100 mg, t = 8 h, 50 mL/min = H_2 flow rate, 100 ml ethanol, and 1.32 g CALD.

The effect of CALD concentration over Pd/CDs catalyst was also studied (Fig. S5.5). Increasing the CALD concentration resulted in a slight increase in the CALD conversion. The selectivity of the catalyst remained the same.

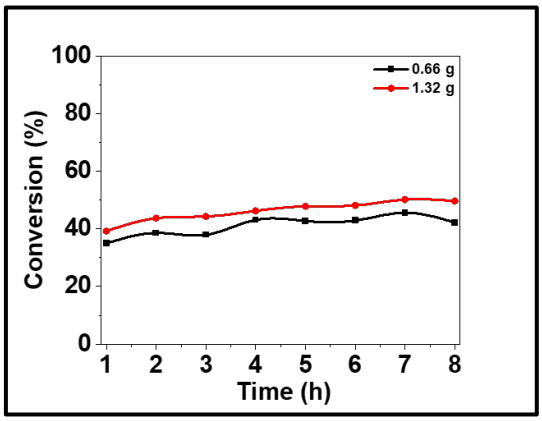

Figure S5.5: The CALD conversion over Pd/CDs catalyst at various CALD concentrations (T = 60 °C, $m_{catalyst}$ = 50 mg, t = 8 h, 50 mL/min = H_2 flow rate, and 100 ml ethanol).

When the activity was calculated per mass of the catalyst used in the hydrogenation of CALD after 7 hours (Fig. S5.6), it can be observed that the catalyst activity increased with a decrease of the catalyst mass used. This could be attributed to a decrease in the number of effective active sites as the amount of Pd present in the catalyst is increased.

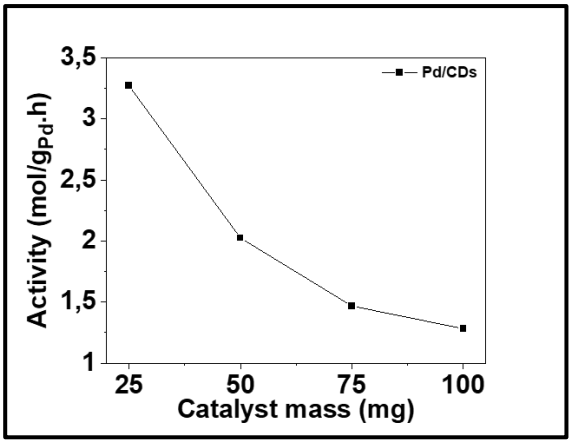

Figure S5.6: Effect of the catalyst mass on the activity of the Pd/CDs catalyst.